University of the Basque Country
-UPV/EHU-

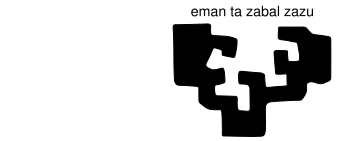

Doctoral Thesis

Millimeter Wave Communications in 5G Networks under Latency Constraints: Machine Intelligence, Application Scenarios and Perspectives

Cristina Perfecto del Amo

Supervised by:
Prof. Dr. Miren Nekane Bilbao
Prof. Dr. Javier Del Ser

A Thesis submitted in fulfillment of the requirements for the degree of Doctor of Philosophy

in the

Department of Communications Engineering

November 22, 2019

"*We should be taught not to wait for inspiration to start a thing. Action always generates inspiration. Inspiration seldom generates action.*"

Frank Tibolt

"*The secret of getting ahead is getting started.*"

Mark Twain

To my parents Gelu and Manu,
for their endless love.

Alberto, "Nire ondoan baziña, ez
legoke itsasorik, ez legoke mendirik zu
eta ni gelditzekorik."
(Gatibu, Nire ondoan baziña)

UNIVERSITY OF THE BASQUE COUNTRY -UPV/EHU-

Abstract

Faculty of Engineering
Department of Communications Engineering

Doctoral Degree

Millimeter Wave Communications in 5G Networks under Latency Constraints: Machine Intelligence, Application Scenarios and Perspectives

by Cristina Perfecto del Amo

Nowadays there is little doubt that wireless communications have been a pivotal player in the irruption and maturity of digital technologies in almost all sectors of activity. Over the years, the society has witnessed how wireless networking has become an essential element of its evolution and prosperity. However, the ever-growing requirements of applications and services in terms of rate, reliability and latency have steered the interest of regulatory bodies towards emergent radio access interfaces capable of efficiently coping with such requisites. In this context, millimeter wave (mmWave) communications have been widely acknowledged as a technology enabler for ultra-reliable, low-latency applications in forthcoming standards, such as fifth generation (5G). Unfortunately, the unprecedented data rates delivered by mmWave communications come along with new paradigms in regards to radio resource allocation, user scheduling, and other issues all across the protocol stack, mainly due to the directivity of antennas and sensitiveness to blockage of communications held in this spectrum band. Consequently, the provision of machine intelligence to systems and processes relying on mmWave radio interfaces is a must for efficiently handling the aforementioned challenges.

This Thesis contributes to the above research niche by exploring the use of elements and tools from Computational Intelligence, Matching Theory and Stochastic Optimization for the management of radio and network resources in mmWave communications. To this end, two different application scenarios are targeted: 1) Vehicular communications, where the high degree of mobility and the recurrent inter-vehicular blockage give rise to complex channel conditions for channel allocation and beam alignment; and 2) mobile virtual reality (VR), where the motion-to-photon (MTP) latency limit raises the hurdle for scheduling the delivery of multimedia content over mmWave. A diversity of intelligent methods for clustering, predictive modeling, matching and optimization for dynamical systems are studied, adapted and applied to the aforementioned scenarios, giving evidences of the profitable advantages and performance gains yielded by these methods. The Thesis complements its technical contribution with a

thorough overview of the recent literature of mmWave communications, leading to the main conclusion stemming from the findings of the Thesis: machine intelligence, provided by any technological means, is a driver to realize the enormous potential of mmWave for applications with unprecedented latency constraints.

Preface

Bilbao: I would like to start by expressing my sincerest gratitude to my supervisors, Assistant Professor Nekane Bilbao and Adjunct Professor Javier Del Ser, for providing the opportunity to pursue my doctoral studies at the University of the Basque Country (UPV/EHU). I wish to specially thank Nekane for her encouragement and perseverance, that eventually succeeded to push me out of my comfort zone to resume my postgraduate studies.

Equally, I would like to thank my colleagues in the Networking, Quality and Security (NQaS) group that, together with the UPV/EHU, provided the financial support for this Thesis allowing me to attend international conferences and summer schools, pay journal publication fees and cover the daily allowances during my research visits. My special thanks go to Armando, an inspirational figure, always ready to provide wise advice. I would probably not be here today if it wasn't for his confidence in me more than 20 years ago. I would also like to thank Luis, my office mate, for his patience and understanding while pretending that he wasn't shocked to find myself self-locked in the office wearing noise-canceling headphones 24/7; yet, you really got me on my nerves! Please forgive me ;)

As for my colleagues at the Department of Communication Engineering, I would like to take the opportunity to thank Ibon and Iñaki Bikandi. Iñaki eskerrik asko pasilotan hainbestetan errepikatu didazun leloagatik, *"Le mieux est l'ennemi du bien"* (Voltaire) to make me realize that everything needs to come to an end. Certainly, the decision to wrap up the Thesis was difficult for me. As for Ibon, I'm deeply grateful to him; whenever I have been in need to cover my lecture/grading duties, I have always found a reliable ally in Ibon. I wish I could buy you a Patricia Urquiola sofa as a thank you present. Unluckily, for that we should have chosen to work on the private sector, right? Hence, feel free to drop by my place and use *my* Patricia Urquiola sofa anytime. Meanwhile you'll have to settle for an assortment of Marimekko Unikko pattern home textiles ;). Finally, I would also like to thank Manolo. Having the Head of the Doctoral Program 6 doors away from your office is invaluable. Even more so, when he is ready to swiftly solve any possible doubt on the procedures or paperwork.

Finland, or more precisely Oulu: This Thesis would have never materialized into its current shape had I not had the audacity to expend my 2015 Xmas alone in Oulu as a visiting researcher at the Radio Access Technologies (RAT) Research Unit in the Centre for Wireless Communications (CWC), University of Oulu. I arrived there with a clean-slate: no first-hand references on anybody and no-idea at all of what to expect. The, on the paper, discouraging average -10°C and 3h of daylight, were soon to become a mere anecdote thanks to the warm and welcoming atmosphere I have enjoyed in every single of my visits there. And, given the 7 times(!) that I will have been to CWC by the time this Thesis proceeds into defense, I could easily fill a whole chapter thanking all the people, many of

them now precious friends, that I have met there along the way. I will try to keep it short, though:

I would like to first and foremost thank former and current members of ICON group at CWC with whom I had the pleasure of working and, occasionally, hanging out: Chen-Feng, Ikram (now in Ericsson, Espoo), Khairy, Kien (now in Nokia Oulu), Mehdi (Head of the group), Mohammed (soon to leave for Nokia Bell-Labs, Espoo), Petri (now in Mediatek), Sumudu and Tamoor (now in Ericsson, Lund). The countless friendly discussions on professional as well as personal matters with them allowed me to stay focused and high-spirited while away from home, for which I am truly grateful.

During my first visit to Oulu I was assigned to office TS415, the former Coffee Room. Having there a fridge, a cooker and a sink plus Shams and Iran by my side (with sporadic visits from Parisa), it really felt like a second home. Iranians are truly the most welcoming people! Back in that time I also met Keigo and Evgeny, who organized the so far my one-and-only tourist visit in Finland to Joulupukin Pajakylä (Santa Claus Village) in Rovaniemi. He also made me taste *salmiakki* (salted licorice) and introduced me to fake Russian gastronomy; Yeah, international restaurants are not Oulu's biggest asset, lol. Big thanks to all of you, and no, salmiakki is not my thing. In my subsequent visits I stayed in TS419 with Tachporn (who kindly volunteered to share her desk and screens with me) and Uditha; later on in TS414 (ICON General Quarters now) with Manosha and Ayo and where, this time, I shared desk with two of my three golden boys: Bamby and Kien. The third one is, of course, Chen-Feng :)

- Chen-Feng, you are the most shy, quiet and reflective of the three. Yet, you were the first person that came to my office and offered me some chat after having spent the whole day sitting alone in the office reading cryptic papers on millimeter waves. I fondly remember our conversations walking back home together in the snow that winter; cooking pasta or buying fresh fish and cheese with Shu-yi and you in the market. Thank you. You will do great things!

- Kien, you were also shy during my first two visits... Then, suddenly, something clicked between us (probably it was caffeine related, as *life without coffee is impossible*); you metamorphosed into *Young&Handsome* and, most importantly, a treasured friend. Seeing how you grew in the face of adversity and remained so self-driven have helped me so much, specially during this last year. For that, for your Chinese Hot Pots and for the *pulla* baking lessons: Thank you, Team Cappuccino rocks!

- Bamby, you missed my first ever lunch party at CWC... Then, shame on you!, you dared ask for a gift before my second visit. And, no, not anything, you specifically asked for *turrón*, lol. Well, almost 4 years later, and after 3 co-authored journals, 1 co-authored conference, 1 co-authored letter and, last but not least, 1 co-authored Coffee Room Silvia espresso machine operating instructions, I think that I have forgiven you ;). I have no words to express how grateful I feel to

have had the privilege (wink, wink) of working with you. Anything you need, and that includes sweats, I'm only one Skype call away from you.

Though a quick screening through the names dropped so far may suggest otherwise, there are actually many Finns working at CWC. Among those in research and research support positions, lämpimät kiitokseni kuuluvat sinulle: Mariella (my Spanish talking pal) and her adorable family, Marja (my contact person in Oulu when I first arrived and she still worked at VTT; Marja, we are so much better now, are we not?) and Kirsi (the most friendly, funny and efficient former Planning Officer and now Research Funding Specialist I have ever met). You all welcomed me at your homes and showed me how the Finns roll :D. Kiitos paljon.

I would also like to thank Jari, Mari and Eija, members of the IT support and administrative staff at CWC, for making my live in CWC/UoO so easy and always encouraging me to join any Xmas/Summer/Faculty Party like part of the staff. While in there, I also learned to appreciate socialization around sauna and its different types; so far *savusauna* and Oulujoki's floating *kesäsauna* being my all-time favorites :).

Lastly, I would also like to extend my gratitude to Prof. Markku Juntti, Head of the Department of Communications Engineering and Dean of the University of Oulu Graduate School (UniOGS), who kindly allowed me in to every single Research Seminar held at the Faculty of Information Technology and Electrical Engineering during my research visits.

Back in Bilbao: Finally, I would like to express my deepest gratitude to my loving family. Your immense love has always encouraged me towards excellence or, should I say "Perfection"? Ama, Aita esker mila beti ere, ta edozertarako, nere ondoan egon izanagatik. Tesi hau zeuei dedikatutakoa da. Mum, Dad, this Thesis is dedicated to you.

I could not conclude without acknowledging the patience of the two living creatures I shared my everyday life with: Ikatz and Alberto. Ikatz, is the King of the house and me just his human food supplier. Yet, listening to him purr while I hold him in my arms and look into his big round pumpkin-colored eyes is so soothing! Playing with him is by far the best therapy after a rough day, and that's priceless.

On the contrary Alberto, my beloved life-companion, often enjoys setting me on fire. Happily, he also knows how to calm me down and help me to disconnect from work when I need it most. Yellowfin, I could never find a better partner in crime for an adventure! Besides, thank you for having always strongly encouraged me to pursue all of my dreams, even when that has meant leaving you behind temporarily. Maite zaitut.

Contents

List of Figures

List of Tables

List of Algorithms

Acronym and Abbreviations

General Terms

2D	**2** **D**imensional
3D	**3** **D**imensional
AoI	**A**ge **o**f **I**nformation
ASIC	**A**pplication **S**pecific **I**ntegrated **C**ircuit
CDF	**C**umulative **D**ensity **F**unction
CPU	**C**entral **P**rocessing **U**nit
DA	**D**eferred **A**cceptance
DPP	**D**rift-**P**lus-**P**enalty
E2E	**E**nd-**T**o-End
FCC	**F**ederal **C**ommunications **C**ommision
GPU	**G**raphical **P**rocessing **U**nit
GPGPU	**G**eneral **P**urpose computing on **G**raphics **P**rocessing **U**nits
HD	**H**igh **D**efinition
i.i.d.	**I**ndependent **A**nd **I**dentically **D**istributed
IF	**I**mpact **F**actor
IP	**I**nternet **P**rotocol
IoT	**I**ntenet **o**f **T**hings
ITU	**I**nternational **T**elecommunications **U**nion
JCR	**J**ournal **C**itation **R**eports
KPI	**K**ey **P**erformance **I**ndicator
LQ	**L**ow **Q**uality
MAC	**M**edium **A**ccess **C**ontrol Layer
M&E	**M**edia **&** **E**ntertainment
NFV	**N**etwork **F**unction **V**irtualization
OEM	**O**riginal **E**quipment **M**anufacturer
PF	**P**roportional **F**air
PHY	**PHY**sical Layer
QoE	**Q**uality **o**f **E**xperience
QoS	**Q**uality **o**f **S**ervice
SD	**S**tandard **D**efinition
SDN	**S**oftware **D**efined **N**etworking
SDTV	**S**tandard **D**efinition **T**ele**V**ision
SoA	**S**tate **o**f the **A**rt
UAV	**U**nmanned **A**erial **V**ehicle
UE	**U**ser **E**quipment
UHD	**U**ltra **H**igh **D**efinition

Wireless/Mobile Communications Related Terms

3C	**C**ommunications, **C**omputing and **C**aching
3GPP	**T**hird **P**artnership **P**roject
4G	**F**ourth **G**eneration
5G	**F**ifth **G**eneration
5G C	**5**G **C**ore
5G NR	**5**G **N**ew **R**adio
5G NSA	**5G N**on-**S**tand**A**lone
5G PPP	**5**G **P**ublic **P**rivate **P**artnership
5G SA	**5G S**tand**A**lone
6G	**S**ixth **G**eneration
AP	**A**ccess **P**oint
BF	**B**eamforming
BS	**B**ase **S**tation
CA	**C**arrier **A**ggregation
CN	**C**ore **N**etwork
CSI	**C**hannel **S**tate **I**nformation
CSMA-CA	**C**arrier-**S**ense **M**ultiple **A**ccess with **C**ongestion **A**voidance
D2D	**D**evice **T**o **D**evice
DC	**D**ual **C**onnectivity
DL	**D**own**L**ink
EHF	**E**xtremely **H**igh **F**requency
eMBB	**E**nhanced **M**obile **B**road**B**and
EPC	**E**volved **P**acket **C**ore
FDM	**F**requency **D**ivision **M**uplexing
HARQ	**H**ybrid **A**utomatic **R**epeat Re**Q**uest
HetNet	**Het**erogeneous **Net**work
HRLLBB	**H**ighly **R**eliable **L**ow **L**atency **B**roadband
IAB	**I**ntegrated **A**ccess and **B**ackhaul
IF	**I**ntermediate **F**requency
IMT	**I**nternational **M**obile **C**ommunications
LOS	**L**ine **O**f **S**ight
LTE	**L**ong **T**erm **E**volution
MBS	**M**acro-cell **B**ase **S**tation
MC	**M**ulti **C**onnectivity
MCS	**M**odulation **a**nd **C**oding **S**cheme
MEC	**M**ulti-access **E**dge **C**computing
MIMO	**M**ultiple **I**nput **M**ultiple **O**utput
mMIMO	**M**assive MIMO
MU-MIMO	**M**ulti-**U**ser MIMO
MNO	**M**obile **N**etwork **O**perator
mmAP	**M**illi**M**eter wave **A**ccess **P**oint
MTC	**M**achine **T**ype **C**ommunications
mMTC	**M**assive **M**achine **T**ype **C**ommunications
MUE	**M**obile **U**ser **E**quipment

mmWave	**M**illi**m**eter **Wave**
NLOS	**N**on **L**ine **O**f **S**ight
NOMA	**N**on **O**rthogonal **M**ultiple **A**ccess
NSA	**N**on **S**tand**A**lone
OFDMA	**O**rthogonal **F**requency **D**ivision **M**ultiple **A**ccess
PER	**P**acket **E**rror **R**ate
QSI	**Q**ueue **S**tate **I**nformation
RAN	**R**adio **A**ccess **N**etwork
RAT	**R**adio **A**ccess **T**echnology
RF	**R**adio **F**requency
RLF	**R**adio **L**ink **F**ailure
RRM	**R**adio **R**esource **M**anagement
RSS	**R**eceived **S**ignal **S**trength
SBS	**S**mall cell **B**ase **S**tation
SCN	**S**mall **C**ell **N**etwork
SFN	**S**ingle **F**requency **N**etwork
SINR	**S**ignal to **I**nterference **P**lus **N**oise **R**atio
SNR	**S**ignal to **N**oise **R**atio
SDMA	**S**pace-**D**ivision **M**ultiple **A**ccess
SO	**S**tochastic **O**ptimization
SON	**S**elf **O**rganizing **N**etwork
SUE	**S**mall **C**ell **U**ser **E**quipment
TDD	**T**ime **D**ivision **D**uplexing
TDM	**T**ime **D**ivision **M**uplexing
TTI	**T**ransmission **T**ime **I**nterval
UDN	**U**ltra **D**ense **N**etwork
UL	**U**p**L**ink
URLLC	**U**ltra-**R**eliable **L**ow-**L**atency **C**ommunication
WiFi	**Wi**reless **Fi**delity
WLAN	**W**ireless **L**ocal **A**rea **N**etwork

Vehicular Communications Related Terms

5GAA	**5G A**utomotive **A**lliance
ADAS	**A**dvanced **D**river **A**ssistance **S**ystems
C-ITS	**C**o-operative **I**ntelligent **T**ransport **S**ystems
C-V2X	**C**ellular **V2X**
DOT	U.S. **D**epartment **o**f **T**ransportation
DSRC	**D**ynamic **S**hort **R**ange **C**ommunication
ESI	**E**xtended **S**ensing **I**nformation
GPS	**G**lobal **P**ositioning **S**ystem
IoV	**I**nternet **o**f **V**ehicles
ITS	**I**ntelligent **T**ransportation **S**ystems
LIDAR	**L**aser **I**maging **D**etection **A**nd **R**anging
LTE-V2X	**LTE**-based **V2X**
NHSTA	**N**ational **H**ighway **S**afety **T**ransportation **A**dministration
NGMN	**N**ext **G**eneration **M**obile **N**etworks Alliance

NR-V2X	5G **N**ew **R**adio based **V2X**
RSU	**R**oad **S**ide **U**nit
V2I	**V**ehicle **T**o **I**nfrastructure
V2N	**V**ehicle **T**o **N**etwork
V2P	**V**ehicle **T**o **P**edestrian
V2V	**V**ehicle **T**o **V**ehicle
V2X	**V**ehicle **T**o **E**verything
vRx	**V**ehicular **R**eceiver
vTx	**V**ehicular **T**ransmitter
vUE	**V**ehicular **U**ser **E**quipment
WAVE	**W**ireless **A**ccess in **V**ehicular **E**nvironments

Virtual Reality Terms

3DoF	**3** **D**egrees **O**f **F**reedom
6DoF	**6** **D**egrees **O**f **F**reedom
AR	**A**ugmented **R**eality
EQR	**EQ**ui**R**ectangular
FoV	**F**ield **O**f **V**iew
HDMI	**H**igh **D**efinition **M**ultimedia **I**nterface
HEVC	**H**igh **E**fficiency **V**ideo **C**oding
HMD	**H**ead **M**ounted **D**evice
mmHMD	**M**illi**m**eter wave **H**ead **M**ounted **D**evice
MR	**M**ixed **R**eality
MTP	**M**otion **T**o **P**hoton
VOR	**V**estibulo **O**cular **R**eflex
VR	**V**irtual **R**eality
VRP	**V**irtual **R**eality **P**layer
XR	**E**xtended **R**eality

Computational Intelligence and Machine Learning Related Terms

ACO	**A**nt **C**olony **O**ptimization
AI	**A**rtificial **I**ntelligence
ANN	**A**rtificial **N**eural **N**etwork
BPTT	**B**ack**P**ropagation **T**hrough **T**ime
CI	**C**omputational **I**ntelligence
DE	**D**ifferential **E**volution
DNN	**D**eep **N**eural **N**etwork
DRNN	**D**eep **R**ecurrent **N**eural **N**etwork
EA	**E**volutionary **A**lgorithm
EC	**E**volutionary **C**omputation
EDA	**E**stimation of **D**istribution **A**lgorithm
ES	**E**volutionary **S**trategy
FA	**F**irefly **A**lgorithm
GA	**G**enetic **A**lgorithm
GP	**G**enetic **P**rogramming

GDR	**G**lobal **D**iscrete **R**ecombination
GRU	**G**ated **R**ecurrent **U**nit
HM	**H**armony **M**emory
HMCR	**H**armony **M**emory **C**onsidering **R**ate
HSA	**H**armony **S**earch **A**lgorithm
ML	**M**achine **L**earning
PAR	**P**itch **A**djustment **R**ate
PSO	**P**article **S**warm **O**ptimization
ReLU	**Re**ctified **L**inear **U**nit
RNN	**R**ecurrent **N**eural **N**etwork
RSR	**R**andom **S**election **R**ate
SA	**S**imulated **A**nnealing
SI	**S**warm **I**ntelligence
SVM	**S**upport **V**ector **M**achine

Symbols and Notations

Indices, Sets and Cardinalities: Agents

i, i'	Targeted and any other vTx
j, j'	Targeted and any other vRx
ℓ_{ij}	Link between a transmitter i and receiver j
b	Base station
u, u'	Targeted UE and any other UE
u_{tr}	Training UE
$\mathcal{C}_k^f$	Targeted Cluster at video frame f
I	Cardinality of vTx
J	Cardinality of vRx
L	Cardinality of links
B	Cardinality of BSs
U	Cardinality of UEs
U_{tr}	Cardinality of training UEs
K	Cardinality of clusters
$\mathcal{I}$	Set of vehicular transmitters
$\mathcal{J}$	Set of vehicular receivers
$\mathcal{L}$	Set of links
$\mathcal{B}$	Set of base stations
$\mathcal{U}$	Set of UEs
$\mathcal{U}_{tr}$	Set of training users
$\mathcal{C}$	Set of clusters

Indices, Cardinalities and Sets: Other

t	Transmission slot index
t_s	Scheduling slot index
T_t	Transmision slot duration
T_s	Scheduling slot duration
T_p	Pilot transmission slot duration
T_{block}	Blockage event re-evaluation interval
T_f	Frame duration

$\mathcal{T}_t$	Set of transmission slots
$\mathcal{T}_s$	Set of scheduling slots
f	Video frame index
f_p	Video frame index for prediction
f_r	Real-time frame index
v	Video
n	Tile index
c_f	Video chunk
F	Cardinality of video frames
V	Cardinality of videos
N	Cardinality of tiles in video frame
$\mathcal{F}$	Set of video frames in a video
$\mathcal{V}$	Set of videos in the catalog
$\mathcal{N}$	Set of tiles in the FoV
$\widetilde{\mathcal{N}}$	Set of tiles in the cluster-level predicted FoV
$\widehat{\mathcal{N}}$	Set of tiles in the predicted FoV

Wireless Channel and Propagation

G	Antenna mainlobe gain
$g_{\triangleleft}$	Antenna sidelobe gain
g_{ij}^{Tx}, g_{ij}^{Rx}	Transmit and Receive antenna gain
θ_{ij}^{Tx}, θ_{ij}^{Rx}	Transmit and Receive antenna alignment error
φ_{ij}^{Tx}, φ_{ij}^{Rx}	Transmitter and Receiver beam-level beamwidth
ψ_{ij}^{Tx}, ψ_{ij}^{Rx}	Transmitter and Receiver sector-level beamwidth
h_{ij}	Channel gain from transmitter i to receiver j
$\boldsymbol{h}$	Channel vector
$\mathbf{H}$	Aggregate global channel state information (CSI)
f_c	Carrier frequency
BW	Channel bandwidth
N_0	Noise power spectral density
p_i	Transmitter vTx transmitted power
I_j	Instantaneous Interference at receiver j
$\hat{I}_j$	Estimated interference at receiver j
$\tilde{I}_j$	Moving-average interference at receiver j
μ_{ij}	Rate from transmitter i to receiver j
$\mu_{\max}$	Maximum rate
$\mu_{b\mathcal{C}_k}$	Rate from BS b to cluster $\mathcal{C}_k$
$\hat{\mu}_{b\mathcal{C}_k}$	Estimated rate from BS b to cluster $\mathcal{C}_k$
μ_{uc_f}	Rate to transmit chunk to user u
τ^{tx}	Transmission delay
τ^{Align}	Beamtraining associated alignment delay

d_{ij}^{2D}	2D distance (in azimuth plane)
d_{ij}^{3D}	3D distance (in elevation plane)
q_i	Transmitter vTx queue
$\bar{q}_i$	Transmitter vTx average queue backlog
$\boldsymbol{q}$	Vector of queues
$\mathbf{Q}$	Aggregate global QSI
q_{max}	Maximum queue backlog size
λ	Average traffic arrival rate
ρ	Traffic load

Matching theory related

U_i^{ij}	Utility of agent vrx for agent vtx
$\hat{U}$	Estimated utility of agent vrx for agent vtx
Ωi, Ωj	Agents i and j matching quotas
$\succ_i$	Strict preference relation for agent i
$\succeq_i$	Non-strict preference relation for agent i

mmWave V2X (Part III) Specific Notations and Symbols

δ	Vehicular channel pathloss exponent
β	Vehicular channel blocker-count related parameter
τ^p	Packet delay
P_s	Packet size
$\bar{\tau}^p$	Average packet delay
$\bar{\tau}^{sch}$	Average delay per packet per scheduling interval
Int	Sensing interest offered
Ext	Sensing extension range
$Avail$	Availability of sensing data
$Area^2$	Sensed area

Mobile VR (Part IV) Specific Notations and Symbols

$B\ell$	Blockage loss
$P\ell$	Pathloss
$S\ell$	Shadowing loss
ς	Shadowing variance
τ^{Commun}	Communication delay
τ^{Comp}	Computing delay
τ^{Edge}	Edge processing delay
τ_{max}	Delay limit
ϵ_d	Delay outage
τ_{MTP}	Motion to photon (MTP) delay

$d_{\mathrm{t2_{MTP}}}$	Time to MTP
τ_{uf}^{tx}	Transmission delay of frame f for user u
$\tau_{uf_r}^{tx}$	Transmission delay of predicted frame index f_p for user u
d_f	Frame deadline
M	Learning model
ϑ	Parameters of the learning model
ν_1	Learning weight in moving average procedure
ν_2	Number of samples moving average procedure
γ	Auxiliary variable
γ_u	Auxiliary variable for user u
r	Traffic admission
$\boldsymbol{r}$	Traffic admission vector
a_u^{tot}	Total traffic admission for user u
$a_{\max}^{tot}$	Maximum total traffic admission
z_u	Virtual queue for auxiliary variable for user u
j_u	Virtual queue for latency constraint for user u
η	Scheduling variable
η_{buc_f}	Scheduling variable for chunk c_f from BS b to UE u
$\boldsymbol{\eta}$	Scheduling vector
s_c	Number of columns in the theater seat layout
s_r	Number of rows in the theater seat layout

Mathematical Operators

$\mathbb{Z}$	Set of integers
$\mathbb{N}$	Set of natural numbers
$\mathbb{R}$	Set of real numbers
$\lvert\cdot\rvert$	Cardinality of the set $(\cdot)$
$\cup$	Union of two sets
$\cap$	Intersection of two sets
$\setminus$	Difference between two sets
$\triangleq$	Equal to by definition
$\mathbb{E}[\cdot]$	Expectation over $[\cdot]$
$\Pr(\cdot)$	Probability of the event
$\mathbb{I}_{(\cdot)}$	Indicator function, i.e. returns 1 if $(\cdot)$ is `TRUE`, 0 otherwise
$\mathscr{L}(\cdot)$	Lyapunov function of $(\cdot)$
$(\cdot)^\star$	Solution of an optimization problem
$[\cdot]^+$	Returns ($[\cdot]$ if $[\cdot] > 0$ and 0 otherwise
$\sigma(\cdot)$	Sigmoid function over $(\cdot)$
$\texttt{tanh}(\cdot)$	Hyperbolic tangent function over $(\cdot)$
$\texttt{ReLU}(\cdot)$	Rectified Linear Unit function over $(\cdot)$
$\boldsymbol{X}^T$	Transpose of $\boldsymbol{X}$

Part I

Introduction

"Begin at the beginning", the King said gravely, "and go on till you come to the end: then stop."

Lewis Carroll, *Alice in Wonderland*

Chapter I.1

Introduction

> "You see, wire telegraph is a kind of a very, very long cat. You pull his tail in New York and his head is meowing in Los Angeles. Do you understand this? And radio operates exactly the same way: you send signals here, they receive them there. The only difference is that there is no cat."
>
> Albert Einstein

This first chapter aims to introduce the reader into the motivation and the main objectives of the Thesis. To that end, it starts by providing an introductory overview on fifth generation (5G) communications and networks. Therein, the focus is set on the wireless radio access network (RAN) part of the mobile network architecture and in the use of higher frequency bands to, over and above many other different approaches, administer the capacity upsurge foreseen to support 5G targeted performance indicators. The distinctive characteristics of the millimeter wave (mmWave) frequency band are briefly presented, and the biggest challenges associated to operating communications in this spectrum are summarized.

The increasing complexity of wireless/mobile networks coupled with the new challenges brought out by the use of higher frequency bands pave the way towards the main motivation behind this Thesis; in a nutshell, the use of inter-disciplinary approaches from wireless communications and from computational intelligence (CI)/machine learning (ML) to optimize the performance of future mmWave applications. Specifically, applications pertaining to two of the currently most promising 5G vertical industries will be considered: the automotive industry through vehicular communications and media & entertainment (M&E) sector through mobile virtual reality (VR).

The last part of the chapter provides a rundown of the structure of the Thesis, providing hints in the form of recommended reading tracks, and summarizing the contents of its different parts. The chapter concludes with several indications on the use of abbreviations and on the enforced mathematical notational conventions throughout the remainder of the document.

I.1.1 Millimeter Wave Communications in 5G and Beyond Networks

5G, the commercial term coined to describe the upcoming-generation of mobile networks ahead of today's fourth generation (4G) Long Term Evolution (LTE), aims at extending radio services to various vertical industries. For that purpose, along with other future communication systems, these networks are expected to serve applications with varying requirements, be adaptive to dynamic topologies, and take autonomous decisions for efficiency and resiliency purposes, by and large rendering more complexity and challenges to wireless communications.

I.1.1.1 5G Core Services

Unlike any other previous cellular network generation upgrade, how 5G is architected and deployed by mobile network operators (MNOs) will strongly depend on how the network is used to provide unique, vastly distinctive requirements that support ultra-high traffic volume density (1000× capacity increase), ultra-high connection density (10x-100x connected devices), ultra-high mobility (up to 500 km/h), Gbps rates, and/or sub-millisecond latencies. Such expectations are perhaps too ambitious and unrealistic to be met holistically. Nonetheless, the dominant 5G feature and key to capitalize on, is precisely the requirement diversity. Indeed, the latter called for the early identification of three core generic services, namely the omnipresent enhanced mobile broadband (eMBB), massive machine type communications (mMTC) and ultra-reliable low-latency communication (URLLC) by ITU-T[1] as reported in [1]. The priority targets in this envisaged core service triangle are succinctly summarized below:

- eMBB is directed towards bandwidth-greedy services, characterized by very high peak data rates over stable/long connections.
- mMTC is devoted to supporting a large density of connected Internet of Things (IoT) devices. These devices, that are only intermittently active to send small data payloads, need to operate under energy efficiency considerations, providing both sensing and actuation functionalities.
- URLLC comprises services with stringent requirements on availability, latency and reliability, and also addresses high mobility.

Fig. I.1.1 provides a graphical representation of the diverging relevance of the eight targeted key performance indicators (KPIs) for the above three 5G core services. The minimum technical performance requirements approved for IMT-2020 are covered in [2].

[1]The International Telecommunications Union (ITU) is the ultimate international standards body in charge of releasing the final 5G standard denoted International Mobile Communications 2020 (IMT-2020), and that should be submitted by the Third Partnership Project (3GPP), the mobile industry standards body, as Release 16 by the end of 2019.

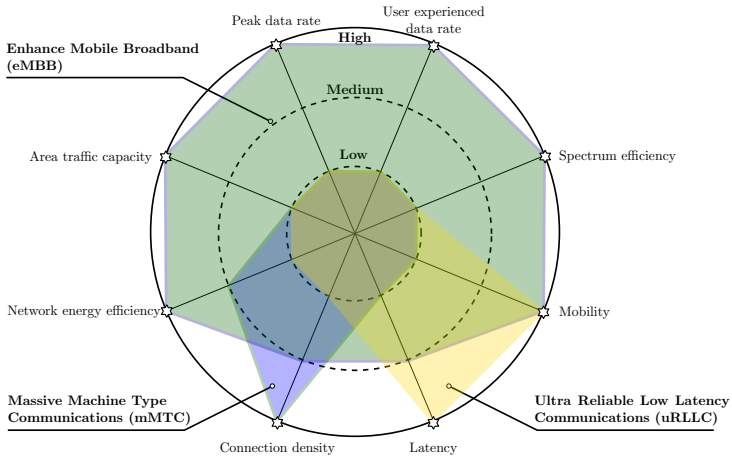

FIGURE I.1.1: Spydergraph showing the importance of eight key 5G capabilities for the envisioned 5G core services. Source: Rec. ITU-R M.2083-0 [1].

5G is expected to allow the coexistence of all these use cases over the same physical infrastructure, by carving dedicated virtual mobile "sub-networks" or *network slices* [3]–[6]. These network slices dynamically scale and timely adapt to heterogeneous end-user service requirements, enabling both multi-tenancy and service-tailored composition of mobile networks. Doubtlessly, the eventual transition of 5G to a cloud native network represents a major transformation in communication network architectures [7] which does not only affect its core network (CN) but also includes the RAN. To that end, for agile, scalable and flexible network management, the concepts of network softwarization, and virtualization [8], in other words, the programmability of the mobile network, are being leveraged with software defined networking (SDN) [9], [10], network function virtualization (NFV) [11] and multi-access edge computing (MEC) [12] as pivotal design principles of the 5G architecture [13], [14].

I.1.1.2 5G NR: Timeline and Characteristics

The roadmap for the rollout of 5G was designed from its inception based on two separate streams: the evolution of the mobile CN and, the development of a new radio access technology (RAT). The focus of the former was enhancing the evolved packet core (EPC) mobile core through improvements in LTE, LTE-Advanced and LTE Pro technologies while designing a new cloud-native 5G Core (5G C). As for the latter, it embodied a major breakthrough with the introduction of a global standard, namely 5G New Radio (5G NR), for an entirely new and flexible air interface[2]. The reason behind this separation is that, as opposed to the deployment

[2]In cellular networks the air interface is the radio frequency portion of the circuit between a mobile device –usually referred as mobile user equipment (MUE)–, and its active base station (BS) which, if the MUE is moving, alternates over time according to a procedure known as handoff/handover.

strategies of all previous mobile generations, in 5G deployments the access and core network no longer need to belong to the same generation. Thus, MNOs may adopt whichever of the available configuration options defined by 3GPP that best suits their migration/deployment strategy [15]. These configurations fall within the broader categories of standalone (SA) and non-standalone (NSA) deployment scenarios depending on whether a single RAT is used or multiple RATs are supported. The overarching goal is to enable a smooth phased evolution and tight interoperability facilitated through dual connectivity (DC)[3] and dynamic spectrum sharing (DSS)[4] features in 5G modems/user equipments (UEs).

Focusing on the new air interface, the first interim set of specifications for 5G NR was released by 3GPP in December 2017 [16], [17]. These specifications defined the use of 5G NR in 5G non-standalone (5G NSA), that is, operating 5G by relying on the existing EPC from the 4G network for the control plane, as opposed to 5G NR, that is focused exclusively on the user plane. In this manner, it is expected that LTE will remain an integral part of the early stage 5G rollouts, and supplement the limited footprint of current 5G networks with a wider coverage. In June 2018, the standard was extended to support 5G NR in 5G standalone (5G SA) mode by providing a complete set of specifications [18], [19] for the next-generation core network 5G C whereby a 5G base station (or gNB) is allowed to act as a master node without backing on any legacy network, neither for signaling nor for information transfer purposes.

The physical layer (PHY) standard for this new RAT lays the foundations to improve the performance, scalability and efficiency of current mobile networks, and provides a flexible structure to support the wide variety of devices (mobile, pc, tablets, wearables), deployments (traditional macro to hotspot) and services encompassed by 5G. Undeniably, 5G NR is decisive to unlock the full potential of 5G beyond eMBB. Accordingly, 5G NR will blend new technologies and operate across diverse spectrum (be that licensed, shared or unlicensed) bands. 5G NR notably extends the range of spectrum in which the radio-access technology operated so far; in addition to the traditional below 1Ghz and below 6 GHz macro-bands, it also includes the use of higher frequencies i.e., the mmWave band.

Some of the most relevant new features in 5G NR as per 3GPP Release 15 include an orthogonal frequency-division multiplexing (OFDM)-based air interface with scalable numerology and, self-contained slot duration and flexible structure to address the aforementioned diversity in spectrum, services and deployments. Besides, the release also features advanced channel coding schemes such as multi-edge low-density parity check (ME-LDPC) or CRC-aided polar (CA-polar) channel coding, reciprocity based multi-user

[3] In DC data may be sent and received from two mobile networks simultaneously e.g., 4G and 5G, to provide much faster connectivity. Once the traffic from each network, each in its own spectrum, reaches the DC-enabled device, contents will be seamlessly aggregated.

[4] DSS allows for the coexistence of 4G LTE and 5G NR users simultaneously in the same frequency band/channel with the MNO's base station (BS), having channel resources dynamically divided at each cell site.

MIMO (MU-MIMO) for an optimized massive MIMO (mMIMO)[5] design and, particularly for the purpose of this Thesis, beamforming and beam tracking for mobile mmWave.

Indeed, the largely anticipated 1000-fold improvement in system capacity –defined in terms of bits per second per square kilometer b/s/km^2– needed to alleviate the capacity crunch will be facilitated in the RAN through the combined use of increased spectrum/bandwidth, higher network densification, and improved spectral efficiency [20]. Accordingly, 5G communications were rightly predicted to be highly heterogeneous, encompassing an amalgamation of technologies spearheaded by the so-called "big three" 5G technologies [20]: ultra-densification, massive multiple input multiple output (MIMO) and, last but not least, mmWave frequency communications. Given the congested sub-6 GHz spectrum, the only feasible option to increase the bandwidth coming into play, is to go up in frequency and, consider mmWave and, in a longer term, Tera-Hertz frequency communications [21], [22].

Across the globe in the first half of 2019 more than 30 launches of the first 5G NSA commercial deployments went underway [23], [24]. Among those, some of the MNOs in North America, Italy, Russia and Japan are doing so by deploying their networks in both sub-6 GHz and mmWave spectrum. Although all these deployments orbit around eMBB operation complemented with moderate latency improvements as per Release 15 [25], in the next years through Release 16 and the soon-to-be-defined scope of Release 17, it is expected that 5G NR will span to areas such as industrial IoT, boundless interconnected extended reality (XR) or evolving 5G for smart transportation through cellular V2X (C-V2X), where the latency plays a prominent role.

I.1.1.3 Millimeter-wave Communications

Motivated by the spectrum shortage below 6 GHz, communications in the radio frequencies encompassing the electromagnetic spectrum from 30 to 300 GHz, i.e. the mmWave or ITU's extremely high frequency (EHF) band, came into the spotlight around 8 years ago. Ever since, they have been attracting a growing attention [20], [26]–[28], to the point of being currently considered the most important foreseen technology to achieve the 10 Gbps peak data rates in upcoming 5G systems [29]. Fig. I.1.2 provides an overall idea of the location of this frequency band in relation to classical mobile/wireless communication bands in microwaves frequencies.

Having abundant available spectrum, the main appeal of mmWave communications comes from the use of generous bandwidths that range from the 0.85 GHz in the 28 GHz band[6] to 5 GHz in the 73 GHz band. These bandwidths are more than ten times greater than LTE's 20 MHz cellular channel [30], and allocate multi-Gbps data rates, important channel

[5]Massive MIMO refers to a communication scenario where the number of antennas in the gNB is much higher than the number of users.

[6]For commercial use, mmWave is the umbrella term used to refer to any frequency band beyond 24 GHz.

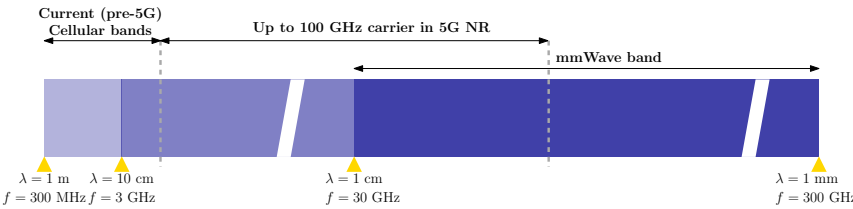

FIGURE I.1.2: Graphical representation of the location of the mmWave frequency band with respect to cellular/wireless operational ranges in the frequency spectrum.

capacity increase favored by the dense spatial reuse [31], and a lower latency that grants unprecedented opportunities in vertical sectors such as transport, media, and manufacturing.

Unfortunately, signal propagation at these frequencies is harsh and inherently different from that at the microwave band [32], experiencing:

- Higher pathloss for equal antenna gains, which is due to a stronger atmospheric attenuation whereby signals are more prone to being absorbed by foliage and rain.
- Higher transmit power consumption to preserve an equal signal-to-noise ratio (SNR) than in lower bands.
- Higher penetration losses, as mmWaves are blocked when trying to pass through walls, buildings, or obstacles.

To overcome these severe propagation issues, high-gain directional antennas together with advanced signal processing techniques that include MIMO [33] and beamforming (BF) are fundamental.

I.1.1.3.1 Main Challenges in Mobile mmWave Communications

In the next chapters a series of proposals will be discussed to quantify and/or reduce the delay incurred, as well as to counteract intermittent blockages and temporal channel disruptions while operating communication links in the mmWave spectrum for vehicle-to-vehicle (V2V) and mobile VR use cases. All these proposals tackle one or several of the three main challenges identified in [34] to scale mmWave communications, and which are described in what follows:

mmWave Beamforming/Beam Training

Due to the shorter wavelengths of mmWaves, it is possible to pack more antenna elements into the phased antenna arrays at the transmitter and receiver devices. Hence, the spatial degrees of freedom granted, favor the use of analog, hybrid or digital BF architectures [36], [37] to build a radiation pattern with narrow beams where, ideally, the energy radiated through the sidelobes is minimized or negligible.

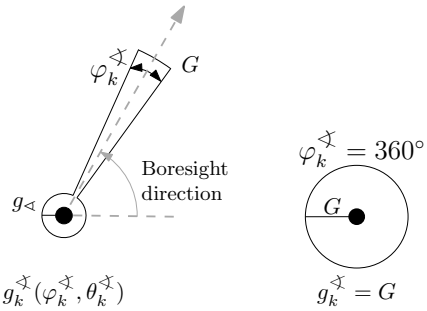

FIGURE I.1.3: Ideal highly-directive antenna (left) vs. omnidirectional antenna (right) radiation patterns. In the directive antenna model as per [35], the alignment error angle, $\theta_k^{\measuredangle}$ will determine if transmission/reception occurs through the mainlobe or sidelobes, with gains G or $g_{\triangleleft}$, respectively. In the former case, the antenna gain will also depend on the beamwidth $\varphi_k^{\measuredangle}$, with narrower beamwidths leading to higher antenna gains.

Yet, to take full advantage of this high-gain directionality, first the most suitable directions for transmission and reception need to be determined. If line-of-sight (LOS) operation is considered, the above implies that the mainlobes of the antenna radiation patterns at both ends of the communication link need to be aligned. The procedure to steer the boresight direction, i.e. the orientation of the mainlobe, of an antenna radiation pattern towards a given target is known as *beam training*, and constitutes an essential mechanism in mmWave both to enable a fast communication link setup, as well as to accommodate to changes in the environment. Moreover, as it will be further detailed, the efficiency of the beam training is crucial and might compromise the overall efficiency of the mmWave communication system.

Analog, digital and hybrid analog-digital BF architectures exhibit different advantages and drawbacks to perform the beamforming/beam training. In fully digital MIMO architectures, all the signal processing is performed at baseband, requiring one dedicated radio-frequency (RF) chain per antenna. Therefore, the elevated number of RF chains required inflicts unaffordably high power consumption and hardware costs, that ultimately discourage its prompt use in the mmWaves frequency band. By contrast, analog BF architectures only involve the use of one RF chain, providing a low hardware and power solution, at the expense of being limited to operate a single data-stream transmission and to have minimal signal adjustment capabilities through analog phase-shifters applied at RF or intermediate frequencies. The latter entails having greater difficulties to fine-tune beams to adapt to varying channel conditions, and may induce substantial performance loss.

Hybrid analog-digital BF, which was agreed to be deployed in 5G systems during the 3GPP RAN-1 meeting [38], strikes a balance between performance, complexity and power. Hybrid BF can be seen as an extension of analog BF to multiple data-streams scenarios; as the number of effective

scatterers in mmWave is limited, users will have a low-rank MIMO channel matrix, leading to an optimal number of data-streams smaller than the number of antennas. Hence, many less RF chains are necessary. Based on this principle, the precoding and combining from traditional digital signal processing are realized in hybrid BF by combining a large-size analog signal processing with a reduced-size digital signal processing stage. However, motivated by its reduced implementation complexity, analog BF has been the adopted scheme for indoor mmWave wireless local area networks (WLANs) operating in the 60 GHz unlicensed band, e.g., in 802.11ad [39], [40] and 802.11ay [41], [42].

Focusing on the specificities of analog beamforming, its beam training procedure involves selecting the most suitable beamforming vectors that, to reduce complexity and overhead, are usually part of a predefined set compiled in a *codebook*, e.g., [43]. To find these vectors, a multi-stage hierarchical search is usually adopted; performing an exhaustive search through all the possible beams and then choosing the one that maximizes the signal-to-interference-plus-noise ratio (SINR) over the link would be highly inefficient and well as being hardly applicable at scale[7]. The whole process encompasses a several search steps described as a *beamforming protocol* or *adaptive beamforming sequence* e.g., [44], [45], aimed to cut down the training overhead by narrowing down the search space.

Other more advanced beamforming techniques exist. For instance, the use of compressive beam training that capitalizes on the the sparseness of the mmWave multipath channel [46]–[48] and hybrid or digital beamforming [49]–[51]. Thanks to their inherent flexibility, they are better suited for adaptivity and are able to probe several directions at the same time effectively reducing the time involved in the process by exploiting multidirectional transmission and reception. Nonetheless, the use of these along with other alternative beamforming techniques, is beyond the scope of the present Thesis.

Impact of Channel Dynamics and Mobility

The difficulties to efficiently find and secure the most suitable beamforming vectors along time are aggravated in dynamic environments. Under these circumstances, time-varying channel impairments and mobility of the transmitter-receiver devices might hinder the communication, leading to beam misalignment or signal blockage [52] calling for protection mechanisms against the mmWave-link intermittency [53].

The strategies to avoid operating mmWave communications through sub-optimal –misaligned– beams or with partially blocked signals entail tracking the counterpart device. The key premise of these strategies is basically to either perform a periodical beam training e.g., the approach adopted in 802.11ad, or trigger a full new directional channel discovery process whenever the SINR drops below a certain threshold. In the latter case, the need to redo the beam training originates from the fact that the

[7]Notice that a substantial training overhead would be needed to sound all directions using a high-resolution narrow beam to obtain an accurate channel estimation.

degradation in the link quality might, otherwise, compromise the correct signal decoding.

Despite the high latencies induced by exhaustive/hierarchical sequential scanning, synchronously or asynchronously starting a new beam training might serve in moderate to low mobility environments. However, for highly dynamic environments, even if the most advanced beam training schemes are enforced, the overhead might turn into a limiting factor to support a seamless data provisioning.

No wonder, beam management [54] has become one of the key aspects to mobilize mmWave for 5G [55]. As such, a large and growing body of literature has investigated novel solutions that either:

1. thrive on information from sub-6 GHz bands[8] [50], [57] to reduce the search space e.g., by estimating the feasible angle of arrival (AoA), or by predicting when a link will be available again [58],

2. use past link information to initiate the feasible antenna sector search, and gradually broaden the search space around it to re-establish a link [59] on the principle that movement is usually continuous,

3. leverage the fact that movement is generally highly predictable [60] to reliably predict future beam steering angles from past information, or

4. benefit from on-device built sensors e.g., accelerometers and gyroscopes, to determine rotation and movement [61].

Of particular interest for the scope of this Thesis is the case of beam management in vehicular networks [62] –which are covered in Part III–. In these network scenarios, vehicles can narrow down their search space and track BSs, road side units (RSUs), or nearby vehicles by merging the abundant information collected from their camera, radar, laser imaging detection and ranging (LIDAR) and global positioning system (GPS) devices [63], [64]. Moreover, this information can be aggregated to learn from and adapt to the environment with ML predicting the locations or the best beams [65]–[67].

AP/BS Selection and/or D2D/V2V device Pairing

In practice in cellular and wireless networks, when a MUE is in the connected state uplink (UL) control channels are used to periodically feed back to the BS/access point (AP) its best transmit beam index; in like manner, downlink (DL) control channels are used to report MUEs' best transmit beams back. Data transmission is then performed through the best beam pair. Yet, beam training has a major impact on the performance of control mechanisms such as initial access [68]–[70], random access/handover [71],

[8] An additional benefit of dual or multi-band devices that are equipped with sub-6 GHz and mmWave interfaces is the ability to provide a communication fallback to supplement/replace relaying in case the mmWave link breaks [56] protecting against the aforementioned mmWave-link intermittency.

or in user association [72], [73] i.e., whenever the information on the best beams is not available in advance and thus hinders getting full benefit from BF.

Any device performing an initial access, that is registering as an active user in a wireless network, must undergo beam training no matter whether the mmWave network is cellular based or wireless-fidelity (WiFi) based. Thus, the challenges faced by the access schemes designed to that purpose are alike. These challenges are mostly related to the need for performing a directional transmission of the control messages. The reason underneath is that the coverage levels offered by mmWave deployments with respect to microwave band ones are mismatched. For instance, even if a device is within the directional transmission range of another device, it might not be so in the omnidirectional coverage range of microwave bands. Analogously, due to uneven susceptibility to penetration and diffraction losses, one device may not reach a second device because the mmWave band signal is blocked, while the devices are perfectly reachable to one another in lower bands.

In random access/handover, the problem is worsened as many potential BSs/APs[9] might be within range. Hence, arbitrarily choosing a single BS/AP to connect to may turn suboptimal and in that it may lead to i) having to operate with a low quality channel, ii) in an overloaded cell or iii) connected to a cell whose coverage area will be soon discontinued due to the mobility of the device, triggering a full new handover. Consequently, the device should perform the beam training with all the BSs/APs in its vicinity; a combinatorial complexity association problem. Device-to-device (D2D) or V2V communications scenarios further exacerbate the association problem, as potentially all the devices within range would need to carry out beam training with each other, so as to facilitate future device pairing. In this context, it is deemed that having *a priori* location-related information is key to make such scenarios feasible at scale.

I.1.2 Motivation and Objectives

Driven by the human-centric nature of communications and the prevalent delay-tolerant content exchanges, wireless networks have been traditionally designed and deployed with a focus on improving throughput and increasing coverage. Achieving ultra-low latencies hand in hand with unprecedented high-reliability levels, was not a mainstream requirement for most wireless networks. Moreover, most current mobile systems employ centralized resource allocation schemes, which are inappropriate as they unleash a significant control overhead and incur into severe latency.

Nonetheless, with the advent of 5G and confronted with the demands of a plethora of socially useful applications and disruptive new uses of wireless communications, the new releases of mobile cellular networks –mainly focusing on 5G NR– are expected to cater for scenarios with extremely strict

[9] mmWave network operation involves dense deployments of BSs/APs to provide good coverage and high capacity connections

requirements in terms of latency. Such scenarios and applications, whose latency requirement range from 1 ms and below to few ms end-to-end depending on the use case, are envisioned for areas as diverse as industrial control, automated driving, unmanned autonomous vehicles (UAVs) flying, mission-critical IoT, remote robotics, smart grid, augmented and virtual reality (AR/VR) and tactile Internet.

Realizing low latency communications poses significant theoretical and practical challenges, requiring a departure from throughput-oriented system design [74] towards a holistic view that includes network architecture, control, and data for guaranteed and reliable end-to-end latency [75], [76]. In this context, the recent advances in artificial intelligence (AI), which is defined as any process or device that perceives its environment and take actions that maximize the chances of success for some predefined goal, including those in ML, hold significant promise for addressing many complex problems in wireless networks. It is appropriate to apply AI technologies to tackle accurate channel modeling, optimized physical layer design, flexible spectrum access, and complicated network deployment, automation, optimization, and management issues in the wireless domain. Emerging ML approaches have also brought excellent opportunities to further investigate essential and so far unexplored characteristics of wireless networks, and to help make breakthrough in wireless communications, via novel radio and networking techniques, including new architectures, algorithms and protocol designs.

The above rationale serves as the main motivation for this Thesis that, from its inception, was conceived with the synergistic resolution of merging optimization techniques from CI, specifically those pertaining to the broad families of heuristic optimization e.g., evolutionary computation (EC), swarm intelligence (SI), etc. and ML, to solve resource allocation problems in next generation wireless communications application scenarios.

Thus, the research hypothesis postulated in this Thesis is that by virtue of their intelligence and self-learning capabilities, CI techniques can be a perfect match to cope with the level of complexity of computational problems underlying mmWave-based applications. In consonance with the aforementioned motivation, and considering the innate characteristics of signal propagation at mmWave communications, the primary goal pursued by the Thesis is:

WHAT?

The **application of CI** techniques **to tackle in an efficient, intelligent and autonomous manner the challenges of** operating **latency-constrained and scalable** wireless **communications in the mmWave frequency band**.

The fulfillment of the above main objective relays on a set of secondary goals that, working at different levels, provide the necessary building blocks or HOWs. The first set those secondary goals is related to becoming proficient on the different areas that constitute the background of the Thesis:

HOW?

1. Acquiring a deep understanding of heuristic solvers and ML algorithms, with an emphasis on their applicability to real problems.
2. Grasping a general understanding of current and prospective wireless/mobile technologies PHY operation, while becoming acquainted with the main challenges of operating communications in the mmWave band.

Once the foundations have been laid, a third goal can be set, which is oriented towards the validation of the first goal over several wireless scenarios:

HOW?

3. Investigating the most common mathematical frameworks for resource allocation and topology optimization. The focus will be set on finding the niche where heuristic optimization solvers and ML could be integrated to complement/extend these mathematical frameworks.

The last set of secondary goals are geared towards validating the applicability of CI in 5G scenarios to bring the desired levels of efficiency, intelligence and autonomy, while the latency is kept bounded. The adopted scenarios to substantiate the original hypothesis are:

WHERE?

1. Vehicular Communications, specially V2V scenarios that, when held over highly-directive mmWave radio interfaces, are prone to blockage and misalignment events due to the high-mobility environment.
2. Mobile VR, where the use of high-capacity mmWave links is envisioned as a replacement to wired/tethered connections to cope with the extremely high bandwidth demands that must be sustained.

To that end, this Thesis proposes both centralized and distributed algorithms for innovative advances in the above areas. During the development of this Thesis, all of these objectives have been addressed individually or jointly. Table I.1.1 provides a visual reference of which parts/chapters of this Thesis cover each of the secondary goals, moreover it also reflects which of these goals are addressed in the scientific production in the form of journal articles and international conference papers produced during the course of the postgraduate studies.

TABLE I.1.1: Twofold mapping between the secondary goals set for the Thesis and 1) their coverage along the Thesis document, 2) derived journal and conference publications.

		Part	Chapter	Scientific Production[10]	
				Journal publication	Conference paper
WHAT	**HOW-1**	II	II.1, Appendix A	[**J5**], [**oJ6**],[**oJ8**]	[**C1**], [**C2**] [**oC14**], [**oC15**]
	HOW-2	I	I.1;III.1;IV.1	[**J3**]	[**C3**]
	HOW-3			[**oJ7**]	[**C4**], [**oC9**],[**oC12**],[**oC13**]
	WHERE-1	III	III.2;III.3	[**J1**]	[**C5**],[**C6**]
	WHERE-2	IV	IV.2;IV.3	[**J2**],[**J4**],[**L1**]	[**C7**]

The advances and proposals from this Thesis spread beyond 5G, as they rise further awareness around the major role of CI, and more generally speaking AI, for all future wireless networks; an unstoppable reality buttressed by recent publications such as [77], that questions the survival of 5G in the absence of AI, or [78], the first whitepaper on sixth generation (6G) networks, that elaborates on the drivers and challenges for 6G wireless intelligence.

I.1.3 Thesis Outline

The main body of this Thesis is structured around five separated parts, each comprising at least one chapter. In addition to these parts, a final supplementary chapter in included as an appendix.

Part I is meant to be a smooth introduction to guide the reading of the core of the Thesis. From this point forward, the contents corresponding to Part II are aimed to provide a general background on the research methods, i.e., the mathematical tools and frameworks used throughout the Thesis. Subsequently, Part III and Part IV comprise an introductory chapter and two application examples for each of the selected scenarios of mmWave communications in 5G networks i.e., mmWave vehicle-to-everything (V2X) communications and mmWave-enabled mobile VR. Part V draws the concluding remarks, details the list of publications derived from the research work, and outlines open challenges rooted on the findings of the Thesis.

The last part of this Thesis, included as Appendix A, is dedicated to the study of the effect of classical versus multi-breeded crossover operations over the topological features of a specific tree coding scheme, the Dandelion code. This work, which was indeed chronologically the first research topic investigated in this Thesis, can find its applications in wireless (and wired) communications when multi-hop scenarios are considered, *e.g.*, in [79]–[81]. Nonetheless is not *per se* specifically related to mmWave communications, being rather agnostic with respect to the underlying technologies.

[10]The complete bibliographical details corresponding to the publications specified here are to be found in Section V.1.2 of Chapter V.1. In that regard, the keys from this table match those of the listings provided in the aforementioned Section.

For this reason, it has been placed separately from the rest of chapters that constitute the main body of the Thesis.

Next, a brief summary of the motivation behind each part/chapter of the Thesis is provided.

I.1.3.1 Part II: Research Methods

This chapter aims to provide an overview of the different techniques used throughout this Thesis to tackle wireless network optimization problems. The ultimate goal of this chapter is to provide an updated, thorough, and rigorous compilation of the tools and possibilities that CI, ML, matching theory and stochastic optimization for queuing networks offer, so that these tools are left defined and their main operation principles explained for the rest the dissertation.

I.1.3.2 Part III: mmWave Application Scenarios: V2X Communications

I.1.3.2.1 Chapter III.1

Recently mmWave bands have been postulated as a means to accommodate the foreseen extreme bandwidth demands in vehicular communications, which result from the dissemination of sensory data to nearby vehicles for enhanced environmental awareness and improved safety level. However, the literature is particularly scarce in regards to principled resource allocation schemes that deal with the challenging radio conditions posed by the high mobility of vehicular scenarios. This first chapter in Part III provides a timely survey on the application of mmWave frequency band for V2X communications, highlighting recent research outcomes and prevailing challenges. Coupled with this primary objective, this chapter also serves as an introduction to the next two chapters, which indeed attempt at tackling some of the identified challenges. Furthermore, the prospective analysis provided is also intended to be an interesting contribution to motivate and guide future research on this field.

I.1.3.2.2 Chapter III.2

The contents of this chapter comprise a first-of-its-kind research conducted by the author of this Thesis on delay performance for mmWave V2V communications, including alignment delay and the effect of transmitting and receiving beam misalignment owing to high mobility. Notably, it presents a novel framework that blends together matching theory and swarm intelligence to dynamically and efficiently pair vehicles and optimize both transmission and reception beamwidths . The latter is accomplished by jointly considering channel state information (CSI) and queue state information (QSI) when establishing V2V links. To validate the proposed framework, extensive simulation results are discussed with a focus on the delay performance. In addition, the latency/reliability trade-off of the proposed approach is assessed and compared to several baseline approaches.

I.1.3.2.3 Chapter III.3

This chapter concentrates on modeling cooperative awareness by extending vehicles' own sensing range with the information exchanged through mmWave-enabled directional beams *ad hoc* established with surrounding vehicles. In vehicular scenarios, context awareness is known to be a key enabler for road safety. However, the amount and range of contextual information that can be collected by a vehicle is stringently limited by the sensor technology itself (e.g., line-of-sight, coverage, weather robustness), as well as by the low bandwidths offered by current wireless vehicular technologies such as dynamic short range communication (DSRC)/802.11p. Motivated by the upsurge of research around mmWave V2X communications, this chapter takes a step forward from the PHY aspects considered in III.2, and introduces a distributed V2V association scheme that favors the use of a quantitative measure of the potential value of the shared contextual information to govern the vehicle pairing process. Hence, the chapter poses the problem of finding the optimum vehicle pairing for each scheduling instance that maximizes the extended sensed information (ESI), and to solve it a many-to-one matching theory game is proposed.

I.1.3.3 Part IV: mmWave Application Scenarios: Mobile VR

I.1.3.3.1 Chapter IV.1

VR is expected to be one of the killer-applications in 5G networks. However a quick survey in the literature clearly shows that, overall, the topic of mobile VR, and certainly mmWave-enabled mobile VR, is still in its infancy. Many technical bottlenecks and challenges need to be overcome to facilitate its wide adoption. In particular, VR requirements in terms of high-throughput, low-latency and reliable communication call for innovative solutions and fundamental research cutting across several disciplines. This first chapter in Part IV, follows the path set in Chapter III.1 by discussing such challenges and enablers for an ultra-reliable and low-latency mobile VR, and introduces the two scenarios to be studied in Chapters IV.2 and IV.3.

I.1.3.3.2 Chapter IV.2

In this second chapter in Part IV, a novel proactive computing and mmWave communication scheme for ultra-reliable and low latency wireless VR is proposed. By leveraging MEC and the information about users' pose, proactive computing and caching are used to precompute and store users' high definition (HD) video frames so as to minimize the computing latency. Furthermore, multi-connectivity is exploited to ensure reliable mmWave links to deliver users' requested HD frames. The performance of the scheme is substantiated over a VR network serving an interactive gaming arcade, where dynamic and real-time rendering of HD video frames is needed, and impulse actions of different players impact the content to be shown.

I.1.3.3.3 Chapter IV.3

Immersive VR applications are known to require ultra-high data rate and low-latency for smooth operation. This third chapter of Part IV tackles the case of a 360° VR theater where multiple users are watching VR videos. Specifically, this chapter aims to improve VR experience in multi-user VR wireless video streaming. To this end, a deep-learning aided scheme for joint quality maximization and scheduling of video chunk requests to base stations is proposed. Therein the correlations in the predicted field of view (FoV) and locations of viewers watching 360 HD VR videos are capitalized on to realize a proactive FoV-centric mmWave physical-layer multicast transmission. The problem is cast as a frame quality maximization problem subject to tight latency constraints. The problem is then decoupled and a matching theory game is formulated to solve the scheduling subproblem by associating requests from clusters of users to mmWave small cell base stations (SBSs) for their unicast/multicast transmission. Furthermore, for realistic modeling and simulation purposes, a real VR head-tracking dataset and a deep recurrent neural network (DRNN) based on gated recurrent units (GRUs) are leveraged.

I.1.3.4 Part V: Concluding Remarks

This last part in the main body of the Thesis summarizes the main conclusions collected during these years of postgraduate studies, and lists the publications that attest the relevance of the research conducted while pursuing the Doctoral Degree. It also compiles some of the envisioned future research lines that stem from the works covered mostly in Part III and Part IV, which could drive the interest of the mmWave research community in years to come.

I.1.3.5 Appendix A

A research line of interest in the last few years has been focused on the derivation of solution encoding strategies suited to deal with the topological constraints imposed by tree graph configurations, particularly when the encoded solution undergoes typical operators from EC. However, in spite of the fast pace at which new evolutionary operators have emerged from the community, specially during the last decade, almost all contributions within this research area still cling to the use of standard crossover and mutation operators from genetic algorithms (GAs) onto the graph topology beneath the encoded individuals.

The latter realization constitutes the ultimate motivation for the research carried out in Appendix A: a deep study of the topological heritability of the so-called Dandelion tree encoding approach under non-conventional operators. In consequence, this chapter first introduces an experimental and application-agnostic based methodology to study the topological transmission of Dandelion-encoded solutions under a certain

class of multi-parent crossover operators that lie at the core of the family of $(\mu + 1)$ evolution strategies (ESs). For that purpose, several metrics intended to define topological heritability and respect are proposed. Following that, the experimental setup is extended to compare within a common, fair comparison framework the performance on a topology preservation level of the multi-parent crossover operator with respect to that of classic two-parent recombination methods in evolutionary algorithm (EA), namely, one-point, two-point and uniform crossover.

The behavior of the four crossover operators is evaluated over a number of convergence scenarios and insightful conclusions are drawn in terms of the preserved structural properties of the newly produced solutions with respect to the initial Dandelion-encoded population, including the equivalence in terms of topological heritability of the multi-parent and uniform crossover operators.

I.1.4 Notes on Reading this Thesis

As stated in Section I.1.3, the contents of this Thesis have been arranged into different logical Parts so as to facilitate its non-sequential reading. Specifically, Fig. I.1.4 reflects the logical dependencies among Parts and Chapters and illustrates some of the possible reading alternatives, identified as tracks or substracks therein, and summarized as:

- **Main Track**, which corresponds to a sequential reading of the entire document. This track is suitable for a reader interested in grasping all contents and contributions of the Thesis.
- **Intensification Subtrack 1** that concentrates on the chapters related to the application of mmWaves in V2X communications.
- **Intensification Subtrack 2** to read about the application of mmWaves to mobile VR.
- **Appendix Subtrack** to cover the subject of topological heritability of tree encoding schemes under EA crossover operation.

Part II includes the detailed explanations related to the different research tools (the means and methods) applied throughout the chapters comprised in Parts III, IV and in Appendix A of this Thesis. Therefore, in line with the background and/or time availability of the reader, it can be skipped to jump directly to any of the *application* parts that have no interdependence between each other and could, thus, be read in any order. Alternatively, it can also be used only as a lookup reference; this latter use gives rise to the **Review Subtrack** as illustrated in Fig. I.1.4. In spite of the writing of the each of the application-specific chapters being self-contained, reading Part II could still be beneficial for a deeper understanding of the remaining material.

Lastly, the concluding remarks from Part V summarize any of the specific *application* chapters. Hence, another approach to the reading of the

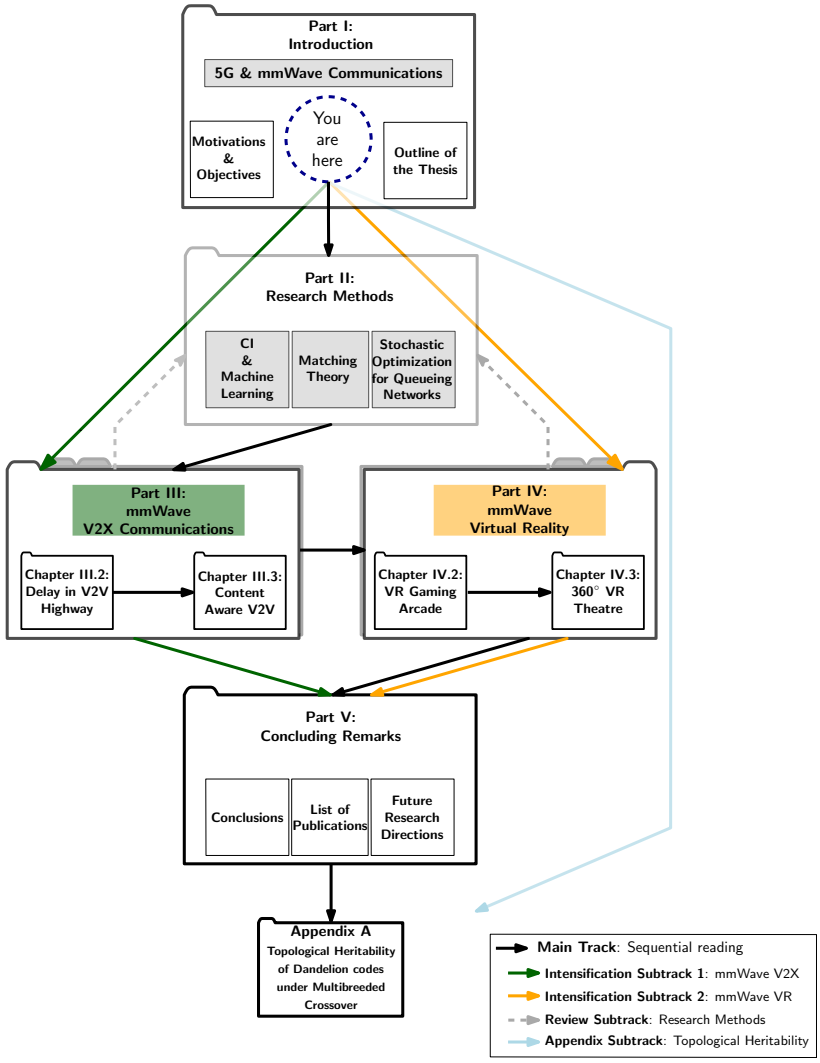

FIGURE I.1.4: Organization of the Thesis and suggested reading options.

Thesis could be alternating the chapters in Part III and Part IV with the last one.

I.1.4.1 Notes on the List of Abbreviations

The List of Acronym and Abbreviations in page xxvii provides a quick, useful reference for the abbreviations and acronyms used along this Thesis. The acronyms therein are first classified according to five application areas, namely, general purpose, mobile communications, vehicular communications, virtual reality and computational intelligence & machine learning, and in alphabetical order within the corresponding category. The following

criteria have been considered throughout the body of the Thesis to use the short/long version of an acronym/abbreviation:

- As default behavior, the first time an acronym/abbreviation is used it will be displayed in its unshortened form, that is, it will be locally defined. In subsequent uses only the short form of the acronym will be provided, *e.g.*, for SVM we will get "support vector machine (SVM)" for the first occurrence and only "SVM" from there onwards.

  Exceptions:

  - The full form will not be displayed if its first instance arises within a floating box, such as the ones employed to summarize the main contributions in each of the *application* chapters.
  - To facilitate non-sequential reading of the Thesis, the acronyms will be reset before the beginning of Part III such that their full form is displayed again.

I.1.4.2 Notes on the Formulation

Each of the chapters in this Thesis is self-contained with respect to the formulations enforced therein. Yet, for reference purposes, the most extensively used notations have been classified and partially compiled in the List of Symbols and Notations in page xxxiii.

Due to the profuse mathematical notation in the body of the Thesis some conventions have been established:

- **Scalars**: are denoted with a lowercase Latin letter. Specifically, for ease of reading, for those scalars denoting indexes throughout Parts III and IV the following naming etiquette has been observed:

  - Temporal indexes are denoted with a starting 't' character, which is customarily followed by a subscript to characterize the specificities of the time scale at hand, *e.g.*, t_s.
  - Video frames related indexes are denoted with a starting 'f' character, followed by a subscript to indicate *e.g.*, predicted frame index f_p or real-time frame index f_r.
  - To index into system users in Part III i and j characters refer, correspondingly, to vehicular transmitters (vTxs) and vehicular receivers (vRxs), whereas in Part IV subscripts u and b are used to denote VR players (or VRP) and mmWave SBSs or mmWave access points (mmAP), respectively.

- **Vectors**: vectors are denoted with lowercase Latin bold letters, e.g., $\boldsymbol{q}$.
- **Matrices**: are denoted with boldface uppercase Latin letters, e.g., $\boldsymbol{D}$.
- **Sets**: are denoted with italic boldface uppercase letters, e.g., $\boldsymbol{\mathcal{A}}$.
- **Overbars** ($\bar{\cdot}$)**, tildes** ($\tilde{\cdot}$) **and hats** ($\hat{\cdot}$): these modifiers are applied to refer to scalars, vectors or sets that have been computed as the result of an averaging, estimation or learning process, e.g., $\hat{I}$.

Part II

Research Methods

Chapter II.1

Research Methods

> "The scientific man does not aim at an immediate result. He does not expect that his advanced ideas will be readily taken up. His work is like that of the planter—for the future. His duty is to lay the foundation for those who are to come, and point the way."
>
> Nikola Tesla, *Problem of Increasing Human Energy*

Due to its inherent practical nature, the field of resource allocation for wireless communications has been object of extensive research in the last years, exploring the many dimensions that stem therefrom. New communication paradigms and the need to investigate the use of higher frequency bands have re-ignited theoretical and practical research interest around this never exhausted area of research.

This chapter intends to distillate the essence and the possibilities offered by a group of selected interdisciplinary techniques and mathematical frameworks that have been explored to different degrees to address several challenges brought up by 5G and future wireless networks. Specifically the techniques described in what follows, have been applied while analyzing and optimizing the different mmWave-enabled V2V and VR scenarios that represent the core of this Thesis.

II.1.1 Computational Intelligence and Machine Learning

II.1.1.1 Introduction

With the exponential growth in the number of connected devices hand in hand with the promise of higher data rates, reduced latency and highly guaranteed reliability levels in 5G, wireless resource allocation related optimization problems are becoming increasingly large and complex in terms of number of input parameters, decision variables, objective functions and landscape complexity. Traditionally these problems have been tackled by using optimization approaches that included greedy algorithms, exact methods (e.g., dynamic programming, branch-and-bound, constraint programming, A*, etc.) and metaheuristics (EA, particle swarm optimization (PSO), ant or bee colonies, simulated annealing (SA), Tabu search, etc.).

However, in the near future, solving efficiently and effectively large and complex problems will require to trade optimality for efficiency, especially for performance-sensitive and mission-critical applications. Besides, the hybridization of these techniques with elements from other disciplines will be also needed. In addition, for many real-world problems e.g., in engineering design, the evaluation of the objective function often consists of the execution of an expensive simulation as a black-box complex system, which poses even more challenging computational constraints for the aforementioned algorithms.

Even if combined with parallel computing, optimization algorithms might fail to solve these simulation-based optimization problems. A typical approach to deal with the computational burden is to use data-driven approximations of the objective function, so-called surrogates or metamodels. A wide range of surrogates was applied during the last decade including: classical regression models such as polynomial regression or response surface methodology, support vector machines (SVMs), artificial neural networks (ANNs), radial basis functions, and kriging or Gaussian processes. Withal, ANNs are probably the most prevalent of them with the recent "explosion" of the deep learning and deep neural networks (DNNs) popularized thanks to the graphical processing units (GPUs).

The above is nothing else than an early example of the manifold of opportunities unleashed by the combination of intelligent optimization techniques and predictive modeling. CI is a term that blends together both algorithmic realms around a single concept: to provide intelligent functionalities to computer systems, just like those supporting wireless communications. In short, while CI technologies can achieve a flexible and self-evolving system design, availability of data can facilitate the use of machine learning techniques, including DNNs, by virtue of which learning the best strategy from complex data becomes possible.

II.1.1.2 Computational Intelligence

As mentioned above, part of the algorithmic developments utilized throughout this Thesis belong to the wide family of CI models [82], [83]. In essence, all CI models share the ability to perform a given task with efficiency, autonomy and adaptability. For this to occur, CI methods contain algorithmic means to capture information from the task at hand (perceive), to learn from this perceived information toward completing the task efficiently, and to retain the captured knowledge in a computational structure e.g., weights and biases in a neural network devised to solve a classification problem. Depending on the nature of the specific task, different algorithmic approaches, model construction methodologies and performance assessment strategies can be adopted to design a CI model.

Since all revolves around computational tasks, we will first elaborate on their formal definition. Conceptually speaking, a computational task can be characterized from a system perspective i.e., as a modeling, simulation or optimization problem. More specifically, a task consists in solving an unknown between the input of a system, the output of a system and the

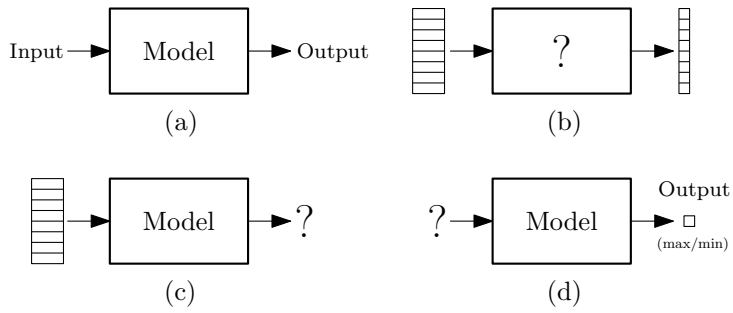

FIGURE II.1.1: Possible tasks to be undertaken by Computational Intelligence methods: (a) a generic model processing inputs to provide outputs; (b) modeling task; (c) simulation task; (d) optimization task. The "?" sign refers to the unknown variable that the CI method aims to resolve.

system itself, wherein a system here is a high-level representation of the CI model itself, and inputs and outputs denote the perceived information and the decision made by the model, respectively. With this analogy in mind, three different classes of computational tasks can be extricated [84], as shown schematically in Fig. II.1.1:

- **Modeling**, by which the unknown to be solved is the system that best relates a series of known inputs and their corresponding outputs. In the context of AI and machine learning, this paradigm is referred to as *supervised learning*, since the outputs can be thought to be an a priori annotation or supervision of the inputs on which the model is built. Depending on the CI model considered a priori, the formulation of the unknown can take the form of thresholds and input variables in the different levels of a decision tree, means and covariance matrices in a Bayes classifier, or any other computational structure alike. Deep learning models fall within the CI techniques that can solve modeling tasks with unprecedented levels of performance, by virtue of their renowned capability to infer hierarchical features of increasing representativeness with respect to the hidden pattern between inputs and outputs [85].

  As will be later shown in Chapter IV.3, this Thesis resorts to this branch of modeling techniques.

- **Simulation**, in which we assume a certain model, and the interest is placed on evaluating the output of the model when fed with a given input. Under the traditional conception of software simulators, the input could be thought to be the configuration parameters of a simulation software, whereas the model (system) could be the simulator itself. However, when the inputs are in the form data instances one can think of simulation to be a process of discovering patterns among them as per a measure of similarity between samples. This is the description of a clustering process [86], by which data instances (inputs) are grouped together in such a way that instances within the

same group are closer to one another (as per a measure of similarity, which is set as one of the parameters of the clustering model) than to instances assigned to other groups.

The contributions of the Thesis described in Chapter IV.3 resort to the use of hierarchical clustering, although many other data-based processes can also be regarded as a simulation task (e.g. manifold learning).

- **Optimization**, in which given a model, we seek the particular input that yields a maximization or minimization of the output of the model. The computational problem resides in the efficient exploration of the space of possible values for the input of the model, especially in those practical situations where the cardinality of this space becomes computationally prohibitive to be traversed via exhaustive search e.g., continuous search spaces. CI models devised to tackle optimization tasks aim at circumventing this search complexity by assorted means, from problem simplification approaches to heuristics capable of tailoring the exploration strategy of the search space by intelligently learning from successive trial-and-error experiments [87].

  Optimization tasks prevail in many application scenarios stemming from diverse sectors and disciplines. Furthermore, this task also comprises problems in which the output of the model can be expressed analytically, namely, without any involvement of data whatsoever. Depending on the characteristics of the optimization task under analysis (linearity of fitness and/or constraints), different solvers can be applied to solve it efficiently. Among them, EC and SI heuristics protrude as powerful search methods for general optimization tasks, especially for those cases with non-convex search spaces and/or problems with non-analytical objectives.

The above taxonomy of computational tasks that are addressable with CI methods can be seen from an alternative, complementary point of view focused on the type of learning algorithm utilized for solving them. Before moving forward and delving into this second taxonomy, it should be noted that the tasks described above must not be conceived as isolated problems decoupled from each other. To exemplify this intersection between tasks, we pause at the case of SVMs, modeling approaches whose learning algorithm consists of solving an optimization task [88]. The same can be said about Neural Networks, another family of methods whose learning algorithm aims at minimizing a loss function –a function of the output of the model– measured over a set of supervised inputs. This is realized by backpropagating the gradient of this loss function through the structure of the network and implementing a gradient descent algorithm over each parameter (weight, loss) of the network. Again, an optimization task embedded into the learning algorithm for a modeling task. Other common avenues between computational tasks arise in optimization problems where the output is to be optimized is produced by a simulation model (as

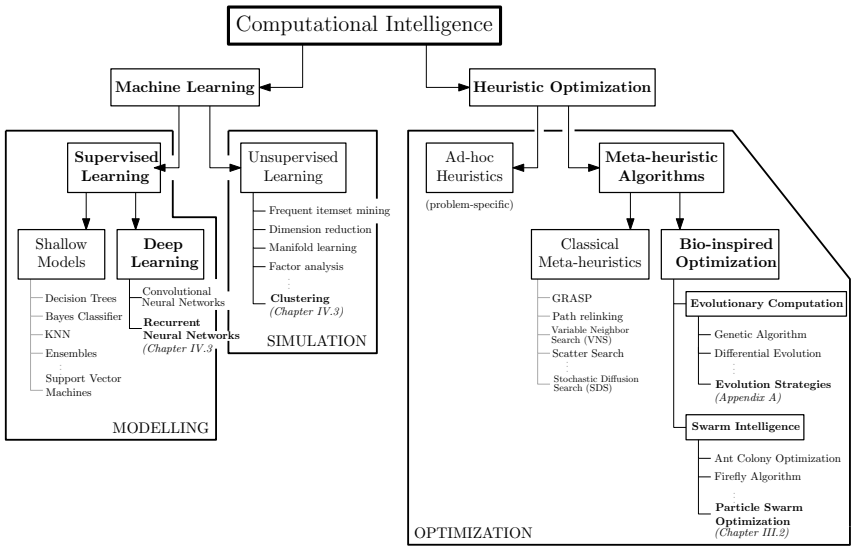

FIGURE II.1.2: Taxonomy relating Machine Learning and Heuristic Optimization under the general umbrella of Computational Intelligence methods.

happens, for instance, in urban vehicular simulators that need to be tuned to match a certain record of origin-destination pairs [89]).

When it comes to the learning algorithm devised to deal a given task, two large family of CI techniques can be identified in close connection to the contributions of this Thesis. Before describing them in depth, it is important to take into account that once again, the categorization of the CI realm from this second axis also undergoes certain level of overlap between categories. Indeed, a plethora of different taxonomies of CI can be found in the literature, with varying granularities depending on the exhaustiveness required by the work proposing them [90], [91]. Bearing this in mind, the following two family of models arranged in the taxonomy of Fig. II.1.2 have been used throughout the Thesis:

II.1.1.3 Machine Learning

Is the term that collectively refers to algorithms capable of solving modeling and simulation problems efficiently [92], [93]. Therefore, machine learning models deal essentially with data. Depending on the computational task to be solved and thereby, the presence of outputs annotated to the inputs to the model, a second-level categorization can be set.

II.1.1.3.1 Supervised learning

On one hand, supervised learning constructs a mathematical model from annotated data instances (training data), with the goal of characterizing the pattern between the inputs and their associated outputs [94]. Once this

pattern has been characterized and represented as per the chosen mathematical model, the model is assumed to be capable of assigning proper output values to unseen input data (namely, to generalize efficiently). For this to occur, the mathematical model must be adjusted to the training data properly, so that once properly fitted, it represents their underlying pattern and does not overfit to potential outliers and noisy data instances. Two main types of supervised learning problems can be formulated at this point:

1. **Classification problems**, where outputs are restricted to a finite alphabet that represent categories to be assigned (predicted) to the inputs to the model. This is the case of binary classification with Boolean inputs, or multiclass classification, whose output alphabet contains several values. A special case worth to be mentioned due to its relevance in Chapter IV.3 is multilabel classification, which corresponds to the problem in which the output of the model is a vector of possible categories whose statistical interdependences call for the adoption of a single modeling approach instead of separate models for each of the output variables in the vector.

2. **Regression problems**, where the output of the model is continuous and can take infinite values. This casuistry often holds when the output to be predicted is produced by a physical phenomenon or is the result of an unquantized process e.g., the raw output of a motion sensor. Despite the simplicity of the difference of this type of problems when compared to classification, it is important to observe that the output characteristics unchain fundamental changes in the learning algorithm of the selected model, to the point of giving rise to regression algorithms exclusively devoted to solving this kind of modeling tasks.

II.1.1.3.2 Unsupervised learning

Conversely, in unsupervised learning a mathematical model is built from data instances without any annotation or supervision, namely, with no associated output known beforehand [95]. The goal of unsupervised learning models, therefore, is to find structure in the data instances as per a certain criterion by which such a structure is assumed to exist. This is in essence a simulation task, in which the simulation is aimed at assessing whether the output of the simulation is plausible to contain, describe or summarize the input data under a certain model choice. Arguably, clustering techniques can be deemed the most representative portfolio of unsupervised learning techniques, as their goal is indeed to group data instances into clusters or categories under assumptions on how similarity among instances is measured, and the characteristics of the cluster space to be sought, e.g., cluster hierarchy, crisp versus fuzzy belongingness to groups, etc.

II.1.1.4 Heuristic Optimization

Is the term to compile those algorithms aimed at solving optimization problems by using a self-learning, adaptive search strategy [96], [97]. The rationale behind the adoption of this family of techniques when facing an optimization problem is often found in the difficulty of addressing it with classical tools from convex optimization and operations research. The non-convexity or multi-modality of the objective function to be optimized, the lack of analytical derivatives, or the impossibility of exhaustively evaluating the solution space in polynomial time with respect to its scales are among the reasons argued to opt for a heuristic approach.

In their search, heuristic solvers rely on stochastic operators that are applied to one or a set of candidate solutions held during the search. It is by virtue of these operators and the criterion followed to retain the individuals along the search that the solution space is traversed efficiently, learning to discriminate good movement directions on the way. A drawback linked to the random exploration of the solution space is the lack of optimality guarantees, i.e., a heuristic approach may not yield optimal results for the problem under target. Nevertheless, their ability to learn how to progressively discover and enter regions of increasing quality makes heuristic algorithms a frequent choice for problems of unmanageable complexity.
Two different subfamilies can be discriminated within heuristic optimization:

1. **Ad-hoc heuristics**, which comprise search operators and strategies closely coupled with the specific characteristics of the problem at hand. It is often the case that ad-hoc heuristics exhibit a superior performance when addressing the problem for which they were designed, at the cost of a lower exportability of their operators for other problems and longer times invested in their design phase. Examples of ad-hoc heuristic algorithms abound in the literature related to wireless communications, such as heuristic routing [98] or radio resource management [99].

2. **Metaheuristics** are intended to be used for addressing a diversity of problems with as little design efforts as possible [100]. For this purpose, metaheuristic optimization algorithms are often analyzed in terms of their global search and their local search strategy: while the former is concerned with the high-level exploration of distant areas in the solution space, the latter refers to the capability of the algorithm to intensify the search around promising regions/solutions identified during the search. This strategy can be defined explicitly by devising isolated global and local search operators within the algorithmic flow or, instead, be implicitly embedded in the operators with no clear discrimination made between both strategies. Other distinctions within metaheuristic optimization algorithms can be made from other perspectives, such as the maintenance of a single or a pool of individuals (single-point versus population-based) or the hybridization of metaheuristic operators with local search methods tightly connected to the problem at hand (memetic algorithms).

Beyond classical metaheuristic approaches [101] such as greedy randomized adaptive search procedure(GRASP), path relinking, variable neighborhood search (VNS) and others alike, a major trend in the related literature has concentrated on biological and physical phenomena as sources of inspiration for the design of metaheuristic search strategies and operators. This vibrant activity has spawned a flurry of research collectively referred to as bio-inspired optimization –also known as bio-inspired computation, [102]–[105]–, featuring two different design mainstreams with implications in the algorithmic behavior of their compounding methods:

(a) **Evolutionary Computation**, which emulate Darwinian evolutionary principles and apply them to a population of individuals (namely, a pool of candidate solutions) over generations [106]–[108]. Mechanisms such as breeding or crossover between individuals, mutation and survival of the fittest, which lie at the core of the human evolution, are applied to the population, so that mutated offspring are potentially better (more fit with regards to the objective function to be optimized) than the parent individuals from where they originated.

Renowned evolutionary algorithms include GAs [109], differential evolution (DE) [110], ESs [111], estimation of distribution algorithms (EDAs) [112], and genetic programming (GP) [113]. Other modern approaches, for instance harmony search algorithm (HSA) [114], are under the spotlight of controversial debates due to the questioned novelty of their search procedure with respect to that of classical evolutionary methods [105]. The findings reported in Appendix A of this Thesis deal with an EC method applied to tree-based optimization problems.

(b) **Swarm Intelligence**, which leverage the behavior observed in certain groups of animals (e.g. such as bird flocks or fish schools) and the emergence of collective knowledge [115], [116]. In these groups, the movement of individuals is dictated by very simple behavioral rules that depend on the proximity and interaction with its peers in the group, as well as on local decisions. When conceived in the context of optimization, each of the individuals within the swarm can be thought to be candidate solutions to the problem at hand, which are varied depending on its relative fitness with respect to other members of the swarm, which makes the entire swarm gravitate towards regions of increasing optimality.

Arguably, the most important aspect of swarm intelligence methods is their straightforward distributed nature, as there is no need for controlling the individuals of the swarm centrally. Instead, the evolution of individuals is delegated to their behavioral rules applied locally, adding a certain degree of randomness to endow the overall swarm with exploration capability. As a result of repeated interactions between individuals, a near-optimal

solution to the problem (represented by the best individual in the swarm at a certain iteration) is eventually achieved.

Analogously to their evolutionary counterparts, examples of metaheuristic optimization approaches harnessing concepts from swarm intelligence include ant colony optimization (ACO) [117], which has been proven to be particularly suitable for problems defined on graphs e.g., routing), or PSO [118], [119], which is used in Chapter III.2 of this Thesis as an efficient means for beamwidth allocation in V2V networks. Recent heuristics with notable momentum in the community are also based on swarm intelligence principles e.g., the firefly algorithm firefly algorithm (FA) [120]), yet they are also under controversy for their close algorithmic resemblance to well-established methods in the same family [121].

II.1.2 Matching Theory

A resource allocation problem that appears in most of the problems tackled in this Thesis, and that has received a considerable interest due to the increasing complexity and heterogeneity of the mobile network landscape, is that of device association. The device association problem can be modeled as a matching problem, which aims at linking entities to each other under a certain measure of preference between them. Though this seminal problem can be solved by assorted algorithmic means, in this Thesis the focus in set on the use of matching theory.

Matching theory is a mathematical framework that aims to analyze the formation of mutually beneficial relationships over time and whose roots lie in labor economics. In general terms, the use of matching theory provides mathematically tractable solutions for combinatorial problems with an emphasis on the notion of *stability*, which motivates its profuse application in Parts III and IV of this Thesis. Hence, in this introductory chapter some preliminary notions about its origins and about the most common matching models will be provided. Following that, several definitions and key solution concepts from matching theory will be disclosed.

II.1.2.1 Brief Historical Perspective and Application to Wireless Communications

David Gale and Lloyd Shapley set the theoretical foundations of matching theory back in the 1960s, when their seminal work on *the math behind pairing people up with partners who returned their affections* was published in [122]. Therein, the College Admission and the Stable Marriage problems were formulated, and an algorithmic implementation that lead in polynomial time to reaching a stable solution was provided: the deferred acceptance (DA) algorithm, also known as Gale-Shapley algorithm. Around twenty years later Alvin E. Roth took over and extended the use of this framework to the practical study of economical markets in from an engineering perspective [123]–[127]. Preserving the underlying principles of

DA, the numerous advances achieved using this framework to improve real-world systems, e.g., for the National Resident Matching Program (NRMP) or for the New England Program for Kidney Exchange, allowing to pair compatible kidney donors and recipients, eventually earned Shapley and Roth the Nobel Prize in Economics in 2012.

In the context of wireless communications, the stringent requirements set for 5G networks in terms of latency, throughput and device density as specified in ITU International Mobile Communications (IMT) IMT-2020 Standard call for the use of complex heterogeneous multi-tiered network architectures. Unfortunately, in such environments, most traditional centralized resource allocation schemes fail to provide a brisk dynamic response.

Matching theory allows to easily capture features inherent to novel communication paradigms and to model complex environments through the use of preference relations and/or utility formulation [128]. Moreover, in many cases, low-complexity algorithmic implementations that are naturally self-organized, work in a distributed fashion and rely only on the use of local information are amenable. As a result, the signaling overhead is significantly reduced if compared to centralized optimization solutions or to other distributed approaches, where agents need to consider the state and actions of the rest of the participants to decide on their best response strategy; the case of non-cooperative game theory for instance.

Motivated by the need to design efficient resource allocation approaches, and thrusted by the timeline set for 2020 for the IMT-2020 Standard to be fully deployed, during the last years matching theory has garned an increasing attention from the wireless research community. Hence, an abundant body of literature on its practical application have flourished with e.g., [129]–[135] to name only a few of the many published works, as well as tutorial-style publications such as [128], [136].

II.1.2.2 Matching Models

Matching problems can be classified according to different *graph theory* related criteria:

Classification I: based on the partitioning

In graph theory, a bipartite match or bigraph $\mathcal{G}(\mathcal{V}, \mathcal{E})$ is defined as a set of graph vertices $\mathcal{V}$ and edges $\mathcal{E}$, that is decomposed into two disjoint sets such that no two graph vertices $x, x' \in \mathcal{V}$ within the same set are adjacent. Conversely, in a unipartite graph all the vertices in the graph belong to a single homogeneous set and, thus, edges are formed between nodes from the same set. According to these definitions, matching theory problems fall into these categories [137]:

1. **Bipartite matchings** are matching problems where agents can be partitioned to form two disjoint sets, such that agents in one set try to match to agents from the opposite set. Coupled with the existence

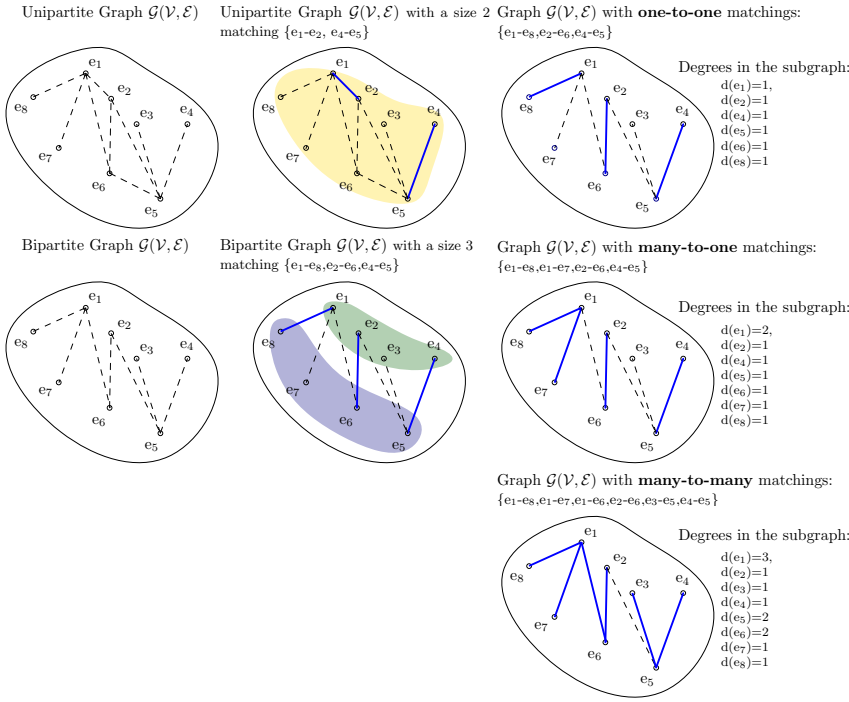

FIGURE II.1.3: Graphical representation of classical Matching Theory models.

of separate sets, further considering the nature of the preferences bipartite matchings are subdivided into:

(a) **Bipartite matchings with two-sided preferences**, if both sets of agents rank the agents in the opposite set following some preference criteria.

(b) **Bipartite matchings with single-sided preferences**, when only the agents from one of the sets rank the agents in the opposite set according to some preference criteria. The agents in the opposite side, no matter what the outcome of the matching, remain indifferent.

2. **Unipartite/Nonbipartite matchings with preferences** are matching problems where each agent ranks according to some preference all or a subset of the agents from the homogeneous set where all belong.

Classification II: based on the quota

However, the most extended classical way to classify matching problems is based on the agents' *quota*, i.e., the maximum number of different matchings a single agent can be part of. Indeed, the idea of the quota is equivalent in graph theory to that of the *degree of a node/vertex*, denoted $\mathrm{d}(\mathrm{e}_x)$ in

TABLE II.1.1: Classification of classical matching game problems

Game	Classification I	Classification II
Stable Marriage	Bipartite matching with two-sided preferences	One-to-one matching
Housing Allocation	Bipartite matching with one-sided preferences	One-to-one matching
College Admission	Bipartite matching with two-sided preferences	Many-to-one matching
Capacitated House	Bipartite matching with one-sided preferences	Many-to-one matching
Stable Roommate	Unipartite matching with preferences	One-to-one matching
Kidney Donor Exchange	Unipartite matching with preferences	One-to-one matching
Stable Fixture	Unipartite matching with preferences	Many-to-many matching

Figure II.1.3, which is formally defined for unweighted graphs as the number of edges incident to the node. Furthermore, a graph is said to be *a regular graph* whenever all the nodes in it have the same degree. According to this principle, and given a graph $\mathcal{G}(\mathcal{V}, \mathcal{E})$, matchings can be classified as follows:

1. **One-to-one matching**: A one-to-one matching is a subgraph of $\mathcal{G}$ where every node has degree 1. In other words a matching where all agents/nodes can be matched at most to another member/node.

2. **Many-to-one matching**: A many-to-one matching is a subgraph of $\mathcal{G}$ where at least one node has degree> 1, implying that one agent/node from one of the sets can be matched to more than one agent from the opposite or from the same set, for bipartite and unipartite matching, respectively.

3. **Many-to-many matching**:A many-to-many matching occurs if at least one agent/node from each set can be matched to more than one agent from the opposite set. This is the most general type of matching games.

Classification III: wireless communications specific

The authors in [128] propose an alternative classification of matching problems into three different categories to embody the subtleties of resource management and resource allocation for wireless communications. This classification is further stretched with a fourth category in [138], as:

1. **Class I: Canonical matchings**: a matching is said to be canonical whenever the preferences of a agent depend exclusively on the information available at the agent at hand, and are not influenced by any other agent decisions or by the evolution of the matchings game itself. Canonical matchings are common in wireless communications whenever the resources that are allocated are orthogonal.

2. **Class II: Matching with externalities**: a matching is said to be subject to externalities if the preferences of an agent show interdependences with the decisions of other agents or with the current state of the matching. Among externalities, two different types are usually distinguished: common externalities and peer effects. In the former, a change in a agent's preference is motivated in response to variations

in the forecasted performance as new matchings are formed, e.g., in wireless communications the most common source of externalities is the presence of interference. In the latter, a agent's preference is influenced by the identity and amount of agents matched to a given resource, which is frequently related to the existence of social ties between agents.

3. **Class III: Matching with dynamics**: the third type of scenario introduces the need to consider the time dimension, due to the evolution of agents preferences in the matching. Class III is specifically designed to fit resource allocation use cases that operate under highly dynamic environments, such as mobility or fast fading effects in the channel.

4. **Class IV: Matching with transfer**: this last class encompasses those scenarios where there exists some kind of transaction between the matched agents, e.g., money for spectrum resources.

II.1.2.3 Definitions and Key Concepts from Classical Matching Theory

For the purpose of providing a minimum coverage of classical matching theory related definitions and key results, subsequent definitions will be focused on a two-sided market with preferences. Specifically we will consider a general many-to-one matching model, as exemplified by the College Admission problem, which belongs to a class I canonical matching as per Classification III.

Canonical Many-to-one Matching games

Let there be a set of students $\mathcal{I}$ and a set of colleges[1] $\mathcal{J}$. Let students belonging to $\mathcal{I}$ be denoted i, i', etc. and let colleges belonging to $\mathcal{J}$ be denoted j, j' and so forth. Being a many-to-one matching model, each student is allowed to attend at most one college, i.e., each student has a *quota* $\Omega_i = 1, \forall i \in \mathcal{I}$ whereas each college is willing to accept multiple students and, accordingly, has a quota $\Omega_j \geq 1, \forall j \in \mathcal{J}$.

Definition 1 (Matching game)**.** *A matching game is defined by two sets of players* $(\mathcal{I}, \mathcal{J})$ *and two preference relations* $\succ_i$, $\succ_j$, *allowing each player* $i \in \mathcal{I}$, $j \in \mathcal{J}$ *to accordingly rank the players in the opposite set.*

To that end, a preference relation is defined as:

Definition 2 (Preference relation)**.** *A preference* $\succ$ *is a complete, reflexive and transitive binary relation between the agents in one set over the agents in the opposite set.*

[1]Notice that the terms student and college from the original formulation represent nothing other than the two families of agents in the matching game.

Let for each student i a preference relation $\succ_i$ be defined over $\mathcal{J} \cup \{\varnothing\}$, i.e., over the set of colleges plus an exogenously given option representing remaining unmatched that is denoted $\varnothing$. Analogously, letting for each college j a preference relation $\succ_j$ be defined over $\mathcal{I} \cup \{\varnothing\}$.

Definition 3 (Acceptability of a matching pair)**.** *A matching between a college j and a student i is said to be acceptable to student i (college j) if it prefers to be matched to j (i) rather than remaining unmatched, i.e., if $j \succ_i \varnothing$ ($i \succ_j \varnothing$).*

Definition 4 (Matching output)**.** *The outcome of a many-to-one matching game is a mapping $\mathbf{\Phi} : \mathcal{I} \times \mathcal{J} \mapsto \mathcal{I} \times \mathcal{J}$ such that $\phi_j = i \Leftrightarrow \phi_i = j$ where $\phi_j \in \mathcal{I} \cup \varnothing$ and $\phi_i \in \mathcal{J} \cup \varnothing$ satisfying $|\phi_j| \leq \Omega_j$, $|\phi_i| \leq 1$.*

For any two colleges $(j, j') \in \mathcal{J} \times \mathcal{J}$ with $j \neq j'$, and two matchings $\mathbf{\Phi}$ and $\mathbf{\Phi}'$ where $\boldsymbol{\phi}_i = j$ and $\boldsymbol{\phi}'_i = j'$, we have that

$$(j, \mathbf{\Phi}) \succ_i \left(j', \mathbf{\Phi}'\right) \Leftrightarrow U_{\mathcal{I}}^{i,j} > U_{\mathcal{I}}^{i,j'}.$$

and, equivalently, for any two students $(i, i') \in \mathcal{I} \times \mathcal{I}$ with $i \neq i'$, and two matchings $\mathbf{\Phi}$ and $\mathbf{\Phi}'$ and $\boldsymbol{\phi}_j = i$ and $\boldsymbol{\phi}'_j = i'$:

$$(i, \mathbf{\Phi}) \succ_j \left(i', \mathbf{\Phi}'\right) \Leftrightarrow U_{\mathcal{J}}^{j,i} > U_{\mathcal{J}}^{j,i'},$$

where $U_{\mathcal{I}}^{i,j}$ and $U_{\mathcal{J}}^{j,i}$ correspondingly denote the utility of college j for student i and the utility of student i for college j.

Definition 5 (Strict preference relation)**.** *If an agent is not indifferent between any two acceptable matches or between being matched or remaining unmatched, then the agent is be said to have strict preferences.*

Strict preferences:	$P_{ref}(i) = j, j', j'', \varnothing$	$[j \succ_i j']$
Indifferent preferences:	$P_{ref}(i) = j, [j', j''], \varnothing$	$[j' \succeq_i j'']$

Under those circumstances, for any student i and any pair of colleges j, j' plus the outside option, $j \succeq_i j'$ holds if and only if $j \succ_i j'$ or $j = j'$. Equivalently for any college j and any pair of students i, i' plus the outside option $i \succeq_j i'$ holds if and only if $i \succ_j i'$ or $i = i'$.

Furthermore, firm preferences over groups of students are assumed, which in its simplest form corresponds to a responsive model, that is defined as follows:

Definition 6 (Responsiveness condition)**.** *In many-to-one or many-to-many matchings, responsiveness condition is satisfied for agent j if, having a finite quota Ω_j and a linear order over the agents in $\mathcal{I}$, its optimal choice from any set of applicants $\mathcal{I}_j$ corresponds to its most preferred acceptable agents (with respect to the aforementioned linear order) up to its quota limit:*

$\forall \mathcal{I}_j \subseteq \mathcal{I}$ with $|\mathcal{I}_j| < \Omega_j$ and with i, $i' \in \mathcal{I} \backslash \mathcal{I}_j$: $\mathcal{I}_j \cup i \succ_j \mathcal{I}_j \cup i'$ if and only if $i \succ_j i'$, and $\mathcal{I}_j \cup i \succ_j \mathcal{I}_j$ if and only if $i \succ_j \varnothing$.

Definition 7 (Individually rational matching)**.** *A matching $\mathbf{\Phi}$ is individually rational if (i) no agent is matched to an unacceptable partner, (ii) no*

Algorithm II.1.1: DA for Many-to-one matching[122]

Input: $\mathcal{I}$, $\mathcal{J}$, and $P_{ref}(i)\ \forall i \in \mathcal{I}, P_{ref}(j), \Omega_j\ \forall j \in \mathcal{J}$.
Arbitrarily break ties if preferences in $P_{ref}(i), P_{ref}(j)$ are not strict.
Apply: Each student applies to its first choice college in $P_{ref}(i)$.
repeat
  PHASE 1 Reject-Defer: Each college rejects all unacceptable applicants.
  if received applications exceed Ω_j **then**
    The response to the most preferred Ω_j applicants is deferred; the rest are rejected.
  else
    The response to all new applicants is deferred.
  end if
  PHASE 2 Update: Each student whose application was rejected in the previous step updates his preference list by removing his former first option college.
  if $|P_{ref}(i)| \neq \emptyset$ **then**
    (Re)-apply: to its *new first option* college.
  end if
until no new proposal is made.
Matching: Each college accepts the students whose admission decisions have been deferred.
Output: a stable matching $\mathbf{\Phi}$.

student is matched with more than one college ($\Omega_i = 1\ \forall i \in \mathcal{I}$), and (iii) no college is matched with more students than its quota $|\phi_j| \leq \Omega_j\ \forall j \in \mathcal{J}$.

Definition 8 (Blocking pair)**.** *A pair of agents (i,j) form a blocking pair for a matching $\mathbf{\Phi}$ if they each prefer to be matched together rather than the current matching outcome. Formally, $i \succ_j \phi_j$ and $j \succ_i \phi_i$.*

Definition 9 (Stability of the matching)**.** *A matching is stable if it is individually rational and there is no blocking pair to it.*

A stable matching is efficient and in the *core*[2]; in the simplified many-to-one model presented above, due to the responsiveness condition, the set of *pairwise* stable matchings equals the core. If responsiveness does not hold, then, for the purpose of stability in many-to-one markets, *group stability* should be considered instead, i.e., proving that the matching can not be blocked by a coalition of agents.

Algorithm II.1.1 provides a high-level summary of the steps involved in the many-to-one adaptation[3] of the DA algorithm proposed in [122] under responsiveness.

Definition 10 (Pareto optimality)**.** *A matching is pareto optimal if there is no other matching in which some applicant is better off whilst no applicant is worse off.*

Finally, for their practical applicability, the following two theorems are which are particularized for a one-to-one (stable-marriage) problem are reproduced here:

[2]In game theory, the core is the set of feasible allocations that cannot be improved upon by a subset of agents.

[3]The algorithmic representation of the original DA for the Stable Marriage problem is straightforward by setting $\Omega_j = 1\ \forall j \in \mathcal{J}$

Theorem 1 ([122], Theorem 2.8)**.** *A stable matching exists for every marriage market.*

Theorem 2 ([122], Theorem 2.12)**.** *When all agents in both sides of the market have strict preferences, there always exists an M-optimal stable matching, and a W-optimal stable matching.*

The first theorem grants the existence of at least one stable solution for every one-to-one matching game with strict preferences; the second points out that the stable solution that is reached will be optimal for the set of players that takes the initiative and proposes.

II.1.3 Stochastic Optimization for Queuing Networks

Particular contributions of the Thesis gravitate on the consideration of queue dynamics for scheduling the delivery of information between transmitters and receiver(s) over mmWave links. Such wireless channels are dynamic by nature, with randomness arriving from both large and small scale fading effects as well as from blockage effects. Furthermore, in some scenarios users and traffic arrivals are also arbitrary, introducing yet another component of uncertainty in the design of wireless communication systems. Stochastic optimization (SO) i.e., the process of maximizing or minimizing a mathematical function in the presence of randomness, is a powerful tool to deal with probabilistic inputs.

In the following subsections, some relevant results of SO for constraint optimization of time averages of network attributes in queuing networks system will be presented.

In this regard, the seminal works of Tassiulas and Ephremides [139], [140] pioneered the application of the Lyapunov drift to solve queue stability problems, by showing that greedy actions that minimize a drift expression $\Delta\mathscr{L}_t$ every slot guarantee the stability. Neely and Georgiadis extended these results in [141], [142] by developing the drift-plus-penalty (DPP) approach whereby joint stability and performance optimization are provided. In DPP a greedy action is selected at every slot to minimize a bound of the drift plus/minus a penalty term in the form of a cost/utility function that is scaled with the parameter $V_\Delta \geq 0$. This parameter V_Δ controls the trade-off between minimizing the queue backlog and approaching the optimal solution. Indeed, the special case where $V_\Delta = 0$ reduces to the stability approach.

Having that on mind, the definitions and theorems presented hereafter are excerpted from [143], [144] where the mathematical theory underlying the use of auxiliary variables and virtual queues methods together with the Lyapunov DPP algorithm are extensively developed both for convex and non-convex utility/cost cases.

II.1.3.1 Model Assumptions

Consider a network operating in slotted time indexed with $t \in \mathbb{N}$ that manages a vector of K queue backlogs $\boldsymbol{q}(t) = [q_1(t), \ldots, q_K(t)]$. Denoting $a_k(t)$ an arbitrary function of time t that expresses queue arrivals, and $\mu_k\big(t, \boldsymbol{\phi}(t), \boldsymbol{h}(t)\big)$ an arbitrary function of time t, control vector $\boldsymbol{\phi}(t)$, and a random variable $\boldsymbol{h}(t)$ that represents queue services, the queue dynamics in the network will be given by

$$q_k(t+1) = [q_k(t) - \mu_k\big(t, \boldsymbol{\phi}(t), h(t)\big)]^+ + a_k(t), \qquad \forall k \in \mathcal{K}. \tag{II.1.1}$$

Assuming that i) the random event process $\boldsymbol{h}(t)$ is independent and identically distributed (i.i.d.) over t following a (possibly unknown) distribution; and that ii) there exists a finite constant $\sigma^2 > 0$ such that, under all possible controls of the control space i.e., $\boldsymbol{\phi}(t) \in \Phi\left(t, \boldsymbol{x}(t)\right)$, the second moments of the arrival and service functions are bounded above by σ^2 i.e.,

$$\mathbb{E}_{\boldsymbol{h}(t)}[a_k^2(t)] \leq \sigma^2, \quad \mathbb{E}_{\boldsymbol{h}(t)}[\mu_k^2\big(t, \boldsymbol{\phi}(\boldsymbol{t}), \boldsymbol{h}(t)\big)] \leq \sigma^2, \qquad \forall k \in \mathcal{K}. \tag{II.1.2}$$

Here, it should be noted that the existence of the bounds on the second moments of the network attributes as per (II.1.2) effectively ensures that the values of their first moments lie also within a bounded region.

The goal is to devise an algorithm that selects actions $\boldsymbol{\phi} \in \Phi$ along time such that a cost function $f_o(\bar{\boldsymbol{\phi}})$ is minimized while the system stability is preserved. In light of the above, the network optimization problem can be formulated as

$$\begin{aligned}
\underset{\boldsymbol{\phi}(t), \forall t}{\text{minimize}} \quad & f_o(\bar{\boldsymbol{\phi}}), && && \text{(II.1.3a)}\\
\text{subject to} \quad & g_k(\bar{\boldsymbol{\phi}}) \leq 0, && \forall k \in K, && \text{(II.1.3b)}\\
& \bar{\boldsymbol{q}} < \infty, && && \text{(II.1.3c)}\\
& \boldsymbol{\phi}(t) \in \Phi\left(t, \boldsymbol{x}\left(t\right)\right), && \forall t, && \text{(II.1.3d)}
\end{aligned}$$

where $g_k(\cdot)$ is a continuous and convex function, and the cost function $f_o(\cdot)$ is a continuous but possibly non-convex function. In addition, the control space $\Phi\left(t, \boldsymbol{x}\left(t\right)\right)$ in (II.1.3d) is a compact and convex set of $\mathbb{R}^U$ and $\bar{\boldsymbol{\phi}}$. In that sense, let the limiting time averages of control vector $\bar{\boldsymbol{\phi}} = \big(\bar{\boldsymbol{\phi}}_1, \ldots, \bar{\boldsymbol{\phi}}_K\big)$ be given by

$$\bar{\boldsymbol{\phi}} \triangleq \lim_{t \to \infty} \frac{1}{t} \sum_{\tau=0}^{t-1} \boldsymbol{\phi}(\tau). \tag{II.1.4}$$

Similarly, let the time average expectation of a queue vector $\bar{q} = (\bar{q}_1, \ldots, \bar{q}_K)$ under a particular policy, assumed to exist, be defined as

$$\bar{\boldsymbol{q}} \triangleq \lim_{t \to \infty} \frac{1}{t} \sum_{\tau=0}^{t-1} \mathbb{E}_{h(\tau)}[\boldsymbol{q}(\tau)]. \tag{II.1.5}$$

With those definition in mind, constraint (II.1.3c) ensures the queue stability.

Definition 11. *A queue $q_k(t)$ is mean rate stable if* $\lim_{t\to\infty} \mathbb{E}\{|q_k(t)|\}/t = 0$.

Definition 12. *A queue $q_k(t)$ is strongly stable if* $\limsup_{t\to\infty} \frac{1}{t}\sum_{\tau=0}^{t-1}\mathbb{E}\{|q_k(\tau)|\}<\infty$

Functions $g_k(\boldsymbol{\phi})$ in (II.1.3b) are continuous, and though not necessary to be differentiable they need to be Lipschitz continuous, i.e.,

$$|g_k(\boldsymbol{\phi}) - g_k(\boldsymbol{\phi}')| \leq \sum_{u=1}^{U} \nu_{k,u}|y_u - y'_u|, \tag{II.1.6}$$

for some non-negative finite constants $\nu_{k,u}$ and any $\boldsymbol{\phi}, \boldsymbol{\phi}' \in \Phi$. Similarly, the cost function $f_o(\boldsymbol{\phi})$ satisfies

$$|f_o(\boldsymbol{\phi}) - f_o(\boldsymbol{\phi}')| \leq \sum_{u=1}^{U} \nu_u|y_u - y'_u|, \tag{II.1.7}$$

for some finite constants $\nu_u \geq 0$ while assumed to be bounded by finite constants f_o^{MIN} and f_o^{MAX}, with $f_o^{\text{MIN}} \leq f_o(\boldsymbol{\phi}(t)) \leq f_o^{\text{MAX}}$.

II.1.3.2 Transforming SO with Auxiliary Variables and Virtual Queues

To optimize (II.1.3) over functions $g_k(\cdot)$ that are possibly non-linear, a set of auxiliary variables $\boldsymbol{\gamma}(t) \in \Phi\big(t, \boldsymbol{x}(t)\big)$ are introduced. As a result, the optimization problem in (II.1.3) is, thus, transformed into

$$\begin{aligned}
\underset{\boldsymbol{\phi}(t),\forall t}{\text{minimize}} \quad & f_o(\bar{\boldsymbol{\phi}}), && \text{(II.1.8a)}\\
\text{subject to} \quad & \text{(II.1.3c)}, \text{(II.1.3d)}, && \text{(II.1.8b)}\\
& \overline{g_k(\gamma(t))} \leq 0 \qquad \forall k \in K, && \text{(II.1.8c)}\\
& \bar{\gamma} = \bar{\boldsymbol{\phi}}, && \text{(II.1.8d)}\\
& \gamma(t) \in \Phi\big(t, \boldsymbol{x}(t)\big) \qquad \forall t, && \text{(II.1.8e)}
\end{aligned}$$

where $\overline{g_k(\gamma(t))}$ and $\bar{\gamma}$ represent the limiting time averages.

Here we note that based on Jensen's inequality over convex functions, we have that $\mathbb{E}[\boldsymbol{\phi}] \in \Phi\left(t, \boldsymbol{x}\left(t\right)\right)$ and $g_k\left(\mathbb{E}[\boldsymbol{\phi}]\right) \leq \mathbb{E}[g_k(\boldsymbol{\phi})]$. As a result, problems (II.1.3) and (II.1.8) are equivalent, i.e., yield same costs at the optimality, due to the equivalence between control and auxiliary vectors reflected in (II.1.8d).

Next, to ensure that inequality constraint in (II.1.8c) and equality constraint in (II.1.8d) are met, two sets of virtual queues, $\boldsymbol{\Psi}(t)$ and $\boldsymbol{\Xi}(t)$, respectively, are introduced. The update equations for these virtual queues being

$$\Psi_k(t+1) = [\Psi_k(t) + g_k(\gamma(t))]^+, \quad \forall k \in K, \tag{II.1.9}$$

$$\Xi_u(t+1) = \Xi_u(t) + \gamma_u(t) - y_u(t), \quad \forall u = 1, \ldots, U. \tag{II.1.10}$$

Note that Ψ_k is non-negative, while Ξ_b can be negative in order to meet the equality constraint.

II.1.3.3 Lyapunov Optimization

Let $\boldsymbol{\chi}(t) = [\boldsymbol{q}(t), \boldsymbol{\Psi}(t), \boldsymbol{\Xi}(t)]$ be the combined queue of the network at time t. As a scalar measure of the size of $\boldsymbol{\chi}$ i.e., of the network congestion, and let a quadratic Lyapunov function $\mathscr{L}(\boldsymbol{\chi}(t))$ be defined as

$$\mathscr{L}(\boldsymbol{\chi}(t)) = \frac{1}{2}\sum_{n=1}^{N} \omega_n \boldsymbol{\chi}_n(t)^T \boldsymbol{\chi}_n(t) = \frac{1}{2}\sum_{n=1}^{N} \omega_n \boldsymbol{\chi}_n(t)^2, \tag{II.1.11}$$

where $\{\omega\}_{n=1}^{N}$ are a collection of positive weights that allow treating different queues differently, though their values are typically set to $\omega_n = 1\ \forall n$. Hence, the one-slot drift of the Lyapunov function denoted $\Delta\mathscr{L}_t$ and defined as $\Delta\mathscr{L}_t = \mathscr{L}\big(\boldsymbol{\chi}(t+1)\big) - \mathscr{L}\big(\boldsymbol{\chi}(t)\big)$ is given by

$$\Delta\mathscr{L}_t = \frac{\big(q^T(t+1)q(t+1) - q^T(t)q(t)\big) + \big(\boldsymbol{\Psi}^T(t+1)\boldsymbol{\Psi}(t+1) - \boldsymbol{\Psi}^T(t)\boldsymbol{\Psi}(t)\big) + \big(\boldsymbol{\Xi}^T(t+1)\boldsymbol{\Xi}(t+1) - \boldsymbol{\Xi}^T(t)\boldsymbol{\Xi}(t)\big)}{2},$$

Dropping the subcripts indices u, k and t for simplicity, and leveraging

$$\begin{aligned} ([q + a - \mu]^+)^2 &\leq q^2 + (a-\mu)^2 + 2q(a-\mu), \\ ([\Psi + g]^+)^2 &\leq \Psi^2 + g^2 + 2\Psi g, \\ (\Xi + \gamma - y)^2 &\leq \Xi^2 + (\gamma - y)^2 + 2\Xi(\gamma - y), \end{aligned}$$

the one-slot drift can be simplified to

$$\Delta\mathscr{L}_t \leq \Delta_0 + q^T(t)\big(\boldsymbol{a}(t) - \boldsymbol{\mu}(t)\big) + \boldsymbol{\Psi}^T(t)\boldsymbol{g}\big(\boldsymbol{\gamma}(t)\big) + \boldsymbol{\Xi}^T(t)\big(\boldsymbol{\gamma}(t) - \boldsymbol{\phi}(t)\big), \tag{II.1.12}$$

where Δ_0 is a uniform bound on the term

$$\big(\boldsymbol{a}(t) - \boldsymbol{\mu}(t)\big)^T\big(\boldsymbol{a}(t) - \boldsymbol{\mu}(t)\big) + \boldsymbol{g}^T\big(\boldsymbol{\gamma}(t)\big)\boldsymbol{g}\big(\boldsymbol{\gamma}(t)\big) + \big(\boldsymbol{\gamma}(t) - \boldsymbol{\phi}(t)\big)^T\big(\boldsymbol{\gamma}(t) - \boldsymbol{\phi}(t)\big).$$

As per [143], [144], [145], the conditional expected Lyapunov drift at time t is defined as

$$\Delta\big(\boldsymbol{\chi}(t)\big) = \mathbb{E}[\mathscr{L}(\boldsymbol{\chi}(t+1)) - \mathscr{L}(\boldsymbol{\chi}(t))|\boldsymbol{\chi}(t)]. \tag{II.1.13}$$

Let $V_\Delta \geq 0$ be a parameter which controls the trade-off between queue length stability and the accuracy of the optimal solution of (II.1.8). Equally, let $\boldsymbol{\phi}^{\text{Avg}}(t) = \frac{1}{t}\sum_{\tau=0}^{t-1}\boldsymbol{\phi}(\tau)$ be the current running time averages of control variables.

By introducing a penalty term $V_\Delta \nabla_{\boldsymbol{\phi}}^T f_o\big(\boldsymbol{\phi}^{\text{Avg}}(t)\big)\mathbb{E}[\boldsymbol{\phi}(t)|\boldsymbol{\chi}(t)]$ in the expression of the conditional expected drift, and by minimizing the upper bound of the DPP,

$$\Delta_0 + V_\Delta \nabla_{\boldsymbol{\phi}}^T f\big(\boldsymbol{\phi}^{\text{Avg}}(t)\big)\mathbb{E}[\boldsymbol{\phi}(t)|\boldsymbol{\chi}(t)] + \mathbb{E}[q_b^T(t)\big(a(t) - \boldsymbol{\mu}(t)\big)|\boldsymbol{\chi}(t)]$$

$$+\,\mathbb{E}[\boldsymbol{\Psi}^T(t)\boldsymbol{g}\big(\boldsymbol{\gamma}(t)\big)+\boldsymbol{\Xi}^T(t)\big(\boldsymbol{\gamma}(t)-\boldsymbol{\phi}(t)\big)|\boldsymbol{\chi}(t)],$$

yields $\boldsymbol{\phi}^\star(t)$, which represents the optimal control policy. In summary, it can be seen that the DPP policy acquires information about $\boldsymbol{\chi}(t)$ and $\boldsymbol{h}(t)$ at every slot t, and chooses the action $\boldsymbol{\phi}(t) \in \Phi\big(t, \boldsymbol{x}(t)\big)$ that minimizes the above upper bound. Moreover, a closer look into this expression shows that the control vector and the auxiliary variables dependent parts therein can be decoupled and rewritten as

$$\Big[\overbrace{\boldsymbol{\Psi}^T(t)\boldsymbol{g}\big(\boldsymbol{\gamma}(t)\big)+\boldsymbol{\Xi}^T(t)\boldsymbol{\gamma}(t)}^{\substack{\text{Impact of virtual}\\ \text{queue and}\\ \text{auxiliary variables}}}\Big]_{\#1}+\Big[\overbrace{V_\Delta\nabla_{\boldsymbol{\phi}}^T f_o\big(\boldsymbol{\phi}^{\text{Avg}}(t)\big)\boldsymbol{\phi}(t)}^{\text{Penalty Term}} - \underbrace{q_b^T(t)\boldsymbol{\mu}(t)}_{\text{Queue and RV}} - \underbrace{\boldsymbol{\Xi}^T(t)\boldsymbol{\phi}(t)}_{\substack{\text{Impact of virtual}\\ \text{queue and controls}}}\Big]_{\#2}, \quad \text{(II.1.14)}$$

where we have decoupled the control variables and the auxiliary variables through terms #1 and #2, respectively. As a result, the subproblems of finding auxiliary variables and control variables can be treated independently presented as below.

II.1.3.4 Evaluation of Auxiliary Variables

Since the auxiliary variables are decoupled from control variables as given in (II.1.14), the formal representation of auxiliary variables evaluation at time t is given by

$$\underset{\boldsymbol{\nu}}{\text{minimize}} \quad \boldsymbol{\Psi}^T(t)\boldsymbol{g}(\boldsymbol{\nu})+\boldsymbol{\Xi}^T(t)\nu, \quad \text{(II.1.15a)}$$

$$\text{subject to} \quad \boldsymbol{\nu} \in \Phi\big(t, \boldsymbol{x}(t)\big), \quad \text{(II.1.15b)}$$

yielding $\boldsymbol{\gamma}^\star(t) = \boldsymbol{\nu}^\star$. It can be noted that the feasible set is a convex hull due to fact that $g_m(\cdot)$ is convex. Depending on the nature of $g_m(\cdot)$ the above convex optimization problem can be solved with the use of an appropriate method [146].

II.1.3.5 Determining the Control Variables

Finally, the optimal control at time t is found by solving the subproblem from term #2 in (II.1.14) as

$$\underset{\boldsymbol{\delta}}{\text{minimize}} \quad V_\Delta\nabla_{\boldsymbol{\phi}}^T f_o\big(\boldsymbol{\phi}^{\text{Avg}}(t)\big)\boldsymbol{\delta}-q_b^T(t)\boldsymbol{\mu}(t,\boldsymbol{\delta})-\boldsymbol{\Xi}^T(t)\boldsymbol{\delta}, \quad \text{(II.1.16a)}$$

$$\text{s.t.} \quad \boldsymbol{\delta} \in \Phi\big(t, \boldsymbol{x}(t)\big), \quad \text{(II.1.16b)}$$

resulting $\boldsymbol{\phi}^\star(t) = \boldsymbol{\delta}^\star$. Based on the nature of function $\mu(\cdot)$ e.g., linear, exponential, etc., the solution to (II.1.16) can be found.

II.1.3.6 Summary

Algorithm II.1.2 provides a summary of the steps involved in solving (II.1.8). In conclusion, using Lyapunov DPP method ensures that the gap between the time average penalty and the optimal solution is bounded by the term $\frac{\Delta_0}{V_\Delta}$ [142], [145]. Thus, the optimality of the solution is ensured by the choice of a sufficiently large V_Δ.

Algorithm II.1.2: Lyapunov Drift-Plus-Penalty (DPP)

Input: $\boldsymbol{q}(t)$, $\boldsymbol{\Psi}(t)$, and $\boldsymbol{\Xi}(t)$ for $t = 0$.
while `True` **do**
  Queue Observation: $\boldsymbol{q}(t)$, $\boldsymbol{\Psi}(t)$, $\boldsymbol{\Xi}(t)$, and running averages $\boldsymbol{\phi}^{\text{Avg}}(t)$.
  Auxiliary variables: $\boldsymbol{\gamma}(t) = \underset{\boldsymbol{\nu}\in\Phi\left(t,\boldsymbol{x}(t)\right)}{\arg\min} \boldsymbol{\Psi}^T(t)\boldsymbol{g}(\boldsymbol{\nu}) + \boldsymbol{\Xi}^T(t)\nu.$
  Control variables:
  $\boldsymbol{\phi}(t) = \underset{\boldsymbol{\delta}\in\Phi\left(t,\boldsymbol{x}(t)\right)}{\arg\min} V_\Delta \nabla_{\boldsymbol{\phi}}^T f_o\left(\boldsymbol{\phi}^{\text{Avg}}(t)\right)\boldsymbol{\delta} - q_b^T(t)\boldsymbol{\mu}(t,\boldsymbol{\delta}) - \boldsymbol{\Xi}^T(t)\boldsymbol{\delta}.$
  Update: $q(t+T)$, $\boldsymbol{\Psi}(t)$, $\boldsymbol{\Xi}(t)$, and $\boldsymbol{\phi}^{\text{Avg}}(t)$.
  $t \leftarrow t+1$
end while

Part III

Application Scenarios for mmWaves in 5G Networks and Beyond: V2X Communications

"A telephone subscriber here may call up and talk to any other subscriber on the Globe. An inexpensive receiver, not bigger than a watch, will enable him to listen anywhere, on land or sea, to a speech delivered or music played in some other place, however distant."

Nikola Tesla, *My Inventions*, 1919

Chapter III.1

mmWave-enabled Vehicular Communications

> "I believe in the potential of all things possibly imagined that can be made into a reality. My uncle was a Swedish scientist, and in the 1970s, he would speak of computers controlling most things in the future and self-driving cars and wireless communication. All the things that we are living with now."
>
> Dean Haglund

The interest in mmWave communications has risen sharply in the last years motivated by their widespread consideration as a technological solution capable of dealing with the stringent rate requirements currently demanded by wireless networks. The momentum gained by mmWave bands springs several technical challenges regarding the allocation of radio resources. This allocation is particularly complex in vehicular networks where reliability/latency constraints are extremely demanding, and links between vehicles are highly influenced by their mobility, being prone to beam misalignment and blockage between counterparts.

Part III of this Thesis builds upon this vibrant area of research. However, before proceeding further, next sections will first introduce the role of communication technologies in the road to autonomous vehicles, as well as open issues regarding their current standardization progress and efforts. Following that, challenges related to the adoption of mmWave communications for vehicular communications will be described. Finally, the two selected use cases that showcase the benefits of bringing wireless intelligence to mmWave V2V communications will be briefly presented.

III.1.1 The Role of Communications Towards Autonomous Vehicles

The automotive industry is set on a path where vehicles are continuously becoming more aware of their environment due to the addition of various types of integrated sensors. At the same time, headed to eventually culminate having fully autonomous driving capabilities without human

TABLE III.1.1: Automation levels towards fully autonomous driving vehicles[1].

Level 0	**Driver Only**	No automation; the **human driver is responsible for all driving tasks**.
Level 1	**Assisted**	The **automated system on the vehicle can assist the human driver** within the defined use cases of the driving task.
Level 2	**Partial Automation**	The automated system on the vehicle conducts multiple parts of the driving task. The **human continues to monitor the driving environment** and perform the remaining driving tasks.
Level 3	**Conditional Automation**	The **automated system conducts multiple parts of the driving task** and **monitors the driving environment** within the defined use cases. The **human driver** must always be **ready to take back control** when the automated system requests.
Level 4	**High Automation**	The automated system conducts the driving task and monitors the driving environment within the defined use cases. **The human need not take back control** while operating **within the defined use cases**. The **human driver assumes control outside of the defined use cases**.
Level 5	**Full Automation**	The **automated system performs all driving tasks** within all use cases that a human driver could perform.

intervention, the dependence on self and collaborative-acquired sensing information in these vehicles is growing more acute. For that purpose, it is pivotal to rely on a communication system based on V2X communications that enhances the performance of automated driving through increased situational awareness, gained both from sensing technologies and radio-based communications.

Automated vehicles are defined by the U.S. Department of Transportation (DOT) in [147] as "any vehicle equipped with driving automation technologies as per SAE J3016". Thus, this term fits any form of driving automation, encompassing all vehicles in SAE J3016 levels 1–5 [148] i.e., those where at least one aspect of a safety-critical control function occurs without direct human-driver input. In line with this definition, autonomous vehicles are a subset of automated vehicles endorsed with self-driving capabilities with very limited –or even in the absence of– connectivity with other vehicles or infrastructures. The aforementioned, and widely adopted, automation levels towards achieving full autonomy in vehicles are described in Table III.1.1. For levels 0-2 therein, the driver is the one in charge of monitoring the environment, whereas from level 3 onward, the automated system undertakes this responsibility without any human assistance.

Coined by the industry and the media, a third term prevails: *connected and automated* vehicles. Therein *connected* relates to vehicles with various levels of connectivity, irrespective of their automation capabilities. This third definition is, indeed, the most relevant for the purpose

[1]The Society of Automotive Engineers International (SAE) categorizes the technology by level of driver intervention and/or attentiveness required for operation.

of this Thesis, as it implies the existence of a communication link established between a vehicle and an outside entity. The nature of this entity gives rise to a whole ecosystem of vehicular communications operated through vehicle-to-vehicle (V2V), vehicle-to-infrastructure (V2I), vehicle-to-pedestrian (V2P), vehicle-to-network (V2N), or any other kind of links. Collectively, these use cases have become known as vehicle-to-everything (V2X) communications.

Hence, two strong technology trends, one in the mobile communications industry and the other in the automotive industry, are becoming interwoven. Together they will compel new capabilities and functionalities for upcoming intelligent transportation systems (ITS) and future driving, as connectivity can provide efficiency and safety benefits independently of, or in conjunction with, automation [149].

In that sense, some of the 6 key connectivity requirements identified in [150] for autonomous driving include the existence of redundant real-time architectures, adaptability to escalating high-speed data demands, operation under considerably lower latencies than LTE's for real-time safety applications, and guaranteeing near 100% reliability in transmissions. How existing V2X communications technologies perform with respect to these and other aspects will be next discussed.

III.1.2 V2X Landscape: DSCR or C-V2X

It is not clear what the predominant subyacent technology providing V2X communications will be in the near future. Until March 2017, when 3GPP finalized C-V2X Rel. 14 specifications, there were only two sets of standards for V2X: DSRC [151] and ITS-G5 [152] issued by the European Telecommunications Standards Institute (ETSI) in response to the final report [153] on the European strategy on Co-operative Intelligent Transport System (C-ITS). These two standards, correspondingly promoted in the U.S. and in Europe, both focused on the use of DSRC/802.11p for V2X. However, nowadays, a closer look at the RAT technologies involved reveals that the real dispute is whether to use a technology with i) a WLAN-oriented protocol stack as DSRC[2], or ii) a cellular-based one, C-V2X, in the form of first LTE-V2X [154], [155], soon to be followed by NR-V2X [156] over 5G NR.

On one hand, the technology maturity, its early adoption by some vehicle manufacturers and, last but not least, potential government mandates on the prompt use of V2X, may tilt the balance in favor of the adoption of DSRC-based systems. On the other hand, 3GPP and mobile operators are willing to cash in on the humongous research and deployments efforts undertaken in previous mobile generations, by promoting an LTE-based V2X cellular system as a stepping stone towards NR-V2X. To that end, 3GPP has studied basic [157] and enhanced [158] V2X requirements. Rooted on those results, Rel. 14 LTE-V2X [159] has been issued to support basic

[2]Wireless access in vehicular environments (WAVE) on top of which DSRC is built, is in itself a bundle of IEEE standards including IEEE 802.11/802.11p for the PHY and medium access control (MAC) layers.

road safety related requirements whereby vehicles are able to exchange their own status information through sidelink[3] with other nearby vehicles, infrastructure nodes or pedestrians. Following that, V2X Phase 2 as per Rel. 15 [160] has introduced a number of new features in sidelink, including: carrier aggregation (CA), high order modulation, latency reduction, and feasibility studies on both transmission diversity and short transmission time interval (TTI) adoption. This enhanced 3GPP V2X Phase 2 will still require co-existance with Rel. 14, since the enhancements are primary based on LTE. As for the study of new use cases for LTE and 5G NR in Rel. 15, they are examined in [161]. Finally in [156] the requirements for V2X operation over 5G NR as per Rel. 16 are investigated; NR-V2X specification is expected to be ready by December 2019, roughly after this Thesis has been deposited.

One of the main assets in favor of the C-V2X alternative is its alleged superior performance, which is underpinned by the new developments affecting the PHY and MAC layers, the cost effectiveness and the 5G compatibility afforded. As opposed to the frantic activity developed by 3GPP on C-V2X, no clear path to enhance the underlying radio standard of DSRC has been set until very recently. Indeed, though the standardization process of DSRC concluded in 2009 and it has ever since been subjected to extensive testing and large extend trials by car makers and other stakeholders [162], initiatives like the Next Generation Mobile Networks Alliance (NGMN) and the 5G Automotive Alliance (5GAA)[4] that promote V2X solutions are pushing hard for the cellular alternative, revealing that there are many interests involved in the selection of one or the other technology. Indeed, in this sense, it is noteworthy that the DSRC deployment model relies on council/state RSU facilities and that, hence, there is no telecommunication operator involved in business with the DSRC/802.11p market.

So far, a number of studies and field trials have evaluated the suitability of DSRC under various V2X scenarios [163], [164] and compared its performance with what is believed that will be achievable in the early deployments of C-V2X [165]–[167]. Yet, there is a general consensus that these present-day vehicular RATs will fail to meet the communication requirements of the most advanced vehicular applications [162], [168], [169]. Thus, the possible evolution paths, and whether the theoretical performance limits of the newest C-V2X and 802.11 amendment –802.11bd– alternatives will guarantee the high reliability, low latency and high throughput demands is now under study.

Next, the aforementioned present-day technologies, namely DSRC and LTE-V2X are concisely compared with an emphasis on their performance limits and in their PHY and MAC layer aspects. It is noteworthy, though,

[3]LTE sidelink is an adaptation of to the original LTE standard to allow direct communication between any two LTE devices without the intervention of any base station.

[4]5GAA is a cross-industry organization of companies from the automotive, technology, and telecommunications industries, created in 2016 and whose 8 initial founding members were AUDI AG, BMW Group, Daimler AG, Ericsson, Huawei, Intel, Nokia, and Qualcomm Incorporated. As of mid-2018, the membership of 5GAA had reached beyond 60 affiliates.

that in line with this Thesis, both IEEE 802.11bd, and NR-V2X consider the use of mmWave bands for V2X applications, particularly for applications that require a short range and high-to-very-high throughputs.

III.1.2.1 DSCR versus C-V2X: Performance, Physical and MAC Layer Aspects

In general terms, DSRC provides a better support for safety applications, while LTE-V2X is more suited for non-safety related applications [170]. The reason lies in the superior performance of LTE-V2X in terms of data rates and reliability, whereas DSRC is better in terms of transmission latency. The introduction of NR-V2X may, however, significantly reduce the latency, revamping C-V2X for safety critical operation [168].

Next the performance of LTE-V2X and DSRC in terms of data rate, coverage, mobility support and latency is compared:

Data rate: The theorical maximum data rates of DSRC range between 3 and 27 Mbps, whereas LTE-V2X offers 20 and 80 Mbps in the UL and DL, respectively.

Coverage: DSRC offers limited coverage, being a short range technology by definition. This poses a significant challenge for high-speed moving vehicles, whose connection time to RSUs will be limited. Cellular coverage is wider and may extend beyond 1 Km. Besides, capillary availability of cellular access backed by existing infrastructure can be leveraged for vehicular communications.

Mobility Support: Transmission held by high-speed moving vehicles are affected by Doppler shift. In this sense the longer the symbol duration, the worse the effect is on the signal. Thus, having a 10 times shorter symbol duration, DSRC shows a better behavior with respect to Doppler shift, and supports speeds of up to 250 Km/h for the 140 Km/h of LTE-V2X.

Latency: LTE-V2X is expected to operate with latencies below 100ms in normal operation, and below 20 ms for emergency situations. In DSRC the theoretical latency is 50 ms, yet during trial tests latencies around 5-10 ms were measured [162].

Some of the radio design aspects of DSRC/802.11p and prospective C-V2X as per 3GPP Releases 14 and 15 affecting the above performance indicators are summarized in Table III.1.2. In a nutshell, the robustness to Doppler shift and recorded latencies in DSRC trials postulate the technology as an enabler for vehicular low-latency communication. Yet, it is ill-suited for ultra-reliable communication scenarios [171], due to its random access scheme that leads to high collision probability in medium to high load regimes.

In view of the identified performance limitations in DSRC and LTE-V2X, besides other evolution paths that include e.g., the interworking of the two technologies to supplement each other[172], [173], the use of mmWave bands [63], [162], [174], [175] for vehicular communications has

TABLE III.1.2: Radio aspects of DSRC 802.11p compared to C-V2X.

Radio Design Parameter	DSRC 802.11p	C-V2X Release 14/15
Synchronization	Asynchronous	Synchronous
Channel Size	10/20 MHz	Rel. 14 10/20 MHz Rel. 15 10/20 MHz/Nx 20MHz
Resource multiplexing across vehicles	TDM	TDM and FDM access
Data channel coding	Convolutional	Turbo
HARQ	No	Rel. 14/15: yes. Rel. 15: Ultra-reliable commun. possible
Waveform	OFDM	Single-Carrier FDM (SC-FDM)
Resource selection	Carrier-sense multiple access with congestion avoidance (CSMA-CA)	Sensing based semi-persistent scheduling (SPS) with frequency domains
MIMO support	No standardized support	2 antennas Rx diversity (mandatory) 2 antennas Tx diversity (supported)
Deployment	Since 2017, OEM rollout in 2019	2020/2021
Roadmap	802.11NGV targeting interoperativity with 802.11p	C-V2X Rel.16 based on 5G NR operating in a different channel from Rel. 14/15

been postulated. The rationale is to complement other vehicular RATs by leveraging reduced cell sizes to seek increased network capacity. The same reasoning holds to consider the use of Terahertz bands [176]. Next, the challenges and opportunities of operating mmWave vehicular communications are examined.

III.1.3 mmWave V2X: Challenges and Opportunities

III.1.3.1 New Opportunities for mmWave V2X

The mmWave bands are attractive for V2V and V2I including cars, high-speed railway, and subway systems since advanced safety and information and entertainment (infotainment) services in connected vehicles will need Gbps date rates, which cannot be achieved in the 10 MHz channel bandwidths at 5.9 GHz in current 4G [30]. In fact, clear niches for the application of mmWave V2X are found in:

Cooperative perception, which enables sharing onboard sensor data (e.g., from cameras, LIDAR, radar, etc.) between nearby vehicles or infrastructures with low latency for safe, efficient, and proactive driving [177]. The most basic cooperative perception based applications are basic safety related and require low latency and modest data rates to implement alert mechanisms for drivers. However, more advanced applications demand high data rates. That is the case of see-through and see-around-corners functionalities that extend the operation range of onboard sensors beyond their original LOS limits, as these limits are often occluded by the presence of surrounding vehicles and objects. Another example of the application of cooperative perception applied to cooperative driving are vehicular platooning systems, where through directional back-to-front wireless communication between subsequent vehicles, onboard sensor data is shared for accurate control and safe operation [178].

HD 3D maps, which will be a critical component for accurate localization in automated driving systems [62]. In order to exchange delay-insensitive data, automated vehicles will need to build an up-to-date map based on short-lived, high data rate connections to nearby infrastructures. Relying on pre-loaded maps is not advisable, as these maps may become quickly outdated in response to fluctuating traffic and road status. Further, rather than mere static elements, these maps should ideally also reflect all the dynamic objects around e.g., other vehicles, bikes and pedestrians, that is, the inputs acquired from sensor data so that these elements are recognized and their trajectories estimated in advance [179]. Moreover, sensor data could be utilized for constructing and timely updating a crowdsourced HD 3-dimensional (3D) Map [180], useful not only for vehicles but also for traffic analysis and communications related dynamic resource allocations at the cloud/edge servers. In this case, the presence of dynamic objects calls for high capacity links to exchange sensing data with very low latency, mmWave links.

Infotainment, whereby vehicle passengers will be able to enjoy on-demand multimedia services through onboard infotainment systems and/or passengers' mobile devices via tethering using in-car hotspots. High-rate and low-latency Internet access is required for this purpose.

III.1.3.2 Challenges to adopt mmWave in V2X

Despite the new opportunities that incorporating mmWaves into the V2X landscape may bring, their application in vehicular environments is faced with serious challenges on the PHY and MAC layer. Indeed, the inherent difficulties of propagation at mmWave frequencies, as described in Section I.1.1.3, are exacerbated by the high-mobility of V2X environments. Yet, recent efforts towards their standardization, starting with the enhancements to Rel. 15 NR for advanced V2X services in sub-6 GHz and mmWave bands as per [181] or with the study of NR-V2X beyond 52.6 GHz [182], followed by the growing literature on the matter [183], [184], evince that the support for mmWave communications will be an integral part of the vehicular communications ecosystem, though not immediately.

The fundamental challenges of using mmWaves in any mobile scenario are directionality and blockage [185]. In fact, the need to adapt existing V2X protocols to operate under directional communications is, undoubtedly, the greatest difficulty that hinders the straightforward integration of mmWave communications into V2X solutions. Table III.1.3 summarizes these and other challenges confronted with the specific characteristics of the upcoming new vehicular RATs: IEEE 802.11bd amendment and NR-V2X. Next, those challenges that are more closely related to the contents of this Thesis will be briefly discussed:

mmWave Vehicular Channel Modeling: The understanding of the unique characteristics of vehicular mmWave channels is still limited, with

Table III.1.3: Millimeter wave challenges in IEEE 802.11bd and NR V2X standards. Src. [184].

	Open Challenges	Explanation
PHY Layer	Numerology design	Longer slots lead to channel variations
	Multiple antenna arrays	Synchronization with distributed antennas
	Joint radar and communication	Based on IEEE 802.11ad (static and indoor) scenarios
	Broad/multi/groupcast communication	Directionality precludes broadcast operations
	Channel estimation	Time-varying channel hinders the use of midambles[5] and may prevent feedback
	Synchronization	Synchronization signals need to be directional
MAC Layer	Mobility management	Directionality complicates vehicle discovery and retransmissions
	Resource allocation	CSMA strategies suffer from an increased deafness
	Interference management	Unscheduled and autonomous sidelink transmission prevents interference coordination
Upper Layers	Multi-hop and routing	Routing is complicated by highly volatile links
	Multi-RAT support	Coexistence between RATs in the same frequency band, vehicle, and/or deployment
	Congestion and flow control	Suboptimal interaction between channel variability and transport layer rate estimation
Modeling	Channel design	Effect of second order statistics, signal correlation, Doppler and fading is not characterized

very few measurement campaigns, specially in the V2V context, where realistic scenarios cannot be easily simulated [186]. Besides its uniqueness with respect to traditional modeling aspects, namely, higher atmospheric attenuation, reduced wavelength originated scattering and reflection, or poorer diffraction and penetration, other aspects that are specific to vehicular channels need to be considered. Among these, discerning whether urban or highway propagation is assumed, the higher susceptibility to signal blockage from moving vehicles or pedestrians, the impact of the antenna arrays location, the density, size and type of vehicles, and channel fluctuations due to fixed and moving scatterers. Figure 2 in [149] summarizes V2X specific considerations for channel modeling. In that respect, the recently presented 3GPP guidebook on how to model the V2V channel [187] might become an invaluable tool.

Beamforming/Beam Tracking under Mobility: Another significant challenge for enabling V2X communications over mmWave spectrum is the potentially large overhead to establish reliable links. As was already mentioned in Section I.1.1.3.1, the issue gets even worse by the constant moving of vehicles and the already mentioned complex vehicular channels at mmWave frequencies. However, some initial results have demonstrated that beam tracking designs that adapt mmWave directions to predicted vehicle locations represent a promising solution. To that end, several approaches have been studied, including position-aided beamtraining [189],

[5]Midambres are specific portions of a frame in between OFDM data symbols, and allow to provide a better channel estimate in fast varying channels [188].

[190], radar-aided [191], out-of-band information aided [192], or LIDAR-data based leveraging deep learning [65]. With a more practical focus [193], tackles the idea of going without beam training. Traditionally, the difficulty in achieving realistic spatial consistency to sustain the data-link connection for high-speed mobility vehicles has been listed as another limitation to V2V connectivity [30]. In fact, the concepts of channel coherence time and beamforming closely interact with the investigation of the coverage of mmWave networks, since they determine the frequency of cell handover and the associated beam management overhead. This aspect is investigated in [194]. It would be particularly interesting to assess how the beam management scales with respect to the vehicle velocity, as well as the ensuing measurement and processing complexity in mmWave environments.

In summary, the tide of negative perception on the feasibility of mmWaves for V2X seems to be slowly turning based on these findings. Next, to wrap up this introductory chapter, the two selected use cases to investigate the use of mmWaves for V2X are briefly outlined.

III.1.4 Selected mmWave-enabled V2V Scenarios

III.1.4.1 Use Case 1: mmWave V2V in a Multilane Highway

In this first use case scenario examined in Chapter III.2, the delay performance of mmWave V2V communications is investigated. Specifically, the chapter considers the exchange of critical safety information captured by vehicle sensors and, thus, likely to be shared among nearby cars for an enhanced reactivity against unexpected eventualities in the road. In this context, the challenge is to guarantee stringent latency and reliability levels under the dynamic topology entailed by the high-speed movement of the vehicles.

Specifically, the chapter will first formulate the beamwidth optimization problem to later delve into analyzing the interplay between the beamwidth assignment and the scheduling period. To this end, the study presented in this chapter presents a comprehensive scheme that considers the directionality of the mmWave link, the effect of the selected beamwidths on the interference at the vehicular receivers, the blockage of intermediate vehicles, the throughput versus alignment delay trade-off, impact of vehicle density and of the speed offset between vehicles on the beam coherence time.

Extensive simulations reveal that, even in simplistic vehicular setups considering vehicles moving along a multilane highway with constant speeds and no overtaking, the throughput performance and the latency/reliability trade-off is affected not only by the selected antenna beamwidths –and their suitability to the radio conditions imposed by the dynamics of the scenario under analysis–, but also by a proper choice of the scheduling interval/beam realignment period.

III.1.4.2 Use Case 2: mmWave V2V to Exchange Sensing Information on an Urban Traffic Junction

The second use case scenario, that is explored in Chapter III.3 is related to one of the niche application scenarios identified for the use of mmWave V2X, that of cooperative perception. In this scenario, that constitutes the entrance-level for the future cooperative driving, the chapter investigates the performance in terms of delay and of the contextual awareness gain achieved when the coverage range is extended beyond the LOS. In particular, the focus is placed on the case when such a coverage extension is attained through mmWave V2V communication links, which are dynamically established among vehicles traversing a traffic-light regulated urban junction.

To provide the scenario with the due realism, SUMO simulated traffic traces of vehicles traversing a traffic-light regulated multi-lane intersection are exploited. Therein prospective vehicular receivers will try to establish mmWave links whereby their sensing range will be effectively *extended*. To that end, a vehicle association strategy is proposed so that not only PHY and MAC aspects of the vehicles involved are contemplated but also, the suitability and timeliness of the information gain obtained by means of the pairing is leveraged. The results of this pairing strategy are compared against a benchmark of classical pairing strategies, and the relevance of bringing higher level information into the pairing process is highlighted.

III.1.5 Conclusions

In this introductory chapter to mmWave-enabled vehicular communications, the main requirements of V2X communications in terms of performance indicators, haves been discussed. After having reviewed the current wireless vehicular communication technology alternatives, a DSRC or C-V2X based V2X stack, the limitations of these solutions under debate in standardization mainstreams have been highlighted. Based on those impediments, the use of mmWave communications is deemed an instrumental pillar in the path to connected and fully automated vehicles, bridging the gap between the wireless communication capacity offered and demanded. Following that, the opportunities granted and the challenges faced by this RAT have been compiled. Finally, the two use cases that will be covered in detail in the remaining two chapters of Part III of the Thesis have been briefly presented: the multilane highway and the urban traffic-junction, which provide a low level examination of the performance of mmWave V2V communications and a toy example of the prospective benefits of applying collaborative perception through mmWave communications.

Chapter III.2

Delay Performance of mmWave V2V Communications in a Multilane Highway

III.2.1 Introduction

As thoroughly discussed in I.1.1, the last few years have witnessed the advent of wireless communications deployed in the mmWave band, as a means to circumvent the spectrum shortage needed to satisfy the stringent requirements of 5G networks [20], [26]. The large amount of free spectrum available in the 60 GHz band –with 14 GHz of unlicensed spectrum, i.e., roughly 15 times as much as all unlicensed WiFi spectrum in lower bands– represents a new opportunity for future communications using channel bandwidths beyond 1 GHz, as evinced by several standards for wireless personal and local area networks (such as IEEE 802.15.3c [195] and IEEE 802.11ad [196]). This stimulating substrate for high-rate communications is the reason why 5G standardization committees and working groups are actively investing enormous research efforts towards leveraging the inherent advantages of mmWave communications e.g., improved interference handling by virtue of highly-directive antennas in cellular scenarios with massive device connectivity.

Among all the above scenarios where mmWave bands have been addressed in the literature, their application to vehicular communications as described in Section III.1.3, has lately grasped considerable attention due to more wireless technologies being integrated into vehicles for applications related to safety and leisure (infotainment), among others [174]. Although certain safety applications may not require high data rates to be captured by the sensors installed in the vehicle e.g., blind spot warning, many other applications are foreseen to require vehicular connectivity with very high transmission rates predicted to surpass the 100 Mbps limit for raw sensor data. For instance, radars designed to operate on the 77-81 GHz band have been shown to enhance functionalities of vehicles such as

automatic cruise control, cross traffic alert and lane change warning [197]. Yet, this sensors require operating data rates that go far beyond the 27 Mbps limit available in in DSRC –the *de facto* standard for short-range vehicular communications [151]– or current 4G cellular communications. Moreover, advanced radar technologies such as those relying on laser technologies like LIDAR to produce high-resolution point-cloud maps compel even more demanding data rates (in the order of tens of Mbps, depending on the spatial resolution and scanning rate). Predictions for autonomous vehicles foresee up to 1 TB of generated data per driving hour, with rates achieving more than 750 Mbps [198], motivating further the adoption of mmWave V2X communications in the automotive sector.

Unfortunately, the challenging radio conditions derived from the mobility of vehicles, their relatively high speed with respect to pedestrians, the dynamic topology of vehicular wireless networks and the higher likelihood to suffer inter-vehicular LOS blockage, are factors that pose significant challenges to be dealt with [199]. Indeed, it has not been until recently when early findings on the propagation characteristics of mmWave vehicular communications [200] and limited work thereafter [201] have highlighted this spectrum band as a promising enabler for high-bandwidth automotive sensing [63], [202] or beamforming in V2I communications [60]. Interestingly, to the best of our knowledge, at the time that the research that originated this chapter was concluded, the literature on mmWave V2V communications was circumscribed to [174], where the impact of directionality and blockage on the SINR are explored via simulations for unicast V2V transmissions over the 60 GHz band. However, the solution proposed therein is based on a vanilla static vehicle association and, neither the delay implications nor the reliability performance associated to data traffic arrivals in the system are contemplated.

III.2.1.1 Main Contributions

The contents of this chapter on mmWave V2V communications can be framed under the scope of URLLC communications, which as briefly covered in I.1.1.1, refer to transmission technologies with stringently bounded end-to-end (E2E) latencies within the order of milliseconds and packet error rate (PER) on the order of 10^{-5} to 10^{-9} [203]. Such operational limits could correspond to critical safety information captured by onboard sensors, and likely to be shared to nearby vehicles for an enhanced reactivity against unexpected eventualities in the road.

In this context, the challenge to be faced is that of guaranteeing stringent latency and reliability levels in a mmWave V2V communication scenario with a dynamic topology entailed by the high speed moving vehicles. The proposed radio resource management (RRM) scheme is comprehensive and includes mmWave propogation aspects such as the effect of directionality (steering) on the mmWave link, the effect of the selected beamwidths on the interference caused at the nearby vRxs, the blockage due to intermediate vehicles, the throughput versus alignment delay trade-off, the

vehicle density and the impact of the speed offset between vehicles on the beam coherence time.

To address the problem, a cross-layer information aware (CSI+QSI) approach is adopted. From the algorithmic point of view, the proposed scheme comprises i) a matching game, as per II.1.2, aimed to solve the association problem between transmitting and receiving vehicles in a distributed fashion is designed, and ii) the use of a SI solver, that as briefly explained in Section II.1.1, is a class of nature-inspired optimization algorithms that simulate the collective behavior observed in certain species so as to discover optimum regions within complex search spaces under a measure of global fitness [116].

For ease of read, the main contributions of this chapter are next summarized:

Main Contributions

1. In line with the principles that govern the exchange of critical safety-related information in vehicular communications, the problem of minimizing for each scheduling period the network-wide average delay per delivered packet is formulated.

2. To tackle the above problem a cross-layer information aware (CSI+QSI) vehicle association and mmWave beamwidth optimization approach is adopted.

   (a) The vehicle association is solved via a one-to-one matching game where the utilities of the transmitting and receiving vehicles are designed with transmission opportunity and data urgency criteria.

   (b) The beamwidth optimization is solved using a SI solver, specifically, PSO.

3. To validate our proposed approach a mmWave vehicular communication simulator is build from scratch. Therein varying densities of vehicles moving along a multilane highway segment in different speeds while exchanging short/long data packets can be configured.

4. Extensive simulations were carried out towards not only exploring the quantitative performance obtained under different setups and parameters of the underlying vehicular scenario, but also as a comparison with several baselines e.g., minimum-distance matching.

   (a) Results demonstrate the superior behavior of the proposed vehicle association scheme in terms of delay/reliability performance and on the amount of paired vehicles.

III.2.1.2 Chapter Organization

The rest of this chapter is structured as follows: in Section III.2.2 we describe the overall system model of the vehicular setup under consideration, and formulate the optimization problem. Section III.2.3 and subsections therein delve into the proposed resource allocation procedure, including the adopted techniques for vehicle pairing and beamwidth optimization. In Section III.2.4 we evaluate the performance of different configurations of the proposed solution under diverse settings of the considered vehicular scenario. Finally, Section III.2.5 concludes the chapter.

III.2.2 System Model and Problem Formulation

This section elaborates on the system model for mmWave V2V communications, introduces the main elements that govern the cross-layer RRM policy and formulates the optimization problem that models the allocation of resources, namely, V2V links and their corresponding transmitting and receiving beamwidths.

III.2.2.1 Network Topology

We consider a multiple lane highway road section where vehicles move at variable speeds in the same direction. Vehicles in the highway incorporate vehicular user equipments (vUEs), further separated into vTxs and vRxs, which communicate through V2V links established on mmWave frequency band operating under time division duplexing (TDD). A co-channel deployment with bandwidth B, uniform transmit power and half-duplex mode are assumed. Let $\mathcal{I} \triangleq \{1, \ldots, I\}$, $\mathcal{J} \triangleq \{1, \ldots, J\}$ and $\mathcal{L} \triangleq \{1, \ldots, L\}$, with $\mathcal{I} \cap \mathcal{J} = \emptyset$, $|\mathcal{L}| \leq \min\{|\mathcal{I}|, |\mathcal{J}|\}$ respectively denote the sets of vTxs, vRxs and links in the system.

In this scenario the relative movement between vehicles causes a varying network topology with changing channel conditions, misalignments between vehicle pairs and uncontrollable blocking effects in the deployed mmWave links. This strong topological variability and the increased complexity of instantaneous, uncoordinated RRM policies impose the need for time-slotted communications, with two different time scales:

- Data transmission slots (ms) denoting the intervals $[t, t + T_t)$, with T_t as the duration of the transmission period.
- Scheduling slots (ms) which hereafter refers to the intervals $[t, t + T_s)$, with T_s representing the duration of the network-wide enforced control actions.

Without loss of generality, each scheduling slot is assumed to comprise an integer number N of transmission slots i.e., $T_s = NT_t$, such that scheduling occurs at $\mathcal{T}_s \triangleq \{t_s \in \mathbb{N} : t_s \mod N = 0\}$, and data transmission is held at $\mathcal{T}_t \triangleq \mathbb{N}$. As shown in Fig. III.2.1 the initial transmission slot

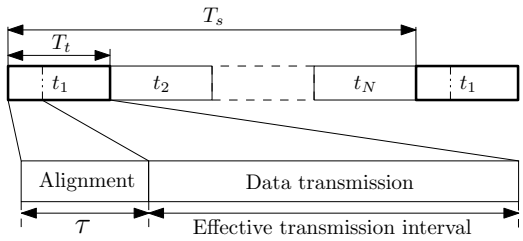

FIGURE III.2.1: Detailed view of the first transmission slot within a scheduling period, divided into alignment and effective data transmission. ([204] ©2017 IEEE)

within a scheduling slot in $\mathcal{T}_s$ will be further divided into two phases: 1) the antenna steering or beam alignment phase, whose duration depends on the beamwidths selected at each vTx/vRx pair; and 2) the effective data transmission phase, which starts once boresight directions have been correctly aligned. This split will only hold at those time intervals where a new scheduling policy is triggered and deployed.

III.2.2.2 Channel Modeling

To model the 60 GHz mmWave channel and simultaneously account for blockage effects on the mmWave signal, the standard log-distance pathloss model proposed in [205] is adopted. Under this model the channel gain h_{ij} on link ℓ_{ij} between vTx i and vRx j is given by

$$h_{ij} = 10\,\delta_{i,j}\log_{10}(d_{i,j}^{\mathrm{2D}}) + \beta_{i,j} + 15\,d_{i,j}^{\mathrm{2D}}/1000, \tag{III.2.1}$$

where the third term represents the atmospheric attenuation at 60 GHz, and the values for parameters $\delta_{i,j}$ –the pathloss exponent– and $\beta_{i,j}$ depend on the number of blockers that obtrude the link connecting a given vTx i with its corresponding pair vRx j. The original model in [205] was recently generalized in [174] by providing values for δ and β when the number of blocking vehicles goes beyond three. Since we deal with a dynamic scenario, the channel gain will vary along time as a result of the relative movement of the vehicles, yielding $h_{ij}(t)$. At the end of any given transmission slot $t \in \mathcal{T}_t$, the aggregate global CSI[1] for the set of $|\mathcal{J}|$ receivers will be given by $\mathbf{H}_{\mathcal{J}}(t) = \{H_j(t) : \forall j \in \mathcal{J}\}$, with $H_j(t) = h_{ij}(t)$ if link ℓ_{ij} exists.

III.2.2.3 Antenna Radiation Pattern

For the sake of tractability directional antenna patterns in vehicles will be approximated by a two-dimensional ideal sectored antenna model as represented by Fig. III.2.2(a). This model captures the four most relevant features of the radiation pattern, namely the boresight direction, the directivity gains in the mainlobe and in the sidelobe (also referred to as

[1]Instantaneous reporting of CSI and QSI related side effects e.g., increased signaling overhead, will be avoided by enforcing a long-term RRM strategy that includes, among others, learning techniques.

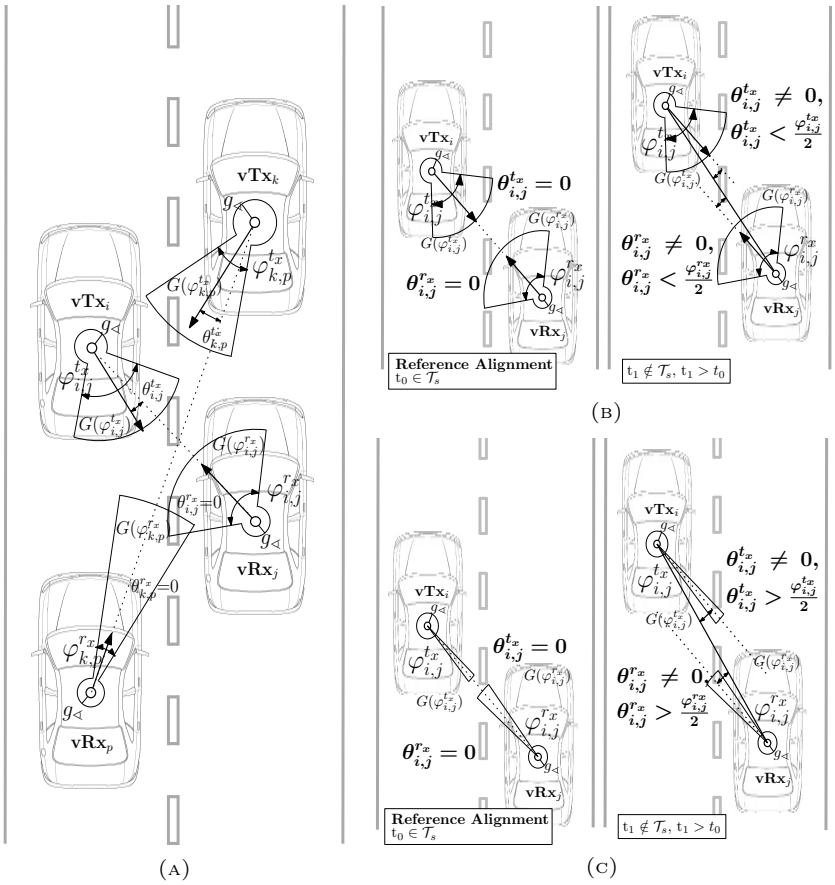

FIGURE III.2.2: (a) Parameters of the ideal sectored antenna model under study. Effect of the misalignment between transmitter and receiver boresight directions on the vTx and vRx antenna gains with (b) wide and (c) narrow beamwidths. ([204] ©2017 IEEE)

front-to-back ratio) and the half-power beamwidth. Transmission and reception directivity gains, $g_{i,j}^{\lessgtr}(t)$ with $\lessgtr \in \{\text{Tx}, \text{Rx}\}$, of vehicles in link ℓ_{ij} during a transmission slot $t \in \mathcal{T}_t$ are given by [35]

$$g_{i,j}^{\lessgtr}(t) = \begin{cases} G\left(\varphi_{i,j}^{\lessgtr}\right) = \dfrac{2\pi - \left(2\pi - \varphi_{i,j}^{\lessgtr}(t)\right) g_{\lhd}}{\varphi_{i,j}^{\lessgtr}(t)}, & \text{if } |\theta_{i,j}^{\lessgtr}(t)| \leq \varphi_{i,j}^{\lessgtr}/2, \\ g_{\lhd}, & \text{otherwise,} \end{cases} \tag{III.2.2}$$

where $\theta_{i,j}^{\lessgtr}(t)$ represents the alignment error between vTx_i and vRx_j antenna steering directions and the corresponding boresight directions of vRx_j and vTx_i, $\varphi_{i,j}^{\lessgtr}(t)$ is the half-power beamwidth of link ℓ_{ij} at transmission ($\lessgtr$=Tx) and reception ($\lessgtr$=Rx) sides set for the scheduling period at hand, and $0 \leq g_{\lhd} \ll 1$ is the non-negligible sidelobe power.

As exemplified in Fig. III.2.2(b) and Fig. III.2.2(c), the likeliness of misalignment impacting on desired links due to a non-continuous steering/beam tracking mechanism may vary depending on several factors, such as the relative speed of the vehicles involved in the link, the width of the mainlobes of the transmitter and receiver antennas, or the length of the scheduling interval. Moreover, the selected beamwidths will impel whether signals from undesired V2V links arrive into the sidelobes or the mainlobe of vRxs, which will severely impact measured SINR levels. For this reason the sought RRM should also include a beamwidth selection strategy that dynamically adapts to the surrounding conditions and, counteracts their negative effect on the transmitted signal –which, in turn, comes along with an impact on the dynamics of the transmission queues–. The latter gains relevance in realistic scenarios, where the dynamics of the vehicle movement involve frequent misalignment events.

III.2.2.4 Alignment Delay and Transmission Rate

As discussed in I.1.1.3.1, numerous alternatives that speed up the beamforming protocol have been proposed in the literature. In this chapter, however, a simplified version of the three-step beam codebook-based approach introduced by [44] is employed due to its robustness and compliance with ongoing standards. Specifically, a two-staged beam alignment process will yield the best steering for the refined beams at both ends of the V2V link. These two stages encompass a sequence of pilot transmissions and use a trial-and-error approach where first a coarse sector-level scan detects best sectors for vTx and vRx and, afterwards, within the limits of the selected sector a finer granularity beam-level sweep searches for best beam-level pairs. In this approach, the well-known alignment delay versus throughput trade-off [206] is exposed: the selection of narrower beamwidths induces longer training overheads and yields reduced effective transmission rates.

Without loss of generality we assume here that for each vehicle in a V2V link before the beam-level alignment phase itself, either the sector level alignment has already been performed or that coarse location of neighboring vehicles has been learned e.g., during the learning process in Section III.2.3.3, effectively reducing the beam search. By applying a continuous approximation [206], the alignment time penalty $\tau_{i,j}^{\text{Align}}(t)$ can be quantified as

$$\tau_{i,j}^{\text{Align}}(t) \triangleq \tau_{i,j}^{\text{Align}}\left(\varphi_{ij}^{\text{Tx}}(t), \varphi_{ij}^{\text{Rx}}(t)\right) = \frac{\psi_i^{\text{Tx}}\psi_j^{\text{Rx}}}{\varphi_{ij}^{\text{Tx}}(t)\varphi_{ij}^{\text{Rx}}(t)} T_p, \tag{III.2.3}$$

where ψ^{Tx} and ψ_j^{Rx} denote the sector-level beamwidths of vTx i and vRx j, and T_p denotes the pilot transmission duration. Constraints coming from the operational array antenna limits, sector level beamwidths and the fact that $\tau_{i,j}^{\text{Align}}(t)$ should not exceed T_t restrict the values taken by the vTx and vRx beamwidths $\varphi_{ij}^{\text{Tx}}(t)$ and $\varphi_{ij}^{\text{Rx}}(t)$, i.e.,

$$\varphi_{ij}^{\text{Tx}}(t)\varphi_{ij}^{\text{Rx}}(t) \geq \frac{T_p}{T_t}\psi_i^{\text{Tx}}\psi_{vrx}^{\text{Rx}}. \tag{III.2.4}$$

Under these assumptions, the maximum achievable data rate $r_{i,j}(t)$ between vTx i and vRx j will depend on whether beam alignment is performed at time slot t with its corresponding induced delay, and on the measured SINR at vRx j, including the interference of other incumbent vTxs on vRx j. The rate for a time slot t of duration T_t over which alignment is performed is expressed as

$$r_{i,j}(t) = \left(1 - \frac{\tau_{i,j}^{\text{Align}}(t)}{T_t}\right) BW \log_2\left(1 + \text{SINR}_j(t)\right), \tag{III.2.5}$$

with the SINR at time slot t under $Z = |\mathcal{Z}|$ simultaneously transmitting vTxs obtained as

$$\text{SINR}_j(t) = \frac{p_i g_{i,j}^{\text{Tx}}(t) h_{ij}(t) g_{i,j}^{\text{Rx}}(t)}{\sum\limits_{\substack{z \in \mathcal{Z} \subseteq \mathcal{I} \\ z \neq i}} p_z g_{z,j}^{\text{Tx}}(t) h_{z,j}(t) g_{z,j}^{\text{Rx}}(t) + N_0 BW}, \tag{III.2.6}$$

with p_i being the transmission power of reference vTx i; $h_{ij}(t)$ the channel gain in the link ℓ_{ij}; $g^{\text{Tx}}(t)$ and $g^{\text{Rx}}(t)$ respectively denoting the antenna gains at the transmitting and receiving ends of the link. The leftmost term $p_z g_{z,j}^{\text{Tx}}(t) h_{z,j}(t) g_{z,j}^{\text{Rx}}(t)$ in (III.2.6) represents the contribution of the interference received at vRx j from vTx z, $\forall z \in \mathcal{Z} \subseteq \mathcal{I}, z \neq i$; while N_0 is the Gaussian background noise power density (dBm/Hz) and BW is the bandwidth of the mmWave bandin the rightmost term. Finally, it is also straightforward to note that the rate $r_{i,j}(t)$ increases when no alignment is performed during the time slot t, as per (III.2.5) with $\tau_{i,j}^{\text{Align}}(t) = 0$.

III.2.2.5 Queues and Delay Modeling

Since our target is to design a adaptive RRM policy appropriate for a delay-sensitive information flow, a model that captures the traffic and queue dynamics is needed. For this purpose each vTx will maintain a queue for data that arrives from upper layers of the protocol stack. Assuming a fixed packet size P_s in bits, let $q_i(t)$ be the queue length in number of packets of vTx i matched to vRx j at the beginning of time slot t.

Let $\mathbf{A}_{\mathcal{I}}(t) = (A_1(t), ..., A_I(t))$ denote the random packet arrivals vector (in number of packets) to the set $\mathcal{I}$ of vTxs at the end of time slot $t \in \mathcal{T}_t$ i.e., new arrivals are observed after the scheduler's action has been performed. We assume that every entry $A_i(t)$ in $\mathbf{A}_{\mathcal{I}}(t)$, $\forall i \in \{1, \ldots, I\}$, is independently and identically distributed (i.i.d) over time slots due to mutually independent packet arrival processes following a Poisson distribution with mean $\mathbf{E}[A_i(t)] = \lambda$ within the stability region of the system. Then, if the rate in ℓ_{ij} is $r_{i,j}(t)$ as per (III.2.5), a maximum of $r_{i,j}(t)T_t/P_s$ packets will be successfully transmitted during slot $t \in \mathcal{T}_t$, and the queue dynamics for vTx i are given by

$$q_i(t+1) = \min\left\{\left[q_i(t) - \frac{r_{i,j}(t)T_t}{P_s}\right]^+ + A_i(t), q_{max}\right\}, \tag{III.2.7}$$

with $q_i(t) \in \mathbb{R}$, and q_{max} the maximum buffer size of the queue, and recalling that $x^+ \triangleq \max\{x, 0\}$. With this notation, we let $\mathbf{Q}_{\mathcal{I}}(t) = \{q_i(t) : \forall i \in \mathcal{I}\}$ represent the aggregate global QSI vector for the set $\mathcal{I}$ of vTxs at the beginning of time slot $t \in \mathcal{T}_t$. Finally, we define the global system state at time slot $t \in \mathcal{T}_t$ as $\mathcal{X}(t) \triangleq (\mathbf{H}_{\mathcal{J}}(t), \mathbf{Q}_{\mathcal{I}}(t)) \in \Upsilon$, with Υ denoting the global system state space.

Upon its arrival to a certain queue, a packet will be either delivered or dropped within $\tau^{\lambda}_{\max}$ ms after entering the queue:

- If link ℓ_{ij} is active and channel conditions in the link are good enough, packet P_i^p (with $p \in \{1, \ldots, A_i(t)\}$) will be transmitted with a delay $\tau^p_{i,j} \leq \tau^{\lambda}_{\max}$ given by
$$\tau^p_{i,j} = t^{p,serv}_{i,j} - t^{p,arr}_i, \tag{III.2.8}$$
with $t^{p,arr}_i$, $t^{p,serv}_{i,j}$ respectively denoting the arrival time of packet P_i^p at the queue and the time when the last of the bits of P_i^p is transmitted to vRx j. In other words, $\tau^p_{i,j}$ is a joint measure of the queue waiting time and transmission delay[2]. In general, the average delay per packet $\bar{\tau}^p_{i,j}(t)$ during transmission slot $t \in \mathcal{T}_t$ can be computed by averaging the delays $\tau^p_{i,j}$ of each packet successfully delivered over this link for the slot at hand, as
$$\bar{\tau}^p_{i,j}(t) = \frac{\sum_{p \in \mathcal{A}^{\checkmark}_i(t)} \tau^p_{i,j}}{\left|\mathcal{A}^{\checkmark}_i(t)\right|}, \tag{III.2.9}$$
where $\mathcal{A}^{\checkmark}_i(t)$ denotes the subset of packets successfully sent towards vRx j at time $t \in \mathcal{T}_t$. From this definition the average delay per delivered packet over the scheduling period $t_s \in \mathcal{T}_s$ will be given by
$$\bar{\tau}^{sch}_{i,j}(t_s) = \frac{\sum_{t=t_s-N+1}^{t_s} \bar{\tau}^p_{i,j}(t)}{N}. \tag{III.2.10}$$
- If link ℓ_{ij} is active but channel conditions in the link are not good enough to deliver pending packets towards receiver vRx j within $\tau^{\lambda}_{\max}$ and, either a new traffic arrival event is triggered at transmitter vTx i or a new scheduling slot starts, unfinished packets will be dropped from the queue. In both cases, the rationale behind the adoption of such a hard requirement is to prioritize newer traffic and to ensure minimum-delay communications. Each time a packet is dropped, a penalty will be incurred and computed in the form of reliability loss. This modeling is often adopted in the context of URLLC [207]. Specifically, the set of dropped packets in a transmission slot $t \in \mathcal{T}_t$ will be denoted as $\mathcal{A}^{\times}_i(t)$, such that both $\mathcal{A}^{\times}_i(t) \cap \mathcal{A}^{\checkmark}_i(t) = \emptyset$ and $|\mathcal{A}^{\times}_i(t)| \cup |\mathcal{A}^{\checkmark}_i(t)| \leq q_i(t)$ are met. Finally, the packet dropping ratio is defined at the scheduling slot level as
$$\Gamma^{\times}_i(t_s) \triangleq \frac{\sum_{t=t_s-N+1}^{t_s} \left|\mathcal{A}^{\times}_i(t)\right|}{\sum_{t=t_s-N+1}^{t_s} A_i(t)} = 1 - \frac{\sum_{t=t_s-N+1}^{t_s} \left|\mathcal{A}^{\checkmark}_i(t)\right|}{\sum_{t=t_s-N+1}^{t_s} A_i(t)}. \tag{III.2.11}$$

[2]By a slight abuse in the notation, we keep subindex j in $t^{p,serv}_{i,j}$ and related delay statistics to explicitly refer to the dependence of such terms on the transmission rate $r_{i,j}(t)$ of the channel from vTx i to its paired vRx j.

III.2.2.6 Problem Formulation

In order to formally define an RRM policy, let $\mathbf{\Phi}(t_s) \triangleq \{\phi_{i,j}(t_s) : i \in \mathcal{I}(t_s),\ j \in \mathcal{J}(t_s)\}$ denote the set of all possible vTx/vRx mappings in the system in a given scheduling slot $t_s \in \mathcal{T}_s$. Note here that $\mathcal{I}(t_s)$ (corr. $\mathcal{J}(t_s)$) denotes the subset of vTx and vRx present on the road scenario at scheduling time t_s. We further define $\mathcal{I}_j(t_s) \subseteq \mathcal{I}(t_s)$ and $\mathcal{J}_i(t_s) \subseteq \mathcal{J}(t_s)$ as the subsets of feasible vTxs for vRx j and the feasible vRxs for vTx i, where feasibility is due to a circular coverage constraint of radius R_c (in meters). In this set, $\phi_{i,j}(t_s)$ will represent the association variable so that for the pair composed by vTx i and vRx j,

$$\phi_{i,j}(t_s) = \begin{cases} 1 & \text{if link } \ell_{ij} \text{ is set, } \forall t \in [t_s, t_s + N), \\ 0 & \text{otherwise.} \end{cases} \tag{III.2.12}$$

Bearing this in mind, $\mathbf{\Phi}(t_s)$ jointly with a proper selection of the beamwidths at both vTx and vRx as defined by

$$\boldsymbol{\varphi}^{\mathrm{Tx}}(t_s) \triangleq \left\{\varphi_{ij}^{\mathrm{Tx}}(t_s) : i \in \mathcal{I}(t_s), j \in \mathcal{J}_i(t_s), \text{ such that } \phi_{i,j}(t_s) = 1\right\}, \tag{III.2.13}$$

$$\boldsymbol{\varphi}^{\mathrm{Rx}}(t_s) \triangleq \left\{\varphi_{ij}^{\mathrm{Rx}}(t_s) : j \in \mathcal{J}(t_s), i \in \mathcal{I}_j(t_s), \text{ such that } \phi_{i,j}(t_s) = 1\right\}, \tag{III.2.14}$$

give rise to the effective instantaneous rate $r_{i,j}(t, \mathbf{\Phi}(t_s))$ of link ℓ_{ij}, as per (III.2.5) and (III.2.6) with $\mathcal{Z} = \mathcal{I}(t_s)$ and relative interferences and gains between pairs given by the prevailing matching policy $\mathbf{\Phi}(t_s)$. Namely,

$$r_{i,j}(t, \mathbf{\Phi}(t_s)) = \left(1 - \frac{\tau_{i,j}^{\mathrm{Align}}(t)}{T_t}\right) BW \log_2 \left(1 + \mathrm{SINR}_j(t, \mathbf{\Phi}(t_s))\right), \tag{III.2.15}$$

if $t = t_s$ i.e., the first transmission slot after scheduling at time $t_s \in \mathcal{T}_s$ has been enforced, while for $t \in [t_s + 1, t_s + N)$,

$$r_{i,j}(t, \mathbf{\Phi}(t_s)) = BW \left(1 + \mathrm{SINR}_j(t, \mathbf{\Phi}(t_s))\right). \tag{III.2.16}$$

Based on this rate and the traffic influx rate defined as $\rho = \lambda P_s$, a fraction of the packets generated at vTx i will be transmitted towards vRx j, producing delays and packet dropping statistics over a given scheduling slot. For that reason, a delay-sensitive RRM policy should take into account not only the finite delay of those packets successfully transmitted towards their destinations (for which queue dynamics are set to prioritize new incoming traffic), but also the interplay between delay and dropped packets enforced by the queuing policy.

The problem tackled in this chapter can be hence formulated as the design of the RRM policy $\{\mathbf{\Phi}(t_s), \boldsymbol{\varphi}^{\mathrm{Tx}}(t_s), \boldsymbol{\varphi}^{\mathrm{Rx}}(t_s)\}$ for $t_s \in \mathcal{T}_s$ such that

$$\underset{\mathbf{\Phi}(t_s), \boldsymbol{\varphi}^{\mathrm{Tx}}(t_s), \boldsymbol{\varphi}^{\mathrm{Rx}}(t_s)}{\text{Minimize}} \quad \sum_{i \in \mathcal{I}(t_s)} \sum_{j \in \mathcal{J}(t_s)} \bar{\tau}_{i,j}^{sch}(t_s) \phi_{i,j}(t_s), \tag{III.2.17a}$$

$$\text{subject to:} \quad \bar{q}_i(t) < \infty, \ \forall t \in (t_s - N, t_s], \tag{III.2.17b}$$

$$\sum_{j\in\mathcal{J}(t_s)} \phi_{i,j}(t_s) = 1, \forall i \in \mathcal{I}(t_s), \tag{III.2.17c}$$

$$\sum_{i\in\mathcal{I}(t_s)} \phi_{i,j}(t_s) = 1, \forall j \in \mathcal{J}(t_s), \tag{III.2.17d}$$

$$\phi_{i,j}(t_s)\in\{0,1\}, \forall i,j\in\mathcal{I}(t_s)\times\mathcal{J}(t_s), \tag{III.2.17e}$$

$$\varphi_{ij}^{\mathrm{Tx}}(t_s)\,\varphi_{ij}^{\mathrm{Rx}}(t_s)\geq\frac{T_p}{T_t}\psi_{i,j}^{\mathrm{Tx}}\psi_{i,j}^{\mathrm{Rx}}, \tag{III.2.17f}$$

$$\varphi_{ij}^{\mathrm{Tx}}(t_s) \leq \psi_{i,j}^{\mathrm{Tx}}, \tag{III.2.17g}$$

$$\varphi_{ij}^{\mathrm{Rx}}(t_s) \leq \psi_{i,j}^{\mathrm{Rx}}, \tag{III.2.17h}$$

where inequality (III.2.17b) indicates that no queue should overflow during the scheduling period at hand; (III.2.17c) through (III.2.17e) denote that vehicles are paired one-to-one; and inequalities (III.2.17f) through (III.2.17h) reflect the bounds imposed on the beamwidths to be allocated as per (III.2.4).

The above optimization problem is difficult to solve analytically and is computationally hard, especially in vehicular environments. This unaffordable complexity calls for efficient distributed solutions. To this end, we decompose the above problem into two problems: the vehicle pairing and the beamwidth optimization. Subsequently, tools from matching theory and from swarm intelligence are leveraged to account, respectively, for the optimization of $\boldsymbol{\Phi}(t_s)$, and the selection of the beamwidths of both sides of each established mmWave V2V link (corr. $\boldsymbol{\varphi}^{\mathrm{Tx}}(t_s)$ and $\boldsymbol{\varphi}^{\mathrm{Rx}}(t_s)$). We will then explore the operational limits in terms of $\bar{\tau}_{i,j}^{sch}(t_s)$ and $\Gamma_i^{\times}(t_s)$ under different scheduling interval durations, traffic packet arrival rates and packet sizes. The ultimate goal of this study is to numerically assess the *reliability* of different RRM policies in mmWave V2V defined as the ratio of the number of packets $\Gamma_i^{\checkmark}(t_s) \triangleq 1 - \Gamma_i^{\times}(t_s)$ of size P_s successfully received at each receiver within a maximum delay $\tau_{\max}^{\lambda}$ [208], [209].

III.2.3 Proposed Scheme

The objective in this chapter is to design a self-organizing mechanism to solve the vehicle-to-vehicle association problem, in a decentralized manner, in which vTxs and vRxs interact and decide to link to each other based on their utilities. To this end, matching theory, as elaborated in Section II.1.2, offers a promising approach for resource management in wireless communications [210]. As depicted schematically in Fig. III.2.3, elements from matching theory are used for allocating mmWave V2V links in the setup at every scheduling slot t_s, with a previous learning process to capture essential information required for the matching game. Learning and matching are then followed by an optimization phase that allocates transmission and reception beamwidths for the matched pairs. Finally, beam alignment is performed. Prior to defining the matching game itself, we will first introduce the framework and specify the utility functions for

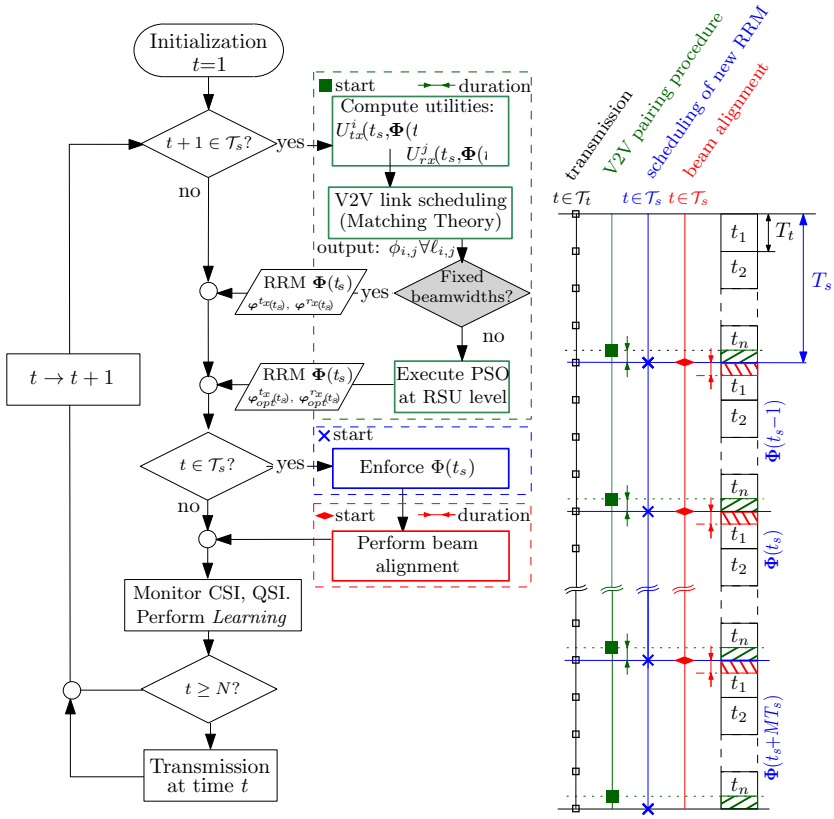

FIGURE III.2.3: Flowchart showing control actions' timing within the scheduling and the transmission timescales. ([204] ©2017 IEEE)

both sets of agents, as well as the learning process upon which utilities will be computed.

III.2.3.1 V2V Link Selection as a Matching Game

In order to properly address the fundamentals of this mathematical framework, several definitions must be recalled from the background material provided in Section II.1.2.3. These definitions are next re-formulated to adjust to the notations and terms of the problem under analysis:

Adapted Definition 1 *A matching game is defined by two sets of players* $(\mathcal{I}_j(t), \mathcal{J}_i(t))$ *corresponding to the sets of vTxs and vRxs, and two preference relations* $\succ_i$, $\succ_j$, *allowing each vTx* $i \in \mathcal{I}_j(t)$, *and vRx* $j \in \mathcal{J}_i(t)$ *to accordingly rank the players in the opposite set.*

Adapted Definition 2 *A preference* $\succ$ *is a complete, reflexive and transitive binary relation between the players in* $\mathcal{I}_j(t)$ *and* $\mathcal{J}_i(t)$. *Therefore, for any vTx* i *a preference relation* $\succ_i$ *is defined over the set of vRxs* $\mathcal{J}_i(t)$ *such that for any two vRx* $(m, n) \in \mathcal{J}_i(t) \times \mathcal{J}_i(t)$ *with* $m \neq n$, *and two matchings*

$\boldsymbol{\Phi}(t)$ *and* $\boldsymbol{\Phi}'(t)$ *so that* $\boldsymbol{\phi}_i(t)=m$ *and* $\boldsymbol{\phi}'_i(t)=n$*, and expressed as*

$$(m, \boldsymbol{\Phi}(t)) \succ_i \left(n, \boldsymbol{\Phi}'(t)\right) \Leftrightarrow U^{i,m}_{vTx}(t) > U^{i,n}_{vTx}(t). \tag{III.2.18}$$

Similarly, for any vRx j *a preference relation* $\succ_j$ *is defined over the set of vTxs* $\mathcal{I}_j(t)$ *such that for any two vTx* $(k,l) \in \mathcal{I}_j(t) \times \mathcal{I}_j(t)$ *with* $k \neq l$*, and two matchings* $\boldsymbol{\Phi}(t)$ *and* $\boldsymbol{\Phi}'(t)$ *so that* $\boldsymbol{\phi}_j(t) = k$ *and* $\boldsymbol{\phi}'_j(t) = l$*, the preference is expressed as*

$$(k, \boldsymbol{\Phi}(t)) \succ_j \left(l, \boldsymbol{\Phi}'(t)\right) \Leftrightarrow U^{j,k}_{vRx}(t) > U^{j,l}_{vRx}(t), \tag{III.2.19}$$

with $U^{i,m}_{vTx}(t)$ *and* $U^{k,j}_{vRx}(t)$ *correspondingly denoting the utility of vRx* m *for vTx* i*, and the utility of vTx* k *for vRx* j*.*

Adapted Definition 4 *The output of a matching game is a matching function* $\boldsymbol{\Phi}(t) = \{\phi_{i,j}(t)\}$ *that bilaterally assigns players* $\boldsymbol{\phi}_i(t) \triangleq \{j \in \mathcal{J}_i(t) : \phi_{i,j}(t) = 1\}$ *and* $\boldsymbol{\phi}_j(t) \triangleq \{i \in \mathcal{I}_j(t) : \phi_{i,j}(t) = 1\}$ *such that* $|\boldsymbol{\phi}_j(t)| = q_j$ *and* $|\boldsymbol{\phi}_i(t)| = q_i$ *are fulfilled. Notice here that* q_i *and* q_j *represent the quota of the player which, for a one-to-one matching game,* $q_i = q_j = 1$*.*

Adapted Definition 8 *A matching is not stable if for a given match* $\boldsymbol{\phi}_i(t) = j$ *and* $\boldsymbol{\phi}_j(t) = i$*, a blocking pair* (i', j') *such that* $i, i' \in \mathcal{I}_j(t)$ *and* $j, j' \in \mathcal{J}_i(t)$ *satisfying* $\boldsymbol{\phi}_i(t) \neq j'$*,* $\boldsymbol{\phi}_j(t) \neq i'$ *and* $j' \succ_i j$*,* $i' \succ_j i$ *exists. That is, if for a given match two players, a vTx and a vRx, prefer to be matched to each other rather than to their current matched partners. A matching is considered pairwise stable if no such blocking pair exists.*

From an algorithmic point of view, DA algorithm provides a polynomial time converging solution for one-to-one canonical matchings i.e., those matching games where preferences of players are not influenced by any other player's decisions. To this end, DA employs an iterative process, as per II.1.1, which finds a stable mapping from the elements of the set of vTxs in the system at every scheduling period to the elements of the set of feasible vRxs. As it has already been noted in Section II.1.2.3, the process relies on the ordering of the preference list that each player on either side compiles over the players from the other set. Let us remark here that DA ensures pairwise stability (as per **Definition 8**), but is not necessarily optimal for all players in the game. In relation to Theorem 2 from II.1.2.3, the traditional form of the algorithm is optimal for the initiator of the proposals whereas the stable, suitor-optimal solution may or may not be optimal for their reviewers. Interestingly for the application tackled in this chapter, DA does not require a centralized controller as the players involved do not need to observe the actions or preferences of other players.

Unfortunately, the existence of interdependencies between the players' preferences (referred to as *externalities*) makes DA unsuitable as the ranking of preferences lying at its core dynamically changes as the matching evolves. Externalities also pose a great challenge to ensure stability in the matching.

III.2.3.2 Utility Formulation

To produce the V2V link allocation that leads to minimum system-wide average delay, participants in the game –namely, the vTxs and vRxs at a given scheduling slot– will determine the utilities perceived towards each other in such a way that this information is captured and used to identify the set of players that offer better delay profiles. The baseline for the formulation of utilities in both vTxs and vRxs will be the α-fair utility function [211] expressed, for $\alpha \geq 0$ and $x \in \{vTx, vRx\}$, as

$$U_x(\mathrm{Rx}(t)) = \omega_x \frac{\mathrm{Rx}(t)^{1-\alpha_x}}{1-\alpha_x}, \tag{III.2.20}$$

where $\alpha = 2$ guarantees a weighted minimum proportional delay fairness, and ω_x allows bringing problem-specific information into the utilities. At this point we recall that $\mathcal{J}_i(t_s)$ and $\mathcal{I}_j(t_s)$ denote the subsets of feasible vRxs for vTx i and feasible vTxs for vRx j at a given scheduling time $t_s \in \mathcal{T}_s$, respectively. With this notation in mind, we define the weighted α-fair utility function for vTx $i \in \mathcal{I}(t_s)$ over vRxs $\mathcal{J}_i(t)$ as

$$U_{vTx}^{i,j}(t_s) \triangleq -\frac{\omega_{vTx}^{i,j}(t_s)}{r_{i,j}(t_s, \mathbf{\Phi}(t_s))}, \tag{III.2.21}$$

where we remark that for notational simplicity we will use $U_{vTx}^{i,j}(t_s)$ instead of $U_{vTx}^{i,j}(t_s, \mathbf{\Phi}(t_s))$ even though the implicit dependence of the utility on $\mathbf{\Phi}(t_s)$. Similarly, the utility of vRx $j \in \mathcal{J}(t_s)$ over $I_j(t_s)$ vTxs for a given matching $\mathbf{\Phi}(t_s)$ will be given by

$$U_{vRx}^{j,i}(t_s) = -\frac{\omega_{vRx}^{j,i}(t_s)}{r_{i,j}(t_s, \mathbf{\Phi}(t_s))}, \tag{III.2.22}$$

so that the system welfare $\mathrm{S}(t_s, \mathbf{\Phi}(t_s))$ to be maximized is

$$\mathrm{S}(t_s, \mathbf{\Phi}(t_s)) \triangleq \sum_{\mathcal{I}(t_s)} \sum_{\mathcal{J}_i(t_s)} \phi_{i,j}(t_s) \left(U_{vTx}^{i,j}(t_s) + U_{vRx}^{j,i}(t_s) \right). \tag{III.2.23}$$

By including in the expressions of the above utilities e.g., through weights $\omega_{vTx}^{i,j}(t_s)$ and $\omega_{vRx}^{j,i}(t_s)$, the traffic influx rate $\rho = \lambda P_s$, the nexus between above utility functions and the fitness in (III.2.17) is straightforward. As a result, the above formulated utility functions will reflect the load of the V2V link in terms of the number of transmission slots to serve λP_s bits with rate $r_{i,j}(t_s, \mathbf{\Phi}(t_s))$. Therefore, the maximization of the system-wide welfare, in turn minimizes the fitness in Expression (III.2.17a).

We finally define weights $\omega_{vTx}^{i,j}(t_s)$ and $\omega_{vRx}^{j,i}(t_s)$ so that under the same other conditions, vTxs are encouraged to select those vRxs moving along the highway at similar speeds –as that implies links being less prone to misalignment events– whereas vRxs will choose those vTxs with longer queues in order to alleviate the system. By denoting the relative speed of vTx i and vRx j averaged over the transmission slot $t_s \in \mathcal{T}_s$ as $\overline{\Delta v}_{i,j}(t_s)$,

and the status of queue i at time t_s as $q_i(t_s, \mathbf{\Phi}(t_s))$, the proposed weights for the above utility functions are expressed as

$$\omega_{vTx}^{i,j}(t_s) = \rho\left(1 + \frac{|\overline{\Delta v}_{i,j}(t_s)|}{|\Delta v|_{\max}}\right), \tag{III.2.24}$$

$$\omega_{vRx}^{j,i}(t_s) = \rho\left(2 - \frac{q_i(t_s, \mathbf{\Phi}(t_s))}{q_\Theta}\right), \tag{III.2.25}$$

where $i \in \mathcal{I}(t_s)$, $j \in \mathcal{J}(t_s)$, and $|\overline{\Delta v}|_{\max}$ and q_Θ represent normalization terms. In the utility (III.2.25) we extend the notation in (III.2.7) as $q_i(t_s, \mathbf{\Phi}(t_s))$ to denote the queue status at vTx i and time t_s when it is paired to vRx j under matching $\mathbf{\Phi}(t_s)$.

In practice the need for information exchanges of the current matching state at an instantaneous scale contradicts our overall approach to the problem. Moreover, the formulation of (III.2.21) and (III.2.22) reflects that the rate on a link ℓ_{ij} will not only depend on the currently matched vTx, but also on whom the rest of the vTxs are matched to, which unveils the existence of externalities. These externalities in our system are the result of the directionality of mmWave links and the variability of the levels of received interference built upon the beam steering. Unless vRxs are aware of the system-wide current matching, they will not be able to know from which directions interference will arrive and be able to foresee the instantaneous rate of a given mmWave link to cast their preferences. So, with the two-fold aim of reducing instantaneous reporting, and of calculating an estimate of $r_{i,j}(t_s, \mathbf{\Phi}(t_s))$, a link exploration and learning procedure will be carried out as explained in the next subsection.

III.2.3.3 CSI/QSI Information Learning Procedure

The evolution of the V2V system dynamics can be described by CSI and QSI as per (III.2.1) and (III.2.7), respectively. As the system evolves, V2V links should be dynamically enforced/released, beamwidths selected and beam steering triggered. However, CSI between devices and QSI at every vTx can only be measured locally and in a distributed fashion. In order to design a CSI/QSI aware long-term RRM policy and yet reduce the exchange of control information, vRxs will collect and process information on measured channel conditions for all transmission slots within a scheduling interval, and exchange it just before the beginning of a new scheduling period. This procedure also holds in the case of vTxs in regards to their QSI estimations.

Upon matching and beam alignment at scheduling slot $t_s - N$, we assume that every vehicle is able to detect and track vTxs and vRxs in its vicinity $\forall t' \in (t_s - N, t_s]$, which can be done by resorting to standard techniques [212] or more elaborated approaches as in [213], [214]. During every transmission interval within the scheduling period at hand, random matchings between vehicles in the vicinity of one another are agreed and set over a mmWave control channel deployed in parallel to the main communication beam. The purpose of this control channel is to allow sampling the CSI

of every receiver $j \in \mathcal{J}_i(t_s - N)$ in the group when it receives information from a certain transmitter $i \in \mathcal{I}_j(t_s - N)$.

This is accomplished by matching at random every single receiver in the system at time t' with any of the transmitters within its neighborhood. From a series of pilot transmissions in this random matching, every receiver $j \in \mathcal{J}(t_s - N)$ infers, based on the received power and by virtue of its knowledge of the relative position and transmit power of the transmitter i to which it is paired and other vehicles nearby, the channel gain h_{ij} as per (III.3.1) and therefrom, an SINR estimation as per (III.2.6). Once this is done, the receiver stores the estimated SINR along with the time instant at which it was produced, and an identifier of the transmitter to whom it was linked to. This process is performed for every receiver in the system and over all transmission slots $t' \in (t_s - N, t_s]$. As a result, all receivers at the end of the scheduling slot have stored a list with entries $\{t', i, \mathrm{SINR}_j(t')\}$, with $\mathrm{SINR}_j(t')$.

To learn an estimate $\bar{r}_{i,j}^{est}(t_s)$ of the average rate that can be expected for the matched pair (i, j) over the next scheduling period, we will inspect the behavior of this rate metric in the recent past i.e., the previous scheduling period. Yet, instead of treating all samples equally, those more recent in time will be emphasized so as to lessen the impact of older ones [215]. Based on this rationale, $\bar{r}_{i,j}^{est}(t_s)$ will be computed as

$$\bar{r}_{i,j}^{est}(t_s) = \sum_{t'=t_s-N}^{T_s} W(t', i) \left(1 - \frac{\tau_{i,j}^{\mathrm{Align}}(t')}{T_t}\right) B \log_2\left(1 + \mathrm{SINR}_j(t')\right), \quad \text{(III.2.26)}$$

where for $\tau_{i,j}^{\mathrm{Align}}(slot')$ calculation, equal parameter values to those used for the main communication channel are adopted. Values for weights $W(t', i)$ will be set such that $W(t', i) \neq 0$ if and only if it exists an entry $\{t', i, \mathrm{SINR}_j(t')\}$ in the CSI samples acquired by receiver j, $W(t', i) \leq W(t'', i)$ if $t' \leq t''$ and imposing $\sum_{t' \in (t_s - N, t_s]} W(t', i) = 1$ for any i to which receiver j may have been associated to all along the link exploration process in the previous scheduling period. Once rates $\bar{r}_{i,j}^{est}(t_s)$ have been estimated at receiver j $\forall i \in \mathcal{I}_j(t_s)$, their values are disseminated to its neighboring transmitters, which are now able to infer the average dynamics under which their queue can be flushed. Now that externalities have been removed from the estimated rates of the system, the average queue status at vTx i when communicating to vRx j is not subject to other matched pairs, and can be estimated as $\bar{q}_{i,j}(t_s) = P_s / \bar{r}_{i,j}^{est}(t_s)$. By inserting this estimated CSI/QSI information in (III.2.21) and (III.2.22), the final utilities to construct the proposed matching game are

$$U_{vTx}^{i,j}(t_s) \triangleq -\frac{\omega_{vTx}^{i,j}(t_s)}{\bar{r}_{i,j}^{est}(t_s)} = -\frac{\rho\left(1 + \frac{|\overline{\Delta v}_{i,j}(t_s)|}{|\Delta v|_{\max}}\right)}{\bar{r}_{i,j}^{est}(t_s)}, \quad \text{(III.2.27)}$$

$$U_{vRx}^{j,i}(t_s) = -\frac{\omega_{vRx}^{j,i}(t_s)}{\bar{r}_{i,j}^{est}(t_s)} = -\frac{\rho\left(2 - \frac{\bar{q}_{i,j}(t_s)}{q_\Theta}\right)}{\bar{r}_{i,j}^{est}(t_s)}. \quad \text{(III.2.28)}$$

Algorithm III.2.1: Proposed CSI/QSI-aware V2V Matching Algorithm ([204] ©2017 IEEE).

Data: Just before $t = t_s$, $\forall t_s \in \mathcal{T}_s$: All vRxs and vTxs are unmatched i.e., $\forall i \in \mathcal{I}(t_s)$, $\forall j \in \mathcal{J}(t_s)$, $\phi_i(t_s) = \emptyset$, $\phi_j(t_s) = \emptyset$).
Result: Convergence to a stable matching $\mathbf{\Phi}(t_s)$.

Phase I - Information exchange;

- Each vRx j sends to vTxs on its vicinity i.e., $\mathcal{I}_j(t_s)$, entries $\{t', i, \mathrm{SINR}_j(t')\}$ collected from pilot transmissions for link exploration.
- $\bar{r}^{est}_{i,j}(t_s)$ is computed as per (III.2.26). Estimated QSI is computed as $\bar{q}_{i,j}(t_s) = P_s/\bar{r}^{est}_{i,j}(t_s)$.

Phase II - Matching game construction;

- Each vTx i, $\forall i \in \mathcal{I}(t_s)$, updates $U^{i,j}_{vTx}(t_s)$ over the $\mathcal{J}_i(t_s)$ vRxs as per (III.2.27);
- Each vRx j, $\forall j \in \mathcal{J}(t_s)$, updates $U^{j,i}_{vRx}(t_s)$ over the $\mathcal{I}_j(t_s)$ vTxs as per (III.2.28);

Phase III - Deferred Acceptance for V2V link allocation;

- For each vRx j, initialize the subset of eligible vTxs, $\mathcal{E}_j \subseteq \mathcal{I}_j$ so that $|\mathcal{E}_j| = |\mathcal{I}_j|$
- Initialize the subsets of unmatched vRxs $\mathcal{S}^{Rx} \subseteq \mathcal{J}(t_s)$, and unmatched vTxs $\mathcal{S}^{Tx} \subseteq \mathcal{I}(t_s)$ so that $|\mathcal{S}^{Rx}| = |\mathcal{J}(t_s)|$ and $|\mathcal{S}^{Tx}| = |\mathcal{I}(t_s)|$

while $|\mathcal{S}| \neq \emptyset$ *and* $\sum_{j \in \mathcal{S}^{rx}} |\mathcal{E}_j| \neq \emptyset$ **do**
  Pick a random vRx $j \in \mathcal{S}^{rx}$;
  if $|\mathcal{E}_j| \neq \emptyset$ **then**
    vRx j sends V2V link proposal to its best ranked vTx n, $n \in \mathcal{E}_j$;
    if $n \in \mathcal{S}^{tx}$ **then**
      Match j and n setting $\phi_j(t_s) = n$ and $\phi_n(t_s) = j$;
      Remove j and n from $\mathcal{S}^{rx}$ and $\mathcal{S}^{tx}$ respectively;
    end
    else
      if $U^{n,j}_{vTx} > U^{n,\phi_n(t_s)}_{vTx}$ **then**
        Reject proposal from $\phi_n(t_s)$; add back $\phi_n(t_s)$ to $\mathcal{S}^{rx}$ and remove n from $\mathcal{E}_{\phi_n(t_s)}$;
        Match j and n setting $\phi_j(t_s) = n$ and $\phi_n(t_s) = j$;
        Remove j from $\mathcal{S}^{rx}$
      end
      else
        Refuse proposal from j;
        Remove n from $\mathcal{E}_j$;
      end
    end
  end
end
Phase IV - Stable matching

That is, as a result of the link exploration and learning mechanism, the final utilities for vTxs and vRxs will no longer change during the formation of the game. Thus, the V2V mmWave link allocation problem can be cast as a one-to-one canonical matching game and solved by applying the adapted DA algorithm, as detailed in Algorithm III.2.1, such that, in accordance with Theorem 1 and 2 from page 40, a stable vRx-optimal matching exists.

III.2.3.4 Beamwidth Allocation using Swarm Intelligence

Once vTxs and vRxs have been paired by virtue of the matching game explained above and following Fig. III.2.3, an optimal allocation of beamwidths $\boldsymbol{\varphi}^{\mathrm{Tx}}(t_s)$ and $\boldsymbol{\varphi}^{\mathrm{Rx}}(t_s)$ for the scheduling slot $t_s \in \mathcal{T}_s$ is performed by using SI, a family of computational methods that, as briefly explained in Section II.1.1 from Chapter II.1, is capable of efficiently dealing with

TABLE III.2.1: Main Simulation Parameters ([204] ©2017 IEEE).

Parameter	Value
Simulation time	30000 ms
Transmission slot (T_t)	2 ms
Scheduling slot (T_s)	[20, 50, 100, 200, 500] ms
Avg. Vehicle Density	[70, 90, 130, 180] vehicles/km
Lane Speed	[140, 130, 125, 110, 90, 70] km/h
Car to Truck ratio	80% (cars), 20% (trucks)
vTx/vRx probability	50% (vTx), 50% (vRx)
Coverage radius (R_c)	100 m
Peak transmit/slot time (T_p/T_s)	0.01
Sector-level beamwidth (ψ^{Tx},ψ^{Rx})	45°
Carrier frequency (f_c)	60 GHz
Bandwidth (BW)	2.16 GHz
Noise Power Spectral density (N_0)	-174 dBm/Hz
vTx transmit power (p_i)	15 dBm
Packet size (P_s)	[3200, 10^6, 2097144, 10^7] bits
Mean traffic arrival rate (λ)	[1/2, 1/6, 1/20, 1/60] packets/ms

convex and non-convex hard optimization problems. To this end, SI relies on systems of interacting agents governed by simple behavioral rules and inter-agent communication mechanisms, such as those observed in certain insects and animal species. In particular we will focus on the use of PSO [118], which has been recently utilized to allocate resources in mmWave 5G networks [216], [217].

Algorithmically the PSO-based beamwidth allocation scheme iteratively updates a K-sized swarm of candidate solutions $\{\mathbf{S}\}_{k=1}^{K}$, which for the problem at hand will be expressed as $\mathbf{S}_k = \boldsymbol{\varphi}_k^{\text{Tx}}(t_s), \boldsymbol{\varphi}_k^{\text{Rx}}(t_s)$ with $k \in \{1, \ldots, K\}$ and $\zeta \triangleq |\mathbf{S}_k|$ equal to the number of effective mmWave links established after the matching phase. The algorithm starts by assigning a fixed beamwidth (5°) to all beamwidths in $\mathbf{S}_k$, and by setting a velocity vector $\mathbf{V}_k = \{V_k^1, \ldots, V_k^\zeta\}$ per every candidate solution with inputs initially drawn uniformly at random from the range [5°, 45°]. The quality of the produced solutions is measured in terms of the average data rate computed over the active mmWave links in the system at time t_s. The PSO optimization procedure continues by refining the velocity vector based on its previous value, the best value of $\mathbf{S}_k$ found by the algorithm until the iteration at hand (denoted as $\mathbf{S}_k^* = (S_k^{1,*}, \ldots, S_k^{\zeta,*})$), and the global best solution $\mathbf{S}_\triangleright = \{S_\triangleright^1, \ldots, S_\triangleright^\zeta\}$ of the entire swarm as

$$V_k^s \leftarrow \varpi v_k^s + \eta r_\eta (S_k^{s,*} - S_k^s) + \xi r_\xi (S_\triangleright^s - S_k^s), \tag{III.2.29}$$

with $s \in \{1, \ldots, \zeta\}$. Once the velocity vector has been updated, the value of every candidate solution $\mathbf{S}_k$ is updated as $\mathbf{S}_k \leftarrow \mathbf{S}_k + \mathbf{V}_k$, from which the best candidates for every particle in the swarm i.e., $\mathbf{S}_k^*$, and the global best candidate $\mathbf{S}_\triangleright$ are recomputed and updated if necessary. Parameters ϖ (inertia), η and ξ permit to drive the search behavior of this heuristic, whereas r_η and r_ξ are realizations of a uniform random variable with support $[0, 1]$. This process is repeated for a fixed number of iterations.

III.2.4 Simulation Setup and Performance Evaluation

In order to assess the performance of the proposed scheme comprehensive computer experiments have been performed over a 500 meter-long highway segment with 6 lanes of 3m width each. Vehicles are assumed to move in the same direction at constant speeds of –leftmost to rightmost lane– 140, 130, 125, 110, 90, and 70 km/h. Vehicles are either cars (80%) or trucks (20%), with cars drawn uniformly at random from a set of 5 different models, each with varying lengths and widths. Four scenarios with traffic densities of $\{70, 90, 130, 180\}$ vehicles/km will be considered in the experiments and will, hereafter, be referred to as `LOW`, `MID`, `HIGH` and `ULTRA`. In order to fix the vehicle density at every scenario, vehicles leaving the segment will trigger the process for new ones to join in, which will be done by prioritizing least crowded lanes, and by guaranteeing a minimum distance to the preceded vehicle. Upon their entrance to the road, vehicles will be declared as transmitters (vTx) or receivers (vRx) with equal probability. Disregarding the role of those vehicles leaving the system, the new ones will be endorsed as vTx or vRx indistinctly.

According to Table III.2.1, the highway road scenario has been simulated for a total time of 30000 ms, with transmission intervals of $T_t = 2$ ms and scheduling intervals $T_s \in \{20, 50, 100, 200, 500\}$ ms. To assess the impact of queue dynamics under different configurations several packet arrival rates and sizes[3] are considered.

As shown in Fig. III.2.3, two variants of our V2V allocation method will be considered for discussion:

- Fixed-beamwidth weighted α-fair matching (α`Fair`), in which the aforementioned deferred acceptance matching algorithm is applied every T_s ms considering the learned utilities as per (III.2.27) and (III.2.28). In this case transmit and receive beamwidths of the mmWave channels are kept equal for every link. In particular beamwidths of 5°, 45° and 360° will be considered.

- PSO weighted α-fair matching (`PSO`), similar to the scheme above but incorporating the beamwidth optimization phase explained in Section III.2.3.4. As detailed therein, this optimization phase is based on the interplay between alignment delay and the throughput in mmWave communications. In all cases the PSO approach uses $K = 30$ particles, $\varpi = 0.5$, $\eta = \xi = 1.5$ and 50 iterations. As opposed to the α`Fair` approach, this scheme requires a central controller e.g., a RSU, to coordinate the selection of transmission and reception beamwidths for each vehicle pair. Nevertheless, it is of interest to explore this solution to address more realistic scenarios subject to more frequent misalignment events between pairs.

[3]Note that packet sizes of $P_s = 3200$ and $P_s = 2097144$ bits are in line with the specifications for the DSRC safety messages length [151] and the 802.11ad maximum payload [196], respectively.

Simulation results for the above approaches will be compared to those produced by 2 different baseline schemes contributed in [174], namely:

- Minimum-distance based pairing (`MIND`), by which every vTx in the system at a given scheduling slot tries to pair with its closest vRx that has not been paired yet. Pairing is conducted in increasing order of the distance from the vehicle to the beginning of the highway segment. Pairing is renewed as in our framework i.e., every T_s ms.

- Asynchronous long-term pairing (`ASYN`), by which a restrictive distance-based pairing is triggered every time a new vehicle enters the highway segment. Specifically, two vehicles are paired if 1) they are eligible for pairing i.e., still single and located within the first 20 meters of the highway segment; and 2) they are in the same or adjacent lanes. Once vehicles are associated, the pair remains unchanged until one of them leaves the segment, forcing the other vehicle to be unmatched while on track.

In all the above methods matching and pairing strategies will be subject to coverage constraints arriving from R_c. Thus, unpaired vTx/vRx might stem from asymmetries in the number of vTx and vRx at a given time slot. Moreover, coverage constraints might yield singleton vTxs and vRxs due to an infeasible association between remaining candidates.

III.2.4.1 Discussion

III.2.4.1.1 Preliminaries

Before further proceeding into discussing the performance, the isolated effects of transmission and reception beamwidths, of vehicle density, of the data traffic arrival rate jointly with packet size, and of the scheduling interval length are next introduced so as to give an intuition of how these parameters might affect the throughput/delay performance in the upcoming subsections:

- **Beamwidth selection**: narrower beamwidths produce higher antenna gains as per (III.2.2). Those gains come, however, at the price of a longer beam alignment process that, as introduced in I.1.1.3.1, spring from the need for scanning many more directions to find the best beams. As a result, the duration of the transmission slot is cut down and, thus, as illustrated in (III.2.5) the effective rate of those transmission slots where the alignment takes place decreases. In addition, it is important to realize that for both very narrow and very wide beamwidths SINR will mainly depend on the strength of the desired link. The logic behind being that most of the interference will arrive to the sidelobes and to the mainlobe, respectively and, thus, the effect of misalignment will be more severe.

- **Scheduling interval:** shorter intervals will trigger more frequent beam alignments that, on one hand, will reduce the likelihood of

misalignment but, on the other, will increase the number of transmission slots affected by alignment delay. The significance of both opposed effects becoming more acute for narrower beamwidths.

- **Vehicle density:** Disregarding the straightforward effect of vehicle density on the overall maximum number of simultaneous transmissions, higher vehicle densities increase the probability of having more blockers obtruding desired V2V links. In turn, with low vehicle density longer distances between vTx may result in i) worse channel conditions for active V2V links due to higher propagation losses, ii) vehicles being left unpaired for longer during the scheduling interval and leading to: high drops if the vehicle who left the system was a vrx, or the overall number of feasible V2V links being reduced due to coverage constraints.

- **Data traffic arrival rate and packet size:** the first will effectively rule when a given vTx is active for transmission whereas the second, in the absence of drops, will compel for how long it will remain active. So, at a given time slot, higher data traffic arrival rates and longer packet sizes will in general lead to more interference.

III.2.4.1.2 Interpretation of the Results

Next, it should be remarked here that a proper interpretation of the obtained results should simultaneously consider delay and reliability statistics. The reason lies in the stringent packet dropping policy adopted in this chapter, which deducts from the delay calculation as per (III.2.10) packets not fulfilling a delay below $\tau^{\lambda}_{\max}$ set for simulations such that $\tau^{\lambda}_{\max} = 1/\lambda$. In this context, packets in queues with associated transmission rates matching or exceeding the traffic influx rate will contribute to delay statistics, whereas those in queues with slower rates will be more likely to be dropped. Therefore, as the number of packets successfully transmitted within $\tau^{\lambda}_{\max}$ decreases, so does the number of transmissions contributing to queue average delay calculations that will be, in any case, upper bounded by $\tau^{\lambda}_{\max}$.

Another indicator that should be considered when evaluating the goodness of the different pairing approaches in this benchmark is the number of effectively matched vehicles. In this regard, it can be expected that the `ASYN` method will fail to pair as many vehicles as the rest of the schemes. These notable differences will be quantified next. Finally, we restrict the discussion to some representative (P_s, λ) combinations: (3200 bits, 1/2 packets/ms), characterizing intensive short-length messages transmissions that are common in safety related V2X communications scenarios; and 2097144 bits with 1/20 packets/ms and with 1/60 packets/ms, which model long packets arriving at lower rates as for infotainment applications.

In the remaining of this subsection, the discussion will be geared towards investigating different effects and purposes.

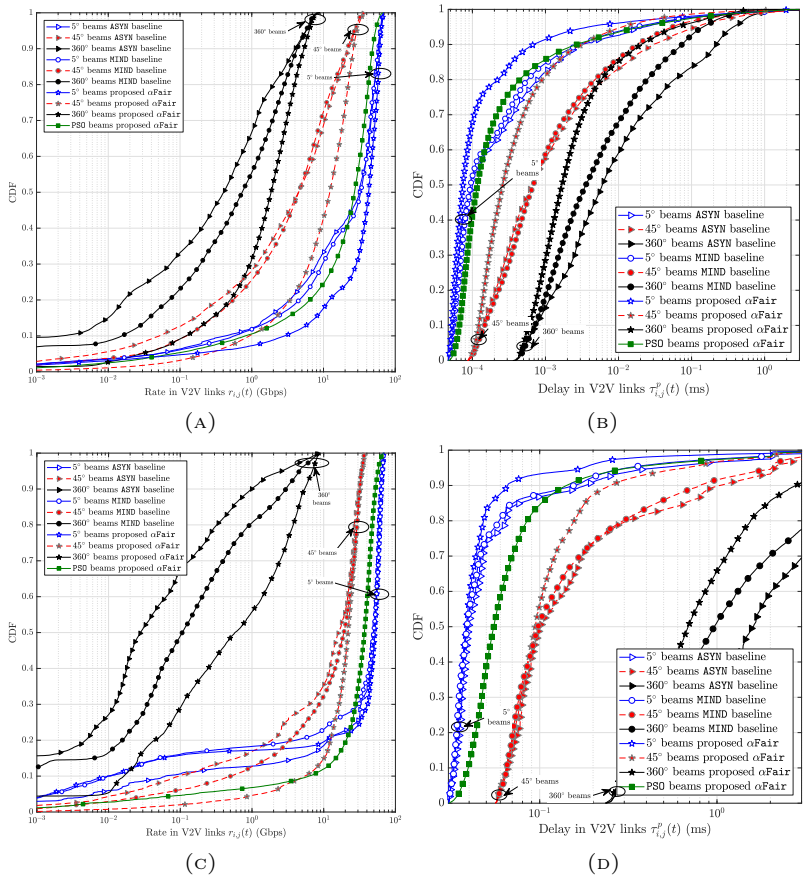

(A) (B)

(C) (D)

FIGURE III.2.4: Rate and delay CDFs of the baseline and proposed approaches in ULTRA density scenario for different beamwidths: (a) and (b) for $P_s = 3200$ bits and traffic arrival rate $\lambda = 1/T_t$ packets/s; (c) and (d) for $P_s = 2097144$ bits and traffic arrival rate $\lambda = 1/10 \cdot T_t$ packets/s. ([204] ©2017 IEEE)

III.2.4.1.3 Impact of the Beamwidth

To begin with, the effect of the beamwidth selection will be analyzed through Fig. III.2.4. Therein the rate and delay per packet[4] cumulative density functions (CDFs) are plotted under ASYN, MIND, and αFair methods for fixed and PSO beamwidths in ULTRA scenario. A closer look to the rate CDFs from Fig. III.2.4(a) and from Fig. III.2.4(c) reveals that the latter shows much longer tails. Serving longer packets even with lower traffic arrival rates implies an increased system utilization –defined as the ratio of slots where vTxs are engaged in transmission– and, consequently, a higher interference which degrades the measured SINR and the link rate. Therefore, the increased delays in Fig. III.2.4(d) as compared to those of Fig. III.2.4(b) cannot be merely attributed to the increased serving time

[4]For all methods with fixed beamwidths the beam alignment delay is given in (III.2.3) and implicitly included in the delay computations.

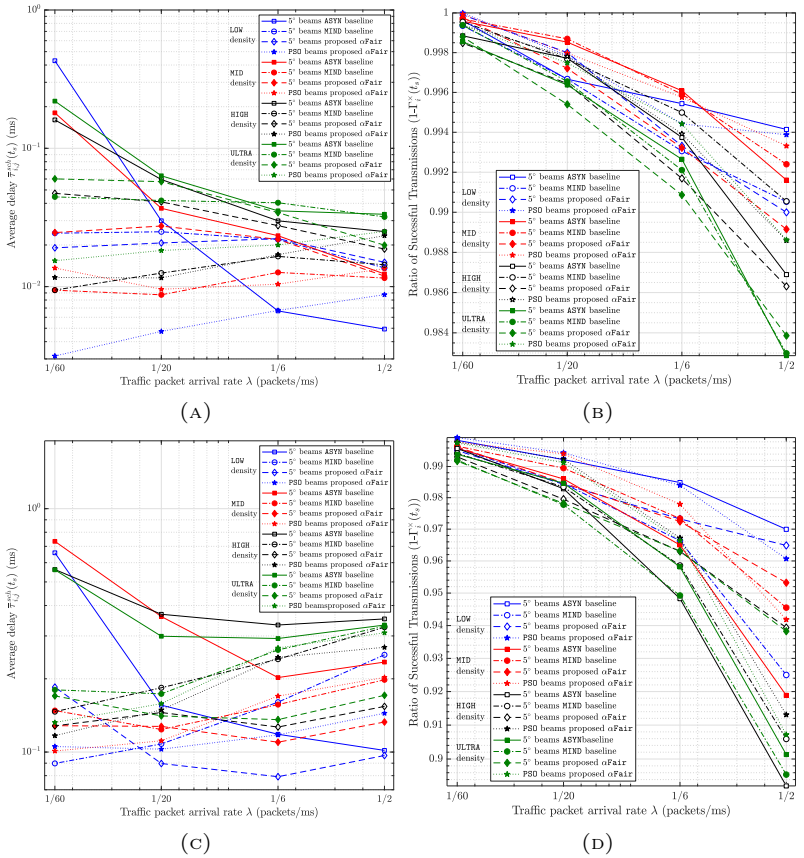

FIGURE III.2.5: Interplay between delay and transmission success under different vehicle densities and traffic arrival rate configurations: (a) delay and (b) successful transmissions for the short packet case, $P_s = 3200$ bits; (c) delay and (d) successful transmissions for the long packet case, $P_s = 2097144$ bits. ([204] ©2017 IEEE)

expected for longer packets. It can be concluded from these plots that narrow beams and PSO-optimized beams render better delay and rate results than any other considered beamwidths. This outperforming behavior holds not only for the plots shown here, but also for other simulated cases that for the sake of conciseness are not provided. Based on this rationale, from this point onwards discussions will be restricted to the methods with narrow beams and the PSO method.

III.2.4.1.4 Effect of the Traffic Load

The discussion follows through Fig. III.2.5, further exposing the combined effect of increasing traffic arrival rates on the average delay –in Fig. III.2.5(a) and Fig. III.2.5(c)– and on the average ratio of successful transmissions –as per Fig. III.2.5(b) and Fig. III.2.5(d)– under `LOW`, `MID`, `HIGH`, and `ULTRA` vehicle density scenarios. The effect of the queue dropping policy on the delay is evinced in these plots; here, as expected, the ratio

of successful transmissions severely decreases as the traffic arrival rate becomes more demanding. Yet, the average delay decreases disregarding the utilized scheme. That is, those cases where no sharp degradation of the average delay arrives with increasing values of λ reflect a better resiliency of the system with respect to the traffic arrival rate. However, it must be interpreted along with the ratio of successful transmissions of the method at hand.

The plots in Fig. III.2.5 evince that the proposed schemes feature the lowest dropping ratio and the most notable delay resiliency for the most demanding setting (`ULTRA` vehicle density, $P_s = 3200$). As the density becomes lower, performance gaps become smaller, to the point where `ASYN` offers the highest success ratio for the `LOW` density scenario. However, the number of vTx paired by the `ASYN` approach is around 25% of the overall number of vTxs, whereas for the remaining schemes this figure is around 60%, increasing to levels above 90% in scenarios with higher density. It is noteworthy that when turning to longer-sized packets, dropping ratios increase significantly (more than one order of magnitude).

III.2.4.1.5 Effect of the Scheduling Interval

In this case, the discussion will focus on two (vehicle density, $\mathrm{P}_s, 1/\lambda$) combinations that produce use cases in opposite ends of the range: (`LOW`, 3200 bits, 1/2ms), to characterize frequent (500 packets per second) short-length messages exchanged between a limited number of vehicles; and (`ULTRA`, 2097144 bits, 1/20ms), which corresponds to long packets arriving at a lower rate but to a much more dense vehicle environment. Simulation results for both use cases are correspondingly collected in Fig. III.2.6 and Fig. III.2.7. In the remaining of this subsection we will assess the performance of the benchmark RRM methods in both scenarios under scheduling intervals of 50 and 500ms. For the sake of clarity it is noticed here that in SINR and delay related CDFs i.e., Figs. III.2.6(a)-(b) and III.2.7(a)-(b), the plots corresponding to 45° have been omitted. As for the drop statistics P_{drop} in Figs. III.2.6(e)-(f) and Figs. III.2.7(e)-(f), they have been obtained by aggregating transmission events over each scheduling period and queue, i.e. $\sum_{t=t_s}^{t_s+T_t} |\mathcal{A}_i^{\times}(t)| / \sum_{t=t_s}^{t_s+T_t} A_i(t)\ \forall t_s$.

Performance statistics for (`LOW`, 3200 bits, 1/2ms) in Fig. III.2.6 show in general little impact of the scheduling interval selection. As a reference, SINR in Fig. III.2.6(a) indicates that for $\varphi = 5°$ around 10%, 5% and 3.5% of the transmission slots under `MIND`, α`Fair` and `ASYN`, correspondingly, are in outage range (-20 dB or less). `ASYN` seems to be the least affected by the scheduling interval selection no matter the beamwidth considered. Yet, only around 22% of its queues did not incur drops along the different scheduling intervals, and its association success reached barely 35% –for values around 50-60% of drop-free events and of 95% association success of its counterparts–. As for α`Fair`, and `MIND`, the latter coming always behind in performance, the probability of reaching a certain SINR is roughly 10% lower for $T_s = 500$ ms. The increased likelihood of misalignment of V2V links inflicted by longer scheduling intervals does not greatly degrade the performance which seems to be hampered by the topology itself.

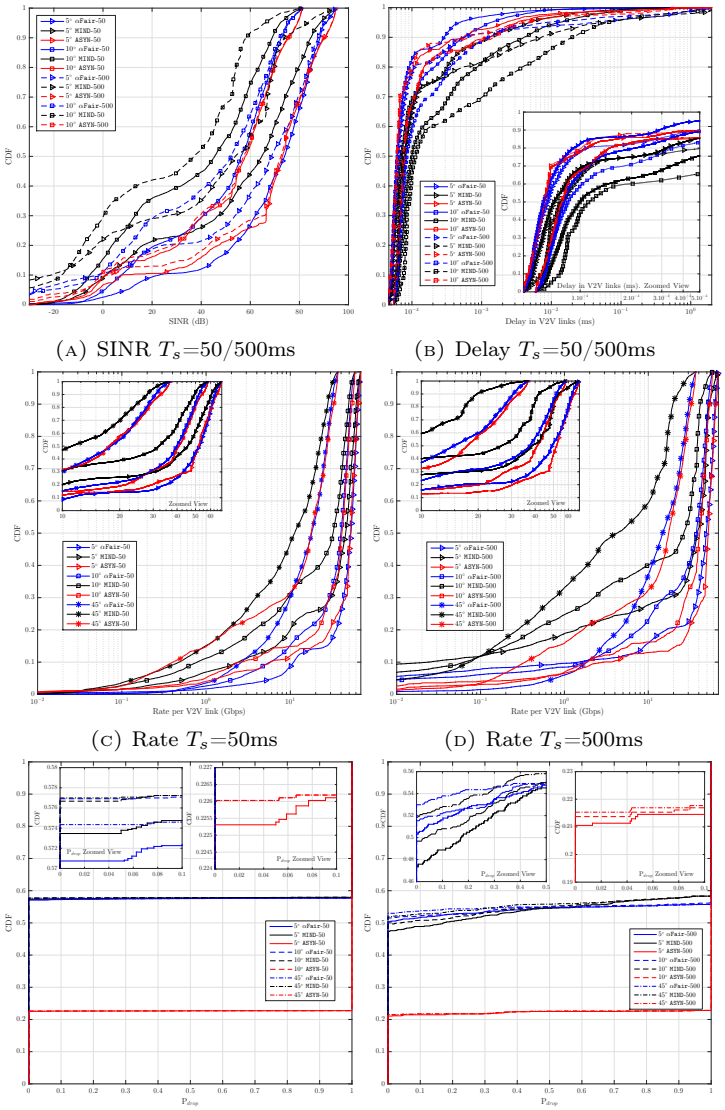

(A) SINR T_s=50/500ms (B) Delay T_s=50/500ms

(C) Rate T_s=50ms (D) Rate T_s=500ms

(E) Drops T_s=50ms (F) Drops T_s=500ms

FIGURE III.2.6: Effect of scheduling interval selection on SINR (a), delay (b), rate (c)-(d), and drops (e)-(f) for `LOW` vehicle density, P_s = 3200 and traffic arrival rate of $1/\lambda = 1/2$ ms. Results in (a)-(f) have been computed from average V2V pairing strategy success ratios of 95.09% α`Fair-50`, 95.59% `MIND-50`, 35.79% `ASYN-50` and ratios of 95.00% α`Fair-500`, 96.72% `MIND-500`, 35.28% `ASYN-500`, respectively.([218] ©2017 IEEE)

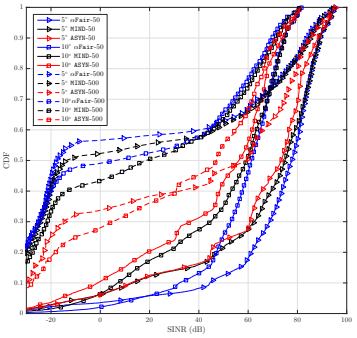

(A) SINR T_s=50/500ms

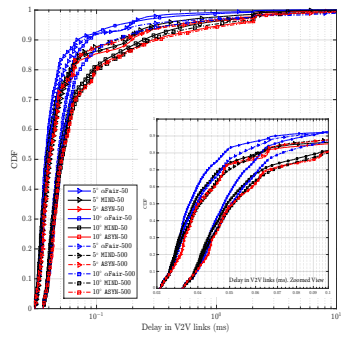

(B) Delay T_s=50/500ms

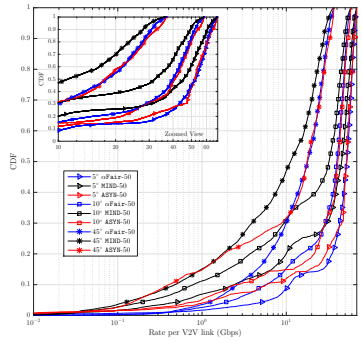

(C) Rate T_s=50

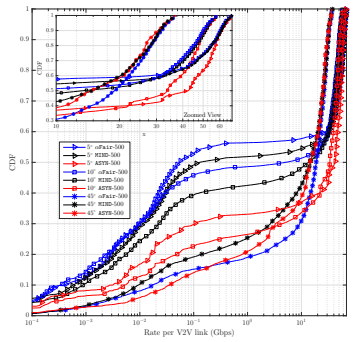

(D) Rate T_s=500ms

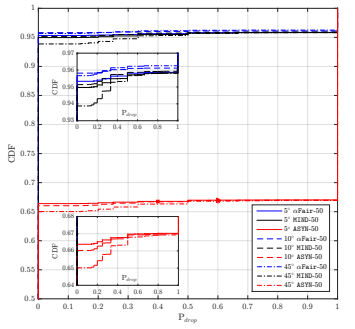

(E) Drops T_s=50

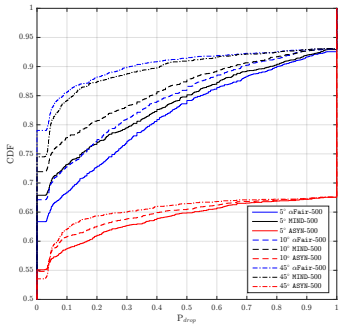

(F) Drops T_s=500

FIGURE III.2.7: Effect of scheduling interval selection on (a) SINR, (b) delay, (c)-(d) rate, and (e)-(f) drops for `ULTRA` vehicle density, P_s = 2097144 and traffic arrival rate of $1/\lambda = 1/20$ ms. Results in (a)-(f) have been computed from average V2V pairing strategy success ratios of 95.86% α`Fair-50`, 95.94% `MIND-50`, 67.34% `ASYN-50` and ratios of 96.01% α`Fair-500`, 95.99% `MIND-500`, 67.08% `ASYN-500`, respectively. ([218] ©2017 IEEE)

A detailed look into Fig. III.2.6(a) and Figs. III.2.6(c)-(d) shows an altogether different case for (ULTRA, 2097144 bits, 1/20 ms): narrowest beamwidths provide the worst performance for T_s=500ms in all three V2V association schemes with an upsurge on outage events from levels below 5% to over 40% for 5° and 10° beamwidths in αFair and MIND. Moreover, a sharp downfall from 95% drop-free events from Fig. III.2.6(e) to 63% and 66% in αFair and MIND respectively is observed in Fig. III.2.6(f). Moreover, comparing Figs. III.2.6(b)-III.2.7(b) and Figs. III.2.6(e)-III.2.7(e) it can be observed that increasing P_s and, at the same time, reducing $1/\lambda$ yields, as expected, longer delays, but also far less drops –specially with $T_s = 50$ ms–; In fact, complementary simulations, omitted for the sake of simplicity and clarity in the exposition, were conducted for both LOW and ULTRA scenarios and $P_s = [3200, 2097144]$ bits with $1/\lambda$=$[1/T_t, 1/3T_t, 1/10T_t, 1/30T_t]$ ms and confirmed that the system is, in terms of reliability, much more sensitive to variations on the traffic inter-arrival rate than to packet size. Also noteworthy is that αFair, which relies in learning techniques and in general outperforms all other approaches, produces the worst results for $T_s = 500$ ms, which suggests that the weighted average learning over such a long period is not efficient, not even in a rectilinear vehicular scenario as the one analyzed in this chapter.

III.2.4.1.6 Joint Latency and Reliability Upper Bounds Compliant Scheduling Intervals

To conclude, the discussion moves now to Table III.2.2 which shows, for the ULTRA vehicle density case, $N = 50$, $\lambda = 1/T_t$ and $P_s = 3200$, the ratio of scheduling periods $t_s \in \mathcal{T}_s$ over the entire simulation with an average delay $\bar{\tau}_{i,j}^{sch}(t_s)$ as per (III.2.17a) and a packet dropping ratio $\Gamma_i^{\times}(t_s)$ as per (III.2.11) –averaged over $t \in [t_s, t_s + NT_t)$– below different upper bounds. For a better understanding of this table, Fig. III.2.8(a) depicts, for every scheme in the benchmark, the average delay and packet dropping ratio of every scheduling period as a scatter plot. The statistics shown in Table III.2.2 correspond to the number of points i.e., scheduling periods, for each matching method that jointly meet upper constraints in both axes. For instance, we can observe that 44.67% of the total scheduling periods simulated for the ASYN scheme and the ULTRA dense scenario achieve an average delay below 0.1 ms and a packet dropping ratio below 1%. Likewise, Table III.2.3 shows the statistics obtained for $P_s = 2097144$ bits and $\lambda = 1/30 \cdot T_t$ over the same ULTRA dense scenario, computed from the scatter plot in Fig. III.2.8(b). Thresholds have been adjusted for each table discussed in this section to ensure that meaningful statistics are produced for comparison.

These tables reveal interesting insights: when dealing with small-sized packets (low P_s) arriving at the queues of the glsvtx at a high rate (high λ), the αFair dominates under loose constraints on the packet dropping ratio i.e., 10%, whereas it is the PSO approach which is the outperforming method as the restriction on the number of dropped packets becomes more stringent. This changing behavior can be explained by the side benefit derived from the beamwidth optimization performed in PSO: narrower

TABLE III.2.2: Percentage of scheduling periods jointly fulfilling $\bar{\tau}_{i,j}^{sch}(t_s)$ and $\Gamma_i^{\times}(t_s)$ upper-bounds in ULTRA, $P_s = 3200$ bits, $\lambda = 1/T_t$ packets/s ([204] ©2017 IEEE).

ULTRA, 3200, 1/2ms			Upper bound for $\Gamma_i^{\times}(t_s)$				
			10%	1%	0.1%	0.01%	0.001%
Upper bound for $\bar{\tau}_{sch}(t_s)$	0.1 ms	ASYN	94.67	44.67	29.67	28.67	28.67
		MIND	96.32	35.79	19.73	18.06	18.06
		αFair	100.00	38.80	21.74	20.07	20.07
		PSO	97.32	58.19	37.46	35.79	35.79
	0.075 ms	ASYN	89.00	44.67	29.67	28.67	28.67
		MIND	90.64	35.79	19.73	18.06	18.06
		αFair	97.99	38.80	21.74	20.07	20.07
		PSO	95.65	58.19	37.46	35.79	35.79
	0.05 ms	ASYN	76.67	44.00	29.33	28.33	28.33
		MIND	79.26	35.79	19.73	18.06	18.06
		αFair	89.97	38.46	21.41	19.73	19.73
		PSO	85.95	56.86	36.79	35.12	35.12
	0.025 ms	ASYN	54.00	39.33	28.33	27.33	27.33
		MIND	51.51	31.77	18.73	17.39	17.39
		αFair	70.57	33.78	19.40	18.06	18.06
		PSO	61.87	47.83	32.44	31.10	31.10
	0.01 ms	ASYN	31.33	26.67	22.33	22.33	22.33
		MIND	30.44	23.41	16.39	15.05	15.05
		αFair	39.80	21.07	15.39	14.05	14.05
		PSO	36.12	31.44	22.74	22.07	22.07

TABLE III.2.3: Percentage of scheduling periods jointly fulfilling $\bar{\tau}_{i,j}^{sch}(t_s)$ and $\Gamma_i^{\times}(t_s)$ upper bounds in ULTRA, $P_s = 2097144$ bits, $\lambda = 1/30 \cdot T_t$ packets/s ([204] ©2017 IEEE).

ULTRA, 2097144, 1/60ms			Upper bound for $\Gamma_i^{\times}(t_s)$				
			20%	15%	10%	1%	0.1%
Upper bound for $\bar{\tau}_{sch}(t_s)$	0.5 ms	ASYN	71.00	71.00	71.00	62.33	62.00
		MIND	89.63	89.63	89.63	64.88	61.87
		αFair	89.63	89.63	89.63	64.55	62.88
		PSO	96.66	96.66	96.66	87.63	86.29
	0.2 ms	ASYN	59.67	59.67	59.67	54.00	53.67
		MIND	79.93	79.93	79.93	59.20	57.53
		αFair	80.60	80.60	80.60	57.86	56.52
		PSO	90.64	90.64	90.64	83.28	81.94
	0.1 ms	ASYN	44.33	44.33	44.33	40.67	40.33
		MIND	70.23	70.23	70.23	51.51	50.17
		αFair	76.25	76.25	76.25	54.52	53.18
		PSO	63.55	63.55	63.55	58.53	57.19
	0.075 ms	ASYN	40.33	40.33	40.33	36.67	36.33
		MIND	59.53	59.53	59.53	42.81	41.47
		αFair	70.90	70.90	70.90	49.83	48.83
		PSO	40.13	40.13	40.13	37.46	36.79
	0.05 ms	ASYN	23.00	23.00	23.00	20.33	20.33
		MIND	37.12	37.12	37.12	26.09	25.08
		αFair	49.16	49.16	49.16	33.11	32.44
		PSO	00.00	00.00	00.00	00.00	00.00

beamwidths would penalize the overall delay (but this penalty is restricted to the first transmission slot of every scheduling period), whereas allocating wider beamwidths make the mmWave channel more resilient against misalignments between already paired vehicles. This ultimately yields lower dropping statistics, as reflected in the table.

A similar observation can be drawn from the statistics obtained for

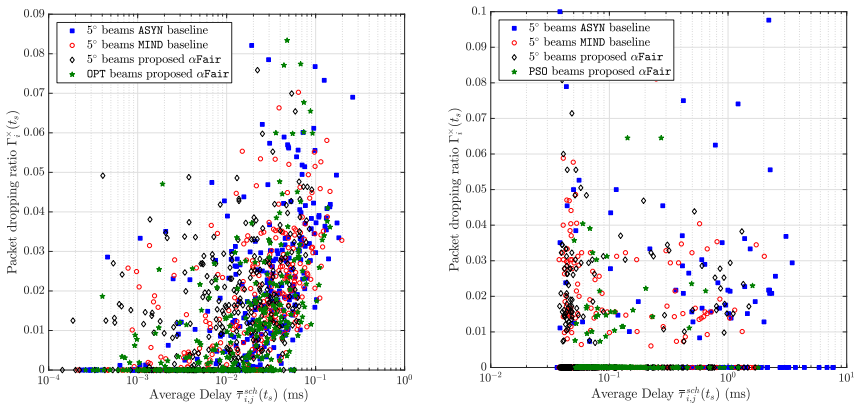

(A) (B)

FIGURE III.2.8: Scatter plots for ULTRA density scenario: (a) $\bar{\tau}_{sch}(t_s)$ with P_s=3200 bits, traffic arrival rate $\lambda = 1/T_t$ packets/s, and (b) $\Gamma_i^{\times}(t_s)$ with P_s = 2097144 bits, traffic arrival rate $\lambda = 1/30 \cdot T_t$ packets/s. ([204] ©2017 IEEE)

P_s = 2097144 bits and $1/\lambda = 1/30 \cdot T_t$ packets/s. In general PSO outperforms the rest of the baselines in the benchmark. Nonetheless, an interesting transition is noted for average delay bounds below 0.1: αFair becomes the dominating scheme and the performance of PSO degrades significantly. The reason for this effect is that a high value of $1/\lambda$ yields long times between transmission events, hence a lower probability that packets are dropped for all schemes in the benchmark. However, once a packet arrives at an empty queue, it takes more time to flush it through the mmWave channel due to their bigger size. It follows that, for low delay thresholds, narrow beamwidths are more effective for delivering the packet to its destination, disregarding whether they are suboptimal for the delay of the scheduling slot. Indeed the PSO scheme fails to meet a minimum average delay of 0.05 ms for any of its scheduling periods, as opposed to the rest of schemes (all of them with 5° beamwidth), for which the αFair scheme meets this bound with a packet dropping ratio below 0.1% in more than 49% of its scheduling intervals.

III.2.5 Conclusions

This chapter has presented a novel distributed association and beam alignment framework for mmWave V2V networks based on matching theory and swarm intelligence. Specifically we have formulated tailored utility functions for the matching game that capture 1) the relative dynamics between vTxs and vRxs in the scenario; 2) the channel and queuing dynamics learned from the past and 3) the particularities of mmWave communications, such as directionality, blockage and alignment delay. This set of utilities is fed to a DA-based algorithm, which allows pairing transmitting

and receiving vehicles in a distributed manner. The matching-based association is followed by an optimization procedure that allocates transmit and receive beamwidths for each established V2V link. Simulation results confirm the expected good performance of our framework over a comprehensive number of configurations for a highway multi-lane scenario with varying vehicle densities.

Next, the performance of this hybrid approach will be assessed in a multi-vUE configuration and with a realistic modeling of vehicles traversing an urban T junction, an scenario that is more likely to experience misalignments between vehicles.

Chapter III.3

Exchanging Sensing Information in an Urban Junction through mmWave V2V Communications

III.3.1 Introduction

Autonomous vehicles equipped with devices for data sensing and transmission lie at the cornerstone where the so-called IoT and cloud computing paradigms meet each other [219]. From a macroscopic point of view, the construction of autonomous navigation routes relies on global positioning, and map services updated with information about current road conditions, which is provided by cloud computing. On the other hand, autonomous vehicles determine their real-time moving strategy and decisions depending on the dynamic surroundings, for which sensing equipment installed on board is of utmost necessity, especially –yet not uniquely– for safety reasons. Indeed, a growing body of literature has emphasized the crucial role of vehicular sensors for the pre-collision detection of obstacles [220] and platooning [221], among many other applications [222], [223].

In this context, a vehicular sensor system is usually composed by LIDAR, radar, GPS, odometry, and computer vision devices [224]. Among this portfolio of sensing technologies, LIDAR has recently garnered the attention of car manufacturers due to the significantly higher spatial resolution provided by this radar technology, to the point of being deemed the "eyes" of driverless vehicles [225]. For instance, a typical commercial LIDAR using 64 laser diodes produces 2.8 million data points per second with a 360° horizontal field of view, a 26.8° vertical field of view and a coverage range of more than 70m in all directions, generating a precise three-dimensional map of a car's surroundings. By virtue of LIDAR, vehicles can detect obstacles and build 3D surroundings for safe navigation in dynamic environments, yet sharing a small fraction of this sensing requires massive data rates. However, the increased contextual awareness enabled by a vehicular sensor is restricted by its covered range centered

on the position of the vehicle itself [226]. To overcome this restriction, as thoroughly examined in Chapter III.1, vehicular communications have been identified as a technology enabler to compensate for the shortcomings of sensors, break the line-of-sight constraint, acquire more data on surroundings e.g., blind area information, and ultimately enhance the overall contextual awareness of connected vehicles, in terms of the geographical spread and/or quality of the information objects representing the monitored environment (contents) [227], [228]. As a result, autonomous vehicles can acquire more valuable traffic data to optimize their driving behavior and increase their safety level [229].

Unfortunately, conventional wireless technologies for vehicular communications have very limited bandwidth. As it has been exemplified in the previous chapter, for example, the maximum bit rate supported by DSRC is 27 Mb/s [151]. On the contrary, traffic sensor data are ever growing, supporting not only LIDAR's 3D imaging but also incorporating high-definition cameras. In this regard, the next-generation mmWave wireless technology has been postulated as a potentially feasible radio solution to solve this dilemma [60], [63], [230]. With mmWave radios, vehicles are able to share real-time sensory data within their transmission ranges, forming a swarm of IoT devices connected through multiple V2V links.

By resorting to V2V mmWave communications, both blind area and bad weather problems that inherently characterize LIDAR and other sensing equipment can be effectively addressed: when a vehicle detects a blind area (as might happen when the vehicle at hand is about to reach a junction), LIDAR or camera data from neighboring vehicles can be retrieved to compensate for the lack of sensing range. Besides, though the LIDAR sensing range is dramatically reduced in bad weather, the degradation undergone by mmWave's transmission range under these conditions is almost negligible. Furthermore, beamforming allows for concurrent mmWave transmissions via space-division multiple access (SDMA), reducing the interference level at receivers. So, by leveraging shared sensed data, a vehicle will be able to reconstruct 3D road conditions by multi-source multi-modal data analysis [231] in a much more efficient manner.

III.3.1.1 Main Contributions

This chapter proposes a distributed multi-beam association scheme for mmWave vehicular scenarios driven by the contextual value of the information shared among vehicles and transmission rate/delay constraints.

The rationale behind the research carried out in this chapter is that vehicles' individual sensing range could benefit from dynamically adding traffic/driving context-aware information sensed by nearby vehicles. Therefore, the candidate vehicle selection underpinning criteria need to be established. The proposed method hinges on a set of novel utility functions for every vTx and vRx, based on which a matching game will be formulated to solve the vehicle association. Simulation results demonstrate that the proposed method increases the average amount of shared *timely and innovative* contextual information when using narrow beams by up to 67% (one-to-one matching) and 71% (many-to-one) with respect to distance-

or delay-based policies. For ease of read, the main contributions of this chapter are summarized as follows:

Main Contributions

1. This chapter focuses on the idea of expanding vehicles own sensing range by leveraging mmWave V2V communications for an increased collaborative awareness.
2. To that end, first a utility function that blends together the quality/resolution, the timeliness and the availability of the offered sensing information, as well as the effective sensing range extension provided by each vehicle is proposed.
3. Then the problem of finding the set of vTxs that maximizes the utility of the sensing information offered to each vRx is formulated, and a distributed matching game is proposed to find a stable many-to-one V2V association.
4. Extensive simulations on the mmWave vehicular communications simulator from III.2 –further enhaced to incorporate realistic vehicle mobility traces from SUMO–adopting a traffic-light regulated multilane junction layout, demonstrate the inherent value of bringing into play context-related information to the V2V association problem.

III.3.1.2 Chapter Organization

The rest of the chapter is structured as follows: Section III.3.2 describes the system model and formulates the optimization problem tackled in this chapter. Next, Section III.3.3 describes the many-to-one matching game utilized for pairing vTx and vRx, taking into account interest and quality of offered information and sensing range extension among others. The simulation setup is presented and numerical results are discussed in Section III.3.4. Finally Section III.3.5 concludes the chapter.

III.3.2 System Model and Problem Formulation

III.3.2.1 System Model

The urban junction scenario depicted in Fig. III.3.1 is considered, i.e., a traffic light regulated multilane cross intersection. In this scenario, it is assumed that vehicles communicate through half-duplex V2V links over the mmWave frequency band with bandwidth BW and uniform transmit power P. Let $\mathcal{I} \triangleq \{1, \ldots, I\}$, $\mathcal{J} \triangleq \{1, \ldots, J\}$ respectively denote the sets of vTxs and vRxs. Without loss of generality, and for sake of simplicity in foregoing discussions, time-slotted communications are adopted, so that transmissions occur periodically every T_t seconds. Likewise, resource scheduling –which includes pairing and beam alignment between vTxs and vRxs– is implemented every T_s seconds, with T_s/T_t simplified to be an integer number M. Therefore, each scheduling slot will span M transmission slots i.e., $T_s = MT_t$, so that scheduling is held at $\mathcal{T}_s \triangleq \{t_s \in \mathbb{N} : t_s \mod M = 0\}$ and data transmission is held at $T_t \triangleq \mathbb{N}$.

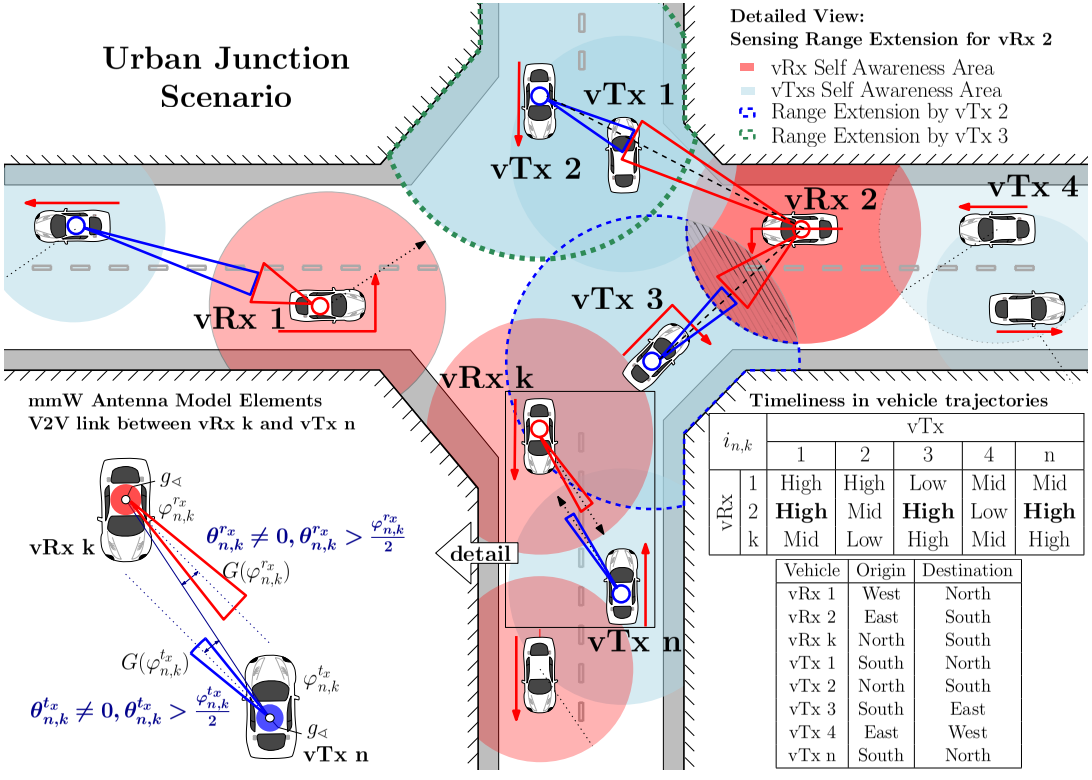

$i_{n,k}$		vTx 1	vTx 2	vTx 3	vTx 4	vTx n
vRx	1	High	High	Low	Mid	Mid
	2	**High**	Mid	**High**	Low	**High**
	k	Mid	Low	High	Mid	High

Vehicle	Origin	Destination
vRx 1	West	North
vRx 2	East	South
vRx k	North	South
vTx 1	South	North
vTx 2	North	South
vTx 3	South	East
vTx 4	East	West
vTx n	South	North

FIGURE III.3.1: Snapshot of a road junction with several transmitters (vTx) and receivers (vRx). vTx 1 and vTx 3 are connected to vRx 2 via mmWave links to increase the context awareness level of the latter depending on their route (marked with →) and the extended area from which contextual data can be sensed and sent by the transmitter (corr. - - - for vTx 3 - - - for vTx 2). ([232] ©2017 IEEE)

A log-distance pathloss model that, through parameters $\delta_{i,j}$ and $\beta_{i,j}$, captures the blocking effect of vehicles located between the transmitting and receiving ends of a 60 GHz mmWave link is adopted [174], [205]. Under this model the channel gain $h_{i,j}$ of the link connecting vTx i to vRx j is

$$h_{i,j} = 10\,\delta_{i,j}\log_{10}(d_{i,j}^{\mathrm{2D}}) + \beta_{i,j} + 15\,d_{i,j}^{\mathrm{2D}}/1000, \tag{III.3.1}$$

where atmospheric attenuation at 60 GHz is represented by the third term, and the values of parameters $\delta_{i,j}$ and $\beta_{i,j}$ are given by the number of blockers in the link. The dynamic nature of the vehicular scenario under analysis yields the above channel gain a function of time, i.e., $h_{i,j}(t)$, through the variation of the number of blocking elements in the link and the relative distance $d_{i,j}^{\mathrm{2D}}$ between vTxs and vRxs.

Furthermore, in-vehicle mmWave directional antennas are modeled through a two-dimensional ideal sectored antenna radiation pattern. The antenna pattern is approximated by resorting to a parametric two-dimensional model that allows defining the boresight direction, the half-power beamwidth and front-to-back ratio for directivity gains in the mainlobe and sidelobe whose transmission and reception antenna gains for vehicles over link (i,j) during a transmission slot $t \in T_t$, $g_{i,j}^{\mathrm{Tx}}(t)$ and $g_{i,j}^{\mathrm{Rx}}(t)$ correspondingly, are given by [35]

$$g_{i,j}^{\measuredangle}(t)=\begin{cases} G(\varphi_{i,j}^{\measuredangle})=\dfrac{2\pi-\left(2\pi-\varphi_{i,j}^{\measuredangle}\right)g_{\lhd}}{\varphi_{i,j}^{\measuredangle}}, & \text{if } |\theta_{i,j}^{\measuredangle}(t)|\leq\dfrac{\varphi_{i,j}^{\measuredangle}}{2} \\ g_{\lhd}, & \text{otherwise.} \end{cases} \tag{III.3.2}$$

In (III.3.2) $\theta_{i,j}^{\measuredangle}(t)$ stands for the alignment error between the steering and boresight directions of vTx i and vRx j, and $\varphi_{i,j}^{\measuredangle}$ is the half-power beamwidth of link (i,j) at transmission ($\measuredangle$=Tx) and reception ($\measuredangle$=Rx) sides established for the active scheduling period. The non-negligible sidelobe power is given by $0 \leq g_{\lhd} \ll 1$.

In order to perform beam alignment, a two-stage mechanism will be considered based on the trial-and-error procedure simplified from [44]. The alignment delay $\tau_{i,j}^{\mathrm{Align}}$ under this procedure is given –on the assumption of availability of a priori sector knowledge provided by the sensing equipment [63]– by $\tau_{i,j}^{\mathrm{Align}} = (\psi_i^{\mathrm{Tx}} \cdot \psi_j^{\mathrm{Rx}}) \cdot T_p/(\varphi_{i,j}^{\mathrm{Tx}} \cdot \varphi_{i,j}^{\mathrm{Rx}})$, where ψ_i^{Tx} and ψ_j^{Rx} denote the sector-level beamwidths of vTx i and vRx j, and T_p denotes the pilot transmission duration. The rate for a time slot t of duration T_t within which alignment has been performed is

$$r_{i,j}(t) = \left(1 - \tau_{i,j}^{\mathrm{Align}}/T_t\right) BW \log_2\left(1 + \mathrm{SINR}_j(t)\right), \tag{III.3.3}$$

$$\mathrm{SINR}_j(t) = \frac{p_i g_{i,j}^{\mathrm{Tx}}(t) h_{i,j}(t) g_{i,j}^{\mathrm{Rx}}(t)}{\sum_{i' \in \mathcal{I}\setminus i} p_{i'} g_{i',j}^{\mathrm{Tx}}(t) h_{i',j}(t) g_{i',j}^{\mathrm{Rx}}(t) + N_0 BW}, \tag{III.3.4}$$

where in the achievable SINR term at time slot t should, not only account for the effective receive power at vRx j from vTx i and to Gaussian noise, but also for other incumbent interfering transmitters $i' \in \mathcal{I}\setminus i$ through their corresponding channel and antenna gains, $g_{i',j}^{c}$ and $g_{i',j}^{\mathrm{Tx}}$, $g_{i',j}^{\mathrm{Rx}}$ respectively. Next, the proposed elements to quantify the value gained by collecting shared sensing contents over a certain established link (i,j) will be described.

III.3.2.2 Evaluation of Information Value

The contextual value gained by sharing sensing contents over an established link (i, j) will be quantified in terms of:

Quality/Resolution Let assorted market penetration levels of the in-vehicle sensing equipment lead to Q quality categories of vehicles with varying sensing radii $\{R_q\}_{q=1}^{Q}$ such that $R_q \geq R_{q'}$ if $q > q'$. Contents for a certain quality level $q \in \{1, \ldots, Q\}$ require at least P_q^{min} packets successfully delivered at the destination vehicle, where $P_q^{min} \geq P_{q'}^{min}$ if $q > q'$. Therefore, the final quality level of contents received through link (i, j) might be reduced due to channel conditions and the number of dropped messages during transmission. This approach models the transmission of scalable contents (e.g., H264/SVC or multi-resolution image coding).

Offered Sensing Range Extension The level of contextual novelty of the area sensed by every vTx is limited by both the urban topology of the road location (e.g., buildings without any contextual safety information for vehicles), and by the overlap between the sensed area $Area_i^2$ by vTx i and that of the receiver j itself (respectively, $Area_j^2$). Intuitively, the value of contents conveyed over link (i, j) should be lower than the fraction of $Area_i^2$ that overlaps with buildings and/or $Area_j^2$. Circular ranges are assumed, so the normalized sensing range extension $Ext_{i,j}$ of vTx i offered to vRx j is given by

$$Ext_{i,j} = \left(Area_i^2 \sqsubset Area_j^2 \sqsubset Area_{\boxplus}^2\right) / \left(\pi R_{q_i}^2\right), \tag{III.3.5}$$

where $q_i \in \{1, \ldots, Q\}$ is the quality of the equipment installed in vTx i; $Area_{\boxplus}^2$ is the total area occupied by buildings and other urban elements lacking contextual information of interest; and the $\sqsubset$ operator denotes area subtraction.

Timeliness The interest of the content for vRx j should depend on the similarity of its future route and that followed by vTx i until transmission. A receiver would prefer to be matched to a transmitter if the route the latter comes from coincides with that to be followed by the former, which can be determined by e.g., comparing the programmed route at the receiver with the GPS trace of the transmitter. This similarity yields a timeliness factor $Int_{i,j} \in [0, 1]$ so that when delivered over link (i, j), the timeliness of the content will be 1 if future (preceding) routes of vRx j (vTx i) are strongly correlated to each other.

Availability This factor stands for the delay by which packets containing the sensed content arrive at vRx j through link (i, j). We consider a fixed packet size P_s, Poisson distributed arrivals with rate $1/\lambda$ and a queue model for the transmitter based on a maximum buffer size of q_{max} packets. When packet p arrives at a queue, it is either delivered to the destination with average delay τ^{tx} (given by the aggregate waiting and service time), or dropped if the entire packet is not delivered within $D_{\max}$ seconds. This queuing policy is justified by the need for low-latency communications in which new safety traffic should be prioritized over outdated contents.

III.3.2.3 Problem Formulation

All the aforementioned factors can be embedded together into a single fitness function $\Psi_{i,j}(q_i, \tau^{tx}, Ext_{i,j}, Int_{i,j}) \in [0, 1]$ that evaluates the overall contextual

value provided to each receiving vehicle j by transmitter i when paired together through mmWave link (i,j). Specifically, the more valuable the connection to i is for the contextual awareness of receiver j, the higher the value of this function will be. With this definition in mind, the formulation of the problem tackled in this chapter follows by defining a matching policy established at time $t_s \in \mathcal{T}_s$ as $\mathbf{\Phi}(t_s) \triangleq \{\phi_{i,j}(t_s)\}_{i\in\mathcal{I}(t_s)}\}_{j\in\mathcal{J}(t_s)}$ with

$$\phi_{i,j}(t_s) = \begin{cases} 1 & \text{if link } (i,j) \text{ is set } \forall t \in [t_s, t_s + M), \\ 0 & \text{otherwise,} \end{cases} \tag{III.3.6}$$

on which we impose that a vRx j (vTx i) should not be simultaneously matched to more than $\Omega_j \in \mathbb{I}$ vTxs (corr. $\Omega_i \in \mathbb{I}$ vRxs), i.e., $\sum_{i\in\mathcal{I}(t_s)} \phi_{i,j}(t_s) \leq \Omega_j \quad \forall j \in \mathcal{J}(t_s)$, where $\mathcal{I}(t_s)$ and $\mathcal{J}(t_s)$ denote the subset of transmitters and receivers in the scenario during the scheduling period t_s. When allowing for several vehicles transmitting concurrently to the same receiver, it is implicitly assumed that each received data stream is captured and processed entirely in parallel with respect to any other beam, without any further implications in terms of processing delay or receiving gain (by virtue of e.g., several antennas deployed on every receiving vehicle). However, the availability of several data streams does affect the contextual novelty provided to the receiver, as overlaps among the areas sensed by transmitters and that of the receiver may arise more likely, ultimately decreasing the overall contextual value of the information transmitted to the receiver. This spatial correlation between sensed areas yields a redefined fitness function that extends its prior counterpart $\Psi_{i,j}(\cdot)$ so as to consider a subset $\mathcal{I}_j(t_s) \subseteq \mathcal{I}(t_s)$ of transmitters paired to a receiver j. Mathematically,

$$\Upsilon_j(\mathbf{\Phi}(t_s)) \equiv \Upsilon_j(\{q_i, \tau^{tx}, Ext_{i,j}, Int_{i,j}\}_{i\in\mathcal{I}_j(t_s)}), \tag{III.3.7}$$

where $\Upsilon_j(\mathbf{\Phi}(t_s)) \in [0,1]$ and $\mathcal{I}_j(t_s) \triangleq \{i \in \mathcal{I}(t_s) : \phi_{i,j}(t_s) = 1\}$. The problem addressed in this chapter can be formulated as the selection of the matching policy $\mathbf{\Phi}(t_s)$ for $t_s \in \mathcal{T}_s$ such that

$$\underset{\mathbf{\Phi}(t_s)}{\text{Maximize}} \quad \sum_{j\in\mathcal{J}(t_s)} \Upsilon_j(\mathbf{\Phi}(t_s)), \tag{III.3.8a}$$

$$\text{subject to:} \quad \sum_{j\in\mathcal{J}(t_s)} \phi_{i,j}(t_s) \leq \Omega_i, \forall i \in \mathcal{I}(t_s), \tag{III.3.8b}$$

$$\sum_{i\in\mathcal{I}(t_s)} \phi_{i,j}(t_s) \leq \Omega_j, \forall j \in \mathcal{J}(t_s), \tag{III.3.8c}$$

$$\phi_{i,j}(t_s) \in \{0,1\}, \forall i,j \in \mathcal{I}(t_s) \times \mathcal{J}(t_s), \tag{III.3.8d}$$

where constraints (III.3.8b) through (III.3.8d) denote that every vRx can be paired to as many as Ω_j vTxs, whereas each vTx is paired to Ω_i vRx at most.

III.3.3 Content-Aware Vehicle Pairing as a Matching Game

The optimization problem formulated in the previous section is difficult to tackle analytically. Furthermore, in vehicular scenarios the design target should be steered towards low-complexity distributed solutions so as to avoid traffic overheads that could eventually compromise the end-to-end delay statistics of the deployed vehicular links.

Based on this rationale, we adopt the framework of matching theory [233] [210], as per II.1.2 to undertake the distributed optimization of $\mathbf{\Phi}(t_s)$. It is important to remark at this point that the ultimate purpose of the research conducted in this chapter is to assess the performance figures of different RRM strategies, with an emphasis on *reliability/delay* metrics and always considering the RRM enforcing time –namely, the length of the scheduling interval T_s– as the driver of our analysis. In this regard, although several algorithmic alternatives from the literature will be included in the simulation benchmark later discussed in the chapter, conclusions will gravitate not only on the relative performance gains among distributed association schemes, but also on the dependence of the obtained metrics with T_s and its consistence over such pairing methods. For the sake of completeness, the key concepts related to matching theory as per the notation followed in this chapter are reformulated from the original definitions provided in II.1.2.3.

From **Definition 1** it is recalled that a matching game is defined by two sets of players $(\mathcal{I}_j(t), \mathcal{J}_i(t))$ and two preference relations $\succ_i, \succ_j$, allowing each player $i \in \mathcal{I}_j(t)$, $j \in \mathcal{J}_i(t)$ to accordingly rank the players in the opposite set. Equally from **Definition 2**, preferences $\succ_i$, $\succ_j$ are reintroduced as complete, reflexive and transitive binary relations between the players in $\mathcal{I}_j(t)$ and $\mathcal{J}_i(t)$. Therefore for any vTx i a preference relation $\succ_i$ is defined over the set of vRx $\mathcal{J}_i(t)$ such that for any two vRx $(j, j') \in \mathcal{J}_i(t) \times \mathcal{J}_i(t)$ with $j \neq j'$, and two matchings $\mathbf{\Phi}(t)$ and $\mathbf{\Phi}'(t)$ so that $\boldsymbol{\phi}_i(t) = j$ and $\boldsymbol{\phi}'_i(t) = j'$:

$$(j, \mathbf{\Phi}(t)) \succ_i \left(j', \mathbf{\Phi}'(t)\right) \Leftrightarrow U^{i,j}_{vTx}(t) > U^{i,j'}_{vTx}(t). \tag{III.3.9}$$

Similarly, for any vRx j a preference relation $\succ_j$ is defined over the set of vTx $\mathcal{I}_j(t)$ such that for any two vTx $(i, i') \in \mathcal{I}_j(t) \times \mathcal{I}_j(t)$ with $i \neq i'$, and two matchings $\mathbf{\Phi}(t)$ and $\mathbf{\Phi}'(t)$ so that $\boldsymbol{\phi}_j(t) = i$ and $\boldsymbol{\phi}'_j(t) = i'$:

$$(i, \mathbf{\Phi}(t)) \succ_j \left(i\prime, \mathbf{\Phi}'(t)\right) \Leftrightarrow U^{i,j}_{vRx}(t) > U^{i\prime,j}_{vRx}(t). \tag{III.3.10}$$

With $U^{i,j}_{vTx}(t)$ and $U^{i,j}_{vRx}(t)$ in (III.3.9)-(III.3.10) respectively denoting the utility of vRx j for vTx i and the utility of vTx i for vRx j, i.e., their measure of motivation of over establishing a mmWave link with a given vRx/vTx.

Likewise, from **Definition 4** it follows that the outcome of a matching game is a matching function $\mathbf{\Phi}(t) = \{\phi_{i,j}(t)\}$ that bilaterally assigns players $\boldsymbol{\phi}_i(t) \triangleq \{j \in \mathcal{J}_i(t) : \phi_{i,j}(t) = 1\}$ and $\boldsymbol{\phi}_j(t) \triangleq \{i \in \mathcal{I}_j(t) : \phi_{i,j}(t) = 1\}$ such that $|\boldsymbol{\phi}_j(t)| = \Omega_j$ and $|\boldsymbol{\phi}_i(t)| = \Omega_i$. Here Ω_i and Ω_j stand for the *quota* of the players, vTx and vRx correspondingly.

Finally, **Definition 8** states that a matching is *not stable* if for a given match $\boldsymbol{\phi}_i(t) = j$ and $\boldsymbol{\phi}_j(t) = i$, a blocking pair (i', j') such that $i, i' \in \mathcal{I}_j(t)$ and $j, j' \in \mathcal{J}_i(t)$ satisfying $\boldsymbol{\phi}_i(t) \neq j'$, $\boldsymbol{\phi}_j(t) \neq i'$ and $j' \succ_i j$, $i' \succ_j i$ exists. That is, if for a given match two players prefer to be matched to each other over their current matched partners. A matching is considered to be *pairwise stable* if no such blocking pair exists.

III.3.3.1 Utilities of vRx and vTx

Having formally described a matching game and its notion of stability, utilities for vTxs and vRxs are next defined with the twofold aim of balancing CSI/QSI information and, at the same time, enhancing the search of prospective V2V

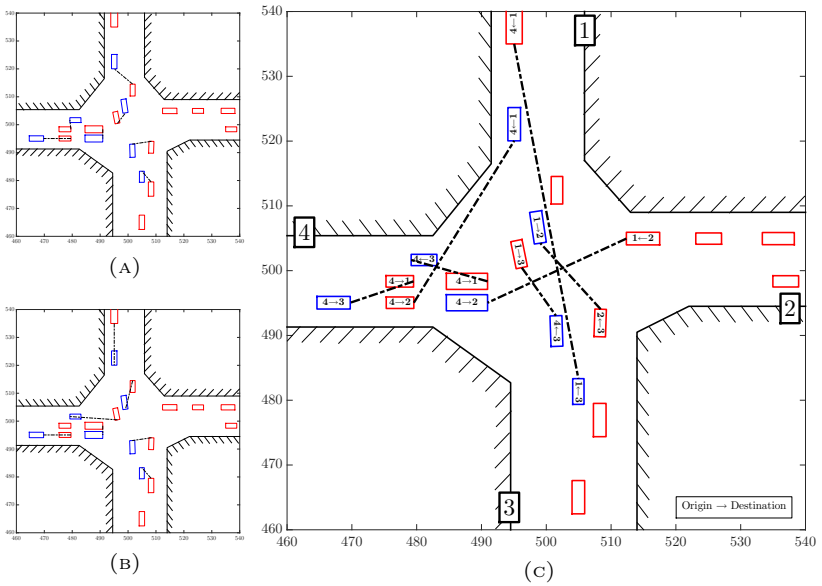

FIGURE III.3.2: Influence of $\{q_i, \tau^{tx}, Ext_{i,j}, Int_{i,j}\}$ in the resulting V2V matching outcome for $\Omega_i = \Omega_j = 1$, at a given time instant with vRx and vTx represented in blue and red, respectively. (a) `MINDist` outcome where none of the above parameters is considered. (b) `DELAYfair` outcome based on learned CSI/QSI, i.e., (ω_d=1, ω_i=0, ω_e=0). (c) `CONTEXTaware` matching with evenly balanced learned CSI/QSI and context awareness (ω_d=0.5, ω_i=0.25, ω_e=0.25). ([232] ©2017 IEEE)

links towards achieving higher levels of valuable traffic context information:

$$U_{vTx}^{i,j}(t_s) \triangleq -((R_{q_j}/R_Q)^2 \hat{r}_{i,j}(t_s))^{-1}, \tag{III.3.11}$$

$$U_{vRx}^{i,j}(t_s) \triangleq -(\omega_d \hat{r}_{i,j}(t_s) + \omega_i Int_{i,j} + \omega_e Ext_{i,j}(t_s))^{-1}. \tag{III.3.12}$$

Moreover, α-fair utility function, which with α=2 provides weighted minimum proportional delay fairness, lies at the core of the formulation of $U_{vTx}^{i,j}(t)$ as per (III.3.11) with R_{q_j}/R_Q incorporating information about the resolution of vRx j; whereas $U_{vRx}^{i,j}(t)$ in (III.3.12) balances rate/delay and context such that $\omega_d + \omega_i + \omega_e$=1 is met. In (III.3.11)-(III.3.12) $\hat{r}_{i,j}(t_s)$ represents the estimation of the average rate expected for the matched vTx i and vRx j pair over the next scheduling period acquired e.g., as proposed in [204]. This estimation is normalized in (III.3.12) for each vRx (corr. for each vTx in (III.3.11)) so as to avoid scale related issues.

The above matching game is solved in a distributed way using DA algorithm [122], as has been utilized in the scenario of the preceding chapter.

III.3.4 Simulation Setup and Performance Evaluation

The performance of the proposed content-aware distributed matching scheme is assessed over a traffic light regulated junction scenario[1]. The scenario comprises a total of $I = 26$ vTx and $VRX = 21$ vRx of varying dimensions to emulate assorted car, bus and trucks. Vehicles' movement is characterized by realistic behavioral driving models –including acceleration, braking and lane changing– using SUMO traces [234]. Bandwidth is set to $BW = 2.16$ GHz centered in 60 GHz, whereas $N_0 = -174$ dBm/Hz and transmit power is equal to $p_i = 15$ dBm $\forall i \in \mathcal{I}$. The simulation time spans a total of 30 seconds, slotted in transmission and scheduling periods of $T_t = 2$ ms and $T_s = 100$ ms ($M = 50$). Transmit and receive beamwidths $\varphi_{i,j}^{t_x}$ and $\varphi_{i,j}^{r_x}$ are kept constant and equal to $\varphi \in \{5^\circ, 15^\circ, 45^\circ\}$ for every link. In all experiments the packet size and arrival rate are $P_s = 10^6$ bits and $1/\lambda = 1/T_t = 500$ packets per second, respectively. Four different levels of sensing equipment are installed on board with ranges $\{R_q\}_{q=1}^4 = \{5, 10, 15, 20\}$ meters, yielding 4 resolutions of the sensed contents with a minimum number $\{P_q^{min}\}_{q=1}^4 = \{1, 2, 3, 4\}$ of packets received at the destination. Queue dynamics are driven by extreme parameter values for low-latency communications, namely, a buffer size of $q_{max} = 1$ packet and $D_{\max} = 2$ ms.

The benchmark discussed in what follows considers matching outcomes for three different matching policies:

- Minimum distance matching (`MINDist`), by which vTxs and vRxs establish V2V links through a matching game that ranks players according to mutual distance.
- Minimum-delay proportional fairness matching (`DELAYfair`), under which vTxs and vRxs are coupled by CSI/QSI aware weighted α-fair utilities.
- Context-aware matching (`CONTEXTaware`) where the quality, novelty, timeliness and volume of the sensing content profile offered are evaluated as per (III.3.11)-(III.3.12).

Before proceeding with the discussion, it should be noticed that the maximum number of feasible V2V links in the junction is subject to limitations arising from the skewness in the number of vTx and vRx at a given instant and the extreme fading effects imposed by blocking buildings. Indeed, schemes that build upon *learned* CSI/QSI will never match vTx and vRx whose LOS is obstructed by a building even if that means remaining unpaired.

III.3.4.1 Discussion

We first focus the analysis of the results on Fig. III.3.2, where the matched vTx-vRx pairs for the different schemes included in the benchmark are depicted for one of the simulated scheduling intervals and $\Omega = 1$. The aim of these plots is to evince the topological differences yielded by the utility functions that characterize such matching criteria. To begin with, `MINDist` (Fig. III.3.2(a)) pairs vehicles exclusively based on their mutual distance, thus giving rise to short-length mmWave links prone to frequent misalignment. Likewise, the consideration of learned rate statistics in the formulated utilities of the `DELAYfair` scheme

[1]Traffic Junction Animated `MINDist` example outcomes are available at:
`https://youtu.be/2Qb4NSCbJ9w` one-to-one ($\Omega = 1$)
`https://youtu.be/VC3_X2fMgJA` many-to-one ($\Omega = 4$)

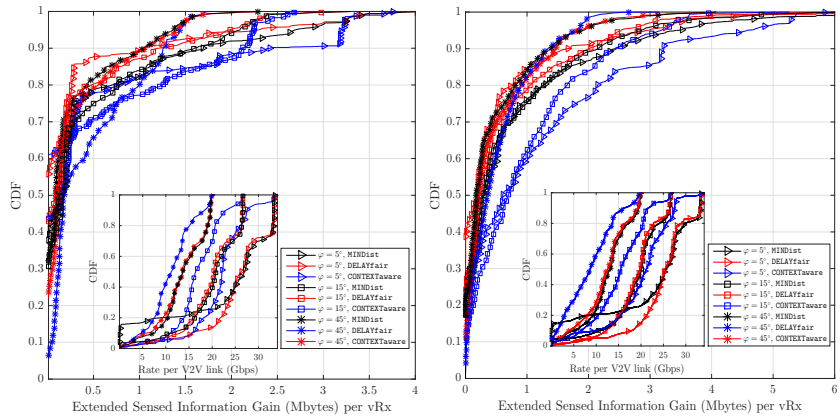

(A) $\Omega_i = \Omega_j = 1$ (B) $\Omega_i = 1; \Omega_j = 3$

FIGURE III.3.3: Rates and granted ESI per V2V link per T_t with (a) a maximum of 1 contributing vTxs per vRx and (b) with up to 3 contributing vTxs per vRx. ([232] ©2017 IEEE)

(Fig. III.3.2(b)) implies topological changes with respect to `MINDist` due to the discovery of better long-term aligned pairs. Finally, the `CONTEXTaware` approach proposed in this chapter with $\omega_d = 0.5$ and $\omega_i = \omega_e = 0.25$ balances the consideration of learned rates and the potential amount of contextual novelty and timeliness provided by vTxs to every receiver as per (III.3.11)-(III.3.12). As clearly shown in Fig. III.3.2(c), mmWave links between vehicles under this scheme are formed not only accounting for their delay statistics, but also enforced by the contextual information gain, as quantified by minimal overlaps between sensing areas and timeliness of the information with respect to the vehicles' routes.

We follow with a discussion of Fig. III.3.3 and Fig. III.3.4, where the CDFs of 1) the ESI gained per vRx and transmission slot; and 2) the packet level experienced delay are depicted for $\Omega_j = \{1, 3\}$. Figs. III.3.3(a) and III.3.3(b) include the CDFs of the instantaneous rates per V2V link as subplots, whereas Fig. III.3.4(a) and Fig. III.3.4(b) include CDFs of packet drop (P_{drop}) –obtained by aggregating successful and failed transmission over each scheduling period and queue– to illustrate the different trade-offs of the simulated scenario. The ESI in bits is defined as

$$\mathrm{ESI}_j(t) = \sum_{i \in \mathcal{I}_j(t)} \phi_{i,j}(t_s) Int_{i,j} Ext_{i,j} (R_{q_i}/R_Q)^2 r_{i,j}(t) T_t, \tag{III.3.13}$$

where $t \in [t_s, t_s + M)$. This notion of ESI reflects the maximum information the rate of an established mmWave link supports to deliver within a transmission slot T_t weighted by the timeliness and the sensing range extension area brought by the transmitter. A quick glimpse at Fig. III.3.3(a) exposes the superior performance of the proposed scheme, providing 43% (percentile 90, $\varphi = 5°$) and 67% (percentile 80, $\varphi = 15°$) more information than the best of the other baselines, no matter the comparatively lower rates achieved in V2V links. The same result holds for Fig. III.3.3(b), with 33% (percentile 90) and 71% (percentile 80) increased information in both cases for $\varphi = 5°$.

As for the results in Fig. III.3.4(a), values of $\varphi = \{5°, 15°\}$ for all schemes

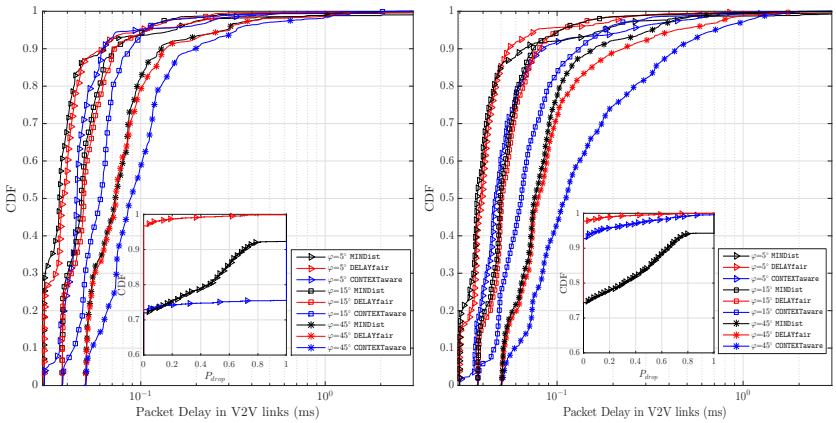

(A) $\Omega_i = \Omega_j = 1$ (B) $\Omega_i = 1; \Omega_j = 3$

FIGURE III.3.4: CDFs of delay and associated drops (inlet) per V2V link per T_t with (a) a maximum of 1 contributing vTxs per vRx and with (b) with up to 3 contributing vTxs per vRx. ([232] ©2017 IEEE)

show delays under 0.1 ms for over 90% of the samples (80% for $\varphi = 45°$ in baselines, 60% in our proposed matching). Similarly, our proposed approach shows a slightly worse delay performance in Fig. III.3.4(b), that is directly related to a significantly improved reliability (93% of successful transmissions) when vRxs are allowed to leverage information arriving from assorted vTxs. The reason lies in the many-to-one matching, which increases the chances of vTxs to match vRxs on top of their ranks i.e., those offering better CSI/QSI profiles; a better CSI/QSI implies reduced drops and more samples contributing to delay calculations. The penalty to be paid, however, comes in the form of a few vRxs monopolizing the access to multi-sourced shared sensing information.

III.3.5 Conclusions

Framed on the ever-growing need for a higher contextual awareness in vehicular environments, this chapter has elaborated on how to properly disseminate contextual sensed information among vehicles using many-to-one mmWave radio links. In particular, a distributed matching game based on delay- and context-driven utilities has been proposed to pair vehicles towards efficiently sharing sensing information. Simulations have been presented and discussed for an urban junction scenario with realistic mobility traces, from where it is concluded that the set of formulated utilities permit to pair vehicles by using different performance objectives: rate/delay, the extended sensing area provided by the transmitter upon pairing and the timeliness of the exchanged information with respect to the vehicles' routes.

Part IV

Application Scenarios for mmWaves in 5G Networks and Beyond: Mobile VR

"Your body is wired. Your spirit is wireless."

Alan Cohen

Chapter IV.1

Mobile VR Application Scenarios

IV.1.1 Introduction

The last two years have witnessed an unprecedented interest both from academia and industry towards mobile/wireless virtual reality (VR), mixed reality (MR), and augmented reality (AR). This interest has been fueled by the promise of a mobile, interconnected VR realized by 5G [235] and a future Tactile Internet [236], [237] called to allow for remote interaction with real and virtual elements (objects or systems) in perceived real-time. Indeed, the ability of VR to immerse the user creates the next generation of entertainment experiences, while MR and AR promise enhanced user experiences that will allow end-users to raise their head from smartphone screens. In the context of the three core-service categories that 5G encompasses, namely eMBB, mMTC, and URLLC, though mobile VR, MR and AR applications are very much use case specific, they all sit somewhere at the crossroads between eMBB and URLLC as they all seek multiple Gbps of data uniformly delivered to end-users and subject to latency constraints. Yet, it is well known that low latency and high reliability are conflicting requirements [238]: ultra-high reliability implies allocating more resources to users to satisfy high transmission success rate requirements, which might increase latency for other users. Therefore, smart network designs are required to realize the vision of interconnected VR/AR that is characterized by smooth and reliable service, minimal latency, and seamless support of different network deployments and application requirements.

Throughout this introductory chapter, the general aspects of XR will be presented, a term that encompasses all virtual or combined real-virtual environment compounds including VR, AR and MR. Following that, the current challenges and the technology enablers to experience a truly mobile and interconnected VR, the second of the selected application scenarios for mmWave in 5G networks and beyond, will be covered. The chapter finalizes by introducing the two selected mmWave-enabled multi-user VR use cases that will be examined in Chapters IV.2 and Chapter IV.3 of this Thesis, an interactive VR gaming arcade and a 360° VR theater, respectively.

IV.1.1.1 Wireless and Mobile VR, MR and AR

In essence VR, MR and AR differ in the proportion in which digital content is mixed with reality. Both AR and MR incorporate some aspects of the real

environment around the user and while real elements are the main focus for AR, virtual elements play a leading role in MR. To accomplish their goal, AR or MR glasses and wearables need not block out the world around, they will overlay digital layers to the current view of the user. As the human eye is very sensitive to incorrect information, in order to "feel real", AR or MR systems need to build a 3D model of the environment to place virtual objects in the right place and handle occlusions. In addition, the lighting of the object needs to be adjusted to the scene. Conversely, VR refers to a 100% virtual, simulated experience. VR headsets or head mounted devices (HMDs) cover the user's FoV and respond to eye tracking and head movements to shift what the screen displays accordingly. That is, in VR the only links to the outside real world are the various inputs arriving from the VR system to the senses of the user that are instrumental in adding credibility to the illusion of living inside the virtually replicated location.

The ultimate VR system implies breaking the barrier that separates both worlds by being unable to distinguish between a real and synthetic fictional world [235]. An important step in this direction is to increase the resolution of the VR systems to match the resolution of the human eye, and to free the user from any cable connection that limits mobility and, when in touch with the body, disrupts the experience.

So far, the use of untethered VR HMDs has been relegated to simple VR applications and discreet-to-low quality video streaming delivered through smartphone headsets such as Samsung Gear VR, or cost efficient ones such as the Google Cardboard. Meanwhile, high-definition multimedia interface (HDMI) connection through 19-wire cable has been favored for PC-based premium VR headsets such as Oculus Rift, HTC Vive or PlayStation VR. The reason can be found in the latency-sensitivity and the resource –communications and computing– intensiveness nature of VR systems. In addition, even premium VR headsets still have a limited resolution of 10 pixels per degree, compared to the 60 pixels per degree with clear (20/20) visual acuity of the human eye. Hence, HD wireless/mobile VR is doubly constrained. It is computing constrained, as GPU power in HMDs is limited by the generated heat in powering these devices and by the bulkiness and weight of the headset itself. Second, it is constrained by the bandwidth limitations of current wireless technologies, operating below 6 GHz, and the resulting inability to stream high resolution video –8K and higher– at high frame rate –over 90 frames per second (fps)–. The success of wireless VR, hence, hinges on bringing enough computing power to the HMD via dedicated application-specific integrated circuits (ASICs) or to the cloud or fog within a latency budget. Yet, recent developments from the VR hardware industry delivered to the market first commercial level standalone VR headgears in 2018 even if still with limited resolution.

A manifold of technological challenges stemming from a variety of disciplines need to be addressed to achieve an interconnected VR experience. An interconnected VR service needs to handle the resource distribution, quality-of-experience (QoE) requirements, and the interaction between multiple users engaging in interactive VR services. It should also be able to handle different applications and traffic scenarios, for example, the aggregate traffic of an enterprise floor where participants share an MR workplace, or an interactive gaming arcade, where each player is experiencing her own VR content.

Therefore, it is envisioned that the next steps towards the future interconnected VR will come from a flexible use of computing, caching and communication resources i.e., the so-called 3C paradigm [239]. To realize this vision, many trade-offs need to be studied [240]. These range from the optimization of local

versus remote computation, to single or multi-connectivity transmission while taking into account bandwidth, latency and reliability constraints[241].

IV.1.2 Requirements and Big Challenges in wireless VR

From a wireless communication point of view, the extremely high data rate demands coupled with ultra-low latency and reliability requirements are the main hurdles before bringing untethered VR into our everyday lives. In what follows, the bandwidth/capacity, latency and reliability requirements associated to several VR use cases will be briefly introduced.

IV.1.2.1 Capacity

Current 5G NR system design efforts aim at supporting the upcoming exponential growth in data rate requirements from resource-hungry applications. Focusing on VR technology, a back-of-the-envelope calculation reveals that with each of the human eyes being able to see up to 64 million pixels (150° horizontal and 120° vertical FoV, 60 pixels per degree) at a certain moment [235], and with 120 fps requirement to generate a real-like view, up to 15.5 billions of pixels per second are needed. By storing each colored pixel in 36 bits, and with the maximum of 1:600 video compression rate typically found in H.265 high efficiency video coding (HEVC) encoding, a required bit rate of up to 1 Gbps is needed to guarantee such a quality.

The values above are clearly unrealizable in 4G. Actually, even early stage and entry-level VR, whose minimum data rate requirements are estimated to reach 100 Mbps[1] will not be supported for multiple concurrent users in many deployments. Adding the required real time response for dynamic and interactive collaborative VR applications, it is not surprising that a significant ongoing research effort is geared towards reducing bandwidth needs in mobile/wireless VR, thereby shrinking the amount of data processed and transmitted. For example, in the context of 360° immersive VR video streaming, head movement prediction is used in [242] to spatially segment raw frames and deliver in HD only their visible portion. A similar approach is considered in [243], splitting the video into separated grid streams and serving grid streams corresponding to the FoV. Alternatively, eye gaze tracking is applied in [244] to deliver high resolution content only at the center of the human vision and to reduce the resolution and color depth in the peripheral field of view.

Such a foveated 360° transmission has the potential to reduce the data rates to about 100 Mbps for a VR system with less than 10 ms round trip time including the rendering in the cloud. Yet, even if generating a foveated 360° transmission took only 5 ms latency, existing networks could not serve 100 Mbps to multiple users with reliable round trip times of less than 5 ms. Secondly, in today's networks computing resources are not available this close to the users. Therefore, there exists a gap between what the current state of the art can do and what will be required as VR seeps into consumer space and forges ahead in terms of network requirements. In view of this, it is anticipated that the millimeter wave (mmWave) communications will bridge the gap by facilitating the necessary capacity increase.

[1]Corresponding to 1K and 2K VR resolution or equivalent 240 pixel lines and SD TV resolution respectively.

IV.1.2.2 Latency

In VR environments, stringent latency requirements are of utmost importance for providing a pleasant immersive VR experience. The human eye needs to perceive accurate and smooth movements with low motion-to-photon (MTP) latency, which is the lapse between a movement e.g., head rotation, and a frame's pixels corresponding to the new FoV have been shown to the eyes. High MTP values send conflicting signals to the vestibulo-ocular reflex (VOR), a dissonance that might lead to motion sickness. There is broad consensus in setting the upper bound for MTP below 15-20 ms [243]–[245]. Meanwhile, the loopback latency of 4G under ideal operation conditions is around 20 to 25 ms [246], [247], so there is still a long path ahead to reach the envisaged latency level in 5G [248].

The challenge for bringing end-to-end latency down to acceptable levels starts by first understanding the various types of delays involved in such systems to calculate the joint computing and communication latency budget. Delay contributions to the end-to-end wireless/mobile VR latency include sensor sampling, image processing or frame rendering computing, network (with queuing and over-the-air) and display refresh delays. Sensor delay's contribution ($<$1 ms) is considered imperceptible by users, and display delay ($\approx$10-15 ms) is expected to drop to 5 ms [249], which leaves 14 ms for computing and communication.

Thus, both computing and communication delay serve as delay bottlenecks in VR systems. Heavy image processing requires high computational power that is often not available in the local HMD GPUs. Offloading computing tasks to remote cloud servers significantly relieves the computing burden from the users' HMDs at the expense of incurring additional communication delay in both directions. Unlike MR and AR where uploading video streams to the cloud may be required, UL communication delay due to offloading the computing task to the server is typically very small in VR, owing to the small amount of data needed e.g., user tracking data and the interactive control decisions. However, the downlink delivery of the processed video frames in full resolution can significantly contribute to the overall delay. Current online VR computing can take as much as 100 ms, whereas communication delay (edge of network to server) reaches 40 ms. Consequently, relying on remote cloud servers is only a suitable approach for low-resolution non-interactive VR applications, where the whole 360° content can be streamed and the constraints on real-time computing are relaxed. Interactive VR applications require real-time computing to ensure responsiveness.

Therefore, it is necessary to shrink the distance between the end users and the computing servers to guarantee minimal latency. Fog computing –also known as multi-access edge computing (MEC)–, where the computation resources are pushed to the network edge close to the end users, serves as an efficient and scalable approach to provide low latency computing to VR systems. MEC is expected to reduce the communication delay to less than 1 ms in metropolitan areas. Another interesting AR scenario for the use of MEC is provided in [250] where, besides latency reduction, energy efficiency is considered. The MEC resource allocation exploits inherent collaborative properties of AR: a single user offloads shared information on an AR scene to the edge servers, which transmit the resulting processed data to all users at once via a shared downlink.

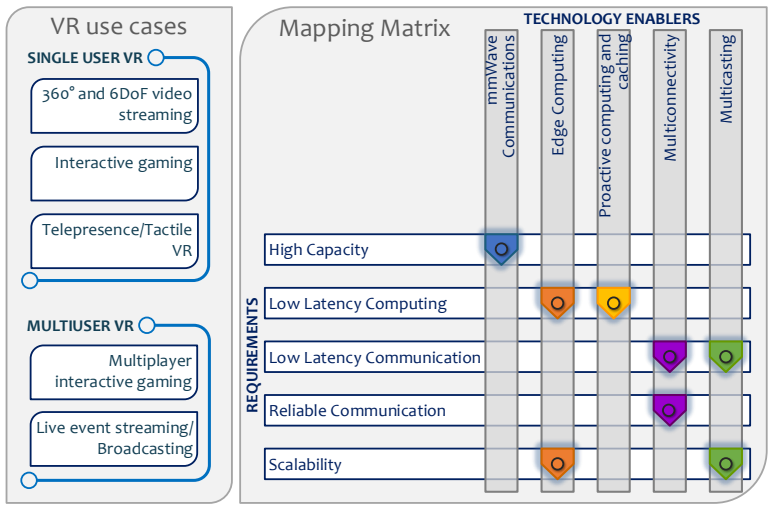

FIGURE IV.1.1: Single and multiple user VR use cases: requirements and enablers. ([251] ©2018 IEEE)

IV.1.2.3 Reliability

Reliability refers to the availability/provisioning of a certain level of communication or computing service with some assured guarantees e.g., 99.99999 percent of the time. Nonetheless, a second interpretation that is widely adopted among wireless communications standardization bodies treats reliability as a probabilistic bound over the maximum allowable latency i.e., it is interpreted as a delay-reliability. No matter in which of its connotations, VR/AR applications need to consistently meet stringent latency and reliability constraints. Lag spikes and dropouts need to be kept to a minimum, or else users will feel detached. Immersive VR demands a perceptible image-quality degradation-free uniform experience. This mandates error-robustness guarantees in different layers, spanning from the video compression techniques in the coding level, to the video delivery schemes in the network level.

In wireless environments where temporary outages are common due to impairments in SINR, VR's non-elastic traffic behavior poses yet an additional difficulty. In this regard, an ultra-reliable VR service refers to the delivery of video frames on time with high success rate. Multi-connectivity (MC), which was developed for enhancing data rates and enabling a reliable transmission, bestows diversity to reduce the number of failed handovers, dropped connections, and radio-link failure (RLF). MC can either operate using the same or separate carriers frequencies. In intra-frequency MC, such as in single frequency networks (SFNs), multiple sources using the same carrier frequency jointly transmit signals to a user. Contrarily, inter-frequency MC, which includes CA, dual connectivity (DC) and the use of different wireless standards, leverages either single or various sources that employ multiple carrier frequencies simultaneously for the same purpose.

Enhancing reliability always comes at the price of using more resources and may result in additional delays. For instance, at the PHY layer the use of parity,

redundancy, and re-transmission will increase the latency. Also, allocating multiple sources for a single user could potentially impact the experienced latency of the remaining users. Another important reliability aspect in 5G is the ultra-high success rate of critical low-throughput packets. In particular, a maximum PER of 10^{-5} is specified in the 3GPP standard. This correlates with the VR/AR tracking message signaling that has to be delivered with ultra-high reliability to ensure smooth VR service.

IV.1.3 VR Latency and Reliability Enablers

As outlined above, there is a substantial amount of work to be done towards achieving a truly immersive VR user experience. The VR QoE is highly dependent on stringent latency and reliability conditions. High MTP delays of 20 ms or more as well as distortions due to low data rate and resulting quality of the projected images, lead to motion sickness and affect the user visual experience. Hence, end-to-end delay and reliability guarantees are key elements of an immersive VR experience. Smart network designs that blend together and orchestrate communication, computing, and caching resources are sorely lacking. Fig. IV.1.1 captures the foreseen requirements and the main technological enablers for both single and multiple user VR use cases. Next, light is shed on the envisioned roles of mmWave communications and MEC as two major thrusts of the future interconnected VR.

IV.1.3.1 Millimeter Wave Communications for VR

As thoroughly discussed in Section I.1.1.3 in Chapter I.1 and briefly summarized in here for the sake of completeness, the possibilities offered by the abundance of available spectrum in the frequency bands above 30 GHz –with bandwidths that in the worst case are one order of magnitude above LTE's– are the main allure to adopt mmWave communications. In turn, the need for beamforming/beam training to find the best transmitter and receiver beam combination such that a sufficient link budget available [252] coupled with the susceptibility to blockage and the lack of diffractions, are commonly listed as their main shortcomings. Yet although best communication conditions are met whenever there is a LOS path between the transmitter and the receiver with the mainlobes of their antenna beams facing each other, partially blocked and single reflection paths might still be usable at a reduced rate. Moreover, directionality and isolation from blockage significantly reduce the footprint of interference, and make mmWave well-suited for dense deployments which, as a matter of fact, is very convenient specially when considering indoor deployments[2].

Bearing in mind the operation of digital, hybrid or analog beamforming and beam-tracking techniques discussed in Section I.1.1.3, it is recalled here that beam training is able to track moving users in slowly time-variant environments and to circumvent blocked LOS paths by finding strong reflectors. In indoor multiuser VR scenarios, the most likely source of sudden signal drop arises from temporal blockages –caused mostly by the users' own limbs e.g., a raising hand, or the bodies of surrounding players– and from movement related transmitter-receiver beam misalignment. In such cases, if the SINR drops below a certain

[2]At this point, due to the broadness of the subject, the interested readers in mmWave communications are referred to I.1.1.3 or to the seminal works on mmWave for 5G [26], [27] on the potentials of mmWave communications, and to [253] to specifically dig into challenges related to achieving URLLC in 5G mmWave cellular networks.

threshold, an alternative directional channel discovering process needs to be triggered. However, beam-tracking through beam training for large antenna arrays involving big codebooks with narrow beams can incur large delays. For that reason, developing efficient beam training and beam-tracking techniques remains an active area of research, specially for fast changing environments. For example, machine learning methods can be used to identify the most likely beam candidates [254], [255] and keep the disruption at a minimum.

In this context, the use of MC to counteract the blockages and temporal disruptions of the mmWave channel is advocated. Specifically, the use non-coherent multisourced VR frame transmission will be showcased as a way to improve SINR and increase the reliability of those links experiencing worse channel conditions. This approach is in line with the idea of overbooking radio and computing resources as a mean to protect against mmWave channel vulnerability [53]. Yet, the literature on the specific application of mmWave technologies for VR is still scarce, with the exception of [256] where the use of a configurable mmWave reflector is proposed to overcome self-body blockage and avoid the need to deploy multiple transmitters. However this latter work does not consider a multi-user VR scenario, which is surely more challenging in terms of scheduling and interference management.

IV.1.3.2 MEC Computing and Caching

Rendering and processing VR HD video frames require extensive computation resources. However, the need for compact and lightweight HMDs places a limit on their computational capabilities. Computation offloading is seen as a key enabler in providing the required computing and graphics rendering in VR environments. Users upload their tracking information, as well as any related data such as gaming actions or video streaming preferences to MEC servers with high computation capabilities. These servers perform the offloaded computing tasks and return the corresponding video frame in the downlink direction.

Cloud computing servers are capable of handling central processing unit (CPU) and GPU-hungry computing tasks due to their high computational capabilities. The distance to computing resources for real-time VR services is limited by the distance light travels during the maximum tolerable latency. The concept of edge computing strikes a balance between communication latency and computing latency by providing high computational resources close to the users. Edge computing is envisioned as a key enabler for latency-critical VR computing services. However, to ensure efficient latency-aware computing services with minimal costs, server placement, server selection, computing resource allocation and task offloading decisions are needed.

Indeed, providing stringent reliability and latency guarantees in real-time applications of VR is a daunting task. Dynamic applications, such as interactive gaming where real-time actions arrive at random, requires massive computational resources close to the users to be served on time. Therefore, the burden on real-time servers has to be decreased through facilitating proactive prefetching tasks and computing of the corresponding users' video frames. Recent studies have shown that VR gaming users' head movement can be predicted with high accuracy for upcoming hundreds of milliseconds [242]. Such prediction information can significantly help relieve the burden on servers of real-time computing following users' tracking data. Based on the estimated future pose of users, video frames can be proactively computed in remote cloud servers and cached in the network edge or the users' HMDs, freeing more edge servers for real-time tasks.

In addition to users' movement, application-specific actions and corresponding decisions can be also proactively predicted. Moreover, since human actions are correlated, modeling the popularity of different actions and their impact on the VR environment can facilitate in predicting the upcoming actions. Accordingly, subject to the available computing and storage resources, video frames that correspond to the speculated actions can be rendered and cached [257], ensuring reliable and real-time service.

IV.1.4 Selected mmWave-enabled Multi-user VR Scenarios

IV.1.4.1 Use Case 1: Interactive VR Gaming Arcade

In this first use case scenario that is investigated in Chapter IV.2, the joint use of communications, computing and caching techniques is investigated to assess the URLLC performance of a multiplayer VR gaming scenario. Such interactive and immersive experiences are known to require very low latency in order to synchronize the positions and interactions (input actions) of a group of players.

Specifically an indoor VR gaming arcade where VR players are equipped with wireless mmWave head-mounted VR displays, served by multiple mmWave band APs operating in 60-GHz indoor band is considered. In this scenario, players can move freely within the limits of individual VR pods, in which their movement in the physical space is tracked and mapped into the virtual space. Moreover, the interactiveness of group gaming is modeled through players' *impulse actions* that arrive at random during the game. These impulse actions may impact the game play and correspondingly affect the video frame content to be displayed to a given subset of the virtual reality players (VRPs).

The APs are connected to an edge computing network, consisting of multiple edge computing servers and a cache storage unit. The real-time tasks of generating users' HD frames based on the players' tracking data, which consists of their 6 degrees-of-freedom (6DoF) pose and gaming impulse actions, can be offloaded to the edge computing network. In addition to real-time computing, it is assumed that the MEC network is able to predict users' poses within a prediction window [242] to proactively compute and cache their upcoming video frames. A player can thus receive and display a proactively computed frame as long as no impulse action that impacts her arrives.

In this regard, an optimization framework to maximize the successful HD frame delivery subject to a probabilistic constraint on the frame delivery delay is proposed. First, a joint proactive computing and caching scheme is developed to render users' HD frames in the network edge. The proposed scheme schedules computing tasks following different priority levels, in which real-time computing is prioritized first in order to process current frames that are affected by randomly arriving game actions. Subsequently, subject to computing and storage resource constraints, the future HD frames that correspond to users' upcoming movement and head rotation and the estimated popular actions are proactively computed and cached. Following the computation of HD frames, a matching algorithm based on the DA matching is considered to allocate mmWave transmission resources to users.

In this scenario, the focus is set on the effect of computation delay in the edge servers and on the effect of the DL communication delay to deliver the computed HD frames.

IV.1.4.2 Use Case 2: The 360° VR Theater

The second use case scenario for mmWave-enabled multi-user VR, which is explored in Chapter IV.3, considers a VR theater with seats arranged in rows and columns. The VR users therein, all wearing mmWave HMDs, will choose to watch an HD 360° VR video from the set of available videos in the catalog. It is assumed that the HD video frames of these videos, owing to their large size and to the limited storage capacity in the HMDs, are cached in the edge network and are delivered to users through a set of SBSs distributed around the theater that are endowed with mmWave multi-beam beamforming capabilities.

The scenario is cast as a frame quality maximization problem subject to tight latency constraints and network stability. And the use of a deep-learning and clustering aided scheme for joint quality maximization and scheduling of video chunk requests to base stations is proposed such that the correlations in the predicted FoV and locations of viewers can be leveraged, and a proactive FoV-centric PHY-layer multicast transmission performed.

The problem is tackled through the Lyapunov framework to develop an online control method that does not require knowledge of the random processes in the optimization problem. Moreover this stochastic formulation enables to consider probabilistic constraints that can be further converted into virtual queues which, when stabilized, ensure the constraints are met with the desired probabilities. Indeed the queues' current backlog is considered as "sufficient statistics" on which the next control decision can be based upon. This alternative approach to enforce the probabilistic constraint, without having to resort to Markov's inequality to linearize it –the approach adopted in Use Case 1 as per Chapter IV.2–, is shown to be able to keep the latency bounded.

IV.1.5 Conclusions

In this introductory chapter to mobile VR the main requirements for an interconnected wireless VR, MR and AR have been discussed. The limitations of current VR applications have been highlighted and some of the key enablers to achieve the vision of future ultra-reliable and low latency VR presented. Among them, the use of mmWave communications is deemed an instrumental pillar together with MEC and proactive caching/scheduling approaches. Following that, the two use cases that will be covered in detail in the remaining two chapters of Part IV of the Thesis have been briefly presented: the interactive VR gaming arcade and the 360° VR theater.

Chapter IV.2

mmWave-Enabled Mobile VR: The Multi-user VR Gaming Arcade

IV.2.1 Introduction

Commercial 5G deployments are not expected to be available before 2020, however the race to showcase a first pre-standard 5G network is on. Hence, all eyes are set on how brand new services that promise to deliver entirely new experiences such as 360-degree immersive VR will be offered. However, multiple technical challenges need to be investigated to deal with the latency-sensitivity and the resource –communications and computing– intensiveness nature of 4K/8K ultra high definition (UHD) immersive VR wireless streaming and to realize the vision of interconnected VR [235].

To accommodate the extensive use of resource-hungry applications, it is foreseen that a 1000-fold boost will be needed in system capacity (measured in bps/km^2). This will be facilitated via an increased bandwidth, higher densification, and improved spectral efficiency. Zooming on the VR requirements, even anticipating the use of 265 HEVC 1:600 video compression rate, a bit rate of up to 1 Gbps [251] would be needed to match the 2x64 million pixel human-eye accuracy. These rates are unrealizable in 4G and challenging in 5G for a disruption-free immersive VR demands. Therefore significant research efforts around VR have focused on reducing bandwidth needs in mobile/wireless VR, thereby shrinking the amount of data processed and transmitted. Many approaches leverage head and eye-gaze tracking to spatially segment 360° frames and deliver in HD only user's FoV matching portion [242], [243]. Alternatively [244] considers a foveated 360° transmission where resolution and color depth are gradually reduced from fovea-centralis area to the peripheral FoV.

Latency is critical for VR; as it was elaborated in IV.1.2.2, the human eye needs to experience accurate and smooth movements with low (<20 ms) MTP latency. High MTP values send conflicting signals to the VOR, and might lead to dizziness or motion sickness. Both computing (image processing or frame rendering) and communication (queuing and over-the-air transmission) delays represent a major bottleneck in VR systems. As has been previously mentioned, heavy image processing requires high computational power that is often not available in the local HMD GPUs. Offloading computing significantly relieves the computing burden at the expense of incurring an additional communication

delay in the DL delivery of the processed video frames in full resolution. Moreover, to ensure responsiveness and real-time computing through minimal latency, computing servers should be readily available and located close to the end users.

VR demands a perceptible image-quality degradation-free uniform experience. However, temporary outages due to impairments in measured SINR are frequent in mobile/wireless environments. In this regard, an ultra-reliable VR service refers to the timely delivery of video frames with high success rate. Provisioning for a higher reliability pays a toll on the use of resources and allocating more resources for a single user could potentially impact the experienced latency of the remaining users.

Leveraging ubiquitous caching and computing at the wireless network edge will radically change the future mobile network architecture [258], and alleviate the current bottleneck for massive content delivery. Research ideas and network engineering geared toward exploiting 3C for future content-centric mobile networks are found in [240], [259], [260].

IV.2.1.1 Main Contributions

This chapter exploits the 3C paradigm to provide an enhanced wireless VR experience. To that end, it blends together the use of mmWave technology and mobile edge/fog computing MEC. The former seeks to deliver multi-Gbps wireless communication between VR headsets and network access points, with reliability guarantees, and the latter carries out advanced image processing, effectively offloading client displays or game consoles while satisfying stringent latency constraints. For ease of read, the main contributions of this chapter are next summarized:

Main Contributions

1. The total perceived delay to compute and deliver HD video frames to players is modeled with a focus on the effect of computation delay in the edge servers and on the DL communication delay.
2. An optimization problem is formulated that maximizes HD video frame delivery subject to latency constraints over the scheduling, caching, and computing matrices optimization variables.
3. After linearizing the probabilistic constraint on the latency, a novel joint proactive computing and mmWave resource allocation scheme that relies on Matching Theory is proposed to solve the problem above such that:
   (a) Reliability is ensured by leveraging MC to enhance the performance of users under channel variability with SFN techniques.
   (b) The proactive computing and user association are optimized to satisfy the latency requirements.
4. Extensive simulation results demonstrate significant gains in reducing the end-to-end delay under several millimeter wave access point (mmAP)-server configurations allowing to identify those configurations where either the communication delay or the computing delay become the bottleneck for the overall delay.

IV.2.1.2 Chapter Organization

The rest of this chapter is organized as follows. Section IV.2.2 describes the system model and problem formulation. The proposed joint computing and matching scheme is introduced in Section IV.2.3. Section IV.2.4 analyzes the performance of the proposed framework. Finally, Section IV.2.5 concludes the chapter.

IV.2.2 System Model and Problem Formulation

Consider an indoor, open plan, VR gaming arcade of dimensions $L \times W \times H$ m^3 where a set $\mathcal{A}$ of A mmWave band access points (mmAP) serves a set $\mathcal{U}$ of U VRPs equipped with wireless mmWave head-mounted VR displays (millimeter wave head mounted device (mmHMD)). VRPs are distributed and move freely within the limits of the R individual and $l \times l$ m^2 sized VR pods such that $R \geq U$. The movement of VRPs in the physical space of each VR pod is tracked and mapped into the virtual space. An illustration of the system model is shown in Fig. IV.2.1. The system operates in a time-slotted mode. The time slots are indexed by $t \in \{1, 2, \ldots\}$ with separate scales to account for scheduling decisions, and for beam alignment.

IV.2.2.1 Interactive VR Frame Rendering Model

A set $\mathcal{I}$ of impulse actions is defined as the actions generated during the interactive gaming either by the VRPs or an external trigger. The arrival of impulse action $m_i \in \mathcal{I}$ impacts the game play of a subset of VRPs $\mathcal{U}_i \subseteq \mathcal{U}$. In this regard, the impact of the impulse actions on the VRPs' game play, namely, the *impact matrix,* is defined as $\Theta = [\theta_{ui}]$, where $\theta_{ui} = 1$ if $u \in \mathcal{U}_i$, and $\theta_{ui} = 0$ otherwise. An example of such an impulse action would be for instance a player firing a gun in a shooting game; As the game play of a subset of players is affected by this action, for any of them a new computed video frame needs to be rendered again.

Mobile edge computing is used to provide the required computation capabilities. Accordingly, a fog network consisting of a set $\mathcal{E}$ of E edge servers with GPU computing capability c_e, and a storage unit of capacity S HD frames, will perform real-time VR environment building related computing[1] to generate HD interactive video frames based on the impulse actions of VRPs and on the real-time 6DoF pose, which is jointly given by the 3D location coordinates and the 3 orientation angles over the X, Y, and Z axes, namely the roll, pitch and yaw. Each VRP u is interested in receiving a unique F-tuple of HD video frames $(V_1^u, V_2^u \ldots, V_F^u)$ throughout its game play. To render an HD video frame, a processing density of κ GPU cycles per bit of frame data is required, with HD frame V_f^u having a data size of L_{fu}^{HD} bits.

In this context, mmAPs act as a two-way middleware between the mmHMDs and the edge servers in the fog network. mmAPs relay pose and action inputs from VRPs arriving through the glsul. After the HD frames are rendered, the mmAPs schedule mmWave time slots in the DL to deliver the resulting video frames. To ensure reliable DL transmission, MC is leveraged in which multiple

[1]The terms computing and rendering are used interchangeably throughout the chapter to describe the process of rendering HD video frames.

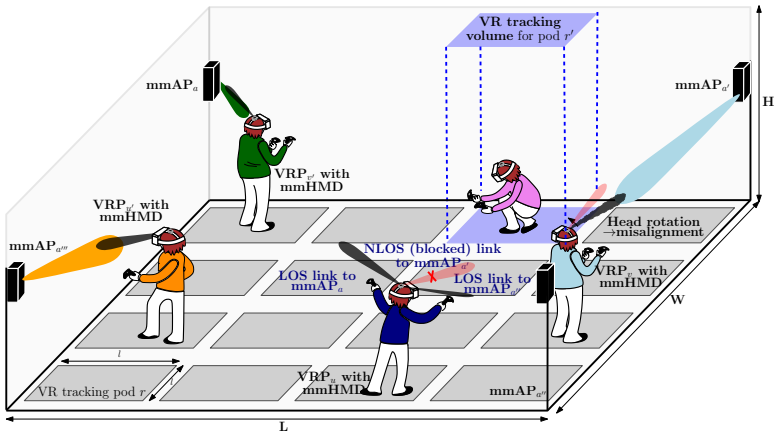

FIGURE IV.2.1: Open-plant VR gaming arcade with VRPs moving freely within their VR tracking pods and getting HD video frames from mmAP ([261] ©2018 IEEE).

mmAPs can jointly transmit the same data to a player with a weak link. Furthermore, to avoid motion sickness associated with high MTP delay, computing and scheduling decisions have to guarantee stringent latency constraints. Therefore, The fog network leverages the predictability of users' poses to proactively compute the upcoming HD video frames within a prediction window T_{w}. VRPs can receive and stream the proactively computed video frames as long as they are not affected by impulse actions arriving afterwards. The proactive computing time dynamics are depicted in Fig. IV.2.2. Moreover, edge servers exploit their idle times to proactively render and cache the HD frames of users affected by the popular impulse actions, such that the computing latency is minimized. Finally, it is assumed that a low quality (LQ) version of the video frame, with data size $L_{fu}^{\text{LQ}} \ll L_{fu}^{\text{HD}}$, can be processed locally in the mmHMD to ensure smooth game play if the HD video frame cannot be delivered on time.

IV.2.2.2 mmWave Communication Model

The mmWave channel is based on measurement results of LOS and non-line-of-sight (NLOS) paths for the 60-GHz indoor channels [262], and includes both pathloss attenuation l_{au} and small Nakagami fading with coefficient $g_{au}(t)$. The channel gain h_{au} from mmAP a to mmHMD in VRP p is thus given by $h_{au}(t) = l_{au}g_{au}(t)$. The pathloss ℓ_{au} is considered LOS when $\nexists$ VRP $u' \in \mathcal{U}\backslash u$ such that the area defined by the d-diameter circle associated to its head+mmHMD intercepts the ray traced from mmAP a to mmHMD receiver of VRP u; the path is considered NLOS otherwise[2]. Neither external interference leakage into the finite area of the arcade nor reflections due to walls, ceiling or the VRPs themselves are explicitly incorporated in the channel model. They are only accounted for in a coarse way through the different LOS and NLOS parameters. Accordingly, the pathloss exponent α_{au} in l_{au} will take value α_L if the link from mmAP a to the mmHMD receiver u is LOS and value α_N otherwise.

[2]Capturing the blockage arriving from game-engagement related limb movements VRPs raising their hands and blocking their own or some other mmWave link is left for future work.

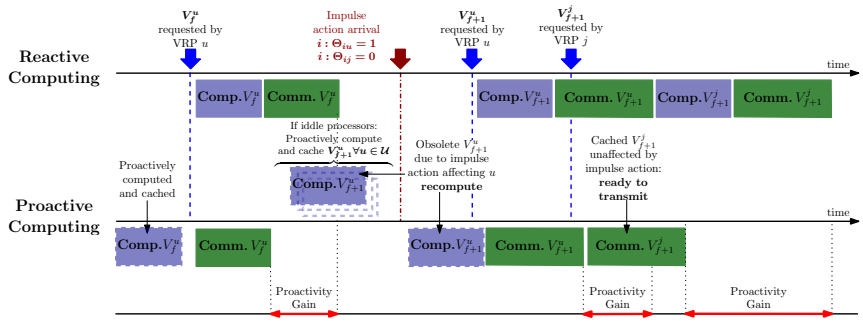

FIGURE IV.2.2: Time dynamics for reactive and proactive computing ([261] ©2018 IEEE).

Similarly, the corresponding Nakagami shape factor m_{au} will take value m_L for LOS and m_N for NLOS paths; it is further assumed that $g_{au}(t)$ is i.i.d. and not temporally correlated.

For tractability, the radiation pattern of actual directional antennas is approximated with a 2-dimensional (2D) sectored antenna model [35]. Let us denote $g_{au}^{\mathrm{Tx}}(\varphi_a, \theta_{au}^{\mathrm{Tx}}(t))$ and $g_{au}^{\mathrm{Rx}}(\varphi_u, \theta_{au}^{\mathrm{Rx}}(t))$ the transmission and reception antenna gains from mmAP a to the mmHMD of VRP u as given by

$$g_{au}^{\measuredangle}(\varphi_a, \theta_{au}^{\measuredangle}(t)) = \begin{cases} \frac{2\pi-(2\pi-\varphi_a)g_{\lhd}}{\varphi_a}, & |\theta_{au}^{\measuredangle}(t)| \leq \frac{\varphi_a}{2}, \\ g_{\lhd}, & \text{otherwise}, \end{cases} \tag{IV.2.1}$$

with $\measuredangle \in \{\mathrm{Tx}, \mathrm{Rx}\}$, and where $\theta_{au}^{\measuredangle}(t)$ stands for the angular deviation from the boresight directions, and $g_{\lhd}$ is the constant sidelobe gain with $g_{\lhd} \ll 1$.

High directionality of mmWave communications motivates a search process to find the boresight directions corresponding to the best path between the mmAP and the mmHMD and take full advantage of beamforming gains as per (IV.2.1). To that end and recalling the procedures detailed in I.1.1.3.1, each of the A mmAPs will periodically and sequentially perform beam training with the $|\mathcal{U}_a|$ VRPs within it coverage area, $\mathcal{U}_a \subset \mathcal{U}$. After the best steerings for all feasible VRPs have been learned, and following a transmission interval level VRP scheduling decision, data transmission begins.

The analog beamformers on the mmAPs and VRPs sides are determined after a two-stage beam training process [44]. Let $=\{_{1,2}, \cdots, _A\}$ denote the vector of alignment delays for the A mmAPs in the system, then on an *a priori* knowledge of mmAPs fixed location and of VRPs sector –a reasonable assumption due to highly accurate and frequent VRP location tracking and to the slowness of human movement at ms scale– the experienced alignment delay due to beam training is $\tau_{au}^{\mathrm{Align}} = \frac{\psi_a}{\varphi_a} T_p$, where T_p is the pilot symbol transmission time and ψ_a, φ_a denote the sector-level and beam-level beamwidths for mmAP a. The overall alignment delay is $\tau^{\mathrm{Align}} = \sum_{a\in\mathcal{A}} \sum_{u\in\mathcal{U}_a} \tau_{au}^{\mathrm{Align}}$.

To overcome vulnerability to channel intermittency due to blockage and misalignment, mmHMDs are assumed to be capable of leveraging MC implemented through coordinated joint transmission of VR player data from multiple mmAPs. An indicator variable $x_{au}(t)$ is therefore defined if mmAP a schedules VRP u at time instant t. The maximum achievable rate for mmHMD u is given by

$$r_u(t) = \left(1 - \tau^{\mathrm{Align}}\right) BW \log_2\left(1 + \mathrm{SINR}_u(t)\right), \tag{IV.2.2}$$

$$\mathrm{SINR}_u(t) = \frac{\sum_{\forall a \in \mathcal{A}} x_{au}(t) p_a h_{au}(t) g^{\mathrm{Tx}}_{au}(t) g^{\mathrm{Rx}}_{au}(t)}{\sum_{\forall a' \in \mathcal{A}} (1 - x_{au}(t)) p_{a'u} h_{a'u}(t) g^{\mathrm{Tx}}_{a'u}(t) g^{\mathrm{Rx}}_{a'u}(t) + N_0 BW}, \quad \text{(IV.2.3)}$$

where the achievable SINR term should, in addition to the effective received power at mmHMD u from mmAPs $a : x_{au}(t) = 1$ and to Gaussian noise, account for the effect of other interfering mmAPs $a' : x_{a'u}(t) = 0$ through channel and antenna gains, $h_{a'u}(t)$ and $g^{\mathrm{Tx}}_{a'u}$, $g^{\mathrm{Rx}}_{a'u}$ respectively.

IV.2.2.3 Problem Formulation

To pose the subsequent optimization problem, the focus is set on the joint effect of the computation delay experienced in the edge servers and of the DL communication delay to transmit the HD video frames from the mmAPs to the VRPs, i.e., the access to the backhaul is assumed to be wired. Under these assumptions, let the computing delay $\tau^{\mathrm{Comp}}_{uf}$ of a the video frame f corresponding to user u be expressed as

$$\tau^{\mathrm{Comp}}_{uf}(t) = \left(\frac{\kappa L^{\mathrm{HD}}_{fu}}{c_e} + W_{uf}(t) \right) z_{fu}(t)(1 - y_{fu}(t)), \quad \text{(IV.2.4)}$$

where c_e is the computation capability of edge server e, $z_{fu}(t)$ and $y_{fu}(t)$ indicate that the video frame f of user u is scheduled for computing, and is cached in the fog network at time instant t, respectively, and W_{uf} is the computation waiting time of HD frame f of user u in the service queue, defined as $Q(t)$.

Furthermore, let the communications delay $\tau^{\mathrm{Commun}}_{uf}$ associated to transmitting a video frame f to a u be defined as

$$\tau^{\mathrm{Commun}}_{uf}(t) = \arg\min_{d_u} \sum_{t' = \tau^{\mathrm{Comp}}_{uf}(t)+1}^{\tau^{\mathrm{Comp}}_{uf}(t)+d_u} \left(T_t r_u(t') \geq L^{\mathrm{HD}}_{fu} \right), \quad \text{(IV.2.5)}$$

where the arg min function is to find the minimum number of time slots needed for the video frame f to be delivered.

The total perceived delay to compute and deliver an HD video frame is expressed as the sum of both delay components, that is

$$D_{uf}(t) = \xi_{fu} \left(\tau^{\mathrm{Comp}}_{uf}(t) + \tau^{\mathrm{Commun}}_{uf}(t) + \tau^{\mathrm{Edge}} \right), \quad \text{(IV.2.6)}$$

where ξ_{fu} is a binary function that equals 1 when the HD video frame is delivered to VRP u and equals 0 if the LQ frame is delivered, $\tau^{\mathrm{Comp}}_{uf}$ and $\tau^{\mathrm{Commun}}_{uf}$ are the computing and communication delays of HD frame f initiated from user u respectively given as per (IV.2.4), (IV.2.5), and τ^{Edge} is the processing latency which accounts for the edge server processing, storage processing and the UL transmission of user pose and action data.

The objective of the proposed approach is to maximize the HD video frame delivery $\boldsymbol{\xi} = [\xi_{fu}]$ subject to latency constraints. The optimization variables are the scheduling, caching, and computing matrices, expressed as $\boldsymbol{X}(t) = [x_{ua}(t)]$, $\boldsymbol{Y}(t) = [y_{fu}(t)]$, and $\boldsymbol{Z}(t) = [z_{fu}(t)]$ respectively. The optimization problem is cast as follows:

$$\max_{\boldsymbol{X}(t), \boldsymbol{Y}(t), \boldsymbol{Z}(t)} \sum_{u=1}^{U} \sum_{f=1}^{F} \xi_{fu} \quad \text{(IV.2.7a)}$$

$$\text{subject to} \quad \Pr(D_{uf}(t) \geq D_{\mathrm{th}}) \leq \epsilon, \forall f \in \mathcal{F}, \forall u \in \mathcal{U}, \quad \text{(IV.2.7b)}$$

$$\sum_{u=1}^{U} x_{ua}(t) \leq 1, \ \forall a \in \mathcal{A}, \tag{IV.2.7c}$$

$$\sum_{u=1}^{U} \sum_{f=1}^{F} y_{fu}(t) \leq S \ , \tag{IV.2.7d}$$

$$\sum_{u=1}^{U} \sum_{f=1}^{F} z_{fu}(t) \leq E, \tag{IV.2.7e}$$

where (IV.2.7b) is a probabilistic delay constraint that ensures the communication latency is bounded by a threshold value D_{th} with probability $1-\epsilon$. Constraint (IV.2.7c) ensures that mmAP serves one VRP at a time. (IV.2.7d) limits the number of cached frames to a maximum of S. Constraint (IV.2.7e) is over the maximum number of simultaneous computing processes.

The above is a combinatorial problem with non-convex cost function and probabilistic constraints, for which finding an optimal solution is computationally complex [263]. The non-convexity is due to the interference from other mmAPs in the rate term in the delay equation. To make the problem tractable, the use the Markov's inequality [263] is adopted to convert the probabilistic constraint in (IV.2.7b) to a linear constraint expressed as $\mathbb{E}\{D_{uf}(t)\} \leq D_{\text{th}}\epsilon$. Hence, it can be rewritten as

$$\mathbb{E}\left[\tau_{uf}^{\text{Comp}}(t) + \tau_{uf}^{\text{Commun}}(t)\right] = \mathbb{E}\left[\tau_{uf}^{\text{Comp}}(t)\right] + \mathbb{E}\left[\tau_{uf}^{\text{Commun}}(t)\right] \leq D_{\text{th}}\epsilon. \tag{IV.2.8}$$

The expectation in (IV.2.8) is hard to calculate due to having the arg min function in the $\tau_{uf}^{\text{Commun}}(t)$. Consequently, the second expectation is rewritten in terms of $\bar{r}_u(t)$, the time-average service rate of VRP u from mmAP p at time instant t, expressed as $\bar{r}_u(t) = \sum_{\tau=1}^{t} r_a(\tau)$, which leads to $\mathbb{E}\{\tau_{uf}^{\text{Commun}}(t)\} = L_{fu}^{\text{HD}}/T_t\bar{r}_u(t)$. Thus, the URLLC constraint can be recast as

$$\frac{L_{fu}^{\text{HD}}}{T_t\bar{r}_u(t)} + \frac{\kappa L_{fu}^{\text{HD}}}{c_e} + \mathbb{E}\left[W_{uf}(t)\right] \leq D_{\text{th}}\epsilon. \tag{IV.2.9}$$

Similarly, the average waiting time can be expressed as

$$\mathbb{E}\left[W_{uf}(t)\right] = \sum_{i|V_f^i \in Q(t)} \frac{L_{fi}^{\text{HD}}}{T_t\bar{r}_i(t)},$$

and, thus, (IV.2.9) rewritten as

$$\frac{L_{fu}^{\text{HD}}}{T_t\bar{r}_u(t)} \leq D_{\text{th}}\epsilon - \sum_{V_f^i \in Q(t)} \frac{L_{fi}^{\text{HD}}}{T_t\bar{r}_i(t)} - \frac{\kappa L_{fu}^{\text{HD}}}{c_e}. \tag{IV.2.10}$$

The average rate $\bar{r}_u(t)$ can be separated into the instantaneous time rate at time instant t and the average rate in the previous time instants that can be online estimated, i.e.,

$$\bar{r}_u(t) = \sum_{\varrho=1}^{t} r_u(\varrho) = r_u(t) + \sum_{\varrho=1}^{t-1} r_u(\varrho). \tag{IV.2.11}$$

In other words, to reach the desired latency requirement, a maximum value of the left-hand side term in (IV.2.10) that satisfies the above formula should be guaranteed to admit a request to an mmAP.

Next, a joint VRP-mmAP matching and scheduling scheme is proposed to solve the optimization problem in (IV.2.7).

IV.2.3 Joint Proactive Computing and Matching

As stated above, the optimization problem in (IV.2.7) is computationally hard to solve. Thus it is decoupled into two subproblems of computation scheduling and VRP association.

IV.2.3.1 Computing and Caching Scheme

During the game play, the edge computing network minimizes the computing service delay by leveraging the pose prediction of users to proactively compute their HD video frames as well as caching the updated HD video frames resulting from randomly arriving impulse actions. In the case that impulse action arrives in which the corresponding frames for the affected users are not computed, the real time computing is giving the highest priority. Therefore, an algorithm comprising three priority levels is proposed to schedule HD frame computing of users. The detailed algorithm is described in Algorithm IV.2.1.

IV.2.3.2 Player-Server Matching

Our next step is to propose a VRP-mmAP association scheme that solves the constrained minimization problem in (IV.2.7). The association problem is formulated as a matching game [131] between the mmAPs and the VRPs as described in II.1.2. In this game, VRPs seek to maximize their VR experience by competing for mmWave time slots from different mmAPs. Whenever a player in the network requests a new HD frame, a new set of matching pairs is found using the proposed approach. The matching game consists of a two sets of players and mmAPs, where each member of one set has a preference profile over the members of the other sets. Preferences of mmAPs and players are denoted by $\succ_a$ and $\succ_u$, and reflect how each member of a set ranks the members of the other set.

Algorithm IV.2.1: Real-time vs. Predictive Computing and Caching priority algorithm ([261] ©2018 IEEE).

Implementation at each time instant t:
Repeat find v = vacant cloudlet
Priority one: real-time scheduling
find u where $V_f^u(t)$ is not computed
$v \rightarrow$ *allocated*, $z_{fu}(t) \rightarrow 1$
Priority two: predictive computing and caching
Find u and t' where $t' \in (t : t + T_{\mathrm{w}})$ and $V_f^u(t')$ is not computed
$v \rightarrow$ *allocated*, $z_{fu}(t) \rightarrow 1$
compute and cache $V_f^u(t')$
Priority three: predictive impulse computing and caching
Sort $\mathcal{I}$ by popularity
Repeat Select i as the most popular $\mathcal{I}$
find u:$\theta_{u,i} = 1$
$v \rightarrow$ *allocated*, $z_{fu}(t) \rightarrow 1$
compute and cache $V_f^u(t+1)$
Until at least one of the following conditions is true
- no vacant cloudlets
- cache is full
- upcoming frames of impacted users from all $\mathcal{I}$ are computed

Definition 13. *Given two disjoint sets of mmAPs and players* $(\mathcal{A},\mathcal{U})$*, a* matching *is defined as a* one-to-one *mapping* Υ *from the set* $\mathcal{E}\cup\mathcal{U}$ *into the set of all subsets of* $\mathcal{A}\cup\mathcal{U}$*, such that for each* $a\in\mathcal{A}$ *and* $u\in\mathcal{U}$*:*

1. $\forall u\in\mathcal{U},\Upsilon(u)\in\mathcal{A}\cup u$, where $\Upsilon(u)=u$ means that a player is not associated to a remote server, and will perform local LQ frame processing.
2. $\forall a\in\mathcal{A},\Upsilon(a)\in\mathcal{U}\cup\{a\}$, where $\Upsilon(a)=a$ means that the mmAP a have no associated players.
3. $\mid\Upsilon(u)\mid=1,\mid\Upsilon(a)\mid=1;\ \ 4)\Upsilon(u)=a\Leftrightarrow\Upsilon(a)=u.$

By inspecting the problem in (IV.2.7), it can be seen that the one-to-one mapping of the matching game satisfies the constraint (IV.2.7c). Moreover, since preference profiles can be defined to capture the cost function of the matching sets. The utility of the mmAPs will essentially reflect the latency constraint in (IV.2.10). Therefore, the utility of associating player u to mmAP a is defined as

$$\Phi_{au}(t)=D_{\text{th}}\epsilon-\sum_{i|V_f^i\in Q(t)}\frac{L_{fi}^{\text{HD}}}{T_t\bar{r}_i(t)}-\frac{\kappa L_{fu}^{\text{HD}}}{c_e}-\frac{L_{fu}^{\text{HD}}}{T_t\bar{r}_u(t)},\tag{IV.2.12}$$

and the mmAP preference as:

$$u\succ_a u'\Leftrightarrow\Phi_{au}(t)>\Phi_{au'}(t),\ a\succ_a u\Leftrightarrow\Phi_{au}(t)<0,\tag{IV.2.13}$$

where the second preference states that a mmAP is not interested in matching to a player that will violate its latency constraint. In other words, the utility of each cloudlet is to seek a matching that maximizes the difference between the right hand side and the left hand side of the inequality in (IV.2.10), such that the constraint is met as a stable matching is reached. To meet the players' reliability target, the preference profiles of the players is defined as to maximize their link quality as follows:

$$a\succ_u a'\Leftrightarrow|h_{au}(t)|^2g_{au}^{\text{Tx}}(t)g_{au}^{\text{Rx}}(t)<|h_{a'u}(t)|^2g_{a'u}^{\text{Tx}}(t)g_{a'u}^{\text{Rx}}(t).\tag{IV.2.14}$$

Since users may not always find a single reliable link, it is proposed to split the users that are matched but with an SINR below a predefined threshold γ^{Th} into multiple players, so that they can be matched to multiple mmAPs and satisfy their link reliability requirements subject to mmAP availability.

Next, matching stability is defined and an efficient multi-stage algorithm based on deferred-acceptance (DA) [126] to solve it. The details of this algorithm were described in Section II.1.2 of Chapter II.1, here the terminology has been adapted to match that of the problem at hand.

Definition 14. *Given a matching* Υ *with* $\Upsilon(a)=u$ *and* $\Upsilon(u)=a$*, and a pair* (u',a') *with* $\Upsilon(a)\neq u'$ *and* $\Upsilon(u)\neq a'$*,* (u',a') *is said to be blocking the matching* Υ *and form a blocking pair if: 1)* $u'\succ_a u$*, 2)* $a'\succ_u a$*. A matching* $\Upsilon*$ *is stable if there is no blocking pair.*

Remark *1. The algorithm described in Algorithm IV.2.2, converges to a two-sided stable matching of players to mmAPs or to their local servers [126].*

IV.2.4 Simulation Setup and Performance Evaluation

In this section, the effectiveness of the proposed solution is numerically validated and the proposed approach is compared against two benchmark schemes:

Algorithm IV.2.2: VR Player-mmWave AP Matching Algorithm ([261] ©2018 IEEE).

Initialization: all players and mmAPs start unmatched.
Each mmAP constructs its preference list as per (IV.2.13)
Each player constructs its preference list as per (IV.2.14)
repeat an unmatched player u, i.e., $\Upsilon(u) = \phi$ proposes to its most preferred mmAP a that satisfies $a \succ_u u$
  if $\Upsilon(a) = \phi$, %not yet matched
    $\Upsilon(a) = u$, $\Upsilon(u) = a$. %player u proposal is accepted
  else %matched to $u' \rightarrow \Upsilon(a) = u'$
    if $u' \succ_a u$ %player u proposal is rejected
      player u removes mmAP a from its preference list
    else %player u proposal is accepted
      $\Upsilon(a) = u$,$\Upsilon(u) = a$, $\Upsilon(u') = \phi$
      player u' removes mmAP a from its preference list
    end if
  end if
  if $\gamma_u < \gamma^{\mathrm{Th}}$
    split u into two players u_1 and u_2, $\Upsilon(u_2) = \phi$
  end if
until all players are either matched with $\gamma_u \geq \gamma^{\mathrm{Th}}$ or not having mmAPs that satisfy $a \succ_u u$ in their preference lists
Output: a stable matching Υ

1. *Baseline 1*, with neither MC nor proactive computing and caching. Requests are computed in real time after they are initiated, and are transmitted through single-connectivity links.
2. *Baseline 2*, without MC, but assumes proactive computing and caching capabilities.

Let a gaming arcade with a capacity of 8×8 VR pods and a set of default parameters be considered. Specifically, 100 impulse actions that arrive following the Zipf popularity model [264] with parameter z are enforced. Accordingly, the arrival rate for the i^{th} most popular action will be proportional to $1/i^z$. In this chapter, $z = 0.8$ is assumed. Moreover, a uniformly distributed impact matrix $\boldsymbol{\theta}$, $D_{\mathrm{th}} = 100$ ms $\epsilon = 0.1$, 10 dBm mmAP transmit power, $L_f^{\mathrm{HD}} = \sim \exp(2)$ Gbit, $\kappa/c_e = 5 * 10^{-8}$, $S/A = 20$ video frames, and $T_{\mathrm{w}} = 100$ ms are also adopted.

IV.2.4.1 Impact of the Number of Players

First, the latency performance of the proposed approach is investigated as the number of players increases. To that end, the number of mmAPs and servers is initially fixed to 4 mmAP and 8 respectively. Furthermore, for each user a rate requirement of 2 Gbps is set. Fig. IV.2.3 compiles the average and the 99^{th} delay performance when $D^{\mathrm{th}} = 20$ ms and $\epsilon = 0.01$ are selected to reflect the motion sickness limit. A close look to Fig. IV.2.3, clearly reveals that the proposed approach minimizes significantly the service delay under different network conditions. Moreover, by inspecting the 99^{th} percentile communication delay, the proposed scheme is found to outperform the proactive Baseline 2 scheme by leveraging MC to minimize the latency of wireless frame delivery.

Secondly, a similar approach is adopted to corroborate the above results when both the number of mmAP and servers is set to 16. Fig. IV.2.4(a), presents the average and the 90^{th} percentile communication delay ($\tau_{uf}^{\mathrm{Commun}}$ 90 percentile) for different schemes, which all increase with the network density. This is due

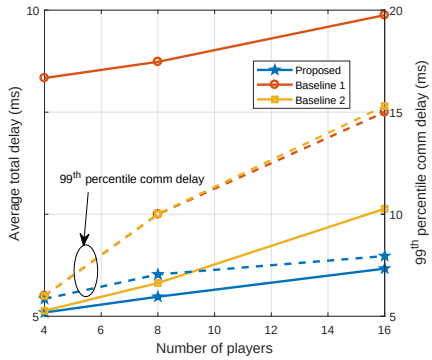

FIGURE IV.2.3: Average delay and 99$^{\text{th}}$ percentile communication delay performance as the number of players varies, with 4 mmAPs and 8 MEC servers. The 99% confidence level margin of error (ME) is $0.01088 \leq \text{ME} \leq 0.0208$ ms for all configurations above.([251] ©2018 IEEE).

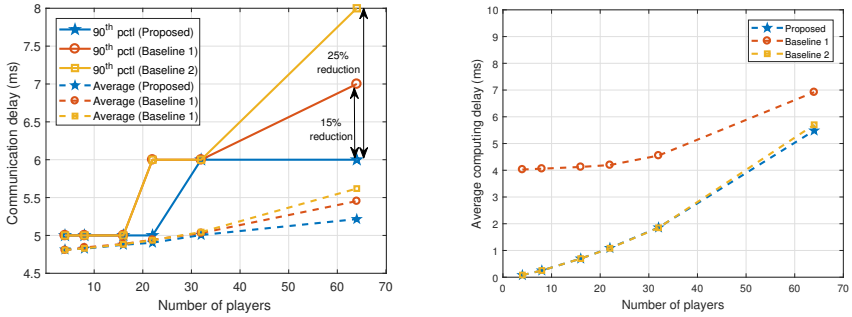

(A) (B)

FIGURE IV.2.4: (a) Average and 90th percentile communication delay versus number of players, for 16 mmAPs. (b) Average computing delay versus number of players, for 16 multi-access edge computing (MEC) servers. ([261] ©2018 IEEE)

to the increase in offered load, as compared to the network capacity, and the higher levels of interference. As the number of players increases, the proposed approach achieves up to 25% reduction in the $\tau_{uf}^{\text{Commun}}$ 90 percentile, due to the MC gain that allows users with weak links to receive from multiple servers. This reduction is more evident in dense network conditions associated with high interference/blockage levels. Fig. IV.2.4(b), displays how an increase in the number of players affects the average computing. Being to leverage proactivity to cut down the rendering latency, both the proposed approach and Baseline 2 achieve a significant reduction in the computing delay.

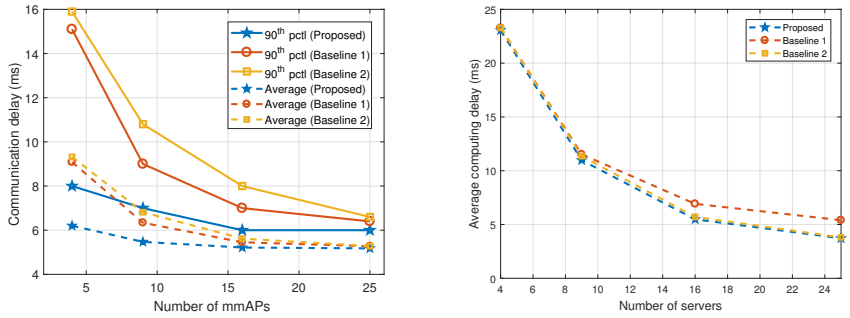

(A) (B)

FIGURE IV.2.5: (a) Average and 90^{th} percentile communication delay versus number of mmAPs, for 64 players. (b) Average computing delay versus number of servers, for 64 players ([261] ©2018 IEEE)

IV.2.4.2 Impact of the Number of mmAPs and Servers

Next, the performance of the proposed approach as the number of mmAPs and servers increase is investigated. To that end, the number of VR players is fixed to the maximum of the gaming arcade capacity i.e., 64. It is further assumed that the number of servers in the fog network also matches the number of mmAPs. First, Fig. IV.2.5(a) shows the average and $\tau_{uf}^{\text{Commun}}$ 90 percentile communication delay performance. Intuitively, a low number of mmAPs will incur higher communication delay due to having higher offered load than what the mmAPs can serve. However, it is observed that at low number of mmAPs, the average delay can be reduced by up to 33% whereas the $\tau_{uf}^{\text{Commun}}$ 90 percentile can be halved by using the proposed approach.

Finally, Fig. IV.2.5(b), shows the computing and communication delay performance. It can be seen that, at low number of servers, the computing delay is always high, due to not having enough computing resources to serve the high number of players. The network can hardly serve the real-time computing requests, leaving no room for proactive computing. Accordingly, higher number of servers are needed to achieve proactive computing gains.

IV.2.4.3 Reliability/Latency and Service Rate Trade-off

Before investigating how other elements such as the cache size and the degree of dynamicity of the play impact on the latency performance, the trade-offs between reliability, latency and service rate performance of the proposed scheme are probed and thereafter illustrated in Fig. IV.2.6. The results therein have been gathered by varying the latency threshold, while setting $\epsilon = 0.01$ and the number of players to 16. Reliability is then measured as the probability of experiencing a communication delay below a threshold of 10 ms. The aforementioned trade-off between the user data rate and the reliability and communication latency is disclosed as Fig. IV.2.6. This figure clearly confirms that imposing stringent latency constraint guarantees achieving high reliability by serving requests with

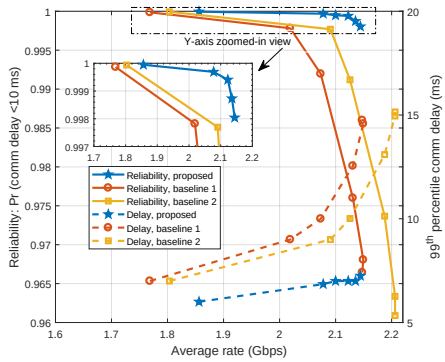

FIGURE IV.2.6: The trade-offs between reliability performance (in terms of ratio of frames delivered within a given delay threshold), average service rate, and 99th percentile communication delay, with 4 mmAPs, 8 MEC servers, and 16 VRPs.([251] ©2018 IEEE).

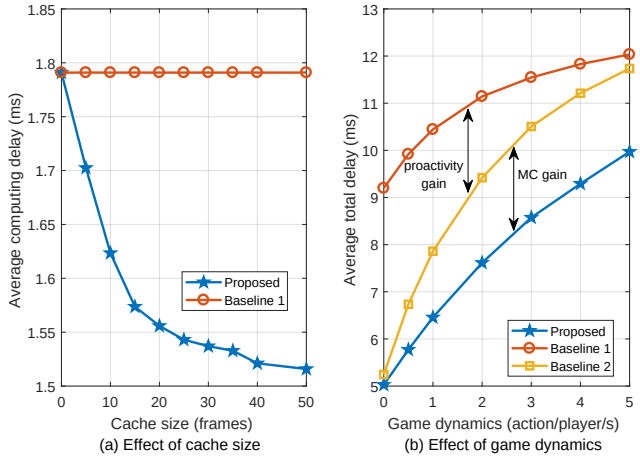

FIGURE IV.2.7: Average delay performance. (a) Average computing delay as the cache size increases, with 4 mmAPs, 8 MEC servers, and 8 VRPs; for all cache sizes and solution configurations above, ME for computing delay is $0.02005 \leq \text{ME} \leq 0.02470$ ms. (b) Average total delay as the game traffic dynamics increase, with 4 mmAPs, 8 MEC servers, and 16 VRPs; for all considered game dynamics and solutions above, ME of the average total delay is $0.00651 \leq \text{ME} \leq 0.02469$ ms.([251] ©2018 IEEE).

tight delay bounds. However, this comes at the expense of experiencing lower service rate and hence, lower frame quality.

IV.2.4.4 Impact of the Network Conditions

Finally, Fig. IV.2.7 compares the total delay performance of the proposed scheme against the reactive and proactive baseline schemes under different network conditions. Specifically, Fig. IV.2.7(a) showcases that as the cache size increases,

the average computing delay is significantly reduced. This reduction is motivated by the availability of enough storage to cache more HD frames following popular game actions, which minimizes the computation delay as compared to the reactive baseline scheme.

The effect of both proactivity and MC on the delay performance is also evident from Fig. IV.2.7(b), where the total VR service delay is plotted against the game dynamics, defined as the impulse action arrival intensity (action per player per second). For all schemes, higher delay values are experienced as the game dynamics increase, due to being enforced to process more frames in real-time. Yet, the proposed scheme is shown to leverage both proactivity and MC to minimize the service delay in different gaming traffic conditions.

IV.2.5 Conclusions

In this chapter, the problem of ultra-reliable and low latency wireless multi-user VR gaming networks has been studied. A joint proactive computing and user association scheme is proposed in mmWave enabled VR for interactive gaming. In the proposed scheme, information about the game players' upcoming pose and game action is leveraged to proactively render their HD video frames such that computing latency is minimized. To ensure reliable and low latency communication, a matching algorithm has been proposed to associate players to mmAPs and enable multi-connectivity, in which multiple mmAPs jointly transmit the video frames to players to overcome the effect of channel variability. Simulation results have shown that the proposed scheme achieves significant reduction in both computing and communication latency under different network conditions, when compared to different baseline schemes.

Chapter IV.3

mmWave-Enabled Mobile VR: The 360° VR Theater

IV.3.1 Introduction

VR reality is expected to revolutionize how humans interact and perceive media by inducing artificial sensory stimulation to the brain and immersing them into an alternative world [235]. Yet, as explained in the previous chapters, for true engagement to succeed, the end-to-end latency or MTP delay needs to be kept below 15-20 milliseconds. Otherwise VR sickness also known as *cyber-sickness* –a phenomenon similar to motion sickness due to the exposure to low quality or delayed VR content– might ruin the experience.

For this reason, high-end VR manufacturers have been long compelled to using wired connections between HMDs and VR servers with high processing and storage capabilities. However, this constraint physically limits the movement of VR users and hence, degrades the QoE, thereby calling for further development of mobile/wireless solutions that are able to provide both convenience and a high-quality VR. Moreover, as access to social VR experiences surges, driven by location-based VR and 360° formats, the gap between the available bandwidth and the prohibitively high demands by mobile immersive VR is likely to prevail. Clearly, disruptive content provisioning paradigms are needed to unleash the plethora of new business opportunities for leisure/entertainment industry that mobile interconnected VR will bring.

In this context, mobile VR spearheads the newly coined highly reliable low latency broadband (HRLLBB) use cases sitting across eMBB and URLLC service categories in 5G networks [251] . The distinctive feature of HRLLBB, if compared to URLLC [74], is the need to reliably provide massive data delivery to multiple users with low-latency.

Focusing on omnidirectional 360° or spherical video format [265] and reducing its bandwidth consumption, video coding solutions that adapt the streaming to users' attention by tracking their visual region of interest are abundant in the literature. Their common goal is to stream in HD[1] only users' *viewports*, i.e., the portion of sphere in a user's FoV while wearing an HMD, and, optionally, in lower quality the rest. To do so, foveated, tile-based and projection/viewport-based FoV-streaming are the most commonly adopted approaches, all requiring real-time tracking of either users' eye-gaze or head angles i.e., the 3 degrees-of-freedom (3DoF) pose expressed by yaw, pitch and roll angles as represented in

[1] In the context of 360°, 4K is widely viewed as the minimum resolution in current HMDs, and ideally 8K or higher is desired.

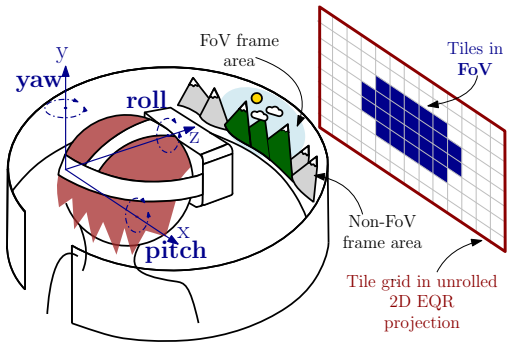

FIGURE IV.3.1: Tiled-FoV mapping of a user's 3DoF pose in the equirectangular (EQR) projection of a 360° video frame. ([271] ©2020 IEEE)

Fig. IV.3.1. Foveated solutions as per [244], [266] are conditioned to availability of advance eye-gaze tracking mechanisms in the HMDs and real-time frame rendering in the servers, whereas for tile and viewport-based solutions, regular head-tracking is enough. The main drawback of projection-streaming [267] lies in its large server storage needs, given that for each frame multiple viewpoints are kept. Lastly, in tile-based streaming approaches as per [242], [268]–[270], the video frame is divided in a grid of regular tiles, which will each be encoded in both HD and at a lower resolution. Then, only the tiles within a user's FoV region are streamed in HD.

Real-time tile-based FoV streaming to a network of VR users involves a number of time-consuming steps: edge controllers/servers need to first acquire pose data, process it to compute the set of tiles within the FoV and lastly schedule their transmission. Then, on-HMD processing will be performed to compose –*stich*–and display the corresponding portion of the video frame. The end-to-end delay of the process in non-negligible. Thus, as the number of users in the network increases, operating this cycle within the MTP delay budget for each frame for every user becomes challenging; even more so if the server/edge controllers and users are not wired.

The latter realization calls for unconventional solutions at different network levels. Among them, the use of proactive transmission of FoV tiles –contingent on the availability of prediction results on the FoV for the upcoming frames– can significantly improve the efficiency of content delivery even with non-perfect prediction accuracy, especially in fluctuating channel environments, as illustrated by the following numerical example:

Let on average for each 360° video frame the FoV provided by the HMD of a given VR user have a total of 32 tiles, and the tile size be 1 Mb. This means that without proactivity, a rate budget of 32 Mb on each frame transmission interval is needed to fully deliver the user's FoV tiles. Let assume that the user's rate budget in the transmission period of two subsequent frames f_1 and f_2 be 70 Mb and 10 Mb, respectively which inevitably would lead to an outage in the second frame. Assume now that during the transmission period of frame f_1, the SBS predicts the user's future FoV for frame f_2 with an accuracy of 75%, i.e., 24 tiles out of the 32 are correctly predicted. Then, using a proactive transmission, the SBS could deliver during the first transmission period the 32 tiles of frame f_1 and the predicted 32 tiles of frame f_2. Once the second transmission period starts and the user reports its actual FoV for frame f_2, the SBS would have to transmit only the remaining 25% of the FoV, i.e., 8 tiles, which the user's rate budget allows handling without experiencing any outage.

IV.3.1.1 Related Work

The need for predicting users' fixation opens the door for harnessing ML in wireless systems [272]. Moreover, public availability of extensive pose and saliency datasets for 360° video equips an invaluable input to optimize VR content streaming through supervised and unsupervised deep learning applied to FoV prediction. To that end, *content-based* [273] or *trajectory-based* [242], [274] strategies can be adopted: the former try to mimic human capacity to detect the most salient regions of an upcoming video frame i.e., its point of interests (PoIs), and predominantly rely on convolutional neural networks (CNNs) to do so. The latter strategies, track head (or eye-gaze) movement of VR users through their HMDs and largely rely on the use of recurrent neural networks (RNNs). However, due to the distinctive nature of 360° videos, the use of content-based information alone might not be suitable since the PoIs in a video frame might fall out of a user's current FoV and not affect the viewing transition [275]. Similarly, both having several PoIs or none within the FoV might be problematic. Nevertheless, the availability of proper video saliency, could strongly improve the accuracy of the head movement prediction by combining saliency-based head movement prediction with head orientation history, as exemplified by [276]–[279].

Recently deep reinforcement learning (DRL) i.e., the hybridization of deep learning with reinforcement learning (RL), have provided the required tractability to deal with highly-dimensional state and action space problems. Hence, its application to 360° video streaming has been facilitated. Good illustration of this new trend are the works in [280], where a DRL-based head movement prediction is proposed, and [281], where a general video-content independent tile rate-allocation framework is presented. Despite the rich recent literature on FoV prediction, most of these and other works provide bandwidth-aware adaptive rate schemes with a clear focus on Internet VR video streaming. Therefore, they do not address the particularities of the mobile/cellular environment.

Furthermore, HMDs have limited computing power and storage capacity, so the above predictions need to be offloaded to the network edge. In this sense, the emerging role of edge computing for wireless VR and its relation with communication has been largely covered in the recent literature [241], [249], [251], [261], [282], [283]. Therein, authors in [251] outlined the challenges and the technology enablers to realize a reliable and low-latency immersive mobile VR experience.

On the other hand, [241], [249], [261], [282], [283], explored different optimization objectives while investigating some fundamental trade-offs between edge computing, caching, and communication for specific VR scenarios.

Yet, most of the few works considering VR multi-user scenarios focus either on direct [284] or D2D-aided [285] content broadcasting, disregarding the potentials for bandwidth savings and caching of existing correlations between VR users or contents [286]. Also the few works that leverage content correlation through ML, such as [287], none capitalizes prediction related information to perform a proactive mmWave multicast transmission. Furthermore, imposing high-reliability and low-latency constraints on such wireless VR service problem has not been studied so far.

Therefore, this chapter proposes to incorporate ML and multicasting into the optimization problem of wirelessly streaming FoV-based HD 360° videos with HRLLBB guarantees. The use of ML to predict users' FoV in advance and leverage inter-user correlations is pivotal to the system. Then, building upon the aforementioned correlations, multicast transmissions aimed for clusters of users with partially or fully overlapping FoVs will be proactively scheduled such that strict latency bounds are kept. Moreover, the adoption of mmWave frequency band communications –where at each time slot a given SBS will steer multiple spatially orthogonal beams towards a cluster of users– to transmit contents is key to benefiting from high transmission rates that contribute to a reduced on-the-air delay.

IV.3.1.2 Main Contributions

For clarity, the main contributions of this chapter are summarized as follows:

Main Contributions

1. To provide high capacity while ensuring bounded latencies in wireless 360° VR streaming, a proactive physical-layer multicast transmission scheme that leverages future content and user location related correlations is proposed.
2. The problem is modeled as a users' HD frame request admission maximization problem and, by borrowing tools from dynamic stochastic optimization, the problem is recast with traffic load stability and latency bound considerations. Subsequently, to solve it, a low complexity and efficient algorithm based on matching theory is proposed.
3. To validate the proposed scheme, for FoV prediction a DRNN based on GRUs that is trained with a dataset of real 360° VR poses is developed. The predicted FoVs for a given time horizon are thus available to dynamically cluster users based on their FoV overlap and proximity within a VR theater, as well as to provide insights on how much the scheme is affected by the accuracy of the prediction and the clustering decisions.
4. Extensive simulations are conducted to investigate the effects of the prediction horizon, of the VR frame size, the clustering, and of the network size, which conclude that the proposed approach outperforms considered reference baselines by delivering more HD quality frames, while ensuring tight transmission delay bounds.

IV.3.1.3 Chapter Organization

The remaining of this chapter is organized as follows: In Section IV.3.2 the system model and the underlying assumptions are described. The optimization problem of wireless VR video content delivery is formulated in Section IV.3.3. Section IV.3.4 presents the proposed matching theory algorithm to schedule wireless multicast/unicast transmission resources for VR video chunks under latency constraints. A detailed description of the FoV prediction and adopted user clustering schemes is provided in Section IV.3.5. Simulation results and performance evaluation are presented in Section IV.3.6. Finally, Section IV.3.7 concludes the chapter.

IV.3.2 System Model

In this section the system model which encompasses the considered deployment scenario, as well as the adopted wireless channel and communication models, is introduced.

IV.3.2.1 Deployment Scenario

A VR theater with seats arranged in s_r rows and s_c columns, and where a network of VR users $\mathcal{U}$ –all wearing mmWave HMDs– are located, is considered. In this scenario, each user chooses to watch an HD 360° VR video $v \in \mathcal{V}$, with $\mathcal{V}$ denoting the set of available VR videos in the catalog. Due to their large size and to the limited storage capacity in the HMDs, the HD frames of videos are cached in the edge network and are delivered to users through $B = |\mathcal{B}|$ SBSs distributed around the theater. To ensure a timely and smooth streaming experience, a lower-quality standard definition (SD) version of the video frames are assumed to be pre-cached in the user's HMD to be streamed if the HD frames are not successfully delivered on time. The SBSs operate in the mmWave band and are endowed with multi-beam beamforming capabilities to boost physical layer multicast transmission [288] of shared video content to users grouped into clusters. The above setting is graphically represented in Fig. IV.3.2.

In the network edge, and without loss of generality, it is assumed that all the videos from the catalog are encoded at the same frame rate $1/T_f$ –with T_f the time between frames– and have the same length i.e., consist of a set of frames $\mathcal{F} = \{f\}_{f=1}^{F} \subset \mathbb{N}$. Moreover, the frames from the spherical videos are unwrapped into a 2D equirectangular (EQR) or lat-long projection with pixel dimensions $P_H \times P_V$ and divided into $\mathcal{N} = \{1, \ldots, N\}$ partitions or *tiles* arranged to form an $N_H \times N_V$ regular grid, so that $N = N_H \cdot N_V$ and each tile is sized $P_H/N_H \times P_V/N_V$ pixels. Therefore, when watching any given video $v \in \mathcal{V}$, the FoV of user $u \in \mathcal{U}$ during frame $f \in \mathcal{F}$ can be expressed as a tile subset $\mathcal{N}_u^f \subseteq \mathcal{N}$.

In a nutshell, two main indices are used in this chapter: one refers to the decision slots indexed by $t = \{1, 2, \cdots\}$ and slot duration T_t which is the prevailing time scale and the one enforced for transmission/scheduling purposes, whereas the second index refers to the video frame index within the video at hand denoted f. Hence, the slotted time index t and frame index f satisfy $f \triangleq \lceil \frac{t \cdot T_t}{T_f} \rceil$ so that $f = \{1, 2, \cdots\} \in \mathbb{N}$. With this division in mind, that is further illustrated in Fig. IV.3.3, *chunk* hereafter denotes the part of the video that corresponds to one frame in time and one tile in EQR space.

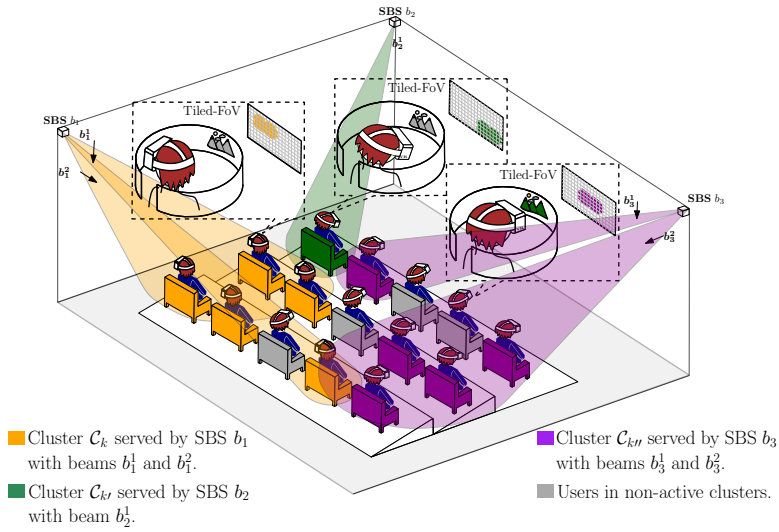

FIGURE IV.3.2: Schematic representation of tiled-FoV mmWave multicast transmissions scheduled to VR users with overlapping FoVs. Users belonging to a given cluster are served by a single mmWave SBS through different non-overlapping beams of variable beamwidth. ([271] ©2020 IEEE)

IV.3.2.2 FoV and Spatial Inter-user Correlation

To leverage FoV and spatial correlations between users in the VR theater deployment from Section IV.3.2.1 , and as outlined in Fig. IV.3.4 , it is assumed that users report in the UL their video index v and their 6DoF pose every T_f ms. This 6DoF pose includes head orientation angles and x, y and z-axis coordinates. It should be noticed here that spherical or 360° video is displayed from a centered perspective, hence users are only allowed to look around and their physical location does not affect their view. Therefore, although the whole 6DoF pose is reported, for FoV prediction purposes only the 3DoF head orientation expressed by pitch, roll and yaw angles needs to be considered. The information is then forwarded from the SBSs to the edge controller where FoV prediction, user-clustering and scheduling decisions take place.

New real-time/proactive chunk scheduling decisions will be taken every T_t such that for all users chunks are scheduled for DL transmission by the SBSs,

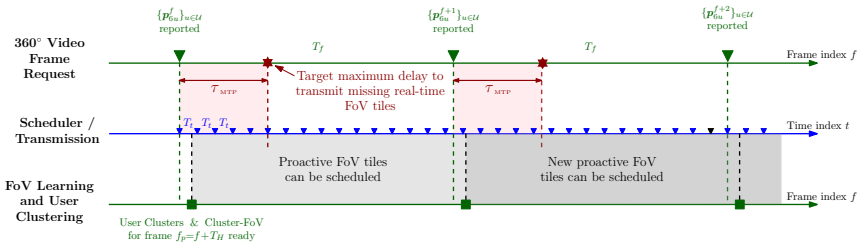

FIGURE IV.3.3: Timing sequence to showcase operation at transmission/scheduling level and at video frame level.

and delivered before the frame deadline d_f expires. In this regard, the chunks that correspond to the real-time, i.e. $f = f_r$, and to predicted future FoVs will be given by $\mathcal{N}_u^{f_r}$ and by $\{\widehat{\mathcal{N}}_u^f\}_{f=f_r+1}^{f_p}$, respectively.

To provide the estimated FoVs, let a supervised ML model $M_{\boldsymbol{\vartheta}}^{v,T_H}$ be defined in the edge controller –with M denoting the model's learning algorithm and $\boldsymbol{\vartheta}$ its parameter set– associated to each VR video $v \in \mathcal{V}$ and time horizon[2] T_H for which the model is constructed as

$$\widehat{\boldsymbol{y}}_u^{f_p} \triangleq M_{\boldsymbol{\vartheta}}^{v,T_H}(\boldsymbol{x}_u^f). \tag{IV.3.1}$$

Once the model's offline training has been completed and its parameters are known, given a sequence $\boldsymbol{x}_u^f$, which consists of the user's last T_P recorded head angles $\boldsymbol{p}_{3u}^f$ with video frame indices $f \in \{f_r - T_P + 1, \ldots, f_r\}$, the model will produce the vector of labels $\widehat{\boldsymbol{y}}_u^{f_p} \triangleq \{\widehat{y}_{u,n}^{f_p}\}_{n=1}^N$ for a frame index $f_p = f + T_H$ as per (IV.3.1). The corresponding set of tiles in the predicted FoV is a mapping such that $\{\widehat{\mathcal{N}}_u^{f_p} = \forall n \in [1, \ldots, N]\colon \widehat{y}_{u,n}^{f_p} = 1\} \forall u \in \mathcal{U}$.

Subsequently, the predicted FoVs and reported poses will be fed into a user-clustering module whereby users watching the same VR video v will be grouped together based on their FoV and spatial correlation. The inputs for the scheduler will therefore be: $\forall u \in \mathcal{U}$ the real-time FoV tile-sets $\mathcal{N}_u^{f_r}$ for the current index frame $f = f_r$ as well as the predicted K user-clusters $\{\mathcal{C}_k^{f_p}\}_{k=1}^{\mathrm{K}} \mid \bigcup_{k=1}^{\mathrm{K}} \mathcal{C}_k^{f_p} = \mathcal{U}$ with their corresponding cluster-level predicted FoVs $\{\widehat{\mathcal{N}}_{\mathcal{C}_k}^{f_p} = \bigcup_{u \in \mathcal{C}_k^{f_p}} \widehat{\mathcal{N}}_u^{f_p}\}_{k=1}^K$.

Since spherical videos are not locally cached, a huge imbalance emerges in the amount of information being sent in the UL vs. DL. Therefore, for the purpose of this chapter, the focus will be exclusively set on the effect of the DL HD 360° video transmission from edge SBSs to VR users, and assume that enough UL resources are available to users for timely pose update and CSI report.

Also, in the remaining of the chapter and for a given time horizon T_H, following the UL report of users' pose, the availability of the real-time and predicted FoVs as well as of user-clustering partitioning results is assumed. The detailed description of the proposed FoV prediction and user-clustering schemes with their algorithmic implementation details to produce such inputs are provided in Section IV.3.5.

Next, the wireless channel model and the communication model between the SBSs and the VR users are presented.

IV.3.2.3 Wireless Channel Model

At mmWave frequencies, due to the quasi-optical nature of electromagnetic wave propagation, signals are highly directional. For that reason channels are composed of a single-path propagation component for the dominant path and a set of multi-path components. For tractability and without loss of generality, in this chapter the multi-path components are assumed to be neglegible and, thus, only the dominant path is considered for the purpose of VR wireless streaming.

In this single-path, the 3GPP recently contributed channel model [289] is adopted. This channel model is valid for frequencies ranging from 0.5 to 100 GHz and bandwidths of up to 10% of the center frequency not exceeding 2 GHz. Among the different scenarios therein, typical indoor deployment cases including office environments and shopping malls, are showcased. Selecting the indoor open office scenario, with user devices and SBSs located at 1 m and 3 m

[2]Without loss of generality, that the time horizon for the prediction T_H is measured as an integer multiple of the frames.

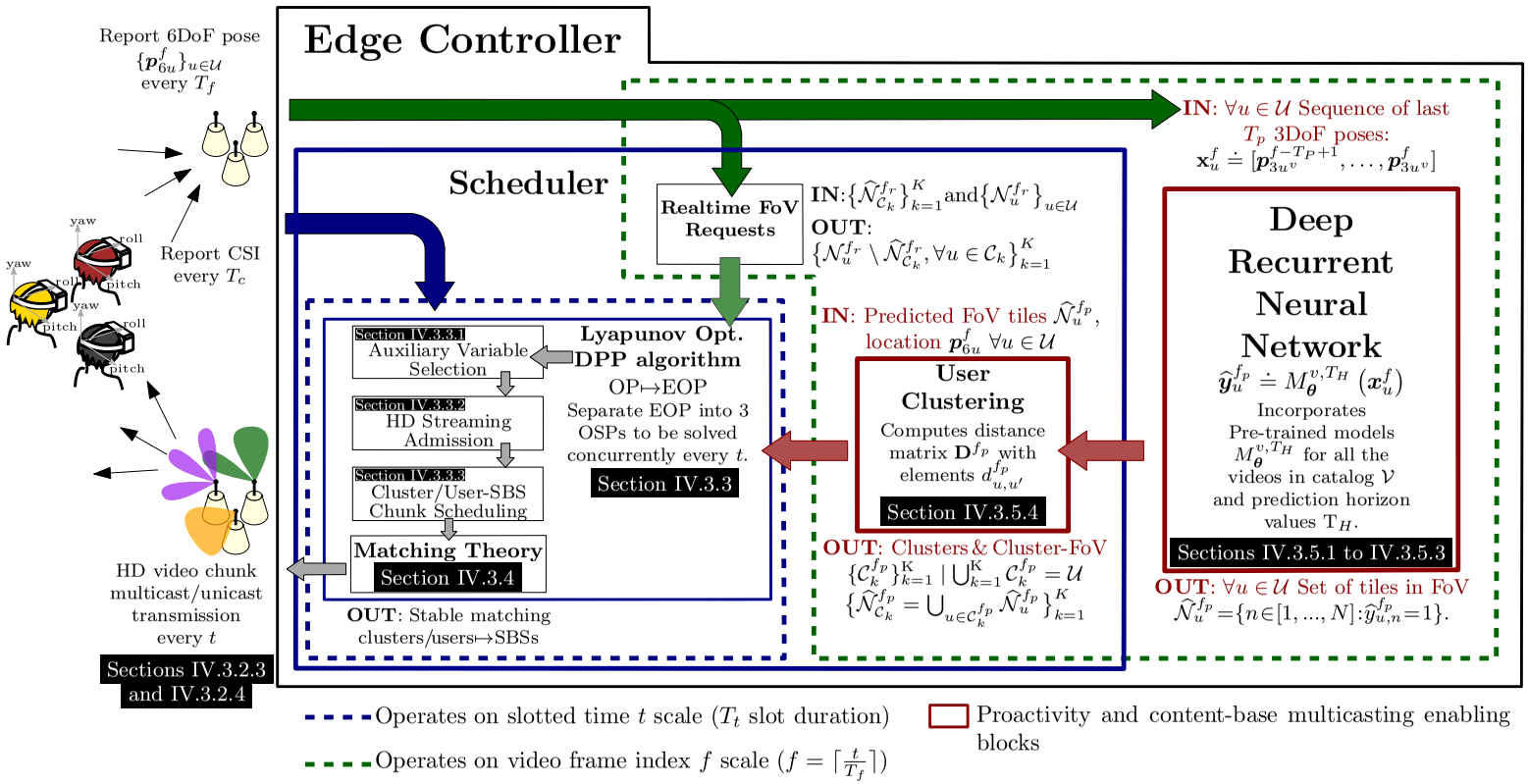

FIGURE IV.3.4: Flowchart of the proposed DRNN-aided wireless scheduling of HD 360° video FoV chunks. Once user pose has been reported in the UL, FOV prediction and user clustering follow. Subsequently, a scheduler balances HD chunk admission vs. queue stability subject to latency constraints. Finally a matching theory algorithm associates scheduled chunks to SBS-user clusters pairs leveraging multi-beam mmWave multicast transmission in the DL. Adapted from ([271] ©2020 IEEE)

height respectively, a distance dependent LOS probability is defined as

$$\Pr(\text{LOS}) = \begin{cases} 1, & d_{bu}^{\text{2D}} \leq 5 \text{ m}, \\ \exp\left(-\frac{d_{bu}^{\text{2D}}-5}{70.8}\right), & 5 \text{ m} < d_{bu}^{\text{2D}} \leq 49 \text{ m}, \\ 0.54\exp\left(-\frac{d_{bu}^{\text{2D}}-49}{211.7}\right), & 49 \text{ m} < d_{bu}^{\text{2D}}, \end{cases} \tag{IV.3.2}$$

where d_{bu}^{2D} stands for the distance in meters between the SBS and the user in the azimuth plane. Subsequently, results from $\Pr(\text{LOS})$ are exploited to calculate the large-scale fading effects in the channel. Specifically, pathloss $P\ell$ is given (in dB) by

$$P\ell_{\text{LOS}} = 32.4 + 17.3 \cdot \log_{10} d_{bu}^{\text{3D}} + 20 \cdot \log_{10} f_c, \tag{IV.3.3}$$

$$P\ell_{\text{NLOS}}^{prev} = 38.3 \cdot \log_{10} d_{bu}^{\text{3D}} + 17.3 + 24.9 \cdot \log_{10} f_c, \tag{IV.3.4}$$

$$P\ell_{\text{NLOS}} = \max(P\ell_{\text{LOS}}, P\ell_{\text{NLOS}}^{prev}), \tag{IV.3.5}$$

with d_{bu}^{3D}, f_c in (IV.3.3) and (IV.3.4) representing the distance in meters between the SBS and the user in the elevation plane and the channel's central frequency normalized with 1 GHz, respectively. A log-normally distributed shadowing fading loss $S\ell$, with standard deviation for the LOS and NLOS cases of $\varsigma_{\text{LOS}}^{S\ell} = 3$ dB and $\varsigma_{\text{NLOS}}^{S\ell} = 8.03$ dB respectively, supplements the large-scale fading calculations.

In addition to the pathloss and shadowing fading, the channel intermittency due to sporadic human blockage is also accounted for. This blockage $B\ell(t_B)$ could hinder the communication by bringing 20-30 dB penalty upon the channel gain. To that end, based on the spatial location of users within the VR theater, the prospective human blockers that might obstruct the direct ray in the azimuth plane between a given user and each of the available SBSs are counted. Thereupon, the count-weighted probabilistic arrival of blockage-events is evaluated every T_{block}, with the value of T_{block} chosen such that $T_{\text{block}}/T_t \gg 1$ and the index t_B satisfy $t_B \triangleq \lceil \frac{t*T_t}{T_{\text{block}}} \rceil$. The reason for operating on larger time-scale lies on correlation between blockage events along several transmission intervals due to the relative slowness of human head and body limb movement with respect to other channel fading effects. Indeed, human blockage durations of few hundreds of ms or more are reported in the literature [52].

By combining the channel as per [289] with the statistic blockage model, both dynamic channel fluctuations and the arrival of sporadic and longer-lasting human blockage events are suitably captured. Accordingly, the channel gain $h_{bu}(t)$ in dB from SBS $b \in \mathcal{B}$ to user $u \in \mathcal{U}$ is given as

$$h_{bu}(t) = P\ell_{bu}(t) + S\ell_{bu}(t) + B\ell_{bu}(t_B). \tag{IV.3.6}$$

IV.3.2.4 Wireless Communication Model

To benefit from multi-beam transmission, SBSs are equipped with a limited number of radio frequency (RF) chains, whereas users' HMDs will have a single RF chain, limiting their beamforming and combining capability. These assumptions are grounded on current high costs and power consumption of analog-to-digital converters for mmWave frequencies. For tractability, the actual antenna radiation pattern is approximated by a 2D sectored antenna model [35] in the SBSs and in the HMDs. In this model antenna gains are considered constant within the mainlobe, and equal to a smaller constant in the sidelobes. Let $g_{bu}^{\text{Tx}}(\varphi^{\text{Tx}}, \vartheta_{bu}^{\text{Tx}}(t))$ and $g_{bu}^{\text{Rx}}(\varphi^{\text{Rx}}, \vartheta_{bu}^{\text{Rx}}(t))$ denote the transmission and reception antenna gains from

SBS b to the HMD of VR user u while using beams of beamwidth φ, given by

$$g_{bu}^{\measuredangle}(\varphi^{\measuredangle}, \theta_{bu}(t)) = \begin{cases} \frac{2\pi - \left(2\pi - \varphi^{\measuredangle}\right) g_{\lhd}}{\varphi^{\measuredangle}}, & |\theta_{bu}(t)| \leq \frac{\varphi^{\measuredangle}}{2}, \\ g_{\lhd}, & \text{otherwise}, \end{cases} \tag{IV.3.7}$$

with $\measuredangle \in \{\mathrm{Tx}, \mathrm{Rx}\}$, where $\theta_{bu}(t)$ stands for the angular deviation from the boresight directions of SBS b and of VR user u, and $g_{\lhd}$ is the constant side-lobe gain with $g_{\lhd} \in [0, 1)$. High directionality of mmWave communication often implies having to search for the best steering directions. In the system model, full knowledge of the seating area layout and of the fixed locations of the B SBSs is assumed. Moreover, as stated before, users in $\mathcal{U}$ will report their 6DoF pose information in the UL with T_f periodicity. With these assumptions, even if both the SBSs and users are aware of each other's location and know a priori what their respective optimal beams' boresight directions are, the above antenna model effectively captures subtle misalignment errors arriving from the limited availability of unique beampatterns common in codebook-based beam alignment approaches under analog beamforming. In other words, the angular deviation $g_{bu}^{\measuredangle}(t)$ in (IV.3.7) reflects the inability of the analog beamformer to direct the mainlobe to any arbitrary location. The SINR for user u served by SBS b is thus given by

$$\mathrm{SINR}_{bu}(t) = \frac{p_b h_{bu}(t) g_{bu}^{\mathrm{Rx}}(t) g_{bu}^{\mathrm{Tx}}(t)}{I_u(t) + BW_b N_0}, \tag{IV.3.8}$$

where the numerator represents the power of the received signal at user u from SBS b under transmit power p_b, and the denominator is the sum of the interference power and Gaussian noise power. In what follows, I_u represents the interference that arrives from the transmission of other SBSs reaching user u through channel, transmit and receive antenna gains, and power level $h_{b'u}(t)$, $g_{b'u}^{\mathrm{Rx}}(t)$, $g_{b'u}^{\mathrm{Tx}}(t)$ and $p_{b'}$, respectively such that $I_u(t) = \sum_{b' \in \mathcal{B} \setminus \{b\}} p_{b'} h_{b'u}(t) g_{b'u}^{\mathrm{Rx}}(t) g_{b'u}^{\mathrm{Tx}}(t)$. Finally, the noise power is given by the noise power spectral density N_0 in watts per hertz multiplied by the system bandwidth BW_b.

Note that since a multicast transmission is considered, the achievable rate of user $u \in \mathcal{C}_k^f$ depends on the composition of $\mathcal{C}_k$ for each frame index f, with the assumptions behind this composition being the FoV and spatial correlation as detailed in Section IV.3.5.4.

IV.3.3 Problem Formulation

In this section, building upon the multi-user VR scenario described in Section IV.3.2, the network-wide optimization problem of scheduling the FoV contents of an HD 360° video frame by a deadline d_f such that VR sickness can be avoided is formulated. The problem formulation explicitly incorporates the proactive/real-time nature of content requests, as well as multicast/unicast transmission capabilities in the SBSs. The problem is posed as a frame quality maximization, while the latency constraints and transmission queues stability are maintained.

For admission purposes, in the scenario considered here, a user u associated during video frame index $f{=}f_p$ to a cluster $\mathcal{C}_k^{f_p} \subset \mathcal{C}$ is allowed to request chunks that belong either to the cluster-level predicted FoV $\widehat{\mathcal{N}}_{\mathcal{C}_k}^{f_p}$ or to its real-time FoV $\mathcal{N}_u^{f_r}$. In this sense, the admission of the predicted FoV proactive requests allows to leverage cluster-level multicast transmissions of shared FoV chunks, i.e. content reuse. On their behalf, real-time FoV chunk requests are the result of missed tiles, i.e. $\mathcal{N}_u^{f_r} \setminus \widehat{\mathcal{N}}_{\mathcal{C}_k}^{f_r} \neq \emptyset$, due to imperfect prediction accuracy in the

DRNN module. In the latter case, these requests need to be expedited to meet MTP latency related constraints and provide a smooth VR experience.

Let $a_u^{tot}(t)$ be the total traffic admission for user $u \in \mathcal{C}_k^f$ with $\bigcup_{k=1}^{\mathrm{K}} \mathcal{C}_k^f = \mathcal{U}, \forall f \in \mathcal{F}$, given by

$$a_u^{tot}(t) = \sum_{f \in \mathcal{F}} \Big(\mathbb{I}_{(f=f_r)} r_{uf}(t) \sum_{c_f \in \mathcal{N}_u^f} L_{c_f} + \mathbb{I}_{(f=f_p)} r_{uf}(t) \sum_{c_f \in \widehat{\mathcal{N}}_{\mathcal{C}_k}^f} L_{c_f} \Big), \tag{IV.3.9}$$

where L_{c_f} is the data size of chunk c_f, and $r_{uf}(t)$ is a binary variable that indicates if the video frame f is admitted for offloading to user u. The aforementioned two-fold nature of the chunk admission requests is evinced through the two separate terms in (IV.3.9). Moreover, it should be noticed here that the value of $a_u^{tot}(t)$ in (IV.3.9) is upper bounded by the maximum value $a_{\max}^{tot}$ such that $a_u^{tot}(t) = a_{\max}^{tot} \Rightarrow r_{uf} = 1,\ \forall f \in \mathcal{F}$, that in practice represents a situation where the system's traffic load is so low that all frames can be admitted in HD without risking queue stability.

Extending the notation of the admission to consider unicast and multicast transmission of chunks in real-time and proactive respectively, the rate of delivering chunk c_f to user u is

$$\mu_{uc_f}(t) = \begin{cases} \sum_{b \in \mathcal{B}} \eta_{buc_f}(t) BW_b \log_2\big(1 + \mathrm{SINR}_{bu}(t)\big), & f = f_r, \\ \min_{u \in \mathcal{C}_k^f | c_f \in \widehat{\mathcal{N}}_u^f} \mu_{uc_f}(t), & \text{otherwise}, \end{cases} \tag{IV.3.10}$$

with $\mu_{bu}(t) = BW_b \log_2\big(1 + \mathrm{SINR}_{bu}(t)\big)$ the unicast real-time rate and $\eta_{buc_f}(t)$ the binary scheduling variable for chunk c_f to user u from base station b. For the proactive multicast case with $f_r < f \leq f_p$, the SBS will adapt its rate to match that of the worst user in the cluster $\mathcal{C}_k^f$ to whom user u has been assigned for the frame index at hand[3]. This way it guarantees that the chunk will be correctly decoded by all the interested cluster-users. Moreover, it is remark here that the value of $\mu_{uc_f}(t)$ in (IV.3.10) is bounded above by a maximum achievable service rate $\mu_{\max}$ that, in practice, is determined by the highest available modulation and coding scheme (MCS) index.

For notational compactness, to express that a requested chunk c_f corresponds either to the user's real-time FoV or to the user's cluster-level predicted FoV, the targeted FoV chunk set is hereafter denoted as $\widetilde{\mathcal{N}}_u^f = \mathbb{I}_{(f=f_r)} \mathcal{N}_u^f + (1 - \mathbb{I}_{(f=f_r)}) \widehat{\mathcal{N}}_{\mathcal{C}_k^f}^f$. Then $q_u(t)$ –namely, the traffic queue of a user u, $\forall u \in \mathcal{C}_k^f$– evolves as

$$q_u(t+1) = \Big[q_u(t) - \sum_{f=[f_r, f_p]} \sum_{c_f \in \widetilde{\mathcal{N}}_u^f} \mu_{uc_f}(t) \Big]^+ + a_u^{tot}(t). \tag{IV.3.11}$$

Notice that although only chunks for frame indices $f = \{f_r, f_p\}$ are admitted, the range of frame indices corresponding to chunks co-existing in a user's queue at a given time may span to values $f = [f_r, f_r + 1, \cdots, f_p]$. A scheduling policy, that is aware of the VR specific latency-reliability constraints, will timely determine which chunks need be expedited from these priority-based queues. Without loss of generality, let be assumed that the video streaming and FoV chunk scheduling start simultaneously, and denote the transmission delay of the video frame $f = f_r$ to user u as $\tau_{uf}^{tx}(t)$. Let $d_{\mathrm{t2MTP}}(t)$ represent the available time to schedule the

[3]In practice, this is accomplished by adapting the MCS that reflects users' perceived channel quality.

frame before the considered MTP delay deadline is exceeded and given by

$$d_{\text{t2MTP}}(t) = [t_a + \tau_{\text{MTP}} - t]^+, \tag{IV.3.12}$$

where t_a corresponds to the timestamp when the chunk was requested, and τ_{MTP} is the constant MTP latency-aware maximum transmission latency.

To realize a mobile VR that operates within MTP bounds a holistic approach that considers transmission, computing, and control latency performance should be considered. Yet, 360° videos require substantially higher data rates to provide acceptable quality to users and pose a greater challenge on the content delivery process. Hence, in this chapter it is argued that the question of how this high data rate transmission can be realized with such latency constraint is on itself important to study and focus on the transmission delay and save a $d_f - \tau_{\text{MTP}}$ budget for other edge-server computing or on-HMD processing delays. In this regard, the following HRLLBB constraint is imposed to ensure that the transmission delay of the current playing frame does not exceed the MTP delay with high probability:

$$\lim_{T\to\infty} \frac{1}{T} \sum_{t=1}^{T} \Pr(\tau_{uf_r}(t) \geq d_{\text{t2MTP}}(t)) \leq \epsilon_d, \tag{IV.3.13}$$

where $\epsilon_d \ll 1$ is a predefined delay reliability metric. The probability in (IV.3.13) is then recast as the expectation over an indicator function, i.e., the constraint is rewritten as:

$$\lim_{T\to\infty} \frac{1}{T} \sum_{t=1}^{T} \mathbb{E}[\mathbb{I}_{(\tau^{tx}_{uf_r}(t) \geq d_{\text{t2MTP}}(t))}] \leq \epsilon_d. \tag{IV.3.14}$$

Collecting the HD frame admission and the binary scheduling variables as $\boldsymbol{r}(t)=\{r_{uf}: \forall u \in \mathcal{U}, \forall f \in \{f_p, f_r\}\}$ and $\boldsymbol{\eta}(t)=\{\eta_{buc_f}(t): \forall b \in \mathcal{B}, \forall u \in \mathcal{U}, \forall c_f \in \widetilde{\mathcal{N}}_u^f\}$ respectively, the optimization problem is to maximize the user's quality by optimizing the HD frame admission and scheduling policies subject to the latency constraints:

$$\textbf{OP:} \max_{\boldsymbol{\eta}(t), \boldsymbol{r}(t)} U\big(\{\overline{a_u^{tot}}\}\big) = \sum_{u\in\mathcal{U}} \big(f(\overline{a_u^{tot}})\big) \tag{IV.3.15a}$$

$$\text{s.t.} \quad \overline{q_u} \leq \infty, \ \forall u \in \mathcal{U}, \tag{IV.3.15b}$$

$$r_{uf}(t) \in \{0,1\}, \ \forall u \in \mathcal{U}, \forall f \in \{f_p, f_r\}, \tag{IV.3.15c}$$

$$a_u^{tot}(t) \leq a_{\max}^{tot}, \ \forall u \in \mathcal{U}, \tag{IV.3.15d}$$

$$\mu_{uc_f}(t) \leq \mu_{\max}, \ \forall u \in \mathcal{U}, \forall c_f \in \widetilde{\mathcal{N}}_u^f, \forall f \in \mathcal{F}, \tag{IV.3.15e}$$

$$\eta_{buc_f}(t) \in \{0,1\}, \ \forall b \in \mathcal{B}, \forall u \in \mathcal{U}, \forall c_f \in \widetilde{\mathcal{N}}_u^f, \forall f \in \mathcal{F}, \tag{IV.3.15f}$$

$$\lim_{T\to\infty} \frac{1}{T} \sum_{t=1}^{T} \mathbb{E}[\mathbb{I}_{(\tau^{tx}_{uf_r}(t) \geq d_{\text{t2MTP}}(t))}] \leq \epsilon_d, \ \forall u \in \mathcal{U}, \tag{IV.3.15g}$$

where $f(\cdot)$ is a non-decreasing and concave function that can be adjusted to reflect different optimization objectives.

To find a tractable solution for the above stochastic optimization problem, a set of auxiliary variables $\{\gamma_u(t)\}, \forall u \in \mathcal{U}$ is first defined. Accordingly, the stochastic optimization problem in (IV.3.15) can be transformed from a utility function of time-averaged variables into an equivalent optimization problem of

time-averaged utility function of instantaneous variables:

$$\textbf{EOP:} \quad \max_{\boldsymbol{r}(t),\boldsymbol{\eta}(t),\{\gamma_u(t)\}} \overline{U\big(\{\gamma_u(t)\}\big)} = \overline{\sum_{u\in\mathcal{U}}\Big(f(\gamma_u)\Big)}$$

$$\text{s.t.} \quad \overline{\gamma_u} \leq \overline{a_u^{tot}},\ \forall u \in \mathcal{U}, \tag{IV.3.16a}$$

$$\gamma_u(t) \leq a_{\max}^{tot},\ \forall u \in \mathcal{U}, \tag{IV.3.16b}$$

$$\text{(IV.3.15b)} - \text{(IV.3.15g)}. \tag{IV.3.16c}$$

Next, by invoking the framework of Lyapunov optimization [143], *virtual queues* are constructed to help satisfy the time-average inequality constraints. By ensuring that these queues are stable, the time average constraints, namely (IV.3.15g) and (IV.3.16a), are guaranteed to be met. Therefore, the $z_u(t)$ and $j_{uf}(t)$ virtual queues, that correspondingly represent the constraints over the auxiliary variables and over the transmission delay, are defined. Accordingly, the virtual queues are updated as follows:

$$z_u(t+1) = \big[z_u(t) - a_u^{tot}(t) + \gamma_u(t)\big]^+, \tag{IV.3.17}$$

$$j_{uf}(t{+}1) = \big[j_{uf}(t) + (\mathbb{I}_{(\tau_{uf_r}^{tx}(t)\geq d_{\mathrm{t2MTP}}(t))} - \epsilon_d) q_u(t{+}1)\big]^+. \tag{IV.3.18}$$

Notice that the virtual queue in (IV.3.18) is built after having scaled-up the constraint in (IV.3.14) by multiplying both sides of it with the actual queue size. Hereinafter, for readability reasons $\mathbb{I}_{(\tau_{uc_f}(t)\geq d_{\mathrm{t2MTP}}(t))}$ will be shortened to $\mathbb{I}_{(d_{\mathrm{t2MTP}}(t))}$ to denote τ_{uc_f} exceeding the MTP delay.

Let $\boldsymbol{\chi}(t) = \{q_u(t), z_u(t), j_{uf}(t) : u \in \mathcal{U}, f \in \mathcal{F}\}$ be the vector of combined traffic and virtual queues with $\boldsymbol{\chi}(t) = [\boldsymbol{\chi}_u(t)]_{u\in\mathcal{U}}$. Then, to represent a scalar metric of the congestion, let the quadratic Lyapunov function be given by

$$\mathscr{L}(\boldsymbol{\chi}(t)) \triangleq \frac{1}{2}\sum_{u\in\mathcal{U}} q_u(t)^2 + \frac{1}{2}\sum_{u\in\mathcal{U}} z_u(t)^2 + \frac{1}{2}\sum_{u\in\mathcal{U}}\sum_{f\in\mathcal{F}} j_{uf}(t)^2, \tag{IV.3.19}$$

and the one-timeslot Lyapunov drift function be $\Delta\mathscr{L}_t = \mathscr{L}\boldsymbol{\chi}(t{+}1) - \mathscr{L}\boldsymbol{\chi}(t)$. Hence, the drift-plus-penalty algorithm is leveraged to find the control actions that greedily minimize a bound of the drift function minus a scaled utility function, i.e., $\Delta\mathscr{L}_t - V_\Delta \mathbb{E}\{U(\{\gamma_u(t)\})\}$, where V_Δ is the parameter that controls the trade-off between minimizing the queue backlog and approaching the optimal solution.

Lemma 1. *At each time instant t, the following bound satisfies the drift-plus-penalty function $\Delta\mathscr{L}_t - V_\Delta\mathbb{E}\{U(\{\gamma_u(t)\})\}$ under any queue state and control strategy:*

$$\Delta\mathscr{L}_t - V_\Delta\mathbb{E}\big\{U(\{\gamma_u(t)\})\big\} \leq \Delta_0(t) - \sum_{u\in\mathcal{U}}\Big[z_u(t)\gamma_u(t) - V_\Delta U(\{\gamma_u(t)\})\Big]_{\#1} - \sum_{u\in\mathcal{U}}\Big[\Big(\alpha_u(t) - z_u(t)\Big)a_u^{tot}(t)\Big]_{\#2} - \sum_{u\in\mathcal{U}}\Big[\alpha_u(t)\sum_{f\in\mathcal{F}}\sum_{c_f\in\mathcal{N}_u^f}\mu_{uc_f}\Big]_{\#3}, \tag{IV.3.20}$$

where $\Delta_0(t)$ is an upperbounded constant parameter at each time slot t in (IV.3.20)*, and $\alpha_u(t)$ collects the terms related to the traffic queue and to the transmission delay virtual queue as*

$$\alpha_u(t) = \alpha_q(t) + \mathbb{I}_{(d_{t2MTP}(t))}\alpha_j(t), \tag{IV.3.21}$$

and given by $\alpha_q(t) = q_u(t)(1+\epsilon_d^2) - \epsilon_d \sum_{f\in\mathcal{F}} j_{uf}(t)$ *and* $\alpha_j(t) = \sum_{f\in\mathcal{F}} j_{uf}(t) + (1-2\epsilon_d)q_u(t)$.

Proof. See Appendix IV.3.A ■

The solution to (IV.3.16) can be found by greedily minimizing the right-hand side of (IV.3.20) for each time slot. Instead, since the optimization variables are decoupled in (IV.3.20), the optimization problem is split into three disjoint subproblems that are solved concurrently based on the observation of the traffic and the virtual queues.

It can be also seen from (IV.3.20) that the optimization problem at a given time slot t is only function of the current states of the traffic and the virtual queues. This means that a solution to the problem does not require the knowledge of the traffic statistics or queue evolution probabilities. The equation also shows that the *separability criteria* [142] is met i.e., that admission and scheduling are not dependent on the variables of each other.

IV.3.3.1 Auxiliary Variable Selection

The first subproblem is the minimization of the term #1 in (IV.3.20), i.e., the selection of the auxiliary variables. The problem can be decoupled on a per user basis as

$$\textbf{OSP1:} \quad \max_{\{\gamma_u\}} V_\Delta U(\gamma_u(t)) - z_u(t)\gamma_u(t) \tag{IV.3.22a}$$

$$\text{s.t. } \gamma_u(t) \le a_{\max}^{tot},\ \forall u \in \mathcal{U}. \tag{IV.3.22b}$$

By selecting a linear utility function, i.e., $U(\gamma_u(t)) = \gamma_u(t)$, the optimal value of the auxiliary variable is found to be

$$\gamma_u(t) = \begin{cases} a_{\max}^{tot}, & z_u(t) \le V_\Delta, \\ 0, & \text{otherwise.} \end{cases} \tag{IV.3.23}$$

It is worth noting here that different utility functions can be selected depending on the network optimization objective. For example, a logarithmic function of the admission rates could be selected to provide proportional fairness between users.

IV.3.3.2 HD Streaming Admission

Next, the HD chunk admission problem is optimized by solving the subproblem given by the term #2 of (IV.3.20). The subproblem is formulated as

$$\textbf{OSP2:} \quad \max_{\boldsymbol{r}(t)} \sum_{u\in\mathcal{U}} \big(z_u(t) - \alpha_u(t)\big) a_u^{tot}(t) \tag{IV.3.24a}$$

$$\text{s.t. } r_{u_f}(t) \in \{0,1\},\ \forall u \in \mathcal{U}, \forall f \in \{f_p, f_r\}. \tag{IV.3.24b}$$

The above admission rate maximization problem is convex and its optimal solution is

$$r_{u_f}(t) = \begin{cases} 1 & z_u(t) \ge \alpha_u(t), \\ 0 & \text{otherwise.} \end{cases} \tag{IV.3.25}$$

In other words, the optimal HD chunk admission control is to either admit or discard the whole frame, depending on the physical and virtual queue state.

IV.3.3.3 User-SBS Chunk Scheduling

The third subproblem aims at scheduling user requests of HD video chunks to base stations. The optimization subproblem is formulated by maximizing the term #3 in (IV.3.20) as follows:

$$\textbf{OSP3:} \quad \max_{\boldsymbol{\eta}(t)} \sum_{u\in\mathcal{U}} \alpha_u(t) \sum_{f=\{f_r,f_p\}} \sum_{c_f\in\widetilde{\mathcal{N}}_u^f} \mu_{uc_f}(t) \tag{IV.3.26a}$$

$$\text{s.t. } \mu_{uc_f}(t) \leq \mu_{\max}, \forall c_f \in \widetilde{\mathcal{N}}_u^f, \forall f \in \mathcal{F}, \forall u \in \mathcal{U}, \tag{IV.3.26b}$$

$$\eta_{buc_f}(t) \in \{0,1\}, \forall b \in \mathcal{B}, \forall u \in \mathcal{U}, \forall c_f \in \widetilde{\mathcal{N}}_u^f, \forall f \in \mathcal{F}. \tag{IV.3.26c}$$

It is emphasized that OSP3 is a combinatorial problem where video chunks for users need to be scheduled by SBSs using a mmWave multicast transmission. Subsequently, a matching algorithm is designed to associate chunk scheduling requests arising either from clusters of users or from individual users to the set of SBSs operating in mmWave band in the theater.

IV.3.4 A Matching Theory approach to HD chunk scheduling

The use of Matching Theory [126] has recently garnered a considerable interest in the context of resource allocation for wireless networks [128]. However, for the sake of completeness first several definitions, adapted to the problem at hand, will be first provided to properly address the fundamentals of this framework. Then, the utility functions that lie at its core for both sets of agents will be motivated.

IV.3.4.1 Matching Theory Preliminaries

Definition 15. *A matching game is defined by two sets of players ($\mathcal{C}$,$\mathcal{B}$) and two preference profiles denoted by $\succ_{\mathcal{B}}$ and $\succ_{\mathcal{C}}$, allowing each player $b \in \mathcal{B}$, $\mathcal{C}_k \in \mathcal{C}$ to accordingly rank the players in the opposite set.*

Definition 16. *The output of a matching game is a matching function $\boldsymbol{\Upsilon}(t) = \{\Upsilon_{b,\mathcal{C}_k}(t)\}$ that bilaterally assigns players $\boldsymbol{\Upsilon}_b(t) \triangleq \{b \in \mathcal{B} : \Upsilon_{b,\mathcal{C}_k}(t) = 1\}$ and $\boldsymbol{\Upsilon}_{\mathcal{C}_k}(t) \triangleq \{\mathcal{C}_k \in \mathcal{C} : \Upsilon_{b,\mathcal{C}_k}(t) = 1\}$ such that $|\boldsymbol{\Upsilon}_{\mathcal{C}_k}(t)| \leq q_{\mathcal{C}}$ and $|\boldsymbol{\Upsilon}_b(t)| \leq q_{\mathcal{B}}$ are fulfilled, with $q_{\mathcal{B}}$, $q_{\mathcal{C}}$ the quota of the players which, for a one-to-one matching game satisfy $q_{\mathcal{B}} = q_{\mathcal{C}} = 1$.*

Definition 17. *A preference $\succ$ is a complete, reflexive and transitive binary relation between the players in $\mathcal{B}$ and $\mathcal{C}$. Therefore, for any SBS $b \in \mathcal{B}$ a preference relation $\succ_b$ is defined over the set of clusters $\mathcal{C}$ such that for any two clusters $(\mathcal{C}_k, \mathcal{C}'_k) \in \mathcal{C} \times \mathcal{C}$ with $\mathcal{C}_k \neq \mathcal{C}'_k$, and two matchings $\boldsymbol{\Upsilon}(t)$, $\boldsymbol{\Upsilon}'(t)$ so that $\Upsilon_b(t) = \mathcal{C}_k$ and $\Upsilon'_b(t) = \mathcal{C}'_k$:*

$$(\mathcal{C}_k, \boldsymbol{\Upsilon}(t)) \succ_b \left(\mathcal{C}'_k, \boldsymbol{\Upsilon}'(t)\right) \Leftrightarrow U_{\mathcal{B}}^{b,\mathcal{C}_k}(t) > U_{\mathcal{B}}^{b,\mathcal{C}'_k}(t). \tag{IV.3.27}$$

Similarly, for any cluster of users $\mathcal{C}_k \in \mathcal{C}$ a preference relation $\succ_{\mathcal{C}_k}$ is defined over the set of SBS $\mathcal{B}$ such that for any two SBSs $(b, b') \in \mathcal{B} \times \mathcal{B}$ with $b \neq b'$, and two matchings $\boldsymbol{\Upsilon}(t)$, $\boldsymbol{\Upsilon}'(t)$ with $\Upsilon_{\mathcal{C}_k}(t) = b$ and $\Upsilon'_{\mathcal{C}_k}(t) = b'$:

$$(b, \boldsymbol{\Upsilon}(t)) \succ_{\mathcal{C}_k} \left(b', \boldsymbol{\Upsilon}'(t)\right) \Leftrightarrow U_{\mathcal{C}}^{\mathcal{C}_k,b}(t) > U_{\mathcal{C}}^{\mathcal{C}_k,b'}(t), \tag{IV.3.28}$$

where $U_{\mathcal{B}}^{b,\mathcal{C}_k}(t)$ and $U_{\mathcal{C}}^{\mathcal{C}_k,b}(t)$ denote the utility of cluster $\mathcal{C}_k$ for SBS b and the utility of SBS b for cluster $\mathcal{C}_k$, correspondingly.

IV.3.4.2 Matching Utility Formulation

The HD chunk scheduling subproblem in (IV.3.26) is formulated as a matching game between the SBSs and the clusters of users. As such, both sides seek to greedily maximize the overall VR experience by efficiently allocating the mmWave transmission resources while VR QoE related constraints are met. Hence, each timeslot with updated information on channel and queue state, new scheduling requests for video chunk transmission will be prioritized in each cluster and in each SBS, and new sets of matching pairs will be found using the

Algorithm IV.3.1: HD chunk scheduling between SBSs and User-clusters. ([271] ©2020 IEEE)

Phase I - Interference learning and candidate chunk selection

- Each $u \in \mathcal{U}$, updates $\hat{I}_u(t)$ as per (IV.3.31) and reports channel in the UL.
- In the edge controller, queues in $\{\boldsymbol{\chi}(t)\}_{u\in\mathcal{U}}$ are updated by solving (IV.3.22), (IV.3.24).
- For each $\mathcal{C}_k \in \mathcal{C}$ a cluster-level chunk request pool is created and requests are assigned an urgency tag $\alpha_{\mathcal{C}_k^{cf}} = \sum_{u\in\mathcal{C}_k | c_f \in \mathcal{N}_u^f} \alpha_u(t)$ with $\alpha_u(t)$ as per (IV.3.21).Then, the request pool is sorted in descending order of $\alpha_{\mathcal{C}_k^{cf}}$.

Phase II - Matching game construction

- Each cluster $\mathcal{C}_k \in \mathcal{C}$, updates $\hat{U}_{\mathcal{C}}^{\mathcal{C}_k,b}$ over the SBSs in $\mathcal{B}$ as per (IV.3.32).
- Each SBS $b \in \mathcal{B}$, updates $\hat{U}_{\mathcal{B}}^{b,\mathcal{C}_k}$ over $\{\mathcal{C}_k\}_{k=1}^{K}$ as per (IV.3.33) evaluating cluster utility by its most urgent chunk-request, i.e. by $\max\{\alpha_{\mathcal{C}_k^{cf}}\}$.

Phase III - Deferred Acceptance for SBS-Cluster allocation

- For each SBS b, initialize the subset of eligible clusters, $\mathcal{E}_{\mathcal{C}}^b \subseteq \mathcal{C}$ with $|\mathcal{E}_{\mathcal{C}}^b| = |\mathcal{C}|$ initially.
- For each SBS b and each cluster $\mathcal{C}_k$, initialize the subset of unmatched clusters $\mathcal{S}_{\mathcal{C}} \subseteq \mathcal{C}$ and SBS $\mathcal{S}_{\mathcal{B}} \subseteq \mathcal{B}$, so that initially $|\mathcal{S}_{\mathcal{C}}| = |\mathcal{C}|$, $|\mathcal{S}_{\mathcal{B}}| = |\mathcal{B}|$.

while $|\mathcal{S}_{\mathcal{B}}| \neq \emptyset$ and $\sum_{b\in\mathcal{B}} |\mathcal{E}_{\mathcal{C}}^b| \neq \emptyset$ **do**
  Pick a random SBS $b \in \mathcal{B}$;
  if $|\mathcal{E}_{\mathcal{C}}^b| \neq \emptyset$ **then**
    SBS b sends a chunk scheduling proposal to its best ranked *eligible* cluster $\mathcal{C}_k$, $\mathcal{C}_k \in \mathcal{E}_{\mathcal{C}}^b$;
    if $\mathcal{C}_k \in \mathcal{S}_{\mathcal{C}}$ **then**
      Match b and $\mathcal{C}_k$ setting $\Upsilon_b(t) = \mathcal{C}_k$ and $\Upsilon_{\mathcal{C}_k}(t) = b$;
      Remove b and $\mathcal{C}_k$ from $\mathcal{S}_{\mathcal{B}}$ and $\mathcal{S}_{\mathcal{C}}$ respectively;
    else
      if $\hat{U}_{\mathcal{C}}^{\mathcal{C}_k,b}(t) > \hat{U}_{\mathcal{C}}^{\mathcal{C}_k,\Upsilon_{\mathcal{C}_k}(t)}(t)$ **then**
        Reject proposal from $\Upsilon_{\mathcal{C}_k}(t)$; remove $\mathcal{C}_k$ from $\mathcal{E}_{\mathcal{C}}^{\Upsilon_{\mathcal{C}_k}(t)}$ and add back $\Upsilon_{\mathcal{C}_k}(t)$ to $\mathcal{S}_{\mathcal{B}}$;
        Match b and $\mathcal{C}_k$ setting $\Upsilon_b(t) = \mathcal{C}_k$ and $\Upsilon_{\mathcal{C}_k}(t) = b$;
        Remove b from $\mathcal{S}_{\mathcal{B}}$;
      else
        Refuse proposal from b;
        Remove $\mathcal{C}_k$ from $\mathcal{E}_{\mathcal{C}}^b$;
      end
    end
  end
end

Phase IV - Stable matching

proposed approach. With the above principles in mind, the utilities for both sets are formulated.

The utility of serving a given cluster of users with at least one pending chunk request from the SBSs point of view will essentially reflect two aspects: the *priority* and *relevance* of the chunk c_f at hand. The priority of the whole frame to which the requested chunk belongs to is controlled by the dynamics of $q_u(t)$ and $j_{uf}(t)$ as per (IV.3.11) and (IV.3.18) through $d_{\mathrm{t2MTP}}(t)$ as given by (IV.3.12). The relevance of the chunk within the cluster FoV is related to its popularity i.e., how many of the cluster members have requested this chunk. Intuitively, the cluster-level multicast approach decreases the wireless network load by transmitting each chunk falling into the cluster-level FoV only once. Moreover, transmitting first the most relevant chunks also contributes to increasing the overall system welfare. Therefore, SBSs will build their preference profile using the following utility function:

$$U_{\mathcal{B}}^{b,\mathcal{C}_k}(t) = \sum_{u\in\mathcal{C}_k} \mathbb{I}_{(c_f\in\widetilde{\mathcal{N}}_u^f)}\alpha_u(t) = \sum_{u\in\mathcal{C}_k} \mathbb{I}_{(c_f\in\widetilde{\mathcal{N}}_u^f)}\big\{\alpha_q(t) + \mathbb{I}_{(d_{\mathrm{t2MTP}}(t))}\alpha_j(t)\big\}. \tag{IV.3.29}$$

Notice that in (IV.3.29) by definition, $\mathbb{I}_{(d_{\mathrm{t2MTP}}(t))}$ can only be non-zero for the currently playing frame index i.e., if the chunk being requested corresponds to the real-time FoV. Otherwise the second term of the summation in $U_{\mathcal{B}}^{b,\mathcal{C}_k}(t)$ will be zero. Similarly, the utility of a SBS from the clusters' perspective will depend on the goodness of the transmission opportunity through the offered rate in (IV.3.10). In other words, the utility is defined as

$$U_{\mathcal{C}}^{\mathcal{C}_k,b}(t) = \mathbb{I}_{(f=f_r)} \min_{\substack{\forall u\in\mathcal{C}_k^f|\\ c_f\in\mathcal{N}_u^f}} \mu_{bu}(t) + (1-\mathbb{I}_{(f=f_r)}) \min_{\substack{\forall u\in\mathcal{C}_k^f|\\ c_f\in\widetilde{\mathcal{N}}_u^f}} \mu_{bu}(t). \tag{IV.3.30}$$

IV.3.4.3 Stability of the Matching

Next, the notion of stability is introduced and an interference estimation method is proposed to guarantee that the HD chunk scheduling game converges to a stable matching.

Definition 18. *Given a matching Υ with $\Upsilon_b = \mathcal{C}_k$ and $\Upsilon_{\mathcal{C}_k} = b$, and a pair $(b', \mathcal{C}'_k)$ with $\Upsilon_b(t) \neq k'$ and $\Upsilon_{\mathcal{C}_k} \neq b'$, (b', k') is said to be blocking the matching Υ and form a blocking pair if: 1) $b' \succ_k b$, 2) $k' \succ_b k$. A matching $\Upsilon*$ is stable if there is no blocking pair.*

Gale-Shapley's DA algorithm [122] provides a polynomial time solution that is guaranteed to be two-sided stable for one-to-one canonical matchings i.e., those matching games where the preference profiles of the players are not affected by any other player's decisions. The influence of a given player's matching over another's is referred to as *externality*. As the game evolves, the existence of externalities triggers dynamic updates in the values of the perceived utilities and, consequently, ensuring the stability of the matching is challenging.

The above matching game cannot be directly solved using DA; the utilities in (IV.3.29)-(IV.3.30) are function of the instantaneous service rate which, in turn depends on the interference –a well-known source of externalities [128]– through the SINR. Moreover, in the context of directional communications, the arrival

direction of the interference caused by other SBSs[4] greatly impacts the service rate. Hence, evaluating the instantaneous interference and casting preferences accordingly implies full knowledge of the system-wide current matching state by all the players, which is impractical in terms of signaling overhead.

Alternatively, to be able to apply a distributed and computationally efficient algorithm, the instantaneous values of the service rate in the utilities are replaced with online estimations. Specifically, an interference learning mechanism based on a moving average procedure will be carried out. Under this procedure, users keep record of the interference experienced at each time instant.

Let the measured inter-SBS interference at user u in the previous time instant $t-1$ be denoted $I_u(t-1)$, and let $\hat{I}_u(t)$ be the estimated inter-SBS interference at time instant t. Adopting an interference estimation procedure with learning parameter ν_1 and moving average inference $\tilde{I}_u^{\nu_2}(t-1)$ with a window of ν_2 samples, the estimated interference is given by

$$\hat{I}_u(t) = \nu_1 I_u(t-1) + (1-\nu_1)\tilde{I}_u^{\nu_2}(t-1). \tag{IV.3.31}$$

Let $\hat{U}_{\mathcal{B}}^{b,\mathcal{C}_k}(t)$, $\hat{U}_{\mathcal{C}}^{\mathcal{C}_k,b}(t)$ be the new utility expressions which exploit the estimated service rate $\hat{\mu}_{bu}(t)=BW_b\log_2\Big(1+\frac{p_b\hat{h}_{bu}(t)g_{bu}^{\mathrm{Rx}}(t)g_{bu}^{\mathrm{Tx}}(t)}{\hat{I}_u(t)+BW_bN_0}(t)\Big)$ through $\hat{\mu}_{uc_f}(t)$, such that

$$\hat{U}_{\mathcal{C}}^{\mathcal{C}_k,b}(t) = \mathbb{I}_{(f=f_r)} \min_{\substack{\forall u\in\mathcal{C}_k^f|\\ c_f\in\mathcal{N}_u^f}} \hat{\mu}_{bu}(t) + (1-\mathbb{I}_{(f=f_r)}) \min_{\substack{\forall u\in\mathcal{C}_k^f|\\ c_f\in\widetilde{\mathcal{N}}_u^f}} \hat{\mu}_{bu}(t), \tag{IV.3.32}$$

$$\hat{U}_{\mathcal{B}}^{b,\mathcal{C}_k}(t) = \sum_{u\in\mathcal{C}_k} \mathbb{I}_{(c_f\in\widetilde{\mathcal{N}}_u^f)}\hat{\alpha}_u(t)(t) = \sum_{u\in\mathcal{C}_k} \mathbb{I}_{(c_f\in\widetilde{\mathcal{N}}_u^f)}\big\{\hat{\alpha}_Q(t) + \mathbb{I}_{(d_{\mathrm{t2MTP}}(t))}\hat{\alpha}_F(t)\big\}. \tag{IV.3.33}$$

Under this new utility formulation there are no longer externalities in the system. Therefore, the HD chunk scheduling matching game can be solved using DA and guaranteed to converge to a stable matching $\boldsymbol{\Upsilon}(t)$. The process described above as well as the details of the matching rounds are described in Algorithm IV.3.1.

IV.3.5 DRNN FoV Prediction and User Clustering

In this section, the DRNN that predicts VR users' FoVs for upcoming video frames and the clustering scheme that leverages FoV and spatial inter-user correlations are described. The selection of the adopted sequential learning model is first motivated and its operation dynamics briefly summarized. Following that, the DRNN architecture implementation details are provided and the training process is explained. Finally, the distance metric driving the user-clustering partitioning and its algorithmic implementation are specified.

[4]Let it be noted here that by matching each SBS to a single cluster with orthogonal non-overlapping beams for the multicast transmission, only the impairment due to inter-SBS interference needs to be considered.

IV.3.5.1 Sequential Deep Learning Model Operation

Predicting a VR user's tiled-FoV is an instance of movement prediction where an input sequence of a user's past and current pose vectors is mapped to a multi-label output. In the output, each label represents one tile in the video frame and its value provides an estimate over the likelihood of the tile belonging to the user's future FoV.

To build the sequential learning model, the GRU [290] architecture is adopted. This architecture is a variant of RNNs that uses two simple gating mechanisms whereby long-term dependencies are effectively tackled and the memory/state from previous activations is preserved. Hence, compared to other models such as long short-term memory (LSTM) units [291], GRUs are faster to train and have proven to perform better for small datasets [292], the case considered in Section IV.3.6.1.

Specifically, for every operation time step –which is measured in terms of video frames and therefore indexed with $f \in \mathcal{F}$– the GRU units update the value of their hidden state $\boldsymbol{h}_f$ as a non-linear function of an input sequence $\boldsymbol{x}_u^f$ and of the previous hidden state $\boldsymbol{h}_{f-1}$. The non-linear function is parameterized by $\boldsymbol{\vartheta}$ following a recurrence relation $\boldsymbol{h}_f = f\big(\boldsymbol{h}_{f-1}, \boldsymbol{x}_u^f; \boldsymbol{\vartheta}\big)$ that is visually sketched in Fig.IV.3.5 and formally described by the following model equations:

$$\Gamma_f = \sigma\big(\boldsymbol{W}_\Gamma \boldsymbol{x}_u^f + \boldsymbol{Z}_\Gamma \boldsymbol{h}_{f-1} + \boldsymbol{b}_\Gamma\big) \tag{IV.3.34}$$

$$r_f = \sigma\big(\boldsymbol{W}_r \boldsymbol{x}_u^f + \boldsymbol{Z}_r \boldsymbol{h}_{f-1} + \boldsymbol{b}_r\big) \tag{IV.3.35}$$

$$\boldsymbol{h}_f = (1 - \boldsymbol{\Gamma}_f) \circledast \boldsymbol{h}_{f-1} + \boldsymbol{\Gamma}_f \circledast \texttt{tanh}\big(\boldsymbol{W} \boldsymbol{x}_u^f + \boldsymbol{Z}\big(\boldsymbol{r}_f \circledast \boldsymbol{h}_{f-1}\big) + \boldsymbol{b}_h\big), \tag{IV.3.36}$$

where weight matrices $\boldsymbol{W}_\Gamma$, $\boldsymbol{Z}_\Gamma$, $\boldsymbol{W}_r$, $\boldsymbol{Z}_r$, $\boldsymbol{W}$, $\boldsymbol{Z}$ and bias terms $\boldsymbol{b}_\Gamma$, $\boldsymbol{b}_r$, $\boldsymbol{b}_h$ represent the model parameters comprised in $\boldsymbol{\vartheta}$ that, with those of the fully connected neural layer in Fig. IV.3.6, are learned during the DRNN offline training process.

The value of the update gate vector $\boldsymbol{\Gamma}_f$, as per (IV.3.34), governs through the linear interpolation in (IV.3.36) the amount of the previous hidden state $\boldsymbol{h}_{f-1}$ and of the new hidden state candidate $\tilde{\boldsymbol{h}}_f = \texttt{tanh}\big(\boldsymbol{W} \boldsymbol{x}_u^f + \boldsymbol{Z}\big(\boldsymbol{r}_f \circledast \boldsymbol{h}_{f-1}\big) + b_h\big)$ contributing to the next hidden state activation $\boldsymbol{h}_f$. Likewise, the reset gate vector $\boldsymbol{r}_f$, as per (IV.3.35), controls the degree of the contribution of the previous hidden state $\boldsymbol{h}_{f-1}$ preserved for the new hidden state candidate $\tilde{\boldsymbol{h}}_f$. When the contribution from the previous state is deemed irrelevant, the next hidden state $\tilde{\boldsymbol{h}}_f$ is reset and will depend only on the input sequence.

IV.3.5.2 DRNN architecture

The building blocks of the proposed deep recurrent learning model $M_{\boldsymbol{\vartheta}}^{v,T_H}$ based on GRU layers and implemented using Keras [293], a high-level neural networks API running on top of a Tensorflow backend, are represented in Fig. IV.3.6.

Input representation: Every T_f, an input sequence of size T_P corresponding to 3DoF pose vectors $\boldsymbol{x}_u^f \triangleq \{\boldsymbol{p}_{3u}^f\}_{f=f_r-T_P+1}^{f_r}$ is fed to the first GRU layer.

Sequence processing: The input is then processed following model equations (IV.3.34)-(IV.3.36) in Section IV.3.5.1 by a T_P time-step GRU cell with a hidden state size equal to 512. Following a rectified linear unit (ReLU) activation that performs a $[z]^+$ operation, the output of the first GRU layer goes through a second GRU layer with the same characteristics. The output state from this second layer $\boldsymbol{h}_f^{(2)} \triangleq \boldsymbol{o}_f^{(2)}$ is then fed to a serial to parallel (S/P) layer before going across a dense neural layer that connects with the N output neurons.

Output representation: Given the multi-label nature of the learning model, a sigmoid activation layer is used to map the N sized dense output into

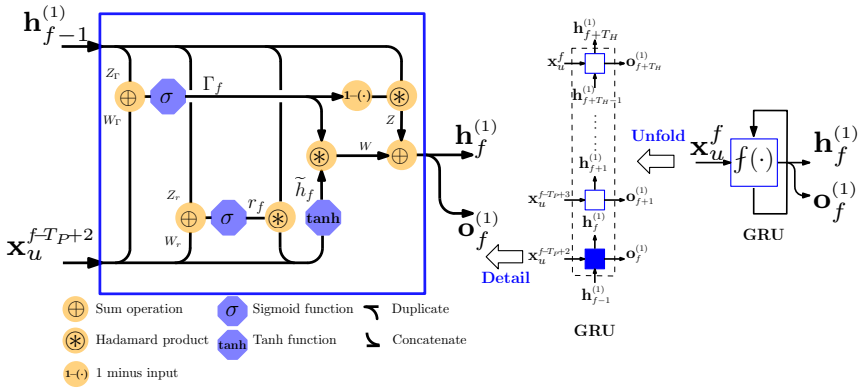

FIGURE IV.3.5: Detailed graphical representation of GRU unfolding and of the $\boldsymbol{h}_f^{(1)}$ computation in the unfolded GRU cell. The notation $(\cdot)^{(1)}$ indicates that the GRU at hand belongs to the first layer, which is highlighted in blue in the DRNN architecture from Fig. IV.3.6. ([271] ©2020 IEEE)

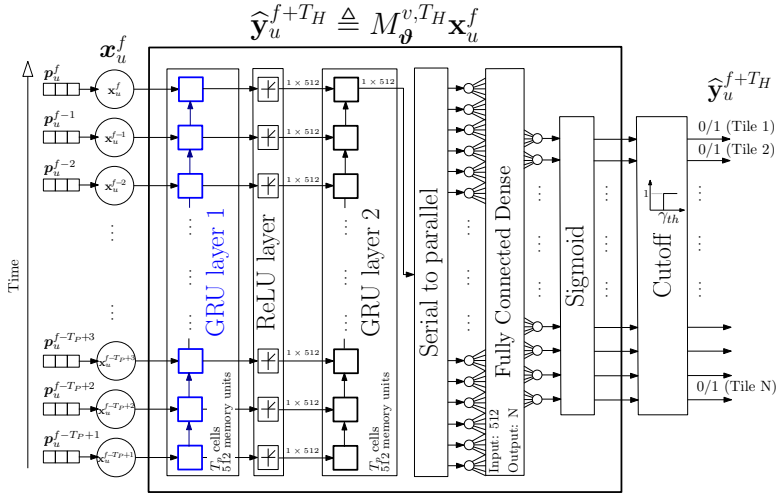

FIGURE IV.3.6: Block diagram of the deep learning model for the edge controller. The DRNN predicts the tiles in the FoV of user u at frame index $f_p = f_r + T_H$, i.e. T_H frames ahead. ([271] ©2020 IEEE)

N probability values or logits $\{\Pr(n) = \sigma(\boldsymbol{W}_d \boldsymbol{h}_f^{(2)} + \boldsymbol{b}_d)_n\}_{n=1}^N$ that are Bernoulli distributed, i.e., the probability of each label is treated as independent from other labels' probabilities. The output of the sigmoid is then binarized with a cutoff layer such that

$$\widehat{y}_{u,n}^{f_p} = \begin{cases} 1, & \sigma(\boldsymbol{W}_d \boldsymbol{h}_f^{(2)} + \boldsymbol{b}_d)_n \geq \gamma_{th}, \\ 0, & \text{otherwise}, \end{cases} \tag{IV.3.37}$$

where $\boldsymbol{W}_d$, $\boldsymbol{b}_d$ are the weights and biases of the dense fully-connected layer and γ_{th} is the threshold value for the cutoff layer, which is chosen to balance accuracy and recall. After the binarization, the predicted FoV for a user u and frame index $f_p = f + T_H$ is retrieved as $\widehat{\mathcal{N}}_u^{f_p} = \{n \in [1, ..., N] \colon \widehat{y}_{u,n}^{f_p} = 1\}$.

IV.3.5.3 DRNN Training

The aim of the training in the supervised deep recurrent learning model $M_{\boldsymbol{\vartheta}}^{v,T_H}$ is to iteratively find the $\boldsymbol{\vartheta}$ parameters that minimize a binary cross-entropy loss function $\mathcal{L}(\boldsymbol{\vartheta})$ for all training instances. This loss function, for model parameters $\boldsymbol{\vartheta}$, labels $y_{u_{tr},n}^{v,f_p}$ and logits $\{\Pr(n)\}_{n=1}^{N}$ captured from the output of the sigmoid layer in Fig. IV.3.6, is expressed as

$$\mathcal{L}(\boldsymbol{\vartheta}) = -\frac{1}{N}\sum_{n=1}^{N}\left[y_{u_{tr},n}^{v,f_p}\log(\Pr(n)) + (1-y_{u_{tr},n}^{v,f_p})\log(1-\Pr(n))\right]. \tag{IV.3.38}$$

During the model offline training, backpropagation through time (BPTT) algorithm [294] and Adam algorithm [295] are used to optimize the gradients. Adam is set with learning rate $\alpha = 0.01$, parameters $\beta_1 = 0.9$, $\beta_2 = 0.999$ and no decay. The gradient backpropagation is performed over data batches of size 512 examples and during 20 training epochs.

Next, the information related to users' physical location and to their predicted FoVs is leveraged to develop a user clustering scheme.

IV.3.5.4 Proposed FoV and Location Aware User Clustering

Once the predictions of the entire set of users $\mathcal{U}$ for a frame index f_p are ready, users viewing the same video v are grouped into clusters based on their spatial and content correlations.

Mathematically, let $\mathcal{C}_k^{f_p}$ denote the k-th cluster in which the set of users $\mathcal{U}$ is partitioned for frame index $f_p = f + T_H$ such that $\bigcup_{k=1}^{K}\mathcal{C}_k^{f_p} = \mathcal{U}$. Here, the cluster partitioning can be obtained by i) computing the $|\mathcal{U}|\times|\mathcal{U}|$ distance matrix $\boldsymbol{D}^{f_p}$, whose $d_{u,u'}^{f_p} = \tilde{d}_{u,u'}^{f_p}\left(d_{uu'}^{\mathrm{2D}}/d_{min}^{\mathrm{2D}}\right)$ element results from quantifying the FoV-related distance or dis-similarity between any pair of users $\{u,u'\}\in\mathcal{U}$ which is given by

$$\tilde{d}_{u,u'}^{f_p} = 1 - \frac{\sum_{n=1}^{N}\mathbb{I}_{\{n\in\widehat{\mathcal{N}}_u^{f_p}\}}\mathbb{I}_{\{n\in\widehat{\mathcal{N}}_{u'}^{f_p}\}}}{\left(N-\sum_{n=1}^{N}\mathbb{I}_{\{n\notin\widehat{\mathcal{N}}_u^{f_p}\}}\mathbb{I}_{\{n\notin\widehat{\mathcal{N}}_{u'}^{f_p}\}}\right)}, \tag{IV.3.39}$$

and ii) by scaling it with their relative physical distance $d_{uu'}^{\mathrm{2D}}$ divided by d_{min}^{2D}, that denotes the minimum value for such relative distance as per the theater dimensions and seat arrangements.

To implement the clustering scheme that builds on the above distance metric, a hierarchical agglomerative clustering with average linkage has been considered. This clustering scheme allows operating over the constructed dendrogram to increase/decrease the number of resulting clusters and, thereby grants flexibility to investigate the trade-offs in terms of communication resource utilization versus achieved performance when many/few clusters, as per K, are used.

Once the clusters $\{\mathcal{C}_k^{f_p}\}_{k=1}^{K}$ have been estimated using the specific clustering strategy, the cluster-level FoV is built and ready to be leveraged in the proposed multicast/unicast scheduling strategy as $\widehat{\mathcal{N}}_{\mathcal{C}_k}^{f_p} = \bigcup_{u\in\mathcal{C}_k^{f_p}}\widehat{\mathcal{N}}_u^{f_p}$.

IV.3.6 Simulation Setup and Performance Evaluation

In this section, the effectiveness of the proposed solution is numerically validated. For that purpose, first the dataset with real head-tracking information for 360° videos and the DRNN FoV prediction accuracy results, which will impact the performance evaluation of the mmWave multicast transmission, will be discussed. Following that, the deployment scenario and the considered baseline schemes are described[5]. Finally, the performance evaluation of the proposed approach is evaluated and some insightful results are discussed.

IV.3.6.1 360° Video Head-tracking Dataset and FoV Prediction Accuracy Results

To validate the proposed approach, the information fed into the DRNN for training and simulation corresponds to 3DoF traces from the dataset in [296] whereby the pose of 50 different users while watching a catalog of $V = 10$ HD 360° videos from YouTube were tracked. The selected videos are 60 s long, have 4K resolution and are encoded at 30 fps. A 100°×100° FoV is considered and, to build the tiled-FoV, the EQR projection of each of the video frames has been divided into $N = 200$ square tiles of 192×192 pixels arranged in a regular grid of $N_V = 10$ and $N_H = 20$ tiles. The dataset provides the ground-truth labels after mapping the 3DoF poses to their corresponding tiled FoVs. In view of the size and characteristics of the dataset, the original 50 users therein have been split into disjoint $\mathcal{U}_{tr}$ and $\mathcal{U}$ sets for training and for test purposes with cardinalities $|\mathcal{U}_{tr}| = 35$ and $|\mathcal{U}| = 15$, respectively.

Results in Table IV.3.1 represent the accuracy of the prediction models for different values of T_H in terms of the Jaccard similarity index, which is defined for each user u viewing a frame f of a video v as the intersection over the union between the predicted and the actual FoV tile sets $J(\widehat{\mathcal{N}}_u^f, \mathcal{N}_u^f) = |\widehat{\mathcal{N}}_u^f \cap \mathcal{N}_u^f| / |\widehat{\mathcal{N}}_u^f \cup \mathcal{N}_u^f|$. In Table IV.3.1, this index has been first averaged over the frames of the video at hand, and then over all the test users, i.e.,

$$J_v^{T_H} = \frac{1}{|\mathcal{U}||\mathcal{F}|} \sum_{u \in \mathcal{U}} \sum_{f \in \mathcal{F}} \frac{|\widehat{\mathcal{N}}_u^f \cap \mathcal{N}_u^f|}{|\widehat{\mathcal{N}}_u^f \cup \mathcal{N}_u^f|}.$$

The results in the table confirm the anticipated decrease of the accuracy as the prediction horizon moves further away from the last reported pose. Similarly, results in Table IV.3.2 show that increasing the depth of the DRNN by adding more GRU layers is counter-productive; it overfits the training data and unnecessarily increases the complexity of the model.

IV.3.6.2 Deployment Details and Reference Baselines

Two VR theater settings are considered; a small size and a medium size capacity theaters with dimensions $\{s_r, s_c\} = \{5, 10\}$ and $\{s_r, s_c\} = \{10, 15\}$ seats, respectively. In both configurations the seats are separated from each other by 2 m, and there is a 4 m distance from the seat area to the walls of the enclosure. As detailed in Section IV.3.2, SBSs are located at ceiling level in the upper 4

[5]For the interested reader, a demo showcasing the qualitative results achieved under these schemes is available at `https://youtu.be/djt9efjCCEw`.

TABLE IV.3.1: FOV Prediction Accuracy: Effect of Prediction Horizon. ([271] ©2020 IEEE)

Video	Category[6]	Jaccard similarity index $J_v^{T_H}$ (mean±std. dev.)			
		$T_H = 5$	$T_H = 10$	$T_H = 20$	$T_H = 30$
SFRSport	NI, SP	0.70±0.06	0.69±0.04	0.63±0.03	0.50±0.05
MegaCoaster	NI, FP	0.68±0.06	0.65±0.05	0.64±0.07	0.61±0.05
RollerCoaster	NI, FP	0.74±0.05	0.70±0.05	0.64±0.04	0.63±0.05
SharkShipwreck	NI, SP	0.53±0.03	0.48±0.03	0.44±0.03	0.36±0.03
Driving	NI, FP	0.76±0.04	0.71±0.04	0.63±0.03	0.58±0.02
ChariotRace	CG, FP	0.71±0.02	0.71±0.02	0.68±0.02	0.65±0.03
KangarooIsland	NI, SP	0.69±0.04	0.65±0.03	0.63±0.03	0.58±0.03
Pac-man	CG, FP	0.83±0.03	0.73±0.05	0.67±0.05	0.66±0.06
PerilsPanel	NI, SP	0.69±0.02	0.65±0.02	0.56±0.03	0.53±0.03
HogRider	CG, FP	0.68±0.04	0.66±0.04	0.65±0.04	0.57±0.05

TABLE IV.3.2: FOV Prediction Accuracy: Effect of the number of GRU Layers. ([271] ©2020 IEEE)

Video	Jaccard similarity index $J_v^{T_H}$ (mean ± std. dev.)			
	T_H	Number of GRU layers		
		1	2	3
MegaCoaster	5	0.52±0.08	0.68±0.06	0.68 ± 0.04
	10	0.50±0.07	0.65±0.05	0.65 ± 0.03
	20	0.46±0.07	0.64±0.07	0.63 ± 0.05
	30	0.32±0.04	0.61±0.05	0.61 ± 0.06
Pac-man	5	0.82±0.04	0.83±0.03	0.76 ± 0.04
	10	0.60±0.07	0.73±0.05	0.73 ± 0.04
	20	0.53±0.05	0.67±0.05	0.67 ± 0.05
	30	0.49±0.06	0.66±0.06	0.65 ± 0.05

corners of the theater. A total of 7 different scenarios are studied for simulation: scenarios sT-$v correspond to the small theater with 10 users per video with $\$ = V = \{1, 3, 5\}$ videos being played; scenarios bT-$v correspond to the big theater with 15 users per video with $\$ = V = \{1, 3, 5, 10\}$ videos being played. The set of default parameter values for simulations is provided in Table IV.3.3. For benchmarking purposes, the following baseline and proposed schemes are considered:

- `UREAC`: Chunk requests are scheduled in real-time for mmWave unicast transmission.
- `MREAC`: Chunk requests are scheduled in real-time and multi-beam mmWave multicast transmission is used.
- `MPROAC`: Chunk requests are proactively scheduled and multi-beam mmWave multicast transmission is used.
- `MPROAC+`: Corresponds to the *proposed* approach which considers `MPROAC` and the HRLLBB constraint in the scheduler.

IV.3.6.3 Discussion

Next, the impact of the FoV prediction horizon, the requested video quality, the maximum number of clusters and, the network size are evaluated. To that

[6]With category codes: NI=Natural Image, CG=Computer Generated, SP=Slow-paced, FP=Fast-paced.

TABLE IV.3.3: Main Simulation Parameters in the Proactive mmWave multicast streaming VR Theater scenario. ([271] ©2020 IEEE)

Parameter	Value
Simulation time	60000 ms
Channel coherence time (T_c)	1ms
Blockage re-evaluation time (T_{block})	100 ms
Transmission slot duration (T_t)	0.25 ms
RF chains	1 per HMD; 4 per SBS
Beam-level Rx beamwidth	5°
Beam-level Tx beamwidths	[5°:5°:45°]
Carrier frequency (f_c)	28 GHz
Bandwidth (BW_b)	0.85 GHz
Noise spectral density (N_0)	-174 dBm/Hz
Noise figure	9 dB
SBS transmit power (p_i)	15 dBm
Motion-to-photon delay (τ_{MTP})	10 ms
Delay reliability metric ϵ_d	0.01
Tiles per frame (N)	200
Video frame duration (T_f)	33 ms (30 fps video)
Videos catalog size (V)	[1, 3, 5, 10]
Users per video	[10, 15]
Number of clusters (K)	[$2V$, $3V$, $4V$]
Prediction horizon (T_H)	[5, 10, 20, 30] frames
DRNN input sequence (T_P)	30 pose values
DRNN cutoff value (γ_{th})	0.5

end, the performance of each scheme is evaluated through its average and the 99th percentile (delay 99 pctl) transmission delays, calculated as the delay until the last tile in the FoV of the requesting user has been delivered. It should be mentioned that focusing merely on the average system performance would fail to capture the real-time aspects of the problem. Consequently, to show that the adopted Lyapunov online control method is able to keep the latency bounded below the τ_{MTP} threshold with the desired probability $1-\epsilon$, the 99th percentile delay is provided as well. Furthermore, alongside with the 99th percentile delay plots, the HD successful delivery rate metrics highlight the trade-off between the utility (maximizing the quality) and the probabilistic latency constraint.

Lastly, for each user u and frame index f the Jaccard similarity index between the successfully delivered chunks and the actual FoV is computed. This index, also referred to as the intersection over the union score is given by $J(\breve{\mathcal{N}}_u^f, \mathcal{N}_u^f) = |\breve{\mathcal{N}}_u^f \cap \mathcal{N}_u^f| / |\breve{\mathcal{N}}_u^f \cup \mathcal{N}_u^f|$, with $\breve{\mathcal{N}}_u^f \subseteq \bigcup\{\widehat{\mathcal{N}}_{\mathcal{C}_k}^f, \mathcal{N}_u^f\}$ denoting the set of tiles correctly decoded at user $u \in \mathcal{C}_k^f$. It is observed here that $\breve{\mathcal{N}}_u^f \setminus \mathcal{N}_u^f$ represents a measure of the multicasting overhead owing to operating with cluster-level predicted FoV chunk requests that, hence, will grow larger the less correlated the FoVs of the cluster-members are. Similarly, $\mathcal{N}_u^f \setminus \breve{\mathcal{N}}_u^f \neq \emptyset$ indicates missed tiles. Therefore, the evolution of this index averaged over all the users and frame indices globally captures the trade-off related to the FoV correlation among cluster members.

IV.3.6.3.1 Impact of the FoV Prediction Horizon

The impact of the DRNN prediction horizon T_H on the performance of the proposed approaches `MPROAC+` and `MPROAC` is first considered and compared to the reactive baselines `UREAC` and `MREAC`, whose performance is not affected. Intuitively, in the proposed scheme longer T_H allow the scheduler to schedule future frames earlier, but increases the overall amount of data to be transmitted due to having lower prediction accuracy, as shown in Table IV.3.1. In Fig. IV.3.7, it can be

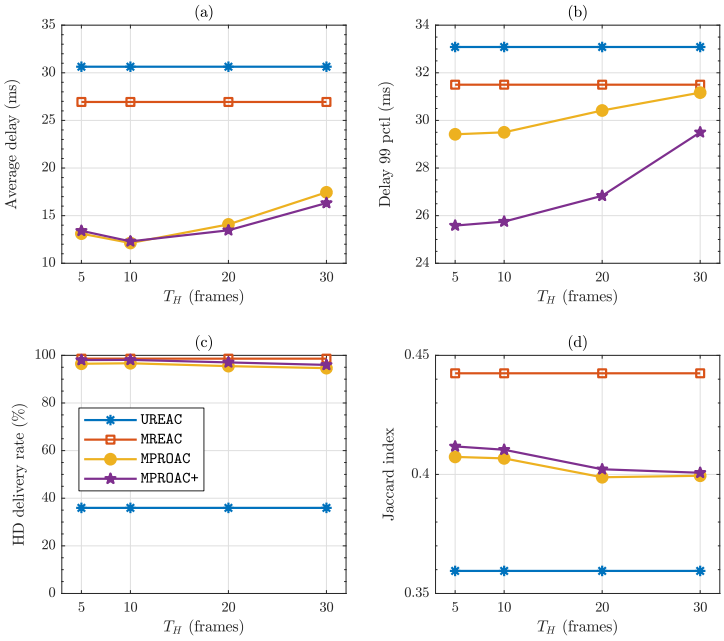

FIGURE IV.3.7: (a) Average delay, (b) 99th percentile delay, and (c) HD delivery rate and (d) Jaccard index performance versus the prediction horizon (in frames) in `bT-3v` with a load of 1 Gbps per user (0.972 Mb chunk size), and $V_\Delta = 1 \cdot 10^8$.([271] ©2020 IEEE)

seen that the scheduler can maintain high HD quality streaming even with long prediction horizons. The frame delay is shown to first decrease, due to having more time to schedule chunks in advance, then increases again, due to having to schedule a higher number of chunks in real-time that were missed by the predictor. Transmitting more in real-time leads to lower utilization of the user's predicted FoV, which decreases the Jaccard index.

IV.3.6.3.2 Impact of the Requested Video Quality

Next, the impact of the requested HD video quality on the performance of the proposed scheme is explored. To that end, looking into both the sT-3v and bT-3v scenarios, the impact of the quality through the HD *chunk size* of the frame shown to the user is evaluated. The performance metrics of each scheme are depicted in Fig. IV.3.8(a)-(d) and Fig. IV.3.8(e)-(h) for the small and big theater scenarios, respectively. The figures clearly show the trade-off between frame delay and HD streaming rate. As the chunk size increases, the average and 99th percentile delays increase for the different schemes. Moreover, comparing `UREAC` with the other schemes, it is shown that multicasting brings $40-50\%$ increase in the HD rate and $33-70\%$ latency reduction through the utilization of common FoVs of different users. At high chunk sizes, the higher network load clearly increases the service delay. By delivering the predicted frames in advance, both the `MPROAC+` and `MPROAC` minimize the average delay without sacrificing the HD quality rate. The proposed `MPROAC+` scheme is shown to also keep the worst delay values bounded due to imposing the HRLLB constraint, as compared to

the MPROAC. Further comparing UREAC to MREAC, it is shown that multicasting significantly reduces the delay due to the utilization of common FoVs of different users.

As the performance of the MPROAC+ and MPROAC schemes for different values of the Lyapunov parameter V_Δ are provided, the trade-off between the frame delay and the quality is further illustrated. Indeed, the results in Fig. IV.3.8 show that as the V_Δ increases, the scheduling algorithm prioritizes maximizing users' HD delivery rate, whereas at lower values of V_Δ, the scheduler prioritizes stabilizing the traffic and virtual queues i.e., keeping the delay bounded with high probability. This comes at the expense of having lower HD delivery rate. The MPROAC+ approach also achieves 17-37% reduction in the 99th percentile latency as compared to MPROAC and MREAC schemes, respectively.

Furthermore, the Jaccard similarity in Fig. IV.3.8(d) and Fig. IV.3.8(h) illustrates the trade-offs of utility and latency versus transmission utilization. At low traffic loads, high quality rate and low latency result in lower Jaccard index, which is due to the large amount of extra data sent due to sending an estimated FoV. As the traffic load increases, the proactive schemes transmits more real-time frames, which increase the Jaccard index. The Jaccard index decreases again at higher traffic loads as the effect of missed frames increases (the average delay approaches the deadline as can be seen in Fig. IV.3.8(a), Fig. IV.3.8(e))

IV.3.6.3.3 Impact of the Number of Clusters

Subsequently, the impact of the number of clusters per video on the performance of the multicast schemes is considered as compared to the UREAC scheme, which operates in unicast. Fig. IV.3.9 shows that a lower number of clusters allows for more utilization of the common FoV of users, which results in lower delay and higher HD quality rate. By making the cluster size smaller, higher number of clusters per video, however, higher Jaccard similarity indices are scored, due to sending less unnecessary chunks to users, as shown in Fig. IV.3.9(d).

IV.3.6.3.4 Impact of the Network Size

Finally, the impact of the network size is investigated. To do so, both the small and the big theater configurations are considered under an increasing amount of users and videos. In Fig. IV.3.10, it is shown that the proposed scheme achieves close to 100% HD streaming rate in scenarios 1, 2, 4, and 5 while maintaining lower frame delay. Moreover, in the congested scenarios with high number of users and videos, i.e., scenarios 3, 6, and 7, the results show that multicasting provides substantial performance improvement through the gains of MREAC over UREAC. This demonstrates the capability of multicasting to minimize the latency of VR streaming to multi-user scenarios. Although the large amount of requested data in these congested scenarios limits the available resources to schedule the predicted frames in advance, the results in Fig. IV.3.10 show that the proposed scheme MPROAC+ can achieve higher HD delivery rate and lower delay compared to the baselines.

IV.3.7 Conclusions

In this chapter, the second of the proposed two mmWave VR scenarios in Part IV has been investigated. To that end, the problem of maximizing users' VR streaming QoE has been formulated as a network-wide HD frame admission maximization problem subject to low latency constraints with very high reliability. A

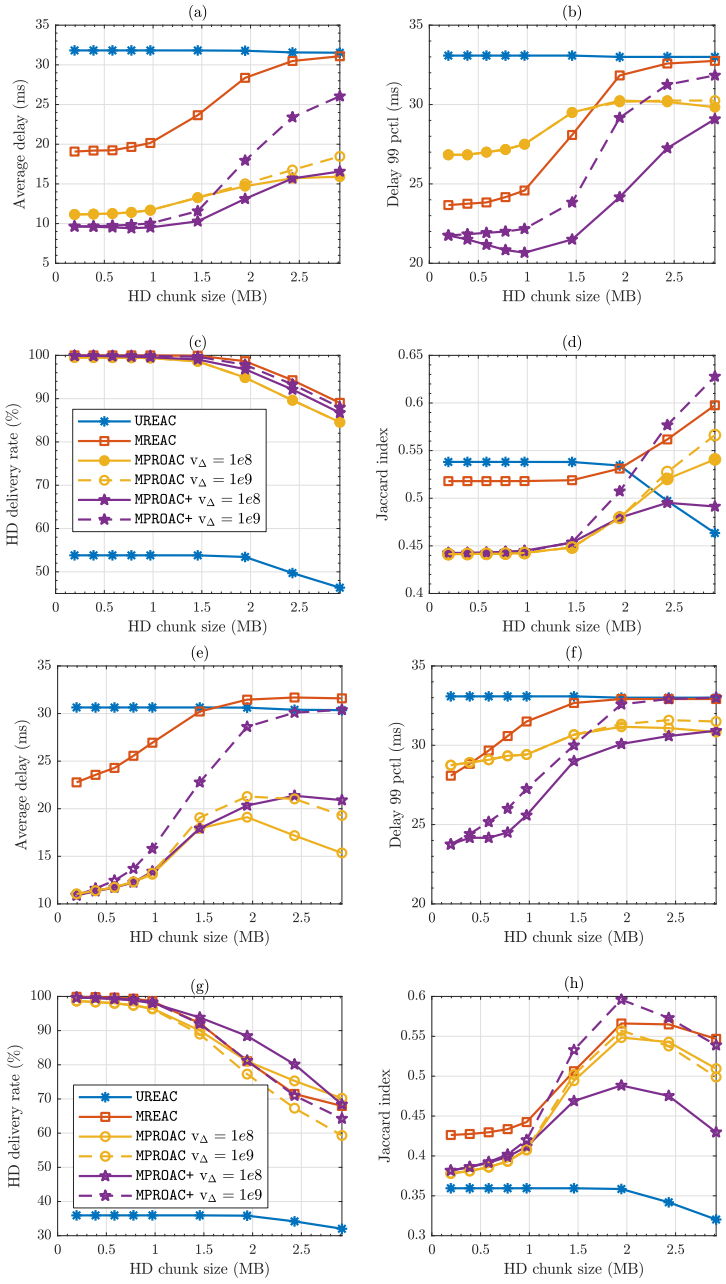

FIGURE IV.3.8: (a) and (e) Average delay, (b) and (f) 99th percentile delay, (c) and (g) HD delivery rate and (d) and (h) Jaccard index performance in `sT-3v` and `bT-3v`, respectively, as a function of the HD chunk size, for $V = 3$ videos, $K = 2 \times V$ clusters, $T_H = 5$ frames, and Lyapunov trade-off $V_\Delta = 1 \cdot 10^8$ and $V_\Delta = 1 \cdot 10^9$.([271] ©2020 IEEE)

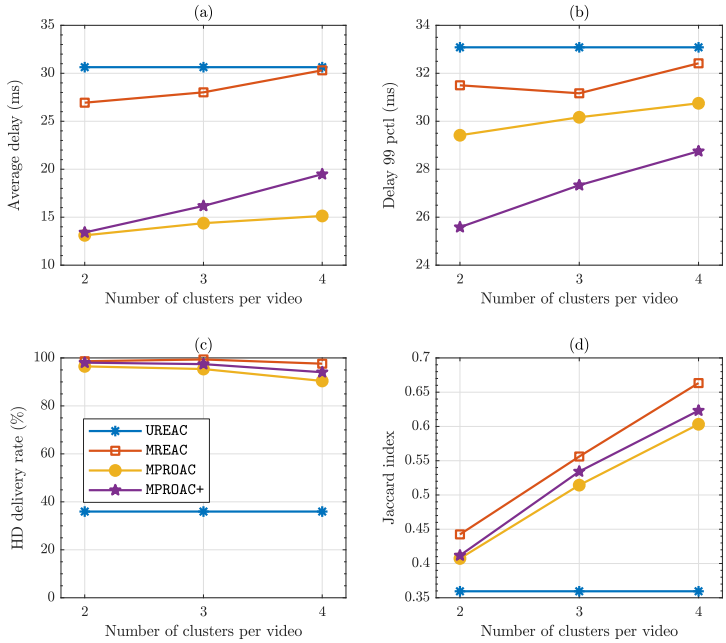

FIGURE IV.3.9: (a) Average delay, (b) 99th percentile delay, and (c) HD delivery rate and (d) Jaccard index performance versus cluster per video, in `bT-3v` with a load of 1 Gbps per user (0.972 Mb chunk size),, and $V_\Delta = 1 \cdot 10^8$.([271] ©2020 IEEE)

Lyapunov-framework based approach has been proposed. This approach transforms the stochastic optimization problem into a series of successive instantaneous static optimization subproblems. Subsequently, for each time instant, a matching theory algorithm is applied to allocate SBS to user clusters and leverage a mmWave multicast transmission of the HD chunks. Using simulations, it has been shown that the proposed DRNN can predict the VR users' future FoV with high accuracy. Predictions are further leveraged to cluster users and proactively schedule the multicast transmission of their future video chunks. Moreover, simulations have provided evidence of the considerable gains achieved by the proposed model when compared to both reactive baseline schemes, notably outperforming the unicast transmission baseline.

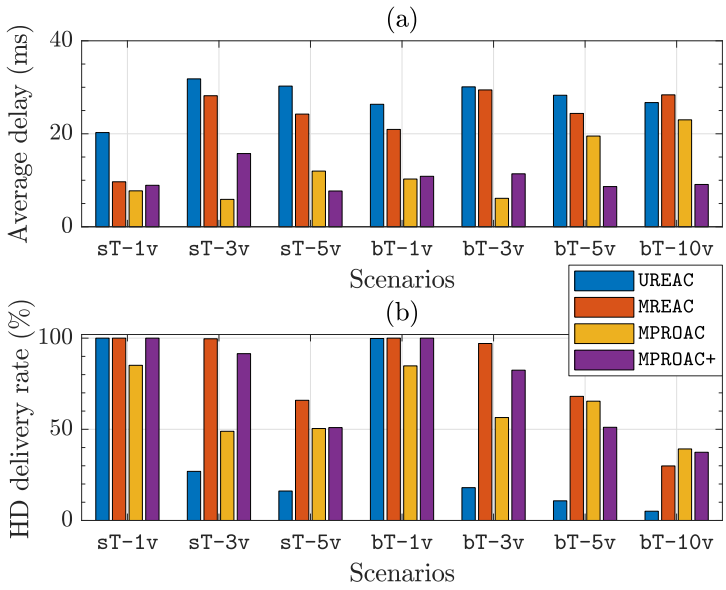

FIGURE IV.3.10: (a) Average delay and (b) HD delivery rate performance for different network scenarios with a load of 1 Gbps per user (0.972 Mb chunk size). ([271] ©2020 IEEE)

Appendix

IV.3.A Proof of Lemma 1

By leveraging the inequality $(\max[x,o])^2 \leq x^2$ for $x \geq 0$, after squaring the physical and virtual queues in (IV.3.11), (IV.3.17) and (IV.3.18) the upper bounds for each of the above terms are derived as:

$$q_u^2(t+1) - q_u^2(t) \leq (a_u^{tot}(t))^2 + \sum_{f=\{f_r,f_p\}} \sum_{c_f \in \widetilde{\mathcal{N}}_u^f} \Big(\mu_{uc_f}^2(t) - 2a_u^{tot}(t)\mu_{uc_f}(t)\Big) - 2q_u(t)\big(\mu_{uc_f}(t) - a_u^{tot}(t)\big), \tag{IV.3.A.1}$$

$$z_u^2(t+1) - z_u^2(t) \leq (a_u^{tot}(t))^2 + \gamma_u^2(t) - 2a_u^{tot}(t)\gamma_u(t) - 2z_u(t)\big(a_u^{tot}(t) - \gamma_u(t)\big), \tag{IV.3.A.2}$$

$$j_{uf}^2(t+1) - j_{uf}^2(t) \leq q_u^2(t+1)\big(\mathbb{I}_{(d_{\text{t2MTP}})} - \epsilon_d\big)^2 + 2j_{uf}(t)\big(\mathbb{I}_{(d_{\text{t2MTP}})} - \epsilon_d\big)q_u(t+1), \tag{IV.3.A.3}$$

with the one time slot Lyapunov drift given by

$$\begin{aligned}\Delta\mathscr{L}_t &\triangleq \mathscr{L}\chi(t+1) - \mathscr{L}\chi(t)\\ &= \frac{1}{2}\sum_{u\in\mathcal{U}}\Bigg\{\Big(q_u^2(t+1) - q_u^2(t)\Big) + \Big(z_u^2(t+1) - z_u^2(t)\Big)\\ &+ \sum_{f\in\mathcal{F}}\Big(j_{uf}^2(t+1) - j_{uf}^2(t)\Big)\Bigg\}.\end{aligned} \tag{IV.3.A.4}$$

Replacing the term $q_u(t+1)$ in (IV.3.A.3) with

$$q_u(t+1) = q_u(t) + \sum_{f=\{f_r,f_p\}} \sum_{c_f \in \widetilde{\mathcal{N}}_u^f} a_u^{tot}(t) - \mu_{uc_f}(t), \tag{IV.3.A.5}$$

due to the fact that having $\mathbb{I}_{(d_{\text{t2MTP}})} = 1$ entails a non-empty queue guarantee, and combining (IV.3.A.1)-(IV.3.A.3), an upperbound on the drift function can be expressed as

$$\Delta\mathscr{L}_t \leq \frac{1}{2}\sum_{u\in\mathcal{U}}\Bigg[\underbrace{-2\big(\mathbb{I}_{(d_{\text{t2MTP}})} - \epsilon_d\big)^2\Bigg\{q_u(t)\Big(\sum_{f=f_r}^{f_p}\sum_{c_f\in\widetilde{\mathcal{N}}_u^f}\mu_{uc_f}(t) - a_u^{tot}(t)\Big)\Bigg\}}_{\#a} \tag{IV.3.A.6}$$

$$+ \underbrace{\big(\mathbb{I}_{(d_{\text{t2MTP}})} - \epsilon_d\big)^2\Bigg\{q_u^2(t) + \Big(\sum_{f=f_r}^{f_p}\sum_{c_f\in\widetilde{\mathcal{N}}_u^f}\mu_{uc_f}(t) - a_u^{tot}(t)\Big)^2\Bigg\}}_{\#b}$$

$$
\begin{aligned}
&+2\big(\mathbb{I}_{(d_{\text{t2MTP}})}-\epsilon_d\big)\Big\{q_u(t)\sum_{f=f_r}^{f_p} j_{uf}(t)\Big\}_{\#c}\\
&-2\big(\mathbb{I}_{(d_{\text{t2MTP}})}-\epsilon_d\big)\Big\{\sum_{f=f_r}^{f_p}\sum_{c_f\in\widetilde{\mathcal{N}}_u^f} j_{uf}(t)\Big(\mu_{uc_f}(t)-a_u^{tot}(t)\Big)\Big\}_{\#d}\\
&+\Big\{\Big(\sum_{f=f_r}^{f_p}\sum_{c_f\in\widetilde{\mathcal{N}}_u^f}\mu_{uc_f}(t)-a_u^{tot}(t)\Big)^2+\Big(a_u^{tot}(t)-\gamma_u(t)\Big)^2\Big\}_{\#e}\\
&-2\Big\{z_u(t)\Big(a_u^{tot}(t)-\gamma_u(t)\Big)\Big\}_{\#f}-2\Big\{q_u(t)\Big(\sum_{f=f_r}^{f_p}\sum_{c_f\in\widetilde{\mathcal{N}}_u^f}\mu_{uc_f}(t)-a_u^{tot}(t)\Big)\Big\}_{\#g}\Big].
\end{aligned}
$$

Note that the terms $\#b$, $\#c$, and $\#e$ in (IV.3.A.6) are quadratic, therefore upper bounded to comply with the assumption of queue stability. Hence, let

$$
\begin{aligned}
\Delta_0(t)\geq \frac{1}{2}\sum_{u\in\mathcal{U}}\Bigg\{&2\big(\mathbb{I}_{(d_{\text{t2MTP}})}-\epsilon_d\big)\Big\{q_u(t)\sum_{f=\{f_r,f_p\}} j_{uf}(t)\Big\}\\
&+\big(\mathbb{I}_{(d_{\text{t2MTP}})}-\epsilon_d\big)^2\Big\{q_u^2(t)+\Big(\sum_{f=\{f_r,f_p\}}\sum_{c_f\in\widetilde{\mathcal{N}}_u^f}\mu_{uc_f}(t)-a_u^{tot}(t)\Big)^2\Big\}\\
&+\Big\{\Big(\sum_{f=\{f_r,f_p\}}\sum_{c_f\in\widetilde{\mathcal{N}}_u^f}\mu_{uc_f}(t)-a_u^{tot}(t)\Big)^2+\Big(a_u^{tot}(t)-\gamma_u(t)\Big)^2\Big\}\Bigg\}
\end{aligned}
\tag{IV.3.A.7}
$$

be the constant parameter at each time instant t collecting the aforementioned terms from the drift above. After subtracting the penalty term $V_\Delta\mathbb{E}\big[U\big(\{\gamma_u(t)\}\big)\big]$ on both sides of (IV.3.A.6), and further operating on $\#a$, $\#d$ and $\#g$ to denote α_u the term

$$
\alpha_u(t)=\big[\big(\mathbb{I}_{(d_{\text{t2MTP}})}-\epsilon_d\big)q_u(t)+\sum_{f\in\mathcal{F}} j_{uf}(t)\big]\big(\mathbb{I}_{(d_{\text{t2MTP}})}-\epsilon_d\big)+q_u(t),
$$

it follows that

$$
\begin{aligned}
\Delta\mathscr{L}_t-V_\Delta\mathbb{E}\Big[U\Big(\Big\{\gamma_u(t)\Big\}\Big)\Big]\leq\Delta_0(t)&-\sum_{u\in\mathcal{U}}V_\Delta\mathbb{E}\Big[U\Big(\big\{\gamma_u(t)\big\}\Big)\Big]\\
&-\sum_{u\in\mathcal{U}}\alpha_u(t)\Big(\sum_{f=\{f_r,f_p\}}\sum_{c_f\in\widetilde{\mathcal{N}}_u^f}\mu_{uc_f}(t)-a_u^{tot}(t)\Big)\\
&-\sum_{u\in\mathcal{U}}z_u(t)\Big(a_u^{tot}(t)-\gamma_u(t)\Big),
\end{aligned}
$$

which after some more rearrangements yields equation (IV.3.20).

Part V

Concluding Remarks

"There will come a time when you believe everything is finished. That will be the beginning."

Louis L'Amour

Chapter V.1

Conclusions, List of Publications and Future Research Directions

> "Let the future tell the truth, and evaluate each one according to his work and accomplishments. The present is theirs; the future, for which I have really worked, is mine."
>
> Nikola Tesla

V.1.1 Conclusions

As it can be ascertained from the huge interest attracted within the research community, mmWave communications have been, and will remain in the upcoming years, one of the most hot research areas in wireless communications. The leap from traditional sub-GHz frequencies to operating GHz, *i.e.*, mmWave, and soon to THz communications seeking for new, much needed, spectrum spots has brought on renewed challenges at PHY and MAC layers. These new challenges will add yet another level of complexity to the envisioned hyper-flexible wireless networking ecosystem. In this context, the role that CI and ML are already playing to learn about the static and dynamic components of the radio environment will not only not die out, but it will undoubtlessly flourish to the point of becoming crucial to exploit configurable radios and adjust to the ever increasing requirements [78], [297].

This Thesis has shed light on practical aspects of the use of mmWave communications and CI techniques in 5G networks. To that end, two specific scenarios that face stringent latency and reliability constraints have been studied: vehicular communications and mobile VR. Being only one of the many pieces in the challenging jigsaw of 5G, the role of mmWave communications in the above scenarios has been combined with other new paradigms such as MEC and caching, to conform the so-called 3C triplet and with techniques such as MC and multicasting for small cell networks (SCNs). In particular, the contributions and findings framed within this Thesis are related to each of the above scenarios and can, therefore be summarized as:

WHAT?

The Thesis has provided informed evidences that techniques brought from the CI realm can efficiently support latency-constrained wireless communications held over the mmWave frequency band. All use cases and scenarios considered herein undergo severe restrictions on the maximum latency admissible for the applications deployed thereon. As a result, different mathematical problems have been formulated to reflect such constraints, which

have been tackled by different CI methods. It is important to note that all utilized techniques aim at providing machine intelligence and autonomy to systems and processes involved in the allocation of resources. As such, elements from machine learning (clustering and Deep Learning predictive learning), stochastic and meta-heuristic optimization, and matching theory have been put to practice and validated as potential technology enablers of the demanding resource allocation and topology optimization paradigms that underlie beneath the challenges of mmWave-based wireless communications.

HOW?

The Thesis has offered an overview of the state of the art of each of the scenarios where the performance of CI techniques has been assessed, which appropriately frames the technical contribution achieved by the author of the Thesis. Furthermore, for the sake of rigor and coherence, a principled research methodology has been followed, ranging from the motivation and mathematical problem statement, to the design of an experimental setup targeting the production of insightful results with respect to the problem(s) under analysis. Where applicable, algorithmic counterparts considered for benchmarking purposes have been argued and described. An emphasis has been also placed on ensuring realism in the simulation environments designed for each scenario, which contributes further to the practical transferability of the research findings to real setups.

WHERE?

The Thesis has revolved in two different general application scenarios: vehicular communications and virtual reality. For both scenarios, solid background and rationale has been given for the noted relevance of latency guarantees in wireless communications held therein.

Specifically, in vehicular communications the Thesis has considered two different use cases:

1. mmWave V2V communications in multilane highways, for which distributed vehicle-to-vehicle association and beam alignment have been studied; and
2. the exchange of sensing information in an urban road junction, where aspects such as the quality/resolution, timeliness and availability of the information has been considered when pairing vehicles through mmWave links.

As for mobile virtual reality, the Thesis has elaborated on another two use cases:

1. A gaming arcade, where optimum scheduling, caching and proactive computation of HD video frames is sought subject to latency constraints; and
2. a 360° VR theater, where the previous proactive computation problem is extended to also consider multicast transmissions, the prediction of future content requests from the spectators, and their relative location in the theater with respect to the directional antennas operating on the mmWave band.

Quantitative measures of the performance of CI techniques when dealing with the allocation of assets (distributed transmitter-to-receiver association, beamwidth optimization, proactive frame scheduling, etc.) have been

gauged and discussed, identifying performance gaps of statistical significance and unveiling future directions of interest for future research, which are presented in Section V.1.3.

On a closing note: as in many other fields and sectors of activity, all algorithmic families falling under the artificial intelligence umbrella (including computational intelligence) are called to play a major role towards solving problems and learning tasks underneath. Wireless communications are not an exception to this claimed relevance, as has been empirically proven in this Thesis over several application scenarios and a diversity of CI techniques.

V.1.2 List of Publications

As a result of the research conducted by the author of this Thesis while pursuing her Doctoral Degree, a total of **7 journal articles**, **1 e-Letter** and **15 international conference contributions** have been **published**. In addition, **1** more **journal submission** is still **under review**.

While, as per Table I.1.1, all the aforementioned publications have served their purpose towards achieving the primary and secondary goals set from its inception for this Thesis, some constitute its core. Accordingly, these contributions are next classified such that those more closely related to the Thesis are first indexed in subsection V.1.2.1, whereas those others that fall outside of the scope of the Thesis are reported in V.1.2.2.

In both lists, for journal and magazine publications, the journal citation reports (JCR) impact factor (IF)[1] and the rank of the journal within its category are provided as an evidence of quality.

V.1.2.1 Publications Related to this Thesis

In what follows, the list of journal and international conference contributions that are related to the contents presented within this Thesis are detailed. Among these contributions, the core of the Thesis is based on the works in [**J5**]–[**J3**], [**L1**] and [**C1**], [**C5**]–[**C7**], which are already published, and in [**J4**] that is still under review. The author of this Thesis had the main responsibility in proposing the original ideas, conducting the analysis, developing and carrying out the simulations, generating the numerical results, and writing the journal papers [**J5**] and [**J1**] as well as conference papers [**C1**], and [**C5**]–[**C6**] while other authors provided invaluable comments, criticism, and support during the process. As for the contributions [**J2**], [**J4**] and [**C7**], both first and second listed authors acknowledge to have equally contributed to the manuscripts.

- **Journal publications**

  [**J1**] C. Perfecto, J. Del Ser, and M. Bennis, "Millimeter-wave V2V communications: Distributed association and beam alignment," *IEEE Journal on Selected Areas in Communications*. Special Issue on Millimeter Wave Communications for Future Mobile Networks, vol. 35, no. 9, pp. 2148–2162, Sep 2017.
  JCR IF 7.172: Rank 5/87 **Q1** *Telecommunications*; 12/260 **Q1** *Eng. Electrical & Electronic*.

[1] Notice that JCR IF is published yearly in the third week of June, therefore at the time of finishing this Thesis the most recent available JCR edition is the 2018 one. Hence, unless otherwise stated, the listed IFs for 2019 publications correspond to the JCR 2018 edition.

[J2] M.S. Elbamby, C. Perfecto, M. Bennis, and K. Doppler, "Toward low-latency and ultra-reliable virtual reality," *IEEE Network*, vol. 32, no. 2, pp. 78–84, March 2018.
JCR IF 7.503: 6/88 **Q1** *Telecommunications*; 14/265 **Q1** *Eng. Electrical & Electronic*; 3/52 **Q1** *Computer Science, Hardware &Architecture*; 4/155 **Q1** *Computer Science, Information Systems.*

[J3] M.S. Elbamby, C. Perfecto, C.F. Liu, J. Park, S. Samarakoon, X. Chen and M. Bennis, "Edge computing with latency and reliability guarantees," (Invited paper) *Proceedings of IEEE.* Special Issue on Edge Computing, vol. 107, no. 8 pp. 1717–1737, Aug 2019.
JCR IF 10.694: 5/265 **Q1** *Eng. Electrical & Electronic.*

[J4] C. Perfecto, M.S. Elbamby, J. Del Ser, and M. Bennis, "Taming the latency in multi-user VR 360°: A QoE-aware deep learning-aided multicast framework," Submitted to *IEEE Transactions on Communications* (in 3rd review round after a Minor Review decision in 2nd review round).
JCR IF 5.690: 9/88 **Q1** *Telecommunications*; 27/265 **Q1** *Eng. Electrical & Electronic.*

[J5] C. Perfecto, M. N. Bilbao, J. Del Ser, and A. Ferro, "A simulation-based quantitative analysis on the topological heritability of dandelion-encoded meta-heuristics for tree optimization problems," *Soft Computing*, vol. 21, no. 17, pp. 4939–4952, Sep 2017.
JCR IF 2.367: 45/132 **Q2** *Computer Science, Artificial Intelligence.*

[L1] C. Perfecto, M.S. Elbamby, J. Park, J. Del Ser, and M. Bennis, "Mobile XR over 5G: A way forward with mmWaves and Edge," (Invited letter) *IEEE MMTC Communications - Frontiers.* SI on Mobile AR/VR/MR and Haptics over 5G and Beyond, vol. 14, no. 2, pp. 29–34, March 2019.

- **Conference publications**

[C1] C. Perfecto, M. N. Bilbao, J. Del Ser, and A. Ferro, "On the heritability of dandelion-encoded harmony search heuristics for tree optimization problems," in *2015 International Symposium on Innovations in Intelligent SysTems and Applications (INISTA)*, Sept 2015, pp. 1–8.

[C2] C. Perfecto, M. N. Bilbao, J. Del Ser, A. Ferro, 'Dandelion-encoded harmony search heuristics for opportunistic traffic offloading in synthetically modeled mobile networks," in *Harmony Search Algorithm. Advances in Intelligent Systems and Computing, vol 382.*, J. H. Kim and Z. W. Geem, Eds. Springer, Berlin Heidelberg, 2016, pp. 133–145.

[C3] C. Perfecto, J. Del Ser, M. I. Ashraf, M. N. Bilbao, and M. Bennis, "Beamwidth optimization in millimeter wave small cell networks with relay nodes: A swarm intelligence approach," in *European Wireless 2016; 22th European Wireless Conference*, May 2016, pp. 1–6.

[C4] M. I. Ashraf, M. Bennis, C. Perfecto, and W. Saad, "Dynamic proximity-aware resource allocation in vehicle-to-vehicle (V2V) communications," in *2016 IEEE Globecom Workshops (GC Wkshps)*, Dec 2016, pp. 1–6.

[C5] C. Perfecto, J. Del Ser, and M. Bennis, "On the interplay between scheduling interval and beamwidth selection for low-latency and reliable V2V mmwave communications," in *2017 20th Conference on Innovations in Clouds, Internet and Networks (ICIN)*, March 2017, pp. 1–8.

[C6] C. Perfecto, J. Del Ser, M. Bennis, and M. N. Bilbao, "Beyond WYSIWYG: Sharing contextual sensing data through mmwave V2V communications," in *2017 European Conference on Networks and Communications (EuCNC)*, June 2017, pp. 1–6.

[C7] M. S. Elbamby, C. Perfecto, M. Bennis, and K. Doppler, "Edge computing meets millimeter-wave enabled VR: Paving the way to cutting the cord," in *2018 IEEE Wireless Communications and Networking Conference (WCNC)*, April 2018, pp. 1–6.

V.1.2.2 Other Publications

Additionally, in parallel with the research leading to this Thesis, and as a means to fulfilling the secondary goals related to HOWs 1-3, the author has also collaborated in other research lines yielding the publications listed below as **[oJ6]**–**[oJ8]** and **[oC9]**–**[oC15]**.

Depending upon the publication, the involvement and contribution to the research leading to these publications ranged from simply providing ideas and comments, or participating in the writing of the manuscripts, to supporting the analysis, by helping to model the problem or coding and simulating some of the algorithms therein.

- **Journal publications**

[oJ6] A. Elola, J. Del Ser, M. N. Bilbao, C. Perfecto, E. Alexandre, and S. Salcedo-Sanz, "Hybridizing cartesian genetic programming and harmony search for adaptive feature construction in supervised learning problems," *Applied Soft Computing*, vol. 52, pp. 760 – 770, 2017.
JCR IF 3.907: 17/132 **Q1** *Computer Science, Artificial Intelligence*, 11/104 **Q1** *Computer Science, Interdisciplinary Applications.*

[oJ7] M. Bilbao, J. Del Ser, C. Perfecto, S. Salcedo-Sanz, and J. Portilla Figueras, "Cost-efficient deployment of multi-hop wireless networks over disaster areas using multi-objective metaheuristics," *Neurocomputing*, vol. 271, pp. 18 – 27, 2018.
JCR IF 4.072: 28/133 **Q1** *Computer Science, Artificial Intelligence.*

[oJ8] J. L. Lobo, J. Del Ser, M. N. Bilbao, C. Perfecto, and S. Salcedo-Sanz, "DRED: An evolutionary diversity generation method for concept drift adaptation in online learning environments," *Applied Soft Computing*, vol. 68, pp. 693 – 709, 2018.
JCR IF 4.873: 20/132 **Q1** *Computer Science, Artificial Intelligence*, 11/106 **Q1** *Computer Science, Interdisciplinary Applications.*

- **Conference publications**

[oC8] J. Del Ser, J. L. Lobo, E. Villar-Rodriguez, M. N. Bilbao, and C. Perfecto, "Community detection in graphs based on surprise maximization using firefly heuristics," in *2016 IEEE Congress on Evolutionary Computation (CEC)*, July 2016, pp. 2233–2239.

[**oC9**] J. Del Ser, M. N. Bilbao, C. Perfecto, and S. Salcedo-Sanz, "A harmony search approach for the selective pick-up and delivery problem with delayed drop-off," in *Harmony Search Algorithm. Advances in Intelligent Systems and Computing, vol 382.*, J. H. Kim and Z. W. Geem, Eds. Springer, Berlin Heidelberg, 2016, pp. 121–131.

[**oC10**] J. Del Ser, M. N. Bilbao, C. Perfecto, A. Gonzalez-Pardo, and S. Campos-Cordobes, "Joint topology optimization, power control and spectrum allocation for intra-vehicular multi-hop sensor networks using dandelion-encoded heuristics," in *Applications of Evolutionary Computation. EvoApplications 2016. Lecture Notes in Computer Science, vol 9597.*, G. Squillero and P. Burelli, Eds. Springer, Cham, 2016, pp. 235–250.

[**oC11**] M. N. Bilbao, C. Perfecto, J. Del Ser, and X. Landa, "On the application of bio-inspired heuristics for network routing with multiple QoS constraints," in *Intelligent Distributed Computing X. IDC 2016. Studies in Computational Intelligence, vol 678*, C. Badica and et al., Eds. Springer, Cham, 2017, pp. 195–204.

[**oC12**] J. Consul, C. Perfecto, M. N. Bilbao, and J. Del Ser, "An analysis of coalition-competition pricing strategies for multi-operator mobile traffic offloading using bi-objective heuristics," in *Harmony Search Algorithm. ICHSA 2017. Advances in Intelligent Systems and Computing, vol 514*, J. Del Ser, Ed. Springer, Singapore, 2017, pp. 157–167.

[**oC13**] M. N. Bilbao, C. Perfecto, M. N. Bilbao, and J. Del Ser, "Cost-Efficient selective network caching in large-area vehicular networks using multi-objective heuristics," in *Harmony Search Algorithm. ICHSA 2017. Advances in Intelligent Systems and Computing, vol 514*, J. Del Ser, Ed. Springer, Singapore, 2017, pp. 168–178.

[**oC14**] J. Del Ser, A. I. Torre-Bastida, I. L.aña, M. N. Bilbao, and C. Perfecto, "Nature-inspired heuristics for the multiple-vehicle selective pickup and delivery problem under maximum profit and incentive fairness criteria," in *2017 IEEE Congress on Evolutionary Computation (CEC)*, June 2017, pp. 480–487.

[**oC15**] M. Carrillo, J. Del Ser, M. Nekane Bilbao, C. Perfecto, and D. Camacho, "Wind power production forecasting using ant colony optimization and extreme learning machines," in *Intelligent Distributed Computing XI. IDC 2017. Studies in Computational Intelligence, vol 737.*, M. Ivanović and et al. Eds. Springer, Cham, 2018, pp. 175–184.

V.1.3 Future Research Directions

There is a wide range of possible extensions of the work proposed in this Thesis. Listed below are some of the most noteworthy concepts to be considered as future lines to extend the scope of the research described so far:

- As the first deployments of 5G cellular systems are taking place, its limitations are continuously being exposed[21]. Subsequently, administrations and manufacturers are starting to gather around worldwide activities [78] to define the next-generation 6G that seamlessly integrates far-reaching applications. Such applications range from autonomous systems to extended reality and haptics. In this context, and with a view to support

latency-critical applications, e.g., the aforementioned autonomous driving vehicles and tactile control, a clear future research line stems from the application of the concept of wireless intelligence [298]. In this envisaged context, a question emerges around the deployment of AI models aimed at providing intelligence over such scenarios and their implications in terms of latency. This intriguing matter has straight connections to the way AI models are constructed and updated, specially those that learn from data produced by non-stationary phenomena. The need for model training and updating may have catastrophic side effects in terms of latency when models are used for supporting latency-critical applications. This is why a closer look is lately being devoted to Edge computing, a paradigm that advocates for implementing part of the aforementioned intelligence closer to the generation of the data from which models are learned. In this regard, an interesting extension of the findings reported in this Thesis is to rethink how methods utilized throughout the considered vehicular and VR/AR scenarios can be transformed so as to allow for their implementation on a computing continuum, roughly like the one postulated by Wireless Intelligence.

- In regards to the exchange of sensing information over mmWave vehicular communications, another open research direction to follow is how to adapt the volume of sensed data to the prevailing capacity of the vehicular channel, also considering latency constraints, and the value and age of the information to be transmitted. Further work needs to be accomplished towards the use of dynamic 3D HD maps as a pivotal information asset for autonomous driving vehicles. Specifically, octree-based map encoding has been suggested in prior work [299] for compressing sensed 3D point clouds (as those provided by e.g., LIDAR imaging devices). In this regard, implications of octree encoding in the end-to-end latency of mmWave vehicular networks will be explored in the future, along with the modifications needed in the framework presented in Chapter III.3 to reflect this selected encoding in the quality of the exchanged information.

Bibliography

Bibliography

[1] ITU-R, "IMT vision – framework and overall objectives of the future development of IMT for 2020 and beyond, Recommendation ITU-R M.2083-0", Sep. 2015 (cited on pp. 4, 5).

[2] ——, "Minimum requirements related to technical performance for IMT-2020 radio interface(s), Report ITU-R M.2410-0", Nov. 2017 (cited on p. 4).

[3] NGMN Alliance, "Description of network slicing concept. 5G P1 requirements & architecture work stream end-to-end architecture", Final Deliverable, Jun. 2016 (cited on p. 5).

[4] M. Richart, J. Baliosian, J. Serrat, *et al.*, "Resource slicing in virtual wireless networks: A survey", *IEEE Trans. Netw. Service Manag.*, vol. 13, no. 3, pp. 462–476, Sep. 2016. DOI: 10.1109/TNSM.2016.2597295 (cited on p. 5).

[5] P. Rost, C. Mannweiler, D. S. Michalopoulos, *et al.*, "Network slicing to enable scalability and flexibility in 5G mobile networks", *IEEE Commun. Mag.*, vol. 55, no. 5, pp. 72–79, May 2017. DOI: 10.1109/MCOM.2017.1600920 (cited on p. 5).

[6] H. Zhang, N. Liu, X. Chu, *et al.*, "Network slicing based 5G and future mobile networks: Mobility, resource management, and challenges", *IEEE Commun. Mag.*, vol. 55, no. 8, pp. 138–145, Aug. 2017. DOI: 10.1109/MCOM.2017.1600940 (cited on p. 5).

[7] P. Rost, A. Banchs, I. Berberana, *et al.*, "Mobile network architecture evolution toward 5G", *IEEE Commun. Mag.*, vol. 54, no. 5, pp. 84–91, May 2016. DOI: 10.1109/MCOM.2016.7470940 (cited on p. 5).

[8] X. Costa-Perez, J. Swetina, T. Guo, *et al.*, "Radio access network virtualization for future mobile carrier networks", *IEEE Commun. Mag.*, vol. 51, no. 7, pp. 27–35, Jul. 2013. DOI: 10.1109/MCOM.2013.6553675 (cited on p. 5).

[9] L. E. Li, Z. M. Mao, and J. Rexford, "Toward software-defined cellular networks", in *2012 European Workshop on Software Defined Networking*, Oct. 2012, pp. 7–12. DOI: 10.1109/EWSDN.2012.28 (cited on p. 5).

[10] M. Y. Arslan, K. Sundaresan, and S. Rangarajan, "Software-defined networking in cellular radio access networks: Potential and challenges", *IEEE Commun. Mag.*, vol. 53, no. 1, pp. 150–156, Jan. 2015. DOI: 10.1109/MCOM.2015.7010528 (cited on p. 5).

[11] R. Mijumbi, J. Serrat, J. Gorricho, *et al.*, "Network function virtualization: State-of-the-art and research challenges", *IEEE Commun. Surveys Tuts.*, vol. 18, no. 1, pp. 236–262, 2016. DOI: 10.1109/COMST.2015.2477041 (cited on p. 5).

[12] ETSI, "Mobile edge computing: A key technology towards 5G", ETSI White Paper No. 11, Sep. 2015 (cited on p. 5).

[13] L. Mamushiane and S. Dlamini, "Leveraging SDN/NFV as key stepping stones to the 5G era in emerging markets", in *2017 Global Wireless Summit (GWS)*, Oct. 2017, pp. 23–27. DOI: 10.1109/GWS.2017.8300496 (cited on p. 5).

[14] B. Blanco, J. O. Fajardo, I. Giannoulakis, *et al.*, "Technology pillars in the architecture of future 5G mobile networks: NFV, MEC and SDN", *Computer Standards & Interfaces*, vol. 54, pp. 216–228, 2017, SI: Standardization SDN&NFV. DOI: https://doi.org/10.1016/j.csi.2016.12.007 (cited on p. 5).

[15] GSMA, "Road to 5G: Introduction and migration", Apr. 2018 (cited on p. 6).

[16] 3GPP, "Study on new radio (NR) access technology physical layer aspects, Tech. Rep. 38.802 Rel-14", Sep. 2017 (cited on p. 6).

[17] ——, "Study on new radio (NR) access technology: Radio access architecture and interfaces, Tech. Rep. 38.801 Rel-14", Apr. 2017 (cited on p. 6).

[18] ——, "Release 15 description, Tech. Rep. 21.915 Rel-15", Jun. 2018 (cited on p. 6).

[19] ETSI, "TS 123 501, System architecture for the 5G system (3GPP TS 23.501 version 15.2.0 Release 15)", Jun. 2018 (cited on p. 6).

[20] J. G. Andrews, S. Buzzi, W. Choi, *et al.*, "What Will 5G Be?", *IEEE J. Sel. Areas Commun.*, vol. 32, no. 6, pp. 1065–1082, Jun. 2014. DOI: 10.1109/JSAC.2014.2328098 (cited on pp. 7, 59).

[21] M. C. Walid Saad Mehdi Bennis, "A vision of 6G wireless systems: Applications, trends, technologies and open research problems", *CoRR abs/1902.10265*, 2019 (cited on pp. 7, 166).

[22] T. S. Rappaport, Y. Xing, O. Kanhere, *et al.*, "Wireless communications and applications above 100 GHz: Opportunities and challenges for 6G and beyond", *IEEE Access*, vol. 7, pp. 78 729–78 757, Jun. 2019. DOI: 10.1109/ACCESS.2019.2921522 (cited on p. 7).

[23] Qualcomm Inc., "Making 5G NR a commercial reality", Mar. 2019 (cited on p. 7).

[24] Qualcomm Inc, "The Future of 5G, 5G Workshop", Sep. (cited on p. 7).

[25] A. Ghosh, A. Maeder, M. Baker, *et al.*, "5G Evolution: A View on 5G Cellular Technology Beyond 3GPP Release 15", *IEEE Access*, vol. 7, pp. 127 639–127 651, Sep. 2019. DOI: 10.1109/ACCESS.2019.2939938 (cited on p. 7).

[26] T. S. Rappaport, R. Mayzus, Y. Azar, *et al.*, "Millimeter wave mobile communications for 5G cellular: It will work!", *IEEE Access*, vol. 1, pp. 335–349, 2013. DOI: 10.1109/ACCESS.2013.2260813 (cited on pp. 7, 59, 108).

[27] S. Rangan and E. Erkip, "Millimeter-wave cellular wireless networks: Potentials and challenges", *Proc. IEEE*, vol. 102, no. 3, pp. 366–385, Mar. 2014. DOI: 10.1109/JPROC.2014.2299397 (cited on pp. 7, 108).

[28] F. Boccardi, R. W. Heath, A. Lozano, *et al.*, "Five disruptive technology directions for 5G", *IEEE Commun. Mag.*, vol. 52, no. 2, pp. 74–80, Feb. 2014. DOI: 10.1109/MCOM.2014.6736746 (cited on p. 7).

[29] M. Xiao, S. Mumtaz, Y. Huang, *et al.*, "Millimeter wave communications for future mobile networks", *IEEE J. Sel. Areas Commun.*, vol. 35, no. 9, pp. 1909–1935, Sep. 2017. DOI: 10.1109/JSAC.2017.2719924 (cited on p. 7).

[30] T. S. Rappaport, Y. Xing, G. R. MacCartney, *et al.*, "Overview of millimeter wave communications for fifth-generation (5G) wireless networks—with a focus on propagation models", *IEEE Trans. Antennas Propag.*, vol. 65, no. 12, pp. 6213–6230, Dec. 2017. DOI: 10.1109/TAP.2017.2734243 (cited on pp. 7, 54, 57).

[31] M. R. Akdeniz, Y. Liu, M. K. Samimi, *et al.*, "Millimeter wave channel modeling and cellular capacity evaluation", *IEEE J. Sel. Areas Commun.*, vol. 32, no. 6, pp. 1164–1179, Jun. 2014. DOI: 10.1109/JSAC.2014.2328154 (cited on p. 8).

[32] I. A. Hemadeh, K. Satyanarayana, M. El-Hajjar, *et al.*, "Millimeter-wave communications: Physical channel models, design considerations, antenna constructions, and link-budget", *IEEE Commun. Surveys Tuts.*, vol. 20, no. 2, pp. 870–913, 2018. DOI: 10.1109/COMST.2017.2783541 (cited on p. 8).

[33] A. L. Swindlehurst, E. Ayanoglu, P. Heydari, *et al.*, "Millimeter-wave massive MIMO: The next wireless revolution?", *IEEE Commun. Mag.*, vol. 52, no. 9, pp. 56–62, Sep. 2014. DOI: 10.1109/MCOM.2014.6894453 (cited on p. 8).

[34] C. Fiandrino, H. Assasa, P. Casari, *et al.*, "Scaling millimeter-wave networks to dense deployments and dynamic environments", *Proc. IEEE*, vol. 107, no. 4, pp. 732–745, Apr. 2019. DOI: 10.1109/JPROC.2019.2897155 (cited on p. 8).

[35] J. Wildman, P. H. J. Nardelli, M. Latva-aho, *et al.*, "On the joint impact of beamwidth and orientation error on throughput in directional wireless poisson networks", *IEEE Trans. Wireless Commun.*, vol. 13, no. 12, pp. 7072–7085, Dec. 2014. DOI: 10.1109/TWC.2014.2331055 (cited on pp. 9, 64, 93, 117, 135).

[36] W. Roh, J. Y. Seol, J. Park, *et al.*, "Millimeter-wave beamforming as an enabling technology for 5G cellular communications: Theoretical feasibility and prototype results", *IEEE Commun. Mag.*, vol. 52, no. 2, pp. 106–113, Feb. 2014. DOI: 10.1109/MCOM.2014.6736750 (cited on p. 8).

[37] S. Kutty and D. Sen, "Beamforming for millimeter wave communications: An inclusive survey", *IEEE Commun. Surveys Tuts.*, vol. 18, no. 2, pp. 949–973, Apr. 2016. DOI: 10.1109/COMST.2015.2504600 (cited on p. 8).

[38] I. Ahmed, H. Khammari, A. Shahid, *et al.*, "A survey on hybrid beamforming techniques in 5G: Architecture and system model perspectives", *IEEE Commun. Surveys Tuts.*, vol. 20, no. 4, pp. 3060–3097, Oct. 2018. DOI: 10.1109/COMST.2018.2843719 (cited on p. 9).

[39] L. Verma, M. Fakharzadeh, and S. Choi, "WiFi on steroids: 802.11ac and 802.11ad", *IEEE Wireless Commun. Mag.*, vol. 20, no. 6, pp. 30–35, Dec. 2013. DOI: 10.1109/MWC.2013.6704471 (cited on p. 10).

[40] T. Nitsche, C. Cordeiro, A. B. Flores, *et al.*, "IEEE 802.11ad: Directional 60 GHz communication for multi-gigabit-per-second WiFi", *IEEE Commun. Mag.*, vol. 52, no. 12, pp. 132–141, Dec. 2014. DOI: 10.1109/MCOM.2014.6979964 (cited on p. 10).

[41] Y. Ghasempour, C. R.C.M. da Silva, C. Cordeiro, *et al.*, "IEEE 802.11ay: Next-generation 60 GHz communication for 100 Gb/s Wi-Fi", *IEEE Commun. Mag.*, vol. 55, no. 12, pp. 186–192, Dec. 2017. DOI: 10.1109/MCOM.2017.1700393 (cited on p. 10).

[42] P. Zhou, K. Cheng, X. Han, *et al.*, "IEEE 802.11ay-based mmWave WLANs: Design challenges and solutions", *IEEE Commun. Surveys Tuts.*, vol. 20, no. 3, pp. 1654–1681, Jul. 2018. DOI: 10.1109/COMST.2018.2816920 (cited on p. 10).

[43] J. Wang, Z. Lan, C. Sum, *et al.*, "Beamforming codebook design and performance evaluation for 60 GHz wideband WPANs", in *2009 IEEE 70th Vehicular Technology Conference Fall*, Sep. 2009, pp. 1–6. DOI: 10.1109/VETECF.2009.5379063 (cited on p. 10).

[44] J. Wang, Z. Lan, C.-W. Pyu, *et al.*, "Beam codebook based beamforming protocol for multi-Gbps millimeter-wave WPAN systems", *IEEE J. Sel. Areas Commun.*, vol. 27, no. 8, pp. 1390–1399, Oct. 2009. DOI: 10.1109/JSAC.2009.091009 (cited on pp. 10, 65, 93, 117).

[45] S. Noh, M. D. Zoltowski, and D. J. Love, "Multi-resolution codebook and adaptive beamforming sequence design for millimeter wave beam alignment", *IEEE Trans. Wireless Commun.*, vol. 16, no. 9, pp. 5689–5701, Sep. 2017. DOI: 10.1109/TWC.2017.2713357 (cited on p. 10).

[46] J. Choi, "Beam selection in mm-Wave multiuser MIMO systems using compressive sensing", *IEEE Trans. Commun.*, vol. 63, no. 8, pp. 2936–2947, Aug. 2015. DOI: 10.1109/TCOMM.2015.2449860 (cited on p. 10).

[47] H. Hassanieh, O. Abari, M. Rodriguez, *et al.*, "Fast millimeter wave beam alignment", in *Proceedings of the 2018 Conference of the ACM Special Interest Group on Data Communication*, ser. SIGCOMM '18, Budapest, Hungary: ACM, 2018, pp. 432–445. DOI: 10.1145/3230543.3230581 (cited on p. 10).

[48] N. J. Myers, A. Mezghani, and R. W. Heath, "Swift-link: A compressive beam alignment algorithm for practical mmwave radios", *IEEE Trans. Signal Process.*, vol. 67, no. 4, pp. 1104–1119, Feb. 2019. DOI: 10.1109/TSP.2018.2886168 (cited on p. 10).

[49] Y. M. Tsang, A. S. Y. Poon, and S. Addepalli, "Coding the beams: Improving beamforming training in mmwave communication system", in *Proc. IEEE Global Telecommun. Conf. (GLOBECOM)*, Dec. 2011, pp. 1–6. DOI: 10.1109/GLOCOM.2011.6134486 (cited on p. 10).

[50] T. Nitsche, A. B. Flores, E. W. Knightly, *et al.*, "Steering with eyes closed: mmWave beam steering without in-band measurement", English, in *Proc. IEEE Conf. Comp. Commun. (INFOCOM)*, Apr. 2015, pp. 2416–2424. DOI: 10.1109/INFOCOM.2015.7218630 (cited on pp. 10, 11).

[51] J. Palacios, D. De Donno, D. Giustiniano, *et al.*, "Speeding up mmWave beam training through low-complexity hybrid transceivers", in *Proc. IEEE 27th Int. Symp. Pers. Indoor Mobile Radio Commun. (PIMRC)*, Sep. 2016. DOI: 10.1109/PIMRC.2016.7794709 (cited on p. 10).

[52] V. Raghavan, L. Akhoondzadeh-Asl, V. Podshivalov, *et al.*, "Statistical blockage modeling and robustness of beamforming in millimeter-wave systems", *IEEE Transactions on Microwave Theory and Techniques*, 2019 (cited on pp. 10, 135).

[53] S. Barbarossa, E. Ceci, and M. Merluzzi, "Overbooking radio and computation resources in mmw-mobile edge computing to reduce vulnerability to channel intermittency", in *Proc. Eur. Conf. on Netw. and Commun. (EuCNC)*, 2017, pp. 1–5. DOI: 10.1109/EuCNC.2017.7980746 (cited on pp. 10, 109).

[54] M. Giordani, M. Polese, A. Roy, *et al.*, "A tutorial on beam management for 3GPP NR at mmWave frequencies", *IEEE Commun. Surveys Tuts.*, 2019. DOI: 10.1109/COMST.2018.2869411 (cited on p. 11).

[55] K. Sakaguchi, T. Haustein, S. Barbarossa, *et al.*, "Where, when, and how mmWave is used in 5G and beyond", *IEICE TRANSACTIONS on Electronics*, vol. E100-C, no. 10, pp. 790–808, Oct. 2017. DOI: 10.1587/transele.E100.C.790 (cited on p. 11).

[56] R. Congiu, H. Shokri-Ghadikolaei, C. Fischione, *et al.*, "On the relay-fallback tradeoff in millimeter wave wireless system", pp. 622–627, Apr. 2016. DOI: 10.1109/INFCOMW.2016.7562151 (cited on p. 11).

[57] A. Ali, N. González-Prelcic, and R. W. Heath, "Millimeter wave beam-selection using out-of-band spatial information", *IEEE Trans. Wireless Commun.*, vol. 17, no. 2, pp. 1038–1052, Feb. 2018. DOI: 10.1109/TWC.2017.2773532 (cited on p. 11).

[58] S. Sur, I. Pefkianakis, X. Zhang, *et al.*, "WiFi-assisted 60 GHz wireless networks", in *Proc. 23rd Annual Int. Conf. on Mobile Comp. and Netw.*, ser. MobiCom '17, Snowbird, Utah, USA: ACM, 2017, pp. 28–41. DOI: 10.1145/3117811.3117817 (cited on p. 11).

[59] A. Patra, L. Simić, and M. Petrova, "Experimental evaluation of a novel fast beamsteering algorithm for link re-establishment in mm-wave indoor WLANs", in *2016 IEEE 27th Annual International Symposium on Personal, Indoor, and Mobile Radio Communications (PIMRC)*, Sep. 2016, pp. 1–7. DOI: 10.1109/PIMRC.2016.7794603 (cited on p. 11).

[60] V. Va, T. Shimizu, G. Bansal, *et al.*, "Beam design for beam switching based millimeter wave vehicle-to-infrastructure communications", in *Proc. IEEE Int. Conf. Commun. (ICC)*, Kuala Lumpur, 2016, pp. 6–11. DOI: 10.1109/ICC.2016.7511414 (cited on pp. 11, 60, 90).

[61] Z. Qi and W. Liu, "Three-dimensional millimetre wave beam tracking based on handset MEMS sensors with extended Kalman filtering", in *Radio Propagation and Technologies for 5G (2016)*, Oct. 2016, pp. 1–6. DOI: 10.1049/ic.2016.0066 (cited on p. 11).

[62] T. Shimizu, V. Va, G. Bansal, *et al.*, "Millimeter wave V2X communications: Use cases and design considerations of beam management", in *Asia-Pacific Microwave Conf. (APMC)*, Nov. 2018, pp. 183–185. DOI: 10.23919/APMC.2018.8617303 (cited on pp. 11, 55).

[63] J. Choi, V. Va, N. Gonzalez-Prelcic, *et al.*, "Millimeter-wave vehicular communication to support massive automotive sensing", *IEEE Commun. Mag.*, vol. 54, no. 12, pp. 160–167, Dec. 2016. DOI: 10.1109/MCOM.2016.1600071CM (cited on pp. 11, 53, 60, 90, 93).

[64] N. González-Prelcic, R. Méndez-Rial, and R. W. Heath, "Radar aided beam alignment in mmWave V2I communications supporting antenna diversity", in *Inf. Theory Appl. Work.*, La Jolla, CA, US, 2016 (cited on p. 11).

[65] A. Klautau, N. González-Prelcic, and R. W. Heath, "LIDAR data for deep learning-based mmWave beam-selection", *IEEE Wireless Communications Letters*, pp. 1–1, 2019. DOI: 10.1109/LWC.2019.2899571 (cited on pp. 11, 57).

[66] A. Asadi, S. Müller, G. H. Sim, *et al.*, "FML: Fast machine learning for 5G mmWave vehicular communications", in *IEEE INFOCOM 2018 - IEEE Conference on Computer Communications*, Apr. 2018, pp. 1961–1969. DOI: 10.1109/INFOCOM.2018.8485876 (cited on p. 11).

[67] G. H. Sim, S. Klos, A. Asadi, *et al.*, "An online context-aware machine learning algorithm for 5G mmWave vehicular communications", *IEEE/ACM Transactions on Networking*, vol. 26, no. 6, pp. 2487–2500, Dec. 2018. DOI: 10.1109/TNET.2018.2869244 (cited on p. 11).

[68] C. N. Barati, S. A. Hosseini, M. Mezzavilla, *et al.*, "Initial access in millimeter wave cellular systems", *IEEE Trans. Wireless Commun.*, vol. 15, no. 12, pp. 7926–7940, Dec. 2016. DOI: 10.1109/TWC.2016.2609384 (cited on p. 11).

[69] M. Giordani, M. Mezzavilla, and M. Zorzi, "Initial access in 5G mmWave cellular networks", *IEEE Commun. Mag.*, vol. 54, no. 11, pp. 40–47, Nov. 2016. DOI: 10.1109/MCOM.2016.1600193CM (cited on p. 11).

[70] M. Giordani, M. Polese, A. Roy, *et al.*, "Initial access frameworks for 3GPP NR at mmWave frequencies", in *2018 17th Annual Mediterranean Ad Hoc Networking Workshop (Med-HocNet)*, Jun. 2018, pp. 1–8. DOI: 10.23919/MedHocNet.2018.8407094 (cited on p. 11).

[71] M. Polese, M. Giordani, M. Mezzavilla, *et al.*, "Improved handover through dual connectivity in 5G mmWave mobile networks", *IEEE J. Sel. Areas Commun.*, vol. 35, no. 9, pp. 2069–2084, Sep. 2017. DOI: 10.1109/JSAC.2017.2720338 (cited on p. 11).

[72] S. Goyal, M. Mezzavilla, S. Rangan, *et al.*, "User association in 5G mmWave networks", in *2017 IEEE Wireless Communications and Networking Conference (WCNC)*, Mar. 2017, pp. 1–6. DOI: 10.1109/WCNC.2017.7925883 (cited on p. 12).

[73] A. S. Cacciapuoti, "Mobility-aware user association for 5G mmWave networks", *IEEE Access*, vol. 5, pp. 21 497–21 507, 2017. DOI: 10.1109/ACCESS.2017.2751422 (cited on p. 12).

[74] M. Bennis, M. Debbah, and H. V. Poor, "Ultrareliable and low-latency wireless communication: Tail, risk, and scale", *Proc. IEEE*, vol. 106, no. 10, pp. 1834–1853, Oct. 2018. DOI: 10.1109/JPROC.2018.2867029 (cited on pp. 13, 127).

[75] P. Popovski, J. J. Nielsen, C. Stefanovic, *et al.*, "Wireless access for ultra-reliable low-latency communication: Principles and building blocks", *IEEE Netw.*, vol. 32, no. 2, pp. 16–23, Mar. 2018. DOI: 10.1109/MNET.2018.1700258 (cited on p. 13).

[76] J. Sachs, G. Wikstrom, T. Dudda, *et al.*, "5G radio network design for ultra-reliable low-latency communication", *IEEE Netw.*, vol. 32, no. 2, pp. 24–31, Mar. 2018. DOI: 10.1109/MNET.2018.1700232 (cited on p. 13).

[77] A. Gatherer, "Can 5G survive without AI?", *IEEE ComSoc Technology News (CTN)*, Nov. 2018 (cited on p. 15).

[78] "Key drivers and research challenges for 6G ubiquitous wireless intelligence, 6G research visions 1", University of Oulu, White Paper, Sep. 2019 (cited on pp. 15, 161, 166).

[79] C. Perfecto, M. N. Bilbao, J. Del Ser, *et al.*, "Dandelion-encoded harmony search heuristics for opportunistic traffic offloading in synthetically modeled mobile networks", in *Harmony Search Algorithm. Advances in Intelligent Systems and Computing, vol 382.*, J. H. Kim and Z. W. Geem, Eds., Springer, Berlin Heidelberg, 2016, pp. 133–145. DOI: 10.1007/978-3-662-47926-1_14 (cited on p. 15).

[80] J. Del Ser, M. N. Bilbao, C. Perfecto, *et al.*, "Joint topology optimization, power control and spectrum allocation for intra-vehicular multi-hop sensor networks using dandelion-encoded heuristics", in *App. of Evol. Comp. EvoApplications 2016. LNCS vol. 9597.*, G. Squillero and P. Burelli, Eds., Springer, Cham, 2016, pp. 235–250. DOI: 10.1007/978-3-319-31204-0_16 (cited on p. 15).

[81] J. Consul, C. Perfecto, M. N. Bilbao, *et al.*, "An analysis of coalition-competition pricing strategies for multi-operator mobile traffic offloading using bi-objective heuristics", in *Harmony Search Algorithm. ICHSA 2017. Advances in Intelligent Systems and Computing, vol 514*, J. Del Ser, Ed., Springer Singapore, 2017, pp. 157–167. DOI: 10.1007/978-981-10-3728-3_16 (cited on p. 15).

[82] A. P. Engelbrecht, *Computational intelligence: an introduction*. John Wiley & Sons, 2007 (cited on p. 26).

[83] A. Konar, *Computational intelligence: principles, techniques and applications*. Springer Science & Business Media, 2006 (cited on p. 26).

[84] A. E. Eiben, J. E. Smith, *et al.*, *Introduction to evolutionary computing*. Springer, 2003, vol. 53 (cited on p. 27).

[85] Y. LeCun, Y. Bengio, and G. Hinton, "Deep learning", *Nature*, vol. 521, no. 7553, p. 436, 2015 (cited on p. 27).

[86] L. Kaufman and P. J. Rousseeuw, *Finding groups in data: an introduction to cluster analysis*. John Wiley & Sons, 2009, vol. 344 (cited on p. 27).

[87] N. Ansari and E. Hou, *Computational intelligence for optimization*. Springer Science & Business Media, 2012 (cited on p. 28).

[88] C. Cortes and V. Vapnik, "Support-vector networks", *Machine Learning*, vol. 20, no. 3, pp. 273–297, 1995 (cited on p. 28).

[89] T. Ma and B. Abdulhai, "Genetic algorithm-based optimization approach and generic tool for calibrating traffic microscopic simulation parameters", *Transportation research record*, vol. 1800, no. 1, pp. 6–15, 2002 (cited on p. 29).

[90] L. Goel, D. Gupta, V. Panchal, *et al.*, "Taxonomy of nature inspired computational intelligence: A remote sensing perspective", in *2012 Fourth World Congress on Nature and Biologically Inspired Computing (NaBIC)*, IEEE, 2012, pp. 200–206 (cited on p. 29).

[91] G. N. Yannakakis and J. Togelius, "A panorama of artificial and computational intelligence in games", *IEEE Transactions on Computational Intelligence and AI in Games*, vol. 7, no. 4, pp. 317–335, 2014 (cited on p. 29).

[92] D. Michie, D. J. Spiegelhalter, C. Taylor, *et al.*, "Machine learning", *Neural and Statistical Classification*, vol. 13, 1994 (cited on p. 29).

[93] C. M. Bishop, *Pattern recognition and machine learning*. Springer, 2006 (cited on p. 29).

[94] I. H. Witten, E. Frank, M. A. Hall, *et al.*, *Data Mining: Practical machine learning tools and techniques*. Morgan Kaufmann, 2016 (cited on p. 29).

[95] H. B. Barlow, "Unsupervised learning", *Neural Computation*, vol. 1, no. 3, pp. 295–311, 1989 (cited on p. 30).

[96] I. Zelinka, V. Snasael, and A. Abraham, *Handbook of optimization: from classical to modern approach*. Springer Science & Business Media, 2012, vol. 38 (cited on p. 31).

[97] A. Auger and B. Doerr, *Theory of randomized search heuristics: Foundations and recent developments*. World Scientific, 2011, vol. 1 (cited on p. 31).

[98] H. Shen and G. Bai, "Routing in wireless multimedia sensor networks: A survey and challenges ahead", *Journal of Network and Computer Applications*, vol. 71, pp. 30–49, 2016 (cited on p. 31).

[99] A. Ahmad, S. Ahmad, M. H. Rehmani, *et al.*, "A survey on radio resource allocation in cognitive radio sensor networks", *IEEE Commun. Surveys Tuts.*, vol. 17, no. 2, pp. 888–917, 2015 (cited on p. 31).

[100] I. H. Osman and J. P. Kelly, "Meta-heuristics theory and applications", *Journal of the Operational Research Society*, vol. 48, no. 6, pp. 657–657, 1997 (cited on p. 31).

[101] J. A. Parejo, A. Ruiz-Cortés, and P. Lozano Sebastián and Fernandez, "Metaheuristic optimization frameworks: A survey and benchmarking", *Soft Computing*, vol. 16, no. 3, pp. 527–561, Mar. 2012. DOI: 10.1007/s00500-011-0754-8 (cited on p. 32).

[102] X.-S. Yang and M. Karamanoglu, "Swarm intelligence and bio-inspired computation: An overview", in *Swarm intelligence and bio-inspired computation*, Elsevier, 2013, pp. 3–23 (cited on p. 32).

[103] F. Dressler and O. B. Akan, "Bio-inspired networking: From theory to practice", *IEEE Communications Magazine*, vol. 48, no. 11, pp. 176–183, Nov. 2010. DOI: 10.1109/MCOM.2010.5621985 (cited on p. 32).

[104] A. K. Kar, "Bio inspired computing – a review of algorithms and scope of applications", *Expert Systems with Applications*, vol. 59, pp. 20–32, 2016. DOI: https://doi.org/10.1016/j.eswa.2016.04.018 (cited on p. 32).

[105] J. Del Ser, E. Osaba, D. Molina, *et al.*, "Bio-inspired computation: Where we stand and what's next", *Swarm and Evolutionary Computation*, vol. 48, pp. 220–250, 2019. DOI: https://doi.org/10.1016/j.swevo.2019.04.008 (cited on p. 32).

[106] T. Bäck, F. Hoffmeister, and H.-P. Schwefel, "A survey of evolution strategies", in *Proc. Int. Conf. on Genetic Algorithms*, Morgan Kaufmann, 1991, pp. 2–9 (cited on p. 32).

[107] T. Bäck, *Evolutionary Algorithms in Theory and Practice: Evolution Strategies, Evolutionary Programming, Genetic Algorithms*. New York, NY, USA: Oxford University Press, Inc., 1996 (cited on p. 32).

[108] T. Bäck, D. B. Fogel, and Z. Michalewicz, *Handbook of evolutionary computation*. CRC Press, 1997 (cited on p. 32).

[109] J. H. Holland, "Genetic algorithms", *Scientific American*, vol. 267, no. 1, pp. 66–73, 1992 (cited on p. 32).

[110] K. V. Price, "Differential evolution", in *Handbook of Optimization*, Springer, 2013, pp. 187–214 (cited on p. 32).

[111] H.-G. Beyer and H.-P. Schwefel, "Evolution strategies–a comprehensive introduction", *Natural computing*, vol. 1, no. 1, pp. 3–52, 2002 (cited on p. 32).

[112] P. Larrañaga and J. A. Lozano, *Estimation of distribution algorithms: A new tool for evolutionary computation*. Springer Science & Business Media, 2001, vol. 2 (cited on p. 32).

[113] J. R. Koza and J. R. Koza, *Genetic programming: on the programming of computers by means of natural selection*. MIT press, 1992, vol. 1 (cited on p. 32).

[114] Z. W. Geem, J. H. Kim, and G. Loganathan, "A new heuristic optimization algorithm: Harmony search", *Simulation*, vol. 76, no. 2, pp. 60–68, 2001. DOI: 10.1177/003754970107600201 (cited on p. 32).

[115] J. Kennedy, "Swarm intelligence", in *Handbook of nature-inspired and innovative computing*, Springer, 2006, pp. 187–219 (cited on p. 32).

[116] C. Blum and X. Li, "Swarm intelligence in optimization", *Swarm Intelligence: Introduction and Applications*, C. Blum and D. Merkle, Eds., pp. 43–85, 2008. DOI: 10.1007/978-3-540-74089-6_2 (cited on pp. 32, 61).

[117] M. Dorigo and M. Birattari, *Ant colony optimization*. Springer, 2010 (cited on p. 33).

[118] J. Kennedy and R. Eberhart, "Particle swarm optimization", in *IEEE Int. Conf. Part. swarm Optim.*, vol. 4, 1995, pp. 1942–1948. DOI: 10.1109/MHS.1995.494215 (cited on pp. 33, 76).

[119] R. Poli, J. Kennedy, and T. Blackwell, "Particle swarm optimization", *Swarm intelligence*, vol. 1, no. 1, pp. 33–57, 2007 (cited on p. 33).

[120] X.-S. Yang, "Firefly algorithm, levy flights and global optimization", in *Research and development in intelligent systems XXVI*, Springer, 2010, pp. 209–218 (cited on p. 33).

[121] M. A. Lones, "Metaheuristics in nature-inspired algorithms", in *Proceedings of the Companion Publication of the 2014 Annual Conference on Genetic and Evolutionary Computation*, ACM, 2014, pp. 1419–1422 (cited on p. 33).

[122] D. Gale and L. S. Shapley, "College admissions and the stability of marriage", *Am. Math. Mon.*, vol. 69, no. 1, pp. 9–15, 1962. DOI: 10.1080/00029890.1962.11989827 (cited on pp. 33, 39, 40, 97, 143).

[123] A. E. Roth, "The economics of matching: Stability and incentives", *Mathematics of Operations Research*, vol. 7, pp. 617–628, 4 1982. DOI: 10.1287/moor.7.4.617 (cited on p. 33).

[124] ——, "The evolution of the labor market for medical interns and residents: A case study in game theory", *Journal of Political Economy*, vol. 92, no. 6, pp. 991–1016, 1984. DOI: 10.1086/261272 (cited on p. 33).

[125] A. E. Roth and E. Peranson, "The redesign of the matching market for american physicians: Some engineering aspects of economic design", *American Economic Review*, vol. 89, no. 4, pp. 748–780, Sep. 1999. DOI: 10.1257/aer.89.4.748 (cited on p. 33).

[126] A. E. Roth and M. O. Sotomayor, *Two-sided matching: A study in game-theoretic modeling and analysis*. Cambridge University Press, 1992 (cited on pp. 33, 121, 141).

[127] A. E. Roth, "The economist as engineer: Game theory, experimentation, and computation as tools for design economics", *Econometrica*, vol. 70, no. 4, pp. 1341–1378, 2002. DOI: 10.1111/1468-0262.00335 (cited on p. 33).

[128] Y. Gu, W. Saad, M. Bennis, *et al.*, "Matching theory for future wireless networks: Fundamentals and applications", *IEEE Commun. Mag.*, vol. 53, no. 5, pp. 52–59, May 2015. DOI: 10.1109/MCOM.2015.7105641 (cited on pp. 34, 36, 141, 143).

[129] E. A. Jorswieck, "Stable matchings for resource allocation in wireless networks", in *17th Int. Conf. on Digital Signal Processing (DSP)*, Jul. 2011. DOI: 10.1109/ICDSP.2011.6004983 (cited on p. 34).

[130] F. Pantisano, M. Bennis, W. Saad, *et al.*, "Matching with externalities for context-aware user-cell association in small cell networks", in *IEEE Glob. Commun. Conf. (GLOBECOM)*, Dec. 2013, pp. 4483–4488. DOI: 10.1109/GLOCOMW.2013.6855657 (cited on p. 34).

[131] O. Semiari, W. Saad, S. Valentin, *et al.*, "Matching theory for priority-based cell association in the downlink of wireless small cell networks", in *2014 IEEE Int. Conf. on Acoustics, Speech and Signal Processing (ICASSP)*, May 2014, pp. 444–448. DOI: 10.1109/ICASSP.2014.6853635 (cited on pp. 34, 120).

[132] K. Hamidouche, W. Saad, and M. Debbah, "Many-to-many matching games for proactive social-caching in wireless small cell networks", in *12th Int. Symposium on Modeling and Optimization in Mobile, Ad Hoc, and Wireless Networks (WiOpt)*, 2014, pp. 569–574. DOI: 10.1109/WIOPT.2014.6850348 (cited on p. 34).

[133] O. Semiari, W. Saad, Z. Dawy, *et al.*, "Matching theory for backhaul management in small cell networks with mmwave capabilities", in *Commun. (ICC), 2015 IEEE Int. Conf.*, 2015, pp. 3460–3465. DOI: 10.1109/ICC.2015.7248860 (cited on p. 34).

[134] M. I. Ashraf, M. Bennis, W. Saad, *et al.*, "Dynamic clustering and user association in wireless small-cell networks with social considerations", *IEEE Transactions on Vehicular Technology*, vol. 66, no. 7, pp. 6553–6568, Jul. 2017. DOI: 10.1109/TVT.2016.2644760 (cited on p. 34).

[135] S. M. A. Kazmi, N. H. Tran, and C. S. Hong, "Matching games for 5G networking paradigms", in *Game Theory for Networking Applications*, J. B. Song, H. Li, and M. Coupechoux, Eds. Cham: Springer International Publishing, 2019, pp. 69–105. DOI: 10.1007/978-3-319-93058-9_6 (cited on p. 34).

[136] S. Bayat, Y. Li, L. Song, *et al.*, "Matching theory: Applications in wireless communications", *IEEE Signal Processing Magazine*, vol. 33, no. 6, pp. 103–122, Nov. 2016. DOI: 10.1109/MSP.2016.2598848 (cited on p. 34).

[137] D. F. Manlove, *Algorithmics of Matching Under Preferences.*: World Scientific, 2013. DOI: 10.1142/8591 (cited on p. 34).

[138] Z. Han, Y. Gu, and W. Saad, *Matching theory for wireless networks*. Springer, 2017. DOI: 10.1007/978-3-319-56252-0 (cited on p. 36).

[139] L. Tassiulas and A. Ephremides, "Stability properties of constrained queueing systems and scheduling policies for maximum throughput in multihop radio networks", *IEEE Trans. Autom. Control*, vol. 37, no. 12, pp. 1936–1948, Dec. 1992. DOI: 10.1109/9.182479 (cited on p. 40).

[140] ——, "Dynamic server allocation to parallel queues with randomly varying connectivity", *IEEE Trans. Inf. Theory*, vol. 39, no. 2, pp. 466–478, Mar. 1993. DOI: 10.1109/18.212277 (cited on p. 40).

[141] M. J. Neely, E. Modiano, and C. Li, "Fairness and optimal stochastic control for heterogeneous networks", in *INFOCOM 2005. 24th Annual Joint Conference of the IEEE Computer and Communications Societies, 13-17 March 2005, Miami, FL, USA*, 2005, pp. 1723–1734. DOI: 10.1109/INFCOM.2005.1498453 (cited on p. 40).

[142] L. Georgiadis, M. J. Neely, and L. Tassiulas, *Resource Allocation and Cross-Layer Control in Wireless Networks*, ser. Foundations and Trends in Networking 1. Now Publishers Inc., 2006, vol. 1. DOI: 10.1561/1300000001 (cited on pp. 40, 45, 140).

[143] M. J. Neely, *Stochastic Network Optimization with Application to Communication and Queueing Systems*, ser. Synthesis Lectures on Communication Networks 1. Morgan and Claypool, 2010, vol. 3, pp. 1–211 (cited on pp. 40, 43, 139).

[144] M. J. Neely, "Stochastic network optimization with non-convex utilities and costs", in *2010 Information Theory and Applications Workshop (ITA)*, Jan. 2010, pp. 1–10. DOI: 10.1109/ITA.2010.5454100 (cited on pp. 40, 43).

[145] M. J. Neely, "Universal scheduling for networks with arbitrary traffic, channels, and mobility", *CoRR abs/1001.0960*, 2010 (cited on pp. 43, 45).

[146] S. Boyd and L. Vandenberghe, *Convex Optimization*. Cambridge University Press, Mar. 2004 (cited on p. 44).

[147] U. D. of Transportation, "Preparing for the future of transportation: Automated vehicles 3.0", Oct. 2018 (cited on p. 50).

[148] SAE, "J3016, Taxonomy and definitions for terms related to driving automation systems for on-road motor vehicles", Standard, Oct. 2018 (cited on p. 50).

[149] M. Fallgren, M. Dillinger, J. Alonso-Zarate, *et al.*, "Fifth-generation technologies for the connected car: Capable systems for vehicle-to-anything communications", *IEEE Vehicular Technology Magazine*, vol. 13, no. 3, pp. 28–38, Sep. 2018. DOI: 10.1109/MVT.2018.2848400 (cited on pp. 51, 56).

[150] T. Connectivity, "6 key connectivity requirements of autonomous driving", *IEEE Spectrum*, Oct. 2018 (cited on p. 51).

[151] J. B. Kenney, "Dedicated short-range communications (DSRC) standards in the United States", *Proc. IEEE*, vol. 99, no. 7, pp. 1162–1182, Jul. 2011. DOI: 10.1109/JPROC.2011.2132790 (cited on pp. 51, 60, 77, 90).

[152] ETSI, "Etsi es 202 663 v1.1.0, Intelligent Transport Systems (ITS); European profile standard for the physical and medium access control layer of Intelligent Transport Systems operating in the 5 GHz frequency band", Jan. 2010 (cited on p. 51).

[153] E. Comission, "Study on the deployment of c-its in europe: Final report, Framework contract on impact assessment and evaluation studies in the field of transport move/a3/119-2013-lot n5 "horizontal"", Standard, Feb. 2016 (cited on p. 51).

[154] G. Araniti, C. Campolo, M. Condoluci, *et al.*, "LTE for vehicular networking: A survey", *IEEE Commun. Mag.*, vol. 51, no. 5, pp. 148–157, May 2013. DOI: 10.1109/MCOM.2013.6515060 (cited on p. 51).

[155] H. Seo, K. Lee, S. Yasukawa, *et al.*, "LTE evolution for vehicle-to-everything services", *IEEE Commun. Mag.*, vol. 54, no. 6, pp. 22–28, Jun. 2016. DOI: 10.1109/MCOM.2016.7497762 (cited on p. 51).

[156] 3GPP, "Tech. Specification 38.885 Release 16, Study on NR vehicle-to-everything (V2X)", Dec. 2018 (cited on pp. 51, 52).

[157] ——, "Tech. Specification 22.185 Release 14, Service requirements for v2x services", Dec. 2015 (cited on p. 51).

[158] ——, "Tech. Specification 22.186 Release 16, Service requirements for enhanced V2X scenarios", Dec. 2018 (cited on p. 51).

[159] ——, "Tech. Specification 22.885 Release 14, Study on LTE support for vehicle-to-everything (V2X) services", Mar. 2015 (cited on p. 51).

[160] ——, "Tech. Report 22.886 Release 16, Study on enhancement of 3GPP support for 5G V2X services", Dec. 2018 (cited on p. 52).

[161] ——, "Tech. Rep. 37.885 Rel-15, Study on evaluation methodology of new vehicle-to-everything (V2X) use cases for LTE and NR", Jun. 2018 (cited on p. 52).

[162] L. Zhao, X. Li, B. Gu, *et al.*, "Vehicular communications: Standardization and open issues", *IEEE Commun. Standards Mag.*, vol. 2, no. 4, pp. 74–80, Dec. 2018. DOI: 10.1109/MCOMSTD.2018.1800027 (cited on pp. 52, 53).

[163] X. Huang, D. Zhao, and H. Peng, "Empirical study of DSRC performance based on safety pilot model deployment data", *IEEE Trans. Intell. Transp. Syst.*, vol. 18, no. 10, pp. 2619–2628, Oct. 2017. DOI: 10.1109/TITS.2017.2649538 (cited on p. 52).

[164] S. E. Carpenter and M. L. Sichitiu, "Analysis of packet loss in a large-scale DSRC field operational test", in *2016 International Conference on Performance Evaluation and Modeling in Wired and Wireless Networks (PEMWN)*, Nov. 2016, pp. 1–6. DOI: 10.1109/PEMWN.2016.7842909 (cited on p. 52).

[165] A. Bazzi, B. M. Masini, A. Zanella, *et al.*, "On the performance of ieee 802.11p and lte-v2v for the cooperative awareness of connected vehicles", *IEEE Trans. Veh. Technol.*, vol. 66, no. 11, pp. 10 419–10 432, Nov. 2017. DOI: 10.1109/TVT.2017.2750803 (cited on p. 52).

[166] W. Anwar, K. Kulkarni, T. R. Augustin, *et al.*, "PHY abstraction techniques for IEEE 802.11p and LTE-V2V: Applications and analysis", in *2018 IEEE Globecom Workshops (GC Wkshps)*, Dec. 2018, pp. 1–7. DOI: 10.1109/GLOCOMW.2018.8644470 (cited on p. 52).

[167] Z. H. Mir and F. Filali, "Lte and ieee 802.11 p for vehicular networking: A performance evaluation", *EURASIP Journal on Wireless Commun. and Netw.*, vol. 2014, no. 1, p. 89, 2014. DOI: 10.1186/1687-1499-2014-89 (cited on p. 52).

[168] "Physical layer evaluation of V2X communications technologies: 5G NR-V2X, LTE-V2X, IEEE 802.11bd, and IEEE 802.11p", in *Proc. IEEE Vehicular Technology Conference (VTC2019-Fall)*, Sep. 2019, Accepted (cited on pp. 52, 53).

[169] G. Naik, B. Choudhury, and J. Park, "IEEE 802.11bd & 5g NR V2X: evolution of radio access technologies for V2X communications", *CoRR*, vol. abs/1903.08391, 2019. arXiv: 1903.08391 (cited on p. 52).

[170] A. Filippi, K. Moerman, V. Martinez, *et al.*, "IEEE 802.11p ahead of LTE-V2V for safety applications, Tech. report, nxp semiconductors", Jan. 2017 (cited on p. 53).

[171] M. Boban, K. Manolakis, M. Ibrahim, *et al.*, "Design aspects for 5G V2X physical layer", in *IEEE Conf. on Standards for Commun. and Netw. (CSCN)*, Oct. 2016, pp. 1–7. DOI: 10.1109/CSCN.2016.7785161 (cited on p. 53).

[172] K. Zheng, Q. Zheng, P. Chatzimisios, *et al.*, "Heterogeneous vehicular networking: A survey on architecture, challenges, and solutions", *IEEE Commun. Surveys Tuts.*, vol. 17, no. 4, pp. 2377–2396, Oct. 2015. DOI: 10.1109/COMST.2015.2440103 (cited on p. 53).

[173] K. Abboud, H. A. Omar, and W. Zhuang, "Interworking of DSRC and cellular network technologies for V2X communications: A survey", *IEEE Trans. Veh. Technol.*, vol. 65, no. 12, pp. 9457–9470, Dec. 2016. DOI: 10.1109/TVT.2016.2591558 (cited on p. 53).

[174] V. Va, T. Shimizu, G. Bansal, *et al.*, "Millimeter wave vehicular communications: A survey", *Foundations and Trends in Networking*, vol. 10, no. 1, p. 107, 2016. DOI: 10.1561/1300000054 (cited on pp. 53, 59, 60, 63, 78, 93).

[175] L. Liang, H. Peng, G. Y. Li, *et al.*, "Vehicular communications: A physical layer perspective", *IEEE Trans. Veh. Technol.*, vol. 66, no. 12, pp. 10 647–10 659, Dec. 2017. DOI: 10.1109/TVT.2017.2750903 (cited on p. 53).

[176] S. Mumtaz, J. M. Jornet, J. Aulin, *et al.*, "Terahertz communication for vehicular networks", *IEEE Trans. Veh. Technol.*, vol. 66, no. 7, pp. 5617–5625, Jul. 2017. DOI: 10.1109/TVT.2017.2712878 (cited on p. 54).

[177] R. Yee, E. Chan, B. Cheng, *et al.*, "Collaborative perception for automated vehicles leveraging vehicle-to-vehicle communications", in *IEEE Intelligent Vehicles Symposium*, 2018, pp. 1099–1106. DOI: 10.1109/IVS.2018.8500388 (cited on p. 54).

[178] F. Dressler, F. Klingler, M. Segata, *et al.*, "Cooperative driving and the tactile internet", *Proceedings of the IEEE*, vol. 107, no. 2, pp. 436–446, Feb. 2019. DOI: 10.1109/JPROC.2018.2863026 (cited on p. 54).

[179] S. M. O. Gani, Y. P. Fallah, G. Bansal, *et al.*, "Message content control for distributed map sharing in vehicle safety communications", in *36th IEEE International Performance Computing and Communications Conference, IPCCC 2017, San Diego, CA, USA, December 10-12, 2017*, 2017, pp. 1–7. DOI: 10.1109/PCCC.2017.8280503 (cited on p. 55).

[180] ——, "A study of the effectiveness of message content, length, and rate control for improving map accuracy in automated driving systems", *IEEE Trans. Intell. Transp. Syst.*, vol. 20, no. 2, pp. 405–420, 2019. DOI: 10.1109/TITS.2018.2812847 (cited on p. 55).

[181] 3GPP, "New SID on NR V2X, Rp-181480", Jun. 2018 (cited on p. 55).

[182] ——, "Rp-181435, New SID: Study on NR beyond 52.6 GHz", Jun. 2018 (cited on p. 55).

[183] M. Giordani, A. Zanella, and M. Zorzi, "Millimeter wave communication in vehicular networks: Challenges and opportunities", in *Int. Conf. on Modern Circuits and Systems Technologies (MOCAST)*, May 2017, pp. 1–6. DOI: 10.1109/MOCAST.2017.7937682 (cited on p. 55).

[184] T. Zugno, M. Drago, M. Giordani, *et al.*, "Towards standardization of millimeter wave vehicle-to-vehicle networks: Open challenges and performance evaluation", *ArXiv*, vol. abs/1910.00300, 2019 (cited on pp. 55, 56).

[185] M. Mezzavilla, M. Polese, A. Zanella, *et al.*, "Public safety communications above 6 GHz: Challenges and opportunities", *IEEE Access*, vol. 6, pp. 316–329, 2018. DOI: 10.1109/ACCESS.2017.2762471 (cited on p. 55).

[186] M. Giordani, T. Shimizu, A. Zanella, *et al.*, "Path loss models for V2V mmWave communication: Performance evaluation and open challenges", in *Proc. IEEE 2nd Connected and Automated Vehicles Symposium*, 2019. arXiv: 1907.10126 [cs.NI] (cited on p. 56).

[187] 3GPP, "Tech. Report 37.885 Release 15, Study on evaluation methodology of new vehicle-to-everything (V2X) use cases for LTE and NR", Jun. 2018 (cited on p. 56).

[188] IEEE, "PHY numerology discussions, Study group on 802.11bd (tgbd) 802.11-19/0686", May 2019 (cited on p. 56).

[189] V. Va, J. Choi, T. Shimizu, *et al.*, "Inverse multipath fingerprinting for millimeter wave v2i beam alignment", *IEEE Trans. Veh. Technol.*, vol. 67, no. 5, pp. 4042–4058, May 2018. DOI: 10.1109/TVT.2017.2787627 (cited on p. 56).

[190] V. Va, T. Shimizu, G. Bansal, *et al.*, "Online learning for position-aided millimeter wave beam training", *IEEE Access*, vol. 7, pp. 30 507–30 526, 2019. DOI: 10.1109/ACCESS.2019.2902372 (cited on p. 56).

[191] N. González-Prelcic, R. Méndez-Rial, and R. W. Heath, "Radar aided beam alignment in mmwave v2i communications supporting antenna diversity", in *2016 Information Theory and Applications Workshop (ITA)*, Jan. 2016, pp. 1–7. DOI: 10.1109/ITA.2016.7888145 (cited on p. 57).

[192] A. Ali, N. González-Prelcic, and R. W. Heath, "Millimeter wave beam-selection using out-of-band spatial information", *IEEE Trans. Wireless Commun.*, vol. 17, no. 2, pp. 1038–1052, Feb. 2018. DOI: 10.1109/TWC.2017.2773532 (cited on p. 57).

[193] A. Loch, A. Asadi, G. H. Sim, *et al.*, "Mm-wave on wheels: Practical 60 ghz vehicular communication without beam training", in *2017 9th Int. Conf. on Commun. Systems and Netw. (COMSNETS)*, Jan. 2017, pp. 1–8. DOI: 10.1109/COMSNETS.2017.7945351 (cited on p. 57).

[194] V. Va, J. Choi, and R. W. Heath, "The impact of beamwidth on temporal channel variation in vehicular channels and its implications", *IEEE Trans. Veh. Technol.*, vol. 66, no. 6, pp. 5014–5029, Jun. 2017. DOI: 10.1109/TVT.2016.2622164 (cited on p. 57).

[195] T. Baykas, C.-S. Sum, Z. Lan, *et al.*, "IEEE 802.15.3c: The first IEEE wireless standard for data rates over 1 Gb/s", *IEEE Commun. Mag.*, vol. 49, no. 7, pp. 114–121, 2011. DOI: 10.1109/MCOM.2011.5936164 (cited on p. 59).

[196] E. Perahia and M. X. Gong, "Gigabit wireless LANs: An overview of IEEE 802.11 ac and 802.11 ad", *ACM SIGMOBILE Mobile Comp. Commun. Review*, vol. 15, no. 3, pp. 23–33, 2011. DOI: 10.1145/2073290.2073294 (cited on pp. 59, 77).

[197] J. Hasch, E. Topak, R. Schnabel, *et al.*, "Millimeter-wave technology for automotive radar sensors in the 77 GHz frequency band", *IEEE Trans. Microw. Theory Tech.*, vol. 60, no. 3, pp. 845–860, 2012. DOI: 10.1109/TMTT.2011.2178427 (cited on p. 60).

[198] A. D. Angelica. (2013). Google's self-driving car gathers nearly 1 GB/sec, [Online]. Available: http://www.kurzweilai.net/googles-self-driving-car-gathers-nearly-1-gbsec (cited on p. 60).

[199] T. S. Rappaport, R. W. Heath Jr, R. C. Daniels, *et al.*, *Millimeter wave wireless communications*. Pearson Education, 2014 (cited on p. 60).

[200] A. Kato, K. Sato, M. Fujise, *et al.*, "Propagation characteristics of 60-GHz millimeter waves for ITS inter-vehicle communications", *IEICE Trans. Commun.*, vol. 84, no. 9, pp. 2530–2539, 2001 (cited on p. 60).

[201] S. Tsugawa, "Issues and recent trends in vehicle safety communication systems", *IATSS research*, vol. 29, no. 1, pp. 7–15, 2005 (cited on p. 60).

[202] P. Kumari, N. Gonzalez-Prelcic, and R. W. Heath, "Investigating the IEEE 802.11 ad standard for millimeter wave automotive radar", in *Proc. IEEE Veh. Technol. Conf. Fall (VTC)*, 2015, pp. 1–5. DOI: 10.1109/VTCFall.2015.7390996 (cited on p. 60).

[203] G. Durisi, T. Koch, and P. Popovski, "Towards massive, ultra-reliable, and low-latency wireless communication with short packets", *Proc. IEEE*, vol. 104, no. 9, 2016. DOI: 10.1109/JPROC.2016.2537298 (cited on p. 60).

[204] C. Perfecto, J. D. Ser, and M. Bennis, "Millimeter-wave V2V communications: Distributed association and beam alignment", *IEEE J. Sel. Areas Commun.*, vol. 35, no. 9, pp. 2148–2162, Sep. 2017. DOI: 10.1109/JSAC.2017.2719998 (cited on pp. 63, 64, 70, 75, 76, 80, 81, 86, 87, 97).

[205] A. Yamamoto, K. Ogawa, T. Horimatsu, *et al.*, "Path-loss prediction models for intervehicle communication at 60 GHz", *IEEE Trans. Veh. Technol.*, vol. 57, no. 1, pp. 65–78, 2008. DOI: 10.1109/TVT.2007.901890 (cited on pp. 63, 93).

[206] H. Shokri-Ghadikolaei, L. Gkatzikis, and C. Fischione, "Beam searching and transmission scheduling in millimeter wave communications", in *Proc. IEEE Int. Conf. Commun. (ICC)*, London, United Kingdom., 2015, pp. 1292–1297. DOI: 10.1109/ICC.2015.7248501 (cited on p. 65).

[207] 3GPP, "3GPP TSG-RAN WG1 #86: URLLC system capacity and URLLC/eMBB multiplexing efficiency analysis" (cited on p. 67).

[208] G. Pocovi, M. Lauridsen, B. Soret, *et al.*, "Automation for on-road vehicles: Use cases and requirements for radio design", in *IEEE Veh. Technol. Conf. Fall (VTC)*, Sep. 2015, pp. 1–5. DOI: 10.1109/VTCFall.2015.7390848 (cited on p. 69).

[209] B. Soret, P. Mogensen, K. I. Pedersen, *et al.*, "Fundamental tradeoffs among reliability, latency and throughput in cellular networks", in *Proc. IEEE Global Telecommun. Conf. (GLOBECOM) Workshops*, 2014, pp. 1391–1396. DOI: 10.1109/GLOCOMW.2014.7063628 (cited on p. 69).

[210] Y. Gu, W. Saad, M. Bennis, *et al.*, "Matching theory for future wireless networks: Fundamentals and applications", *IEEE Commun. Mag.*, vol. 53, no. 5, pp. 52–59, 2015. DOI: 10.1109/MCOM.2015.7105641 (cited on pp. 69, 96).

[211] J. Mo and J. Walrand, "Fair end-to-end window-based congestion control", *IEEE/ACM Trans. Netw.*, vol. 8, no. 5, pp. 556–567, 2000. DOI: 10.1109/90.879343 (cited on p. 72).

[212] T. Q. Quek, G. de la Roche, İ. Güvenç, *et al.*, *Small cell networks: Deployment, PHY techniques, and resource management*. Cambridge University Press, 2013 (cited on p. 73).

[213] H. Park, Y. Kim, T. Song, *et al.*, "Multiband directional neighbor discovery in self-organized mmwave ad hoc networks", *IEEE Trans. Veh. Technol.*, vol. 64, no. 3, pp. 1143–1155, 2015. DOI: 10.1109/TVT.2014.2329303 (cited on p. 73).

[214] M. Kim, Y. S. Kim, and W. Lee, "Analysis of directional neighbour discovery process in millimetre wave wireless personal area networks", *IET Networks*, vol. 2, no. 2, pp. 92–101, 2013. DOI: 10.1049/iet-net.2012.0095 (cited on p. 73).

[215] C. G. Atkeson, A. W. Moore, and S. Schaal, "Locally weighted learning for control", *Artificial Intelligence Reviews*, vol. 11, no. 1-5, pp. 75–113, 1997. DOI: 10.1023/A:1006511328852 (cited on p. 74).

[216] C. Perfecto, J. Del Ser, M. I. Ashraf, *et al.*, "Beamwidth optimization in millimeter wave small cell networks with relay nodes: A swarm intelligence approach", in *Proc. 22nd Eur. Wireless Conf.*, May 2016, pp. 1–6 (cited on p. 76).

[217] S. Scott-Hayward and E. Garcia-Palacios, "Multimedia resource allocation in mmwave 5G networks", *IEEE Commun. Mag.*, vol. 53, no. 1, pp. 240–247, 2015. DOI: 10.1109/MCOM.2015.7010540 (cited on p. 76).

[218] C. Perfecto, J. D. Ser, and M. Bennis, "On the interplay between scheduling interval and beamwidth selection for low-latency and reliable V2V mmwave communications", in *20th Conf. on Innov. in Clouds, Internet and Netw. (ICIN)*, Mar. 2017, pp. 1–8. DOI: 10.1109/ICIN.2017.7899242 (cited on pp. 83, 84).

[219] M. Gerla, E.-K. Lee, G. Pau, *et al.*, "Internet of vehicles: From intelligent grid to autonomous cars and vehicular clouds", in *Internet of Things (WF-IoT), 2014 IEEE World Forum on*, 2014, pp. 241–246. DOI: 10.1109/WF-IoT.2014.6803166 (cited on p. 89).

[220] J. Park, J.-H. Lee, and S. H. Son, "A survey of obstacle detection using vision sensor for autonomous vehicles", in *Embedded and Real-Time Comp. Syst. Appl. (RTCSA), 2016 IEEE 22nd Int. Conf. on*, IEEE, 2016, pp. 264–264. DOI: 10.1109/RTCSA.2016.54 (cited on p. 89).

[221] D. Jia, K. Lu, J. Wang, *et al.*, "A survey on platoon-based vehicular cyber-physical systems", *IEEE Commun. Surveys Tuts.*, vol. 18, no. 1, pp. 263–284, 2016. DOI: 10.1109/COMST.2015.2410831 (cited on p. 89).

[222] H. Vahdat-Nejad, A. Ramazani, T. Mohammadi, *et al.*, "A survey on context-aware vehicular network applications", *Veh. Commun.*, vol. 3, pp. 43–57, 2016. DOI: 10.1016/j.vehcom.2016.01.002 (cited on p. 89).

[223] A. Broggi, A. Zelinsky, Ü. Özgüner, *et al.*, "Intelligent vehicles", in *Handbook of Robotics*, Springer, 2016, pp. 1627–1656. DOI: 10.1007/978-3-319-32552-1_62 (cited on p. 89).

[224] J. Baber, J. Kolodko, T. Noel, *et al.*, "Cooperative autonomous driving: Intelligent vehicles sharing city roads", *IEEE Robot. Autom. Mag.*, vol. 12, no. 1, pp. 44–49, 2005. DOI: 10.1109/MRA.2005.1411418 (cited on p. 89).

[225] R. Rasshofer and K. Gresser, "Automotive radar and lidar systems for next generation driver assistance functions", *Adv. Radio Sci.*, vol. 3, no. B. 4, pp. 205–209, 2005. DOI: 10.5194/ars-3-205-2005 (cited on p. 89).

[226] F. Sattar, F. Karray, M. Kamel, *et al.*, "Recent advances on context-awareness and data/information fusion in ITS", *Int. J. Intell. Transp. Syst Research*, vol. 14, no. 1, pp. 1–19, 2016. DOI: 10.1007/s13177-014-0097-9 (cited on p. 90).

[227] F. Chiti, R. Fantacci, Y. Gu, *et al.*, "Content sharing in Internet of Vehicles: Two matching-based user-association approaches", *Veh. Commun.*, 2016. DOI: 10.1016/j.vehcom.2016.11.005 (cited on p. 90).

[228] M. Fanaei, A. Tahmasbi-Sarvestani, Y. P. Fallah, *et al.*, "Adaptive content control for communication amongst cooperative automated vehicles", in *Proc. IEEE 6th Int. Symp. Wirel. Veh. Commun. (WiVeC)*, 2014. DOI: 10.1109/WIVEC.2014.6953213 (cited on p. 90).

[229] J. Santa and A. F. Gomez-Skarmeta, "Sharing context-aware road and safety information", *IEEE Pervasive Comput.*, vol. 8, no. 3, 2009. DOI: 10.1109/MPRV.2009.56 (cited on p. 90).

[230] L. Kong, M. K. Khan, F. Wu, *et al.*, "Millimeter-Wave Wireless Communications for IoT-Cloud Supported Autonomous Vehicles: Overview, Design, and Challenges", *IEEE Commun. Mag.*, vol. 55, no. 1, pp. 62–68, Jan. 2017. DOI: 10.1109/MCOM.2017.1600422CM (cited on p. 90).

[231] S. Qian, T. Zhang, C. Xu, *et al.*, "Multi-modal event topic model for social event analysis", *IEEE Trans. Multimedia*, vol. 18, no. 2, pp. 233–246, 2016 (cited on p. 90).

[232] C. Perfecto, J. D. Ser, M. Bennis, *et al.*, "Beyond WYSIWYG: Sharing contextual sensing data through mmwave V2V communications", in *2017 Eur. Conf. on Netw. and Commun. (EuCNC)*, Jun. 2017, pp. 1–6. DOI: 10.1109/EuCNC.2017.7980726 (cited on pp. 92, 97, 99, 100).

[233] A. E. Roth and M. A. Oliveira Sotomayor, *Two-sided matching: a study in game-theoretic modeling and analysis*, ser. Econometric Society Monographs. Cambridge University Press, 1992 (cited on p. 96).

[234] D. Krajzewicz, J. Erdmann, M. Behrisch, *et al.*, "Recent development and applications of SUMO - Simulation of Urban MObility", *International Journal On Advances in Systems and Measurements*, vol. 5, no. 3&4, pp. 128–138, Dec. 2012 (cited on p. 98).

[235] E. Baştuğ, M. Bennis, M. Médard, *et al.*, "Toward interconnected virtual reality: Opportunities, challenges, and enablers", *IEEE Commun. Mag.*, vol. 55, no. 6, pp. 110–117, Jun. 2017. DOI: 10.1109/MCOM.2017.1601089 (cited on pp. 103–105, 113, 127).

[236] G. P. Fettweis, "The tactile internet: Applications and challenges", *IEEE Veh. Technol. Mag.*, vol. 9, no. 1, pp. 64–70, Mar. 2014. DOI: 10.1109/MVT.2013.2295069 (cited on p. 103).

[237] M. Simsek, A. Aijaz, M. Dohler, *et al.*, "The 5g-enabled tactile internet: Applications, requirements, and architecture", in *2016 IEEE Wireless Communications and Networking Conference*, Apr. 2016, pp. 1–6. DOI: 10.1109/WCNC.2016.7564647 (cited on p. 103).

[238] B. Soret, P. Mogensen, K. I. Pedersen, *et al.*, "Fundamental tradeoffs among reliability, latency and throughput in cellular networks", in *Proc. IEEE Global Telecommun. Conf. (GLOBECOM) Wksh.s*, 2014, pp. 1391–1396. DOI: 10.1109/GLOCOMW.2014.7063628 (cited on p. 103).

[239] H. Liu, Z. Chen, and L. Qian, "The three primary colors of mobile systems", *IEEE Commun. Mag.*, vol. 54, no. 9, pp. 15–21, Sep. 2016. DOI: 10.1109/MCOM.2016.7565182 (cited on p. 104).

[240] Y. Mao, C. You, J. Zhang, *et al.*, "A survey on mobile edge computing: The communication perspective", *IEEE Commun. Surveys Tuts.*, vol. PP, no. 99, pp. 1–1, Aug. 2017. DOI: 10.1109/COMST.2017.2745201 (cited on pp. 104, 114).

[241] Y. Sun, Z. Chen, M. Tao, *et al.*, "Communication, computing and caching for mobile VR delivery: Modeling and trade-off", in *IEEE Int. Conf. on Commun. (ICC)*, May 2018, pp. 1–6. DOI: 10.1109/ICC.2018.8422519 (cited on pp. 105, 129, 130).

[242] F. Qian, L. Ji, B. Han, *et al.*, "Optimizing 360 ◦ video delivery over cellular networks", in *Proc. Int. Conf. Mobile Comp. and Netw. (MOBICOM)*, New York City, New York, 2016, pp. 1–6. DOI: 10.1145/2980055.2980056 (cited on pp. 105, 109, 110, 113, 128, 129).

[243] R. Ju, J. He, F. Sun, *et al.*, "Ultra Wide View Based Panoramic VR Streaming", in *Proc. ACM SIGCOMM. Wksh. on VR/AR Network*, 2017. DOI: 10.1145/3097895.3097899 (cited on pp. 105, 106, 113).

[244] K. Doppler, E. Torkildson, and J. Bouwen, "On wireless networks for the era of mixed reality", in *Proc. Eur. Conf. on Networks and Commun. (EuCNC)*, Jun. 2017, pp. 1–6. DOI: 10.1109/EuCNC.2017.7980745 (cited on pp. 105, 106, 113, 128).

[245] M. Chen, W. Saad, and C. Yin, "Virtual reality over wireless networks: Quality-of-service model and learning-based resource management", *IEEE Trans. Commun.*, vol. 66, no. 11, pp. 5621–5635, Nov. 2018. DOI: 10.1109/TCOMM.2018.2850303 (cited on p. 106).

[246] TelecomTV, *Lower latency is one of the big gains on offer from 5G. turns out it's fairly easily improved in LTE too*, Mar. 2018 (cited on p. 106).

[247] Wireless One, *LTE latency today 9 ms. Down to 2 ms 2019*, Mar. 2018 (cited on p. 106).

[248] I. Parvez, A. Rahmati, I. Guvenc, *et al.*, "A survey on low latency towards 5G: RAN, core network and caching solutions", *IEEE Commun. Surveys Tuts.*, vol. 20, no. 4, pp. 3098–3130, 2018. DOI: 10.1109/COMST.2018.2841349 (cited on p. 106).

[249] S. Mangiante, K. Guenter, M. D. Silva, *et al.*, "VR is on the edge: How to deliver 360 ◦ videos in mobile networks", in *Proc. ACM SIGCOMM. Wksh. on VR/AR Network*, 2017. DOI: 10.1145/3097895.3097901 (cited on pp. 106, 129, 130).

[250] A. Al-Shuwaili and O. Simeone, "Energy-efficient resource allocation for mobile edge computing-based augmented reality applications", *IEEE Wireless Commun. Lett.*, vol. 6, no. 3, pp. 398–401, Jun. 2017. DOI: 10.1109/LWC.2017.2696539 (cited on p. 106).

[251] M. S. Elbamby, C. Perfecto, M. Bennis, *et al.*, "Toward low-latency and ultra-reliable virtual reality", *IEEE Netw.*, vol. 32, no. 2, pp. 78–84, Mar. 2018. DOI: 10.1109/MNET.2018.1700268 (cited on pp. 107, 113, 123, 125, 127, 129).

[252] I. Rodriguez, H. C. Nguyen, T. B. Sorensen, *et al.*, "Analysis of 38 ghz mmwave propagation characteristics of urban scenarios", in *Proc. 21th Eur. Wireless Conf.*, May 2015, pp. 1–8 (cited on p. 108).

[253] R. Ford, M. Zhang, M. Mezzavilla, *et al.*, "Achieving ultra-low latency in 5G millimeter wave cellular networks", *IEEE Commun. Mag.*, vol. 55, no. 3, pp. 196–203, Mar. 2017. DOI: 10.1109/MCOM.2017.1600407CM (cited on p. 108).

[254] S. Amuru, "Beam learning", in *2017 IEEE International Conference on Communications (ICC)*, May 2017, pp. 1–6. DOI: 10.1109/ICC.2017.7996561 (cited on p. 109).

[255] A. Klautau, P. Batista, N. González-Prelcic, *et al.*, "5G MIMO data for machine learning: Application to beam-selection using deep learning", in *2018 Information Theory and Applications Workshop (ITA)*, Feb. 2018, pp. 1–9. DOI: 10.1109/ITA.2018.8503086 (cited on p. 109).

[256] O. Abari, D. Bharadia, A. Duffield, *et al.*, "Cutting the cord in virtual reality", in *Proc. 15th ACM Wksh. on Hot Topics in Netw. (HotNets)*, Atlanta, GA, USA, 2016, pp. 162–168. DOI: 10.1145/3005745.3005770 (cited on p. 109).

[257] K. Lee, D. Chu, E. Cuervo, *et al.*, "Outatime: Using Speculation to Enable Low-Latency Continuous Interaction for Mobile Cloud Gaming", in *Proc. Annu. Int. Conf. on Mobile Syst., Appl. and Serv. (MobiSys)*, Florence, Italy, 2015, pp. 151–165. DOI: 10.1145/2742647.2742656 (cited on p. 110).

[258] E. Zeydan, E. Bastug, M. Bennis, *et al.*, "Big data caching for networking: Moving from cloud to edge", *IEEE Communications Magazine*, vol. 54, no. 9, pp. 36–42, Sep. 2016. DOI: 10.1109/MCOM.2016.7565185 (cited on p. 114).

[259] F. Bonomi, R. Milito, J. Zhu, *et al.*, "Fog computing and its role in the internet of things", in *Proc. 1st Edition of the MCC Wksh. on Mobile Cloud Computing*, ser. MCC '12, Helsinki, Finland, 2012, pp. 13–16. DOI: 10.1145/2342509.2342513 (cited on p. 114).

[260] M. S. Elbamby, M. Bennis, and W. Saad, "Proactive edge computing in latency-constrained fog networks", in *Proc. Eur. Conf. on Netw. and Commun. (EuCNC)*, Jun. 2017, pp. 1–6. DOI: 10.1109/EuCNC.2017.7980678 (cited on p. 114).

[261] M. S. Elbamby, C. Perfecto, M. Bennis, *et al.*, "Edge computing meets millimeter-wave enabled VR: Paving the way to cutting the cord", in *2018 IEEE Wireless Commun. and Netw. Conf. (WCNC)*, Apr. 2018, pp. 1–6. DOI: 10.1109/WCNC.2018.8377419 (cited on pp. 116, 117, 120, 122–124, 129, 130).

[262] H. Xu, V. Kukshya, and T. S. Rappaport, "Spatial and temporal characteristics of 60-GHz indoor channels", *IEEE J. Sel. Areas Commun.*, vol. 20, no. 3, pp. 620–630, Apr. 2002. DOI: 10.1109/49.995521 (cited on p. 116).

[263] A. Mukherjee, "Queue-aware dynamic on/off switching of small cells in dense heterogeneous networks", in *IEEE Global Commun. Conference Workshops (GLOBECOM Wkshps)*, Dec. 2013, pp. 182–187. DOI: 10.1109/GLOCOMW.2013.6824983 (cited on p. 119).

[264] E. Baştuğ, M. Bennis, and M. Debbah, "Living on the edge: The role of proactive caching in 5G wireless networks", *IEEE Commun. Mag.*, vol. 52, no. 8, pp. 82–89, Aug. 2014. DOI: 10.1109/MCOM.2014.6871674 (cited on p. 122).

[265] M. Zink, R. Sitaraman, and K. Nahrstedt, "Scalable 360 ∘ video stream delivery: Challenges, solutions, and opportunities", *Proceedings of the IEEE*, vol. 107, no. 4, pp. 639–650, Apr. 2019. DOI: 10.1109/JPROC.2019.2894817 (cited on p. 127).

[266] P. Lungaro, R. Sjoberg, A. Valero, *et al.*, "Gaze-aware streaming solutions for the next generation of mobile vr experiences", *IEEE Trans. Vis. Comput. Graphics*, vol. 24, no. 4, pp. 1535–1544, 2018. DOI: 10.1109/TVCG.2018.2794119 (cited on p. 128).

[267] X. Corbillon, G. Simon, A. Devlic, *et al.*, "Viewport-adaptive navigable 360-degree video delivery", in *IEEE Int. Conf. on Commun. (ICC)*, IEEE, 2017, pp. 1–7. DOI: 10.1109/ICC.2017.7996611 (cited on p. 128).

[268] M. Hosseini and V. Swaminathan, "Adaptive 360 VR video streaming: Divide and conquer", in *IEEE Int. Symp. on Multimedia (ISM)*, Dec. 2016, pp. 107–110. DOI: 10.1109/ISM.2016.0028 (cited on p. 128).

[269] M. Xiao, C. Zhou, Y. Liu, *et al.*, "Optile: Toward optimal tiling in 360-degree video streaming", in *Proc. of ACM Conf. on Multimedia*, ser. MM '17, Mountain View, California, USA, 2017, pp. 708–716. DOI: 10.1145/3123266.3123339 (cited on p. 128).

[270] A. Ghosh, V. Aggarwal, and F. Qian, "A rate adaptation algorithm for tile-based 360-degree video streaming", *CoRR*, vol. abs /1704.08215, 2017. arXiv: 1704.08215 (cited on p. 128).

[271] C. Perfecto, M. S. Elbamby, J. D. Ser, *et al.*, "Taming the latency in multi-user VR 360 ∘ : A QoE-aware deep learning-aided multicast framework", *CoRR*, vol. abs/1811.07388, 2018. arXiv: 1811.07388 (cited on pp. 128, 132, 134, 142, 146, 149–151, 153–155).

[272] M. Chen, U. Challita, W. Saad, *et al.*, "Machine learning for wireless networks with artificial intelligence: A tutorial on neural networks", *CoRR*, vol. abs/1710.02913, 2017. arXiv: 1710.02913 (cited on p. 129).

[273] M. Cornia, L. Baraldi, G. Serra, *et al.*, "Predicting human eye fixations via an lstm-based saliency attentive model", *IEEE Trans. Image Proc.*, vol. 27, pp. 5142–5154, 2018 (cited on p. 129).

[274] Y. Bao, H. Wu, T. Zhang, *et al.*, "Shooting a moving target: Motion-prediction-based transmission for 360-degree videos", in *IEEE Int. Conf. on Big Data*, Dec. 2016, pp. 1161–1170. DOI: 10.1109/BigData.2016.7840720 (cited on p. 129).

[275] V. Sitzmann, A. Serrano, A. Pavel, *et al.*, "Saliency in vr: How do people explore virtual environments?", *IEEE Trans. Visualization and Comp. Graphics*, vol. 24, no. 4, pp. 1633–1642, Apr. 2018. DOI: 10.1109/TVCG.2018.2793599 (cited on p. 129).

[276] A. Nguyen, Z. Yan, and K. Nahrstedt, "Your attention is unique: Detecting 360-degree video saliency in head-mounted display for head movement prediction", in *Proceedings of the 26th ACM International Conference on Multimedia*, ser. MM '18, Seoul, Republic of Korea: ACM, 2018, pp. 1190–1198. DOI: 10.1145/3240508.3240669 (cited on p. 129).

[277] A. Nguyen and Z. Yan, "A saliency dataset for 360-degree videos", in *Proceedings of the 10th ACM Multimedia Systems Conference*, ACM, 2019, pp. 279–284 (cited on p. 129).

[278] C.-L. Fan, J. Lee, W.-C. Lo, *et al.*, "Fixation prediction for 360 ∘ ; video streaming in head-mounted virtual reality", in *Proc. Wksp on Network and Op. Sys. Support for Dig. Audio and Video*, Taipei, Taiwan: ACM, 2017, pp. 67–72. DOI: 10.1145/3083165.3083180 (cited on p. 129).

[279] C. Li, W. Zhang, Y. Liu, *et al.*, "Very long term field of view prediction for 360-degree video streaming", 2019. arXiv: 1902.01439 (cited on p. 129).

[280] M. Xu, Y. Song, J. Wang, *et al.*, "Predicting head movement in panoramic video: A deep reinforcement learning approach.", *IEEE Trans. Pattern Analysis and Machine Intelligence*, 2018 (cited on p. 129).

[281] Y. Zhang, P. Zhao, K. Bian, *et al.*, "Drl360: 360-degree video streaming with deep reinforcement learning", in *IEEE Conf. on Comp. Commun. (INFOCOM 2019)*, Apr. 2019, pp. 1252–1260. DOI: 10.1109/INFOCOM.2019.8737361 (cited on p. 129).

[282] X. Hou, Y. Lu, and S. Dey, "Wireless VR/AR with edge/cloud computing", in *2017 26th International Conference on Computer Communication and Netw. (ICCCN)*, Jul. 2017, pp. 1–8. DOI: 10.1109/ICCCN.2017.8038375 (cited on pp. 129, 130).

[283] J. Chakareski, "VR/AR immersive communication: Caching, edge computing, and transmission trade-offs", in *Proc. ACM SIGCOMM. Wksh. on VR/AR Network*, Los Angeles, CA, USA, 2017, pp. 36–41. DOI: 10.1145/3097895.3097902 (cited on pp. 129, 130).

[284] A. Prasad, M. A. Uusitalo, D. Navrátil, *et al.*, "Challenges for enabling virtual reality broadcast using 5g small cell network", in *2018 IEEE Wireless Commun. and Netw. Conf. Wksh.s (WCNCW)*, Apr. 2018, pp. 220–225. DOI: 10.1109/WCNCW.2018.8368976 (cited on p. 130).

[285] A. Prasad, A. Maeder, and M. A. Uusitalo, "Optimizing over-the-air virtual reality broadcast transmissions with low-latency feedback", in *IEEE 5G World Forum (5G-WF)*, Santa Clara, California, US, Jul. 2018 (cited on p. 130).

[286] N. Carlsson and D. Eager, "Had you looked where i'm looking: Cross-user similarities in viewing behavior for 360 video and caching implications", *arXiv preprint arXiv:1906.09779*, 2019 (cited on p. 130).

[287] M. Chen, W. Saad, C. Yin, *et al.*, "Echo state transfer learning for data correlation aware resource allocation in wireless virtual reality", in *Asilomar Conf. Signals, Syst., and Comp.*, Oct. 2017. DOI: 10.1109/ACSSC.2017.8335683 (cited on p. 130).

[288] N. D. Sidiropoulos, T. N. Davidson, and Z.-Q. Luo, "Transmit beamforming for physical-layer multicasting", *IEEE Trans. Signal Process.*, vol. 54, no. 6, pp. 2239–2251, Jun. 2006. DOI: 10.1109/TSP.2006.872578 (cited on p. 131).

[289] 3. G. P. P. (3GPP), "ETSI TR 138 901 V14.3.0: 5G; Study on channel model for frequencies from 0.5 to 100 GHz (3GPP TR 38.901 version 14.3.0 release 14)", Tech. Rep., 2018 (cited on pp. 133, 135).

[290] K. Cho, B. van Merriënboer, Ç. Gülçehre, *et al.*, "Learning phrase representations using RNN encoder–decoder for statistical machine translation", in *Proc. Conf. Emp. Methods Natural Lang. Process. (EMNLP)*, Oct. 2014 (cited on p. 145).

[291] S. Hochreiter and J. Schmidhuber, "Long short-term memory", *Neural Comput.*, vol. 9, no. 8, pp. 1735–1780, Nov. 1997. DOI: 10.1162/neco.1997.9.8.1735 (cited on p. 145).

[292] J. Chung, C. Gulcehre, K. Cho, *et al.*, "Empirical evaluation of gated recurrent neural networks on sequence modeling", English (US), in *NIPS 2014 Wksh. on Deep Learning*, 2014 (cited on p. 145).

[293] F. Chollet *et al.*, *Keras*, https://keras.io, 2015 (cited on p. 145).

[294] P. J. Werbos, "Backpropagation through time: What it does and how to do it", *Proc. IEEE*, vol. 78, no. 10, pp. 1550–1560, Oct. 1990. DOI: 10.1109/5.58337 (cited on p. 147).

[295] D. P. Kingma and J. Ba, "Adam: A method for stochastic optimization", *CoRR*, vol. abs/1412.6980, 2014. arXiv: 1412.6980 (cited on p. 147).

[296] W.-C. Lo, C.-L. Fan, J. Lee, *et al.*, "360◦ video viewing dataset in head-mounted virtual reality", in *Proc. ACM Conf. on Multimedia Syst.*, Taipei, Taiwan, 2017, pp. 211–216. DOI: 10.1145/3083187.3083219 (cited on p. 148).

[297] C. Jiang, H. Zhang, Y. Ren, *et al.*, "Machine learning paradigms for next-generation wireless networks", *IEEE Wireless Commun. Mag.*, vol. 24, no. 2, pp. 98–105, Apr. 2017. DOI: 10.1109/MWC.2016.1500356WC (cited on p. 161).

[298] R. Shafin, L. Liu, V. Chandrasekhar, *et al.*, *Artificial intelligence-enabled cellular networks: A critical path to beyond-5G and 6G*, 2019. arXiv: 1907.07862 [cs.IT] (cited on p. 167).

[299] D. Meagher, "Geometric modeling using octree encoding", *Computer graphics and image processing*, vol. 19, no. 2, pp. 129–147, 1982 (cited on p. 167).

Appendix A

Dandelion-encoded Trees under Multi-breeded Crossover Operation:

A simulation-based quantitative analysis of topological heritability

A.1 Introduction

Since the very advent of Telecommunications, Operations Research and Industrial Engineering many optimization problems stemming from these fields have been traditionally modeled as graph optimization paradigms. In such problems the graph embodying a potential solution is composed by nodes representing the variables to be optimized and edges interconnecting them as driven by a function of structural fitness and/or the constraints imposed in the formulation of the problem at hand. In recent years the number of optimization scenarios whose solutions can be modeled as graphs (in particular, tree graphs) has ignited fast at the pace of new interesting paradigms in bioengineering (e.g. automated delineation of dendritic trees [appA1], finance [appA2] and social network analysis (e.g. influence epidemics [appA3]). Research on tree optimization, however, dates back several decades ago with the seminal work of Borůvka [appA4], Kruskal [appA5] and Prim [appA6] around the minimum spanning tree problem. Since then alternative formulations to this problem have been extensively studied by incorporating new measures of structural fitness, imposing constraints to the graph and/or using novel optimization algorithms (a comprehensive survey can be found in [appA7]).

In this context, the ever-growing scales of tree optimization problems and the computational complexity of deterministic approaches have motivated the need for techniques not only aimed at efficiently exploring the space of possible tree configurations, but also at hybridizing them with repair methods to address topological constraints. This is the rationale for the upsurge of tree solution strategies for metaheuristic algorithms proposed in the last decade. When modeling a given optimization problem, it is of utmost importance to use a phenotype

representation in such a way that search operators preserve most of the properties and constraints of the represented genotype. This is particularly complex in graph genotypes, specially when there are a priori structural constraints imposed over the solution. When tackling tree optimization problems with e.g. Genetic Algorithms, these topological constraints require that the phenotype representation of a newly produced chromosome (after crossover and mutation operators), should inherit structural properties of the parents from which its phenotype was built (crossover) and maintain a level of topological vicinity when small changes are made to the phenotype (mutation). These desirable properties for tree phenotypes (referred to as *heritability* and *locality*) have been so far targeted by different encoding proposals for tree optimization problems. This chapter delves into one of such tree encoding strategies: the Dandelion code [appA8], which belongs to the broad family of Cailey codes and has been shown to feature good topological preservation characteristics when processed through conventional crossover and mutation operators from Genetic Algorithms. As a result, applications using this encoding abound in the literature, such as the design of networks [appA9], [appA10], [11], [appA12], the structure of call centers [appA13] and the layout of energy distribution grids [appA14], among others.

Besides tree encoding strategies, in the last years the research community has witnessed an upsurge of new bio-inspired metaheuristic solvers that rely on rather different operators than those featured by naïve GAs. Examples abound and mimic very diverse processes observed in Nature and Social Sciences, from the mutual attraction between individuals in firefly swarms [appA15] to reproduction, competitive colonization and predation processes in coral reefs [appA16].

This chapter focuses on an specific crossover operator that differs from standard procedures in the fact that it essentially embodies a stochastic component-wise multi-parent strategy. In words: any given component (i.e. gene in Genetic Algorithms) of the new individual (correspondingly, chromosome) can be inherited from any other individual within the population. This particular recombination method has gained momentum in the last few years by virtue of its role as the compounding operator harmony memory considering rate (HMCR) of the so-called HSA, a population-based solver proposed in [appA17] that imitates the process of music composition observed in jazz bands. However, it has not been until recently when several studies have exposed HSA as a particular instance of $(\mu + 1)$ ESs [appA18] just using a different terminology [appA19], [appA20]. It should be remark here that this study focuses on this operator from an impartial standpoint with respect to this noted controversy, and empirically analyzes its topological preservation properties when applied to Dandelion-encoded populations under different values of its control parameter.

Specifically, this chapter extends the preliminary work published in [21] by 1) mathematically defining different measures of topological heritability; 2) including results from differently emulated convergence stages of the algorithm; and 3) comparing the obtained figures for the multi-parent operator at hand to those rendered by one-point, two-points and uniform crossover operators in EA. As the results will evince, in terms of topological inheritance there is no difference between a naïve uniform crossover and the multi-parent recombination method under study except for a change in the scaling of their controlling parameters.

A.1.1 Main Contributions

Next the main contributions of this chapter are summarized:

Main Contributions

1. A problem-agnostic methodology, ensuring both a broader scope and utility of results without any problem-specific bond is proposed to investigate the performance of the crossover featured by HSA/$(\mu + 1)$ES, *i.e.*, HMCR/GDR, in the context of Dandelion-coded tree optimization.
   (a) The use of a dissimilarity metric in the phenotype space, *i.e.*, of topological resemblance is proposed, with a two-fold purpose:
      i. Provide information about how far/close the algorithm is to convergence based on and the topological resemblance that is given by the dissimilarity ratio ρ, of the population.
      ii. Under the premise that as $R_* \to 1$, $\mathbf{Q} \to \mathbf{P}$, compare how tightly the edge distribution of the new solutions $\mathbf{Q}$ fits that of the benchmark original population represented by the aggregated connectivity matrix $\mathbf{P}$.
   (b) The use of the Kullback-Leibler divergence $D(\mathbf{P} \parallel \mathbf{Q})$ is proposed as a measure of transmission together with three new indicators defined *ad hoc* to shed light on different aspects of topological heritability by quantifying *lost* edges, *new* edges and *amplified* edges.
2. An extension to the experimental setup is proposed to apply the original methodology to one-point, two-point and uniform crossover EA operators defining a *parenthood ratio* parameter to govern in what proportion the crossover process chooses the second parent whenever in need of selecting the origin of the feature at hand to spawn the first offspring.
   (a) Extensive simulations evince that the multi-parent and the conventional uniform crossover are almost equivalent to each other, except for a scaling in their parameters under a near-convergence stage of the population.

A.1.2 Organization

The chapter is structured as follows: Section A.2 describes Evolutionary Algorithms and enumerates the desirable properties of tree solution encoding strategies. Next, Dandelion-like codes, HSA operation, and the multi-parent recombination operator under study are introduced in Sections A.3, A.4 and A.5, respectively. Section A.6 establishes the adopted methodology and metrics to evaluate the heritability of the heuristics, and Section A.7 discusses the obtained experimental results. Finally, Section A.8 ends the chapter by drawing several conclusions from the experimental results.

A.2 Evolutionary Algorithms and Tree Encoding Schemes

As recapitulated in Section II.1.1 from Chapter II.1 regarding heuristic optimization, EAs and ESs are inspired by concepts from natural evolution e.g., reproduction with variation, selection based on fitness, inheritance and survival of the fittest [appA22]. Under this simile, the evolution of individuals is deeply

influenced by the selection of a suitable encoding strategy (phenotype) for the solutions to the problem at hand. Over these solutions a number of operators that resemble the aforementioned evolutionary processes are subsequently applied. Genetic Algorithms, perhaps the most renowned EAs to date, are characterized by crossover and mutation operators that iteratively refine a set of candidate solutions or chromosomes: the first combines phenotypical information from two parent chromosomes, whereas the second models the diversity in the offspring of new generations of individuals by randomly modifying gene Equations (i.e. values of the candidate solution). The fitness of each solution or chromosome imposes the likelihood of subsequently produced new offspring to inherit phenotypical information from the individual at hand, as the Genetic Algorithm favors the survivability of those chromosomes with better fitness. Therefore, as new generations succeed each other, chromosomes that represent better solutions survive and propagate their genetic material to their offspring.

Evolutionary Algorithms are utilized in a number of optimization problems where an optimal tree is to be sought according to a given measure of structural fitness. Generally speaking the success of any metaheuristic solver (not only EAs) and its search efficiency rely on the interaction and matching between the solution encoding scheme under which candidate solutions are represented and the operators that generate offspring solutions from the existing population. Bearing this in mind, in tree optimization problems it is crucial to study how a given tree encoding scheme behaves under evolutionary operators in terms of topological locality and heritability. On the one hand, a high locality of any encoding strategy implies that small changes to the phenotype of the encoded chromosome gives rise to an equally minor variation of the genotype of the represented solution, i.e. locality is a measure of the interaction between a encoding scheme and any *mutation* operator. On the other hand, heritability can be generally defined as the proportion of observed variations in a particular trait that can be attributed to inherited genetic factors in contrast to environmental ones. When contextualized in EAs, heritability can be defined as the capability of a coding scheme to preserve attributes of the parent solutions in the produced offspring after a crossover has been applied.

The evaluation of the level of heritability of any given encoding approach can be performed separately by addressing two related concepts: *transmission* and *respect*. Transmission is obtained if all genotypical characteristics possessed by an offspring were originally exhibited in at least one of its parents, whereas respect is scored if all characteristics shared by both parents are also present in their offspring. As such, a phenotypical encoding for tree graphs will exhibit low locality when offspring trees share few edges in common with the original trees from where they have been produced. This also unveils the fact that the EA at hand will not be able to exploit the similarities and complementarity between iteratively refined solutions when producing new offspring, hence reducing the self-learning capability of the solver to a mere selective random search procedure driven strictly by a mutation procedure.

Locality in tree optimization problems can be evaluated in a quantitative manner by computing the average and maximum number of modified edges when one symbol in the phenotype is changed at random. On the other hand, transmission and respect can be measured by counting the number of edges in the offspring that are not present in any of the parents, as well as the number of edges present in both parent trees that are not found in the offspring. In fact high locality and heritability have been highlighted by many research studies as desirable characteristics [appA23]–[appA25], jointly with several other properties that when met, guarantee that a tree-coding scheme is well-suited for exploiting

the exploratory power of a EA. Palmer and Kershembaum [appA23] summarize them as: full coverage or completeness (the code can represent all possible trees), zero bias (all trees are represented by the same number of codes), perfect feasibility or closure (codes represent only valid solutions, i.e. trees), efficiency/linear complexity in encoding/decoding operation, and locality (level of topological preservation of the tree when its encoded representation is changed).

As mentioned in the introduction, this chapter gravitates on how the Dandelion code performs in terms of topological preservation under the effect of multi-parent recombination operators. To this end, Dandelion codes will be next introduced.

A.3 Dandelion and Dandelion-like Codes

Dandelion and Dandelion-like codes [appA26] are a subset of Cayley codes and, as such, are a bijection between the set of labeled unrooted trees on n nodes and $n-2$ tuples of node labels, i.e., each tree matches to a single string or code and vice versa. All bijections are naturally endowed with full coverage, zero-bias and perfect feasibility. Moreover, a Cayley string undergoing mutation or crossover between two Cayley strings will always produce another valid Cayley string. Cayley codes can be further separated into two separate subcategories: Deletion or Prüfer-like Cayley codes, with poor properties for evolutionary search [appA27] and Transformation or highly local Cayley codes. The Blob Code, the Dandelion Code, the Happy Code [appA8], the MHappy Code [appA28] and the Theta Code [appA29] and in general all Dandelion-like codes fulfill the two additional premises enunciated in [appA23]: they all show linear complexity and high locality. Linear-time encoding and decoding algorithms are common in literature for all Dandelion-like codes and [appA30] provided unique parallel encoding and decoding algorithms that, when properly parametrized, can be used for all dandelion-like mappings. Finally, [appA31] proved that Dandelion-like codes outperform all other Cayley codes in terms of locality and heritability. This work also hypothesized and later verified via experimental results that the Dandelion code shows a bounded locality of 5: with independence of the length of the code, a random change of one single symbol in the code will modify at most five edges in the resulting tree with respect to the original one. [appA26] extended this result to all dandelion-like codes and [appA32] further mathematically justified and explained it. To summarize, both theoretical and experimental results have proven that the Dandelion code positively satisfies all five properties enunciated by Palmer and Kershembaum, hence concluding that it is a suitable tree encoding choice for an efficient tree representation.

The study presented in this work demands an extensive use of Dandelion decoding. Therefore the so-called "fast algorithm" proposed in [appA8] will be briefly described for the sake of completeness. The procedure to decode the n-node tree represented by the Dandelion code $C = \{C_2, C_3, \ldots, C_{n-1}\}$, and output a tree $T \in \Gamma_n$, with Γ_n denoting the set of possible tree configurations connecting n nodes, comprises the following steps:

Step 1: A $2 \times (n-2)$ matrix $\mathbf{A}_c$ is constructed by arranging the elements $\{2, 3, 4, \ldots, n-1\}$ in the first row and the elements of C in the second row. As exemplified in Fig. A.1 for $C = \{1, 6, 7, 12, 4, 3, 4, 9, 5, 9\}$, $\mathbf{A}_c$ results in

$$\mathbf{A}_c = \begin{bmatrix} 2 & 3 & 4 & 5 & 6 & 7 & 8 & 9 & 10 & 11 \\ 1 & 6 & 7 & 12 & 4 & 3 & 4 & 9 & 5 & 9 \end{bmatrix}. \tag{A.3.1}$$

Step 2: $f_C : [2, n-1] \to [1, n]$ is defined such that $f_C(i) = C_i$ for each $i \in [2, n-1]$. Note that $f_C(i)$ corresponds to the i-th position C_i of the code.

Step 3: The cycles $\{Z_1, \ldots, Z_L\}$ associated to the function f_C are computed. In the example f_C has 2 cycles: (4 7 3 6) and (9). Let b_l be the maximum element in cycle Z_l, with $l \in \{1, \ldots, L\}$. Cycles are then reordered such that b_l is the rightmost element of Z_l, and that $b_l > b_{l'}$ if $l < l'$, i.e. cycle elements rotated so that the largest element becomes the rightmost. Finally cycles and sorted so that cycle maxima decreases from left to right. In the example this step results in $\{Z_1, Z_2\} = \{(9), (3\ 6\ 4\ 7)\}$

Step 4: a single list π of the elements in $\{Z_1, Z_2, \ldots, Z_L\}$ is composed in the order they occur in the cycle list, from the first element of Z_1 to the last entry of Z_L. $\pi = \{(9)(3\ 6\ 4\ 7)\}$.

Step 5: the tree $T \in \Gamma_n$ corresponding to C is constructed by creating a path from node 1 to node n by following the list π from left to right and by creating the edge between the nodes labelled with i and C_i for every $i \in \{2 \ldots, n-1\}$ not occurring in π.

The tree corresponding to the Dandelion code $C = (1, 6, 7, 12, 4, 3, 4, 9, 5, 9)$ is given in Fig. A.1, where edge orientation has been provided for clarity.

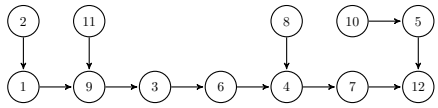

FIGURE A.1: Tree representation corresponding to the dandelion code $C = \{1, 6, 7, 12, 4, 3, 4, 9, 5, 9\}$. (Reprinted by permission from: Springer Nature [33] ©2017)

A.4 Harmony Search Algorithm

Since the seminal work by Geem et al in [appA17], the HSA algorithm has been thenceforth applied to solve optimization problems arising in very diverse knowledge fields as recently surveyed in [34], [35]. In a similar fashion to how populations are evolved in EAs, HSA maintains a set of candidate solutions or *harmonies* – referred to as the harmony memory (HM) – which are iteratively refined via intelligent permutation and randomization operators. Such operators resemble the improvisation process of musicians when guessing musical notes (correspondingly, optimization variables) that jointly sound pleasantly under an aesthetic standard of musical fitness. This improvisation procedure is repeated until a stop criterion is met, e.g. a maximum number of iterations is reached. The fact that HSA applies its operators on a per-note basis – with independent probability distributions – to each of the instruments involved in creating the harmony allows balancing the intensification and diversification capacities of HSA.

The nominal search process of the HSA algorithm comprises four steps aimed at progressively enhancing the optimality of the produced solution for a given optimization problem:

- Step 1 (initialization of HM): first the values of the HSA parameters are specified, such as HM size, stopping criteria, probabilities of its constituent operators and solution encoding approach. Next, a memory of φ harmonies

of length N is initialized in the form of a $\varphi \times n$ matrix $\mathbf{S}$, where each row represents a solution vector for the given problem. In those cases where no a priori knowledge of the solution space is available $\mathbf{S}$ is populated with harmonies whose individual elements have been drawn uniformly at random from their alphabet.

- Step 2 (improvisation of a new harmony vector): after initializing the set of stored solutions, a new solution vector $\{x_1, ..., x_n\}$ is improvised. For each position $j \in \{1, ..., n\}$ at least one of the three probabilistic operators (namely PAR, HMCR and RSR) are applied. As elaborated by [36] the three resources of a musician during the improvisation process are 1) playing a tone exactly as remembered from his or her memory; 2) playing a slightly different version of the original tone; or 3) composing new or random notes. Each of these three options links directly to one of the three components of HSA in the form of its operators: usage of harmony memory, pitch adjusting and randomization, as follows:
  - The **Harmony Memory Considering Rate**, controlled by the probabilistic parameter HMCR $\in [0, 1]$, allows emulating the idea of recalling past memories of pitches that led to aesthetically good or pleasant harmonies and thus reuse them for the generation of newly improvised solutions. Specifically, HMCR denotes the probability that the new improvised value for a note is selected from the values of the same note in the $\varphi - 1$ harmonies remaining in the memory.
  - The **Pitch Adjustment Rate**, driven by the parameter pitch adjustment rate (PAR)PAR $\in [0, 1]$, mimics the effect of a frequency change in a note. PAR represents the probability that the value for a given note is replaced with that of any of its corresponding neighboring values. Here the notion of *neighborhood* should be established by the fitness function itself rather than by a naive value-based ordering.
  - The **Random Selection Rate** operator, with parameter random selection rate (RSR) $\in [0, 1]$, reflects the creativity of the musician when improvising new notes in a more explorative manner than through the aforementioned pitch adjustment rate. RSR operates in a similar fashion to the mutation process of genetic algorithms, e.g. by spanning the selection of the new note value to all the alphabet rather than within the neighborhood of the value to be changed.

  The HMCR procedure ensures that good harmonies are considered as elements of new candidate solutions, while the PAR and RSR operators allow neighboring or completely new note values to become part of the new harmony. These three operators work together to provide HSA with a good balance between global exploration and local exploitation.
- Step 3 (evaluation of new harmonies and update of the Harmony Memory): if the fitness of the new harmony results to be better than the objective value of the worst solution in the memory, the new solution $\{x_1, \ldots, x_n\}$ replaces the worst solution vector in the memory.
- Step 4 (termination): if the stopping criterion is met (e.g. a given number of iterations), the search process is terminated, and the solution in HM with the best value of the fitness function is declared as the solution found by the algorithm. Otherwise steps 2 to 4 are again performed.

A.5 Multi-parent Crossover Operation

As has been mentioned in the introduction, the multi-parent recombination method considered in this work plays a central role in the definition of $(\mu+1)$ ES, and embodies one of the constituent improvisation operators of the HSA solver described above. At a first glance the procedure under which the pool of candidate solutions evolve in HSA does not differ significantly from EAs: in essence a set of candidate solutions or *harmonies* undergoes several combination and randomization operators that resemble those of GA, ES and other evolutionary solvers alike. It is indeed in the metaphor behind the definition of its operators where the main difference between both metaheuristic solvers is claimed to reside: the HSA operators (namely, HMCR, PAR and RSR) imitate the improvisation process of jazz musicians when guessing musical notes (correspondingly, optimization variables) that sound pleasantly under an aesthetic standard of musical fitness. Furthermore, HSA applies its operators on a per-note basis, with independent probability distributions and without any prior selection procedure.

All in all, this crossover method has been shown in [appA20] to be generalizable as a particular instance of the GDR operator extensively addressed in the literature related to ES [appA37], by which each optimization variable takes its value from a randomly selected solution in the current population. As shown in this recent contribution, the GDR operator can be complemented with two stochastically driven mutation operators similar to the PAR and RSR processes in HSA. By properly setting the probabilities that trigger such mutation operators HSA can be formally shown to be equivalent to a $(\mu + 1)$ ES, with μ equal to the size of the memory of harmonies in HSA.

Nonetheless, this chapter provides empirical evidence of the performance of the crossover featured by this metaheuristic framework in the context of Dandelion-coded tree optimization without entering any *debate* about its originality. To this end we will define a generic *multi-parent crossover* rate R_* such that, if the population is denoted as $\{\mathbf{x}^{\phi}\}_{\phi=1}^{\varphi}$ (with φ denoting its size and $\mathbf{x}^{\phi} \doteq \{x_1^{\phi}, \ldots, x_n^{\phi}\}$ the ϕ-th individual), the new value $x_i^{\phi,\prime}$ for a given optimization variable x_i^{ϕ} will be given by

$$x_i^{\phi,\prime} = \begin{cases} \mathcal{X}_i^{\phi} & \text{if } \mathcal{U}(0,1) < R_*, \\ x_i^{\phi} & \text{otherwise,} \end{cases} \tag{A.5.1}$$

where $\mathcal{X}_i^{\phi}$ is a realization of a uniformly distributed discrete random variable with support $\{x_i^1, \ldots, x_i^{\phi-1}, x_i^{\phi+1}, \ldots, x_i^{\phi}\}$, and $\mathcal{U}(0,1)$ is the output of a uniformly distributed continuous random variable with support $[0,1]$. It should be noted that this defined rate serves as a generalization of the multi-parent crossover targeted in this study, and permits to gain insight on its inherent utility for Dandelion-coded tree optimization with impartiality with respect to the controversy around HSA.

Before proceeding further it should be remarked that the present study does not span towards the study of the locality properties of vicinity-constrained mutation operators like the one proposed in the HSA framework (namely, PAR). Algorithmically speaking there is no difference between the PAR operator of HSA and the standard mutation procedure of GA. Instead, it is in how the values of the alphabet of each optimization variable are sorted depending on the fitness function at hand where the main difference between the PAR and the standard mutation operator lies. Besides, since an application-agnostic methodology is followed for this study the PAR operator reduces to a upper- and lower-bounded mutation applied to the encoded individual. Therefore, the locality preservation

properties of Dandelion-encoded solutions under conventional mutation operators inspected in [appA26], [appA31], [appA32] will hold in this case.

A.6 Quantifying Locality, Transmission and Respect

Beyond the initial findings for Dandelion-encoded EAs reported in [appA31], several aspects of the operator under study motivated the preliminary study from a fitness-agnostic perspective published by the authors in [21]. Specifically:

- The polygamist nature of the multi-parent crossover involves that any newly improvised solution could potentially inherit characteristics from the entire population. As a result, is it difficult to trace back the parenthood of each individual feature of the newly produced candidate solution.
- The element-wise application of the operator over the Dandelion encoded tree unchains a search process of finer granularity than regular crossover schemes, allowing for a more flexible randomized variability of the produced solutions with respect to their parents.

Although the selected problem-agnostic methodology ensures a broader scope and utility of results without any problem-specific bond, it also implies that candidate solutions will not be evaluated under a given fitness so as to rank them and further proceed with subsequent iterations of the search algorithm. Without any such ranking criterion the only intuition about how far/close the algorithm is to convergence will come from assessing to what degree candidate solutions in the current population resemble one to each other, i.e. measuring the (dis)similarity in the phenotype space.

By adopting the topological resemblance as the criterion about how far the algorithm is from converging, three different hypothesized situations should be considered during the search procedure of every crossover strategy:

- Initialization: during the early stages of the search process, exploration dominates exploitation as the population contains solutions that bear little or no genotypical alikeness at all to each other. Operators and fitness-based sorting have not yet guided the algorithm to potentially optimal regions of the search space. As new solutions are produced from an heterogeneous set of parents, it is not expected that the crossover operation, whatsoever, would render good transmission or respect properties during these initial iterations of the algorithm.
- Intermediate stages: by virtue of the joint effect of the operators and fitness-based sorting procedure, the population will be filled with candidate solutions that feature a progressively higher similarity to each other.
- Convergence: in the final stages of the algorithm all candidate solutions in the population will be strongly similar to each other. Therefore their represented trees will be characterized by a strong topological similarity. This scenario should permit measuring the effect of crossover operators in their attempt at locally exploiting the contents of the population of individual solutions.

In all the above stages a high correlation among encoded individuals in the phenotype space is presumed to propagate to an equivalently high topological closeness by virtue of the reported high locality of Dandelion codes.

A.6.1 Experimental Setup

The study of heritability preservation of Dandelion codes undertaken in [21] is the baseline required for understanding how one-point, two-point and uniform crossover schemes can be fine tuned to produce comparable results to those produced by the R_*-driven procedure. Monte Carlo simulations will be used due to the probabilistic nature of the parameters controlling the operators that comprise the benchmark. This methodology is summarized in the following subsections.

A.6.1.1 Candidate Population Generation

A complete set of 30 different populations was created for each tuple (φ, n, ρ), namely population size, number of nodes in the tree and dissimilarity ratio between solutions/chromosomes within the population.

Experiments consist of a Dandelion code that will undergo the crossover operation dictated by Equation (A.5.1), and a population whose contained φ solutions may hold a certain degree of resemblance between them given by $\rho \in [0, 1]$. Similarity for Dandelion encoded trees can be established by different means; in this case a baseline solution is generated uniformly at random, whereas the remaining $\varphi - 1$ are produced by randomly changing $\rho \cdot (n - 2)$ elements of the baseline Dandelion code.

Increasing ρ will result in an augmented distance between the trees represented by the baseline solution and the newly produced candidate solution. Therefore, populations generated by using high values of ρ will reflect a significant genotypical randomization within the individuals, which is characteristic of early stages of the search procedure. Likewise, low values of ρ will emulate the situation where trees within the population are topologically similar to each other as a result of the metaheuristic/EA search procedure coming to an convergence state. Values of ρ will be tuned so as to provide sets of populations in initial, intermediate, and near-convergence stages for each tuple (φ, n), and thus allow to assess whether conclusions drawn for the near-convergence state hold for the initialization or intermediate stages.

A.6.1.2 Topological Heritability Indicators

During the initialization phase each dandelion code will be decoded to yield a directed connectivity matrix $\mathbf{P}(\phi)$, with $\phi \in \{1, \ldots, \varphi\}$. By summing and normalizing over all such matrices an aggregate connectivity matrix $\mathbf{P}$ is computed. This aggregate connectivity matrix represents the base edge probability distribution that the crossover operators – depending on the value of their controlling parameter – should asymptotically impose on the newly produced candidate solutions. Likewise, the successive application of the crossover operator at hand will give rise to a series of new Dandelion codes whose decoding will produce a set of connectivity matrices. After aggregation and normalization, the resulting matrix denoted as $\mathbf{Q}$ will reflect the experimental edge distribution arising from the application of the crossover operation to the initial population. It should be clear that when $R_* \to 1$, $\mathbf{Q} \to \mathbf{P}$, i.e. the edge distribution of the new solution should more tightly fit that of the entire benchmark population from which it was produced. In this scenario:

- *Transmission* will be given by the ratio of parental edges that remain present in the new solution. It is upper-bounded by the number of non-zero probability edges in $\mathbf{P}$. Full transmission will be obtained if $\forall p_{ij} \in \mathbf{P}$ such

that $p_{ij} \neq 0$, its corresponding $q_{ij} \in \mathbf{Q}$ fulfills $q_{ij} \neq 0$ for $i, j \in \{1, \ldots, n\}$[1]. Another indicator of statistical similarity is the so-called Kullback-Leibler divergence, which represents a non-symmetric measure of the difference between two probability distributions. It is indeed a measure of the information lost when $\mathbf{Q}$ is used to approximate $\mathbf{P}$, being $\mathbf{P}$ a base distribution and $\mathbf{Q}$ a experimental distribution. The Kullback-Leibler divergence is given by

$$D(\mathbf{P} \parallel \mathbf{Q}) = \sum_{\substack{ij \\ p_{ij},\, q_{ij} \neq 0}} \left(p_{ij} \ln \frac{p_{ij}}{q_{ij}} + (1 - p_{ij}) \ln \frac{1 - p_{ij}}{1 - q_{ij}} \right), \tag{A.6.1}$$

i.e., it is only defined if $\forall q_{ij} = 0$ implies $p_{ij} = 0$, and whenever $p_{ij} = 0$ its contribution to the sum is considered zero. The lower $D(\mathbf{P} \parallel \mathbf{Q})$ is, the closer $\mathbf{P}$ and $\mathbf{Q}$ will be.

- *Respect* can be equally measured as the ratio of mutually shared parental edges in candidate solutions. Due to the polygamy of the multi-parent crossover operator, only those edges appearing in all Dandelion-coded trees within the initial population may contribute to the computation of respect. For that reason, respect will be upper bounded by $|\{p_{ij} \in \mathbf{P} : p_{ij} = 1\}|$, where $|\cdot|$ denotes cardinality. Respect will be achieved if $\forall p_{ij} \in \mathbf{P}$ such that $p_{ij} = 1$ its corresponding q_{ij} in $\mathbf{Q}$ equals 1. Respect is thus a special case of full transmission and as such, will be separately evaluated.

Other interesting indicators of topological heritability that can be inferred from the experiments include:

- *Lost* edges: they refer to parental edges that no longer appear in candidate solutions, i.e. edges that having been present in the initial population have disappeared during the crossover process and, thus, do not arise in successively iterated solutions. These lost edges can be mathematically quantified as $|\{(i, j) \in \{1, \ldots, n\} \times \{1, \ldots, n\} : p_{ij} \neq 0, q_{ij} = 0\}|$, with $\times$ denoting Cartesian product. A high number of lost edges is an indicative of poor inheritance performance or low transmission.
- *New* edges, i.e. non-parental edges showing in the new solution. Their number is given by $|\{(i, j) \in \{1, \ldots, n\} \times \{1, \ldots, n\} : p_{ij} = 0, q_{ij} \neq 0\}|$. A high number of new edges is an indicative of a highly exploratory behaviour in the algorithm.
- *Amplified* edges: they denote those edges that having been present in the population with $0 < p_{ij} < 1$, yield $q_{ij} = 1$ after the iterative application of the crossover operator. A high number of amplified edges simply indicates that the foreseen crossover iterations are insufficient, as increasing the repetitions makes it more difficult that a given edge is present at every single repetition of the operator.

It is important to note that due to numerical stability *new*, *lost* and *fully transmitted* edges can not be included in the divergence in Equation (A.6.1); therefore they will be analysed separately. Similarly, the number of amplified edges has been empirically found to be negligible for the number of selected iterations in subsequent simulations, and will be omitted in what follows.

[1] In formulations where subindices i and j are involved it is implicitly assumed that $i > j$, i.e. undirected trees.

A.6.2 Extended Experimental Setup

The ultimate goal of this research work is to compare the performance on a topology preservation level of a multi-parent crossover operator and classic two-parent recombination methods of EAs within a common, fair comparison framework. To this end we will use the same set of populations for all operators, i.e. the initialization phase as described in Section A.6.1.2 will be run just once for all crossover mechanisms being tested. Consequently, the set of aggregate connectivity matrices $\mathbf{P}$ representing the edge probability distribution that crossover operators should asymptotically impose on the newly produced offspring is thus known beforehand. The successive application of one-point/two-point/uniform crossover operators to generate offspring originating from 1) a randomly produced first parent and 2) a second parent randomly picked from those in the population will then follow. This will yield a series of new Dandelion codes whose decoding give rise to a set of connectivity matrices. After aggregation and normalization, those resulting matrices denoted as $\mathbf{Q}_{one-X}$, $\mathbf{Q}_{two-X}$ and $\mathbf{Q}_{u-X}$ will reflect the experimental edge distribution following from the application of parameter-controlled one-point/two-point/uniform crossover operation to the initial population. The most essential difference with respect to the application of the original experimental setup is the fact that the EA crossover operations will indeed output two matrices, one for the first offspring and a second for the complementary offspring, rather than a single one as with the R_*-driven operation.

The most distinctive of the crossover in Equation (A.5.1) is its probabilistically driven, component-wise and multi-parent nature. The next subsections explain how uniform, one-point, and two-point crossover methods have been tuned for the sake of fairness in their comparison to their multi-parent counterpart.

A.6.2.1 Uniform Crossover

The fact that uniform crossover has a probability-driven element-wise nature by itself makes it, a priori, the closest form of classical crossover to the R_*-driven operator. Let us define the parenthood ratio for uniform crossover PhR_{u-X} as the probability under which uniform crossover chooses the second parent whenever in need of selecting the origin of the feature at hand to spawn the first offspring. Likewise, 1-PhR_{u-X} will be the probability under which uniform crossover endorses element-wise the first parent for composing the first offspring or equivalently, the second parent for composing the second offspring.

Fig. A.2 illustrates how the R_*-driven recombination and the uniform crossover would generate new candidates from a given random parent: randomly picking values for every variable from the pool of candidate solutions in the population (R_*), or also at random but always considering the same candidate solution in the population (uniform-crossover). It should be clear that if the first offspring is considered, when $\mathrm{PhR}_{u-X} \to 1$ $\mathbf{Q}_{u-X} \to \mathbf{P}$, i.e. the edge distribution of the new candidate should follow more closely that of the entire population from which its second parent has been produced, with growing involvement of the latter due to the bias introduced through the element-wise PhR_{u-X} in the offspring formation.

A.6.2.2 One-point Crossover

The parenthood ratio for one-point crossover PhR_{one-X} is the ratio of the distance measured from the right end of the crossover mask to the crossover point where the origin of selected values for the first offspring switches from being the

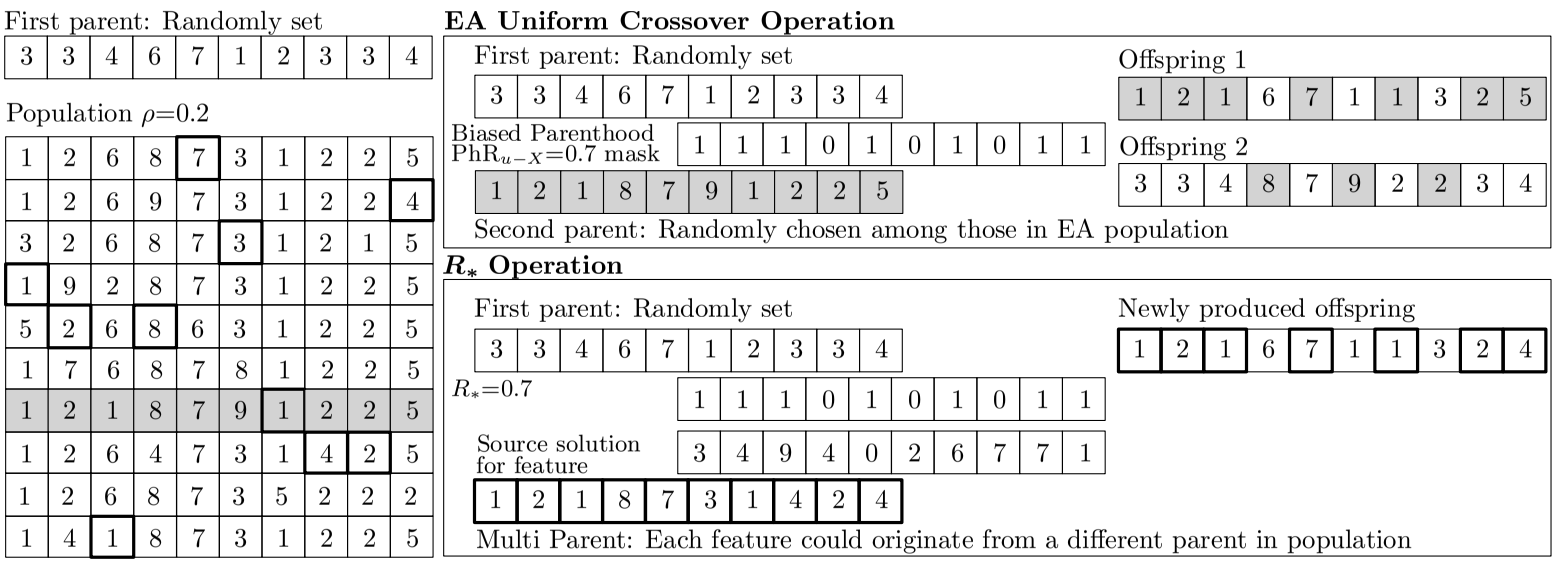

FIGURE A.2: Illustration of the effect of $R_* = 0.7$ and uniform crossover with Parenthood ratio 0.7 over a population of individuals with $\rho = 0.2$. (Reprinted by permission from: Springer Nature [33] ©2017)

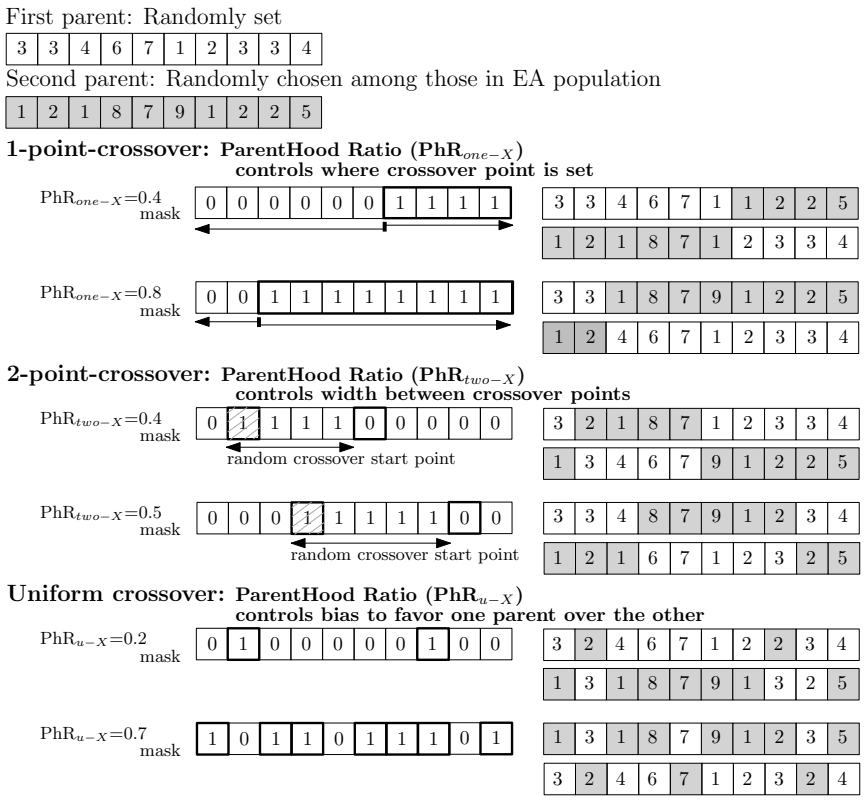

FIGURE A.3: Interpretation of the parenthood ratio to control one-point/two-point/uniform crossover parameters. (Reprinted by permission from: Springer Nature [33] ©2017)

randomly generated parent to being the one randomly picked from the population. Accordingly, 1-PhR$_{one-X}$ will be ratio of the distance to the crossover point where one-point crossover favors the random parent as origin of forthcoming values for the formation of the second offspring. It should be clear that as for the first offspring, $\mathbf{Q}_{one-X} \rightarrow \mathbf{P}$ when PhR$_{one-X} \rightarrow 1$, i.e. the edge distribution of the new solution should follow that of the entire population from which it is produced as the crossover point gets closer to the left-end of the mask.

A.6.2.3 Two-point Crossover

The parenthood ratio for two-point crossover PhR$_{two-X}$ stands for the ratio of the width of the candidates that is comprised between a first crossover point and the second crossover point in the crossover mask. In other words, it establishes the proportion of the width of the first offspring whose values will be taken from the parent randomly picked from the population. Correspondingly, 1-PhR$_{two-X}$ will denote the ratio of the width outside such crossover points where features derive from the random parent for the first offspring or the width inside crossover point where features come from random parent for the second offspring.

When it comes to the first offspring $\mathbf{Q}_{two-X} \rightarrow \mathbf{P}$ if PhR$_{two-X} \rightarrow 1$, i.e. the edge distribution of the new candidate solution should follow that of the

entire population from which it is produced. Fig. A.3 exemplifies this operation for offspring breeding as formally defined for the one-point/two-point/uniform crossovers.

A.7 Results and Discussion

In order to achieve statistically significant results, a number of experiments have been conducted for different population sizes $\vartheta \in \{10, 20, 50, 100\}$, number of nodes $n \in \{10, 100\}$ and number of independent iterations of the crossover operator at hand (correspondingly, $\{10^2, 10^3, 10^4\}$). These experiments have been operated over four hypothesized compositions of the memory given by dissimilarity ratios $\rho \in \{0.01, 0.1, 0.2, 1\}$. Dissimilarity ratio $\rho = 0.01$ corresponds to topologically very interrelated solutions within the population; $\rho = 0.1$ and $\rho = 0.2$ allow for intermediate convergence stages; and $\rho = 1$ stands for a completely randomized population to characterize early stages of the algorithms.

Nevertheless, and for the sake of non-repetition most of the discussion will gravitate around results corresponding to $\varphi = 100$, $n = 100$ and $\{100, 10000\}$ iterations, as for the stages, discussion will mainly correspond to near convergence state and results for $\rho \in \{0.1, 0.2, 1\}$ will be jointly examined in view of that all of them share a similar trend only scaled by a different factor. Equally, when analysing the effect of increasing parenthood ratios for EA crossovers only the first offspring will be examined. The reason being that from the way offspring has been spawn, it is straightforward that whatever the observed behaviour for the first is, that of the second will be just the opposite. Evolution plots of $D(\mathbf{P} \parallel \mathbf{Q})$ with $\mathbf{Q} = \mathbf{Q}_{u-X}$ as R_* and the crossover-dependent parameter PhR increases will be provided as a guarantee that disregarding the number of edges involved in its calculation, for sufficiently high values of R_* and PhR the divergence between $\mathbf{P}$ and $\mathbf{Q}$ drops asymptotically to zero[2].

A.7.1 Intuitions and Previous Results for R_* in Convergence

The discussion starts by recalling some prior intuitions and results from [21] in regards to multi-parent crossover operation with $\rho = 0.01$:

- Respect is a very restrictive condition to be achieved when dealing with polygamist breeding strategies, hence no fully transmitted edges should be expected for low/medium values of the R_* parameter.
- The mathematical stability in the computation of $D(\mathbf{P} \parallel \mathbf{Q})$ requires non-zero probability in both $\mathbf{P}$ and $\mathbf{Q}$. As R_* increases, so will do the number of elements from the initial population engaged in breeding the newly produced solution, i.e. edges participating in the divergence. Transmission should be better secured for higher R_* values.
- A similar reasoning holds for lost and new edges: the more the elements of the initial memory involved in the construction of a new solution by virtue of a higher R_*, the fewer the lost and new edges should be.

Three different R_* intervals (Fig. A.4a) were identified, namely:

- Very low R_* values: non-parental edges increase, while the number of transmitted edges is kept low. Almost as many lost edges as the upper bound

[2] A similar behavior was observed for $\mathbf{Q} \in \{\mathbf{Q}_{one-X}, \mathbf{Q}_{two-X}\}$.

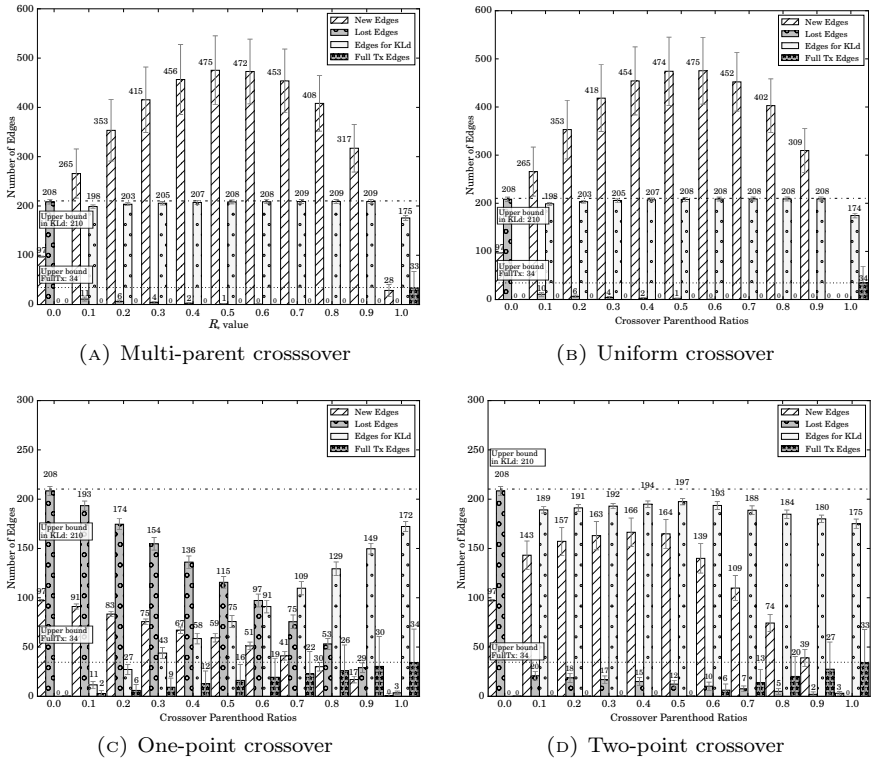

(A) Multi-parent crosssover

(B) Uniform crossover

(C) One-point crossover

(D) Two-point crossover

FIGURE A.4: Edge evolution under multiparent (a), uniform (b), 1-point (c) and 2-point (d) crossover strategies in near convergence stage, i.e., population variability ρ=0.01 and 10^4 iterations. (Reprinted by permission from: Springer Nature [33] ©2017)

participants for $D(\mathbf{P}||\mathbf{Q})$ are obtained. The crossover process does not propagate the topological characteristics of the initial population under such low values of its controlling parameter, hence jeopardizing the exploitation capability expected from this operator. To buttress this statement a closer look at the low R_* range is given in Fig. A.5a (left) for 10^2 iterations of the operator. This plot shows a smooth continuity in the number of lost edges and those participating in the divergence within $R_* = 0$ to $R_* = 0.06$.

- Intermediate values ($0.4 < R_* < 0.6$): an inflection point is noticed in the evolution of the number of non-parental/new edges. In this interval, given a sufficient number of iterations to properly characterize $\mathbf{Q}$, the number of edges for the computation of the divergence becomes nearly steady around its upper limit. The exploitation provided by R_* becomes relevant.
- High R_* values: edges participating in the measure of divergence will either remain steady near their upper bound, or eventually decrease in the case edges capable of being fully transmitted actually start to reach that status. This fact comes along with a decrease in the number of new edges in benefit of the set of edges participating in the computation of the divergence, from which a fraction will be amplified and eventually consolidated as fully

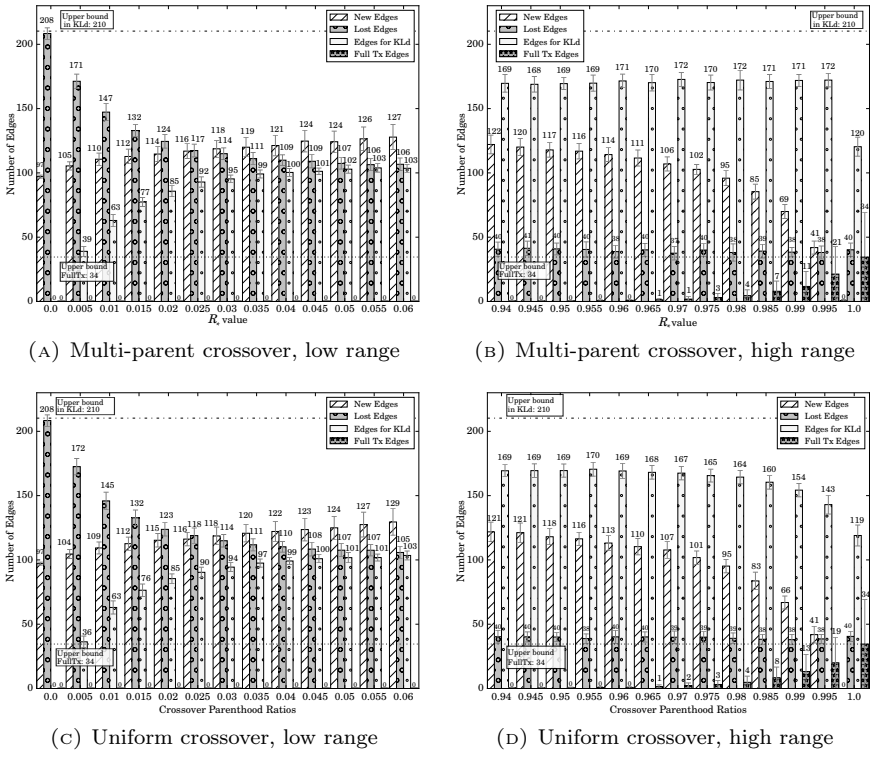

(A) Multi-parent crossover, low range

(B) Multi-parent crossover, high range

(C) Uniform crossover, low range

(D) Uniform crossover, high range

FIGURE A.5: Magnified views of edge evolution for multi-parent (a) and (b) and uniform crossover (c) and (d) when operating in R_* and PhR lowest $[0, 0.06]$ and highest $[0.94, 1.0]$ ranges and 10^2 iterations. (Reprinted by permission from: Springer Nature [33] ©2017)

transmitted edges. A closer look at R_* values in the range $[0.94, 1.00]$ for 100 iterations is given in Fig. A.5b, where continuity is again evinced in the number of fully transmitted and new edges in the depicted range.

A.7.2 Similarities and Differences between Multi-parent and Standard Crossover Operators

All the previous being discussed, the analysis follows by Fig. A.4 that depicts edge evolution plots for all considered crossover schemes. A close look to Fig. sA.4b and A.4a suffices for noticing the clear equivalence between the multi-parent recombination and the uniform crossover for highly correlated populations. This conformity is further buttressed by the magnified plots with fine-grained values for R_* and PhR_{u-X} over the lowest and highest operational ranges shown in Fig. A.5, as well as by the measured $D(\mathbf{P}||\mathbf{Q})$ evolution graphs in Fig. A.6.

Again focusing on highly correlated populations, the following facts can be inferred in terms of heritability:

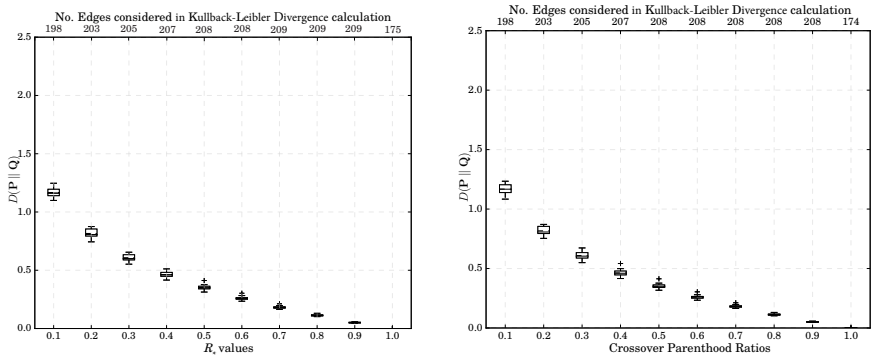

(A) Multi-parent crossover (B) Uniform crossover

FIGURE A.6: Evolution of Kullback-Leibler divergence $D(\mathbf{P}||\mathbf{Q})$ for the first crossover offspring and the individual produced by the R_*-driven multi-parent operator with ρ=0.01 and 10^4 iterations. (Reprinted by permission from: Springer Nature [33] ©2017)

- Respect is best preserved in one-point crossover. Increasing the number of crossover points of the crossover operator at hand delays the presence of full-transmitted edges. First fully transmitted edges occur as soon as PhR_{one-X}=0.1 for one-point crossover, while for two-point, uniform or multi-parent crossovers rates need to grow up to $\text{PhR}_{two-X} = 0.6$, $\text{PhR}_{u-X} = 0.9$ and $R_* = 0.9$, respectively.
- Fail Transmission (i.e. lost edges) behave quite the opposite way because parental information is better kept by multi-parent crossover and the uniform crossover. In both cases the number of lost edges drops dramatically before reaching $\text{PhR} = R_* = 0.1$ and completely disappears around $\text{PhR} = R_* = 0.6$. For one-point and two-point crossover lost edges remain until PhR=1 is reached. While this asymptotic drop after PhR=0 still holds for two-point crossover, it is noticeable that for one-point crossover even if the number of lost edges still decreases, their amount multiplies by 10 that observed for two-point crossover.
- Partial Transmission (i.e. edges participating in $D(\mathbf{P}||\mathbf{Q})$) behaves in between the previous two extremal patterns, as the overall summation of fully transmitted edges, lost edges, and edges for $D(\mathbf{P}||\mathbf{Q})$ calculation should remain invariable and should fully characterize the population at hand under any given value of the crossover parameter.
- Exploration capability (i.e. the generation of new edges) will be higher as the number of crossover points increases. An exception occurs for one-point crossover, whose mixture of values is abrupt and results in the number of new edges describing a bell-shaped curve with respect to PhR, reaching its top for intermediate values.

Generally speaking the lack of heritability preservation is manifest in randomness. However, when dealing with topologically uncorrelated solutions within the initial population the evolution of the divergence will still obey the same decreasing behavior as in the previously discussed scenario. This trend only reflects an *homogenization* of $\mathbf{Q}$ towards an already uniformly distributed $\mathbf{P}$. Consequently, no fully transmitted edges are achieved and PhR and R_* values as high

as 1 cannot refrain lost edges from appearing. Summarizing, for random (ρ=1) or loosely correlated ($\rho = 0.1$) populations several relevant behaviors in regards to heritability can be observed (Fig. A.7):

- Respect or full transmission completely disappear for all crossover methods and populations only differing by 10%.
- Fail Transmission is sustained no matter how high PhR/R_* is.
- The multi-parent crossover is found to be the most exploratory operator in this benchmark at initial and intermediate stages of the search process. Its capability to generate new edges is superior as Fig. A.7g ($\rho = 0.1$) and Fig. A.7h ($\rho = 1$) clearly show. However, it should be remarked that in practice the apparently lower exploration of the other recombination methods could be compensated by higher values of their mutation operators.

A.8 Conclusions

This chapter has elaborated on the topological preservation of Dandelion encoded trees under different recombination schemes: one-point, two-point and uniform crossover operators found in naïve Evolutionary Algorithms, and a stochastically-driven multi-parent crossover approach originally known as Global Discrete Recombination, which has been recently utilized for unveiling the similarities of the Harmony Search algorithm and ($\mu + 1$) Evolution Strategies. The particularities (stochastically-driven, symbol-wise, polygamy) of the multi-parent operator motivated previous work where measures of statistical divergence and statistics of different edge classes were analyzed to explain how inheritance was affected by such particularities. This work spans beyond this initial study to include, within the same framework, heritability figures produced by one-point, two-point and uniform crossover schemes. From the discussed simulation results it is concluded that the multi-parent and the conventional uniform crossover are almost equivalent to each other, except for a scaling in their parameters under a near-convergence stage of the population. This has been evinced by the results discussed in this chapter, where the exploration capabilities of the multi-parent crossover, measured in terms of the number of produced "new" edges, is only matched by that of a conventional uniform crossover if the control parameter of the latter is conveniently tweaked.

This must be conceived as an application-agnostic, non-biased result in the context of tree optimization that falls in line with ongoing discussions within the community around the real need for new metaheuristic operators [38], [39]. The often referred outstanding performance of different metaheuristics in comparison with other solvers should be carefully assessed and supported by 1) a justified choice of the value controlling the operators of each algorithm; 2) the incorporation of problem-specific knowledge in the definition of the operators, along with a proof of the statistically significance of the obtained performance enhancement; 3) a solid application-agnostic study aimed at clearly evincing performance without any problem-related design bias, such as the one presented here for Dandelion-coded populations.

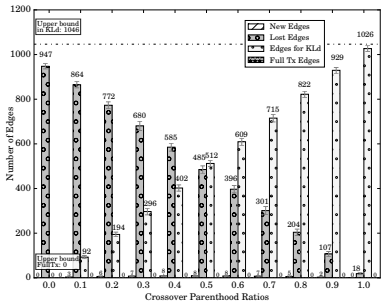

(A) One-point crossover, ρ=0.1

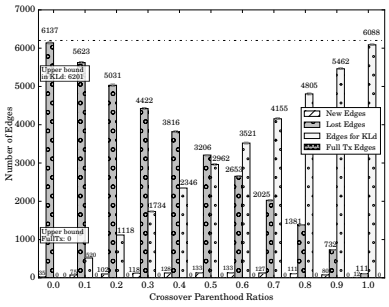

(B) One-point crossover ρ=1

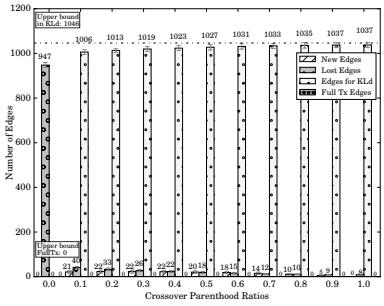

(C) Two-point crossover, ρ=0.1

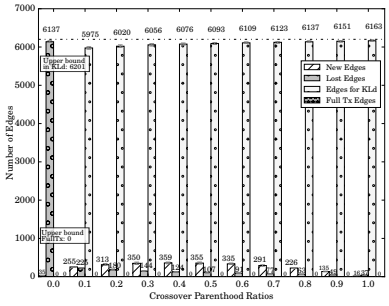

(D) Two-point crossover, ρ=1

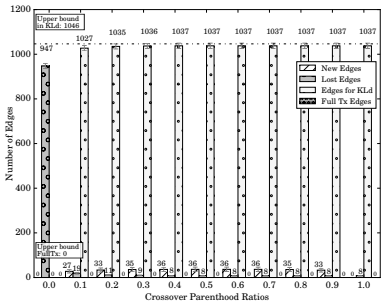

(E) Uniform crossover, ρ=0.1

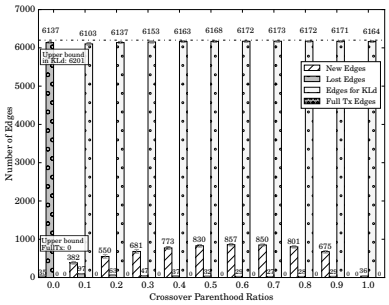

(F) Uniform crossover, ρ=1

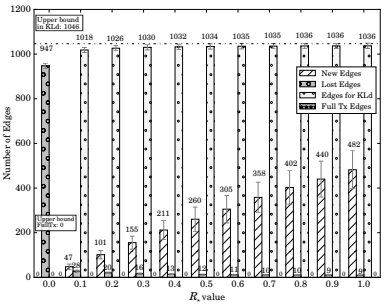

(G) Multi-parent crossover, ρ=0.1

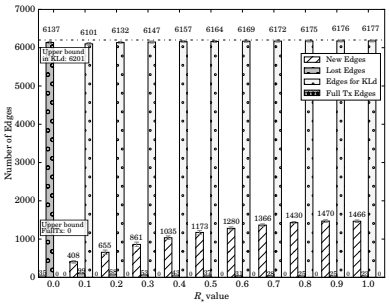

(H) Multi-parent crossover, ρ=1

FIGURE A.7: Edge evolution under one-point/two-point/uniform/multi-parent crossovers with ρ=0.1 (left) and ρ=1 (right) and 10^4 iterations. (Reprinted by permission from: Springer Nature [33] ©2017)

References

[appA1] E. Türetken, G. González, C. Blum, *et al.*, "Automated reconstruction of dendritic and axonal trees by global optimization with geometric priors", *Neuroinformatics*, vol. 9, no. 2, pp. 279–302, Sep. 2011. DOI: 10.1007/s12021-011-9122-1 (cited on p. 199).

[appA2] M. A. Djauhari and S. L. Gan, "Optimality problem of network topology in stocks market analysis", *Physica A: Statistical Mechanics and its Applications*, vol. 419, pp. 108–114, 2015. DOI: https://doi.org/10.1016/j.physa.2014.09.060 (cited on p. 199).

[appA3] R. Durrett, "Some features of the spread of epidemics and information on a random graph", *Proc. Natl. Acad. Sci.*, vol. 107, no. 10, pp. 4491–4498, 2010. DOI: 10.1073/pnas.0914402107 (cited on p. 199).

[appA4] O. Borůvka, "On a minimal problem", *Práce Moravské Pridovedecké Spolecnosti*, vol. 3, pp. 37–58, 1926 (cited on p. 199).

[appA5] J. B. Kruskal, "On the shortest spanning subtree of a graph and the traveling salesman problem", *Proc. Amer. Math. Soc.*, vol. 7, no. 1, pp. 48–50, 1956. DOI: 10.1090/S0002-9939-1956-0078686-7 (cited on p. 199).

[appA6] R. C. Prim, "Shortest connection networks and some generalizations", *Bell Syst. Tech. J.*, vol. 36, pp. 1389–1401, 1957 (cited on p. 199).

[appA7] C. F. Bazlamaçcı and K. S. Hindi, "Minimum-weight spanning tree algorithms a survey and empirical study", *Computers & Operations Research*, vol. 28, no. 8, pp. 767–785, 2001. DOI: 10.1016/S0305-0548(00)00007-1 (cited on p. 199).

[appA8] S. Picciotto, "How to encode a tree", PhD thesis, University of California, San Diego, 1999, p. 136 (cited on pp. 200, 203).

[appA9] A. M. Pérez-Bellido, S. Salcedo-Sanz, E. G. Ortíz-García, *et al.*, "A dandelion-encoded evolutionary algorithm for the delay-constrained capacitated minimum spanning tree problem", *Comput. Commun.*, vol. 32, no. 1, pp. 154–158, 2009. DOI: 10.1016/j.comcom.2008.09.030 (cited on p. 200).

[appA10] I. Landa-Torres, D. Manjarres, S. Gil-López, *et al.*, "A preliminary approach to near-optimal multi-hop capacitated network design using grouping-dandelion encoded heuristics", in *2012 IEEE 17th Int. Work. Comput. Aided Model. Des. Commun. Links Networks, CAMAD 2012*, IEEE, 2012, pp. 85–89. DOI: 10.1109/CAMAD.2012.6335385 (cited on p. 200).

[appA12] L. Zhang, M. Lampe, and Z. Wang, "Topology design of industrial ethernet networks using a multi-objective genetic algorithm", in *2011 6th International ICST Conference on Communications and Networking in China (CHINACOM)*, Aug. 2011, pp. 735–741. DOI: 10.1109/ChinaCom.2011.6158251 (cited on p. 200).

[appA13] S. Salcedo-Sanz, M. Naldi, Á. M. Perez-Bellido, *et al.*, "Evolutionary optimization of service times in interactive voice response systems", *IEEE Trans. Evol. Comput.*, vol. 14, no. 4, pp. 602–617, Aug. 2010. DOI: 10.1109/TEVC.2009.2039142 (cited on p. 200).

[appA14] J. Sabattin, C. Contreras-Bolton, M. Arias, *et al.*, "Evolutionary optimization of electric power distribution using the dandelion code", *Journal of Electrical and Computer Engineering*, vol. 2012, 2012. DOI: 10.1155/2012/738409 (cited on p. 200).

[appA15] X.-S. Yang, *Nature-Inspired Metaheuristic Algorithms*. Frome, UK: Luniver Press, 2008 (cited on p. 200).

[appA16] S. Salcedo-Sanz, J. Del Ser, I. Landa-Torres, *et al.*, "The coral reefs optimization algorithm: A novel metaheuristic for efficiently solving optimization problems", *The Scientific World Journal*, vol. 2014, 2014. DOI: 10.1155/2014/739768 (cited on p. 200).

[appA17] Z. W. Geem, J. H. Kim, and G. Loganathan, "A new heuristic optimization algorithm: Harmony search", *Simulation*, vol. 76, no. 2, pp. 60–68, 2001. DOI: 10.1177/003754970107600201 (cited on pp. 200, 204).

[appA18] I. Rechenberg, *Evolutionsstrategie — Optimierung technischer Systeme nach Prinzipien der biologischen Evolution*. Fromman-Holzboog-Verlag, 1973. DOI: 10.1002/fedr.19750860506 (cited on p. 200).

[appA19] D. Weyland, "A rigorous analysis of the harmony search algorithm: How the research community can be misled by a "novel" methodology", *Int. J. Appl. Metaheuristic Comput.*, vol. 1, no. 2, pp. 50–60, Apr. 2010. DOI: 10.4018/jamc.2010040104 (cited on p. 200).

[appA20] ——, "A critical analysis of the harmony search algorithm—how not to solve sudoku", *Operations Research Perspectives*, vol. 2, pp. 97–105, 2015. DOI: 10.1016/j.orp.2015.04.001 (cited on pp. 200, 206).

[appA22] T. Bäck, *Evolutionary Algorithms in Theory and Practice: Evolution Strategies, Evolutionary Programming, Genetic Algorithms*. New York, NY, USA: Oxford University Press, Inc., 1996 (cited on p. 201).

[appA23] C. Palmer and A. Kershenbaum, "Representing trees in genetic algorithms", in *Proc. First IEEE Conf. Evol. Comput. IEEE World Congr. Comput. Intell.*, IEEE, 1994, pp. 379–384. DOI: 10.1109/ICEC.1994.349921 (cited on pp. 202, 203).

[appA24] F. Rothlauf, *Representations for Genetic and Evolutionary Algorithms*. Springer-Verlag Berlin Heidelberg, 2006. DOI: 10.1007/3-540-32444-5 (cited on p. 202).

[appA25] M. Gen and R. Cheng, *Genetic Algorithms and Engineering Optimization*. Hoboken, NJ, USA: John Wiley & Sons, Inc., 2000, p. 512 (cited on p. 202).

[appA26] T. Paulden and D. K. Smith, "Recent advances in the study of the dandelion code, happy code, and blob code spanning tree representations", in *IEEE Int. Conf. Evol. Comput. (CEC)*, IEEE, 2006, pp. 2111–2118. DOI: 10.1109/CEC.2006.1688567 (cited on pp. 203, 207).

[appA27] J. Gottlieb, B. A. Julstrom, G. R. Raidl, *et al.*, "Prüfer Numbers: A Poor Representation of Spanning Trees for Evolutionary Search", in *Spector L (ed) GECCO'01 Proc. of the 3rd Annual Conference on Genetic and Evolutionary Computation*, San Francisco, 2001, pp. 343–350 (cited on p. 203).

[appA28] S. Caminiti and R. Petreschi, "String coding of trees with locality and heritability", in *Computing and Combinatorics*, L. Wang, Ed., Berlin, Heidelberg: Springer Berlin Heidelberg, 2005, pp. 251–262. DOI: 10.1007/11533719_27 (cited on p. 203).

[appA29] Ö. Eğecioğlu and J. B. Remmel, "Bijections for Cayley trees, spanning trees, and their q-analogues", *J. Comb. Theory, Ser. A*, vol. 42, no. 1, pp. 15–30, May 1986. DOI: 10.1016/0097-3165(86)90004-X (cited on p. 203).

[appA30] S. Caminiti and R. Petreschi, "Parallel algorithms for dandelion-like codes", in *Computational Science – ICCS 2009*, G. Allen, J. Nabrzyski, G. D. Seidel Edward and van Albada, *et al.*, Eds., Berlin, Heidelberg: Springer Berlin Heidelberg, 2009, pp. 611–620. DOI: doi:10.1007/978-3-642-01970-8_60 (cited on p. 203).

[appA31] E. Thompson, T. Paulden, and D. K. Smith, "The dandelion code: A new coding of spanning trees for genetic algorithms", *IEEE Trans. Evol. Comput.*, vol. 11, no. 1, pp. 91–100, Feb. 2007. DOI: 10.1109/TEVC.2006.880730 (cited on pp. 203, 207).

[appA32] T. Paulden and D. K. Smith, "From the Dandelion Code to the Rainbow code: a class of bijective spanning tree representations with linear complexity and bounded locality", *IEEE Trans. Evol. Comput.*, vol. 10, no. 2, pp. 108–123, 2006. DOI: 10.1109/TEVC.2006.871249 (cited on pp. 203, 207).

[appA37] T. Bäck, F. Hoffmeister, and H.-P. Schwefel, "A survey of evolution strategies", in *Proc. Int. Conf. on Genetic Algorithms*, Morgan Kaufmann, 1991, pp. 2–9 (cited on p. 206).